Modelling Eruptions and Edge Stability in Tokamak Plasmas

Amelia Elizabeth Louise Lunniss

Doctor of Philosophy

University of York

Physics

September 2016

Abstract

In the high confinement mode (H-mode) of tokamak operation, sharp gradients and the resulting high bootstrap current near the edge of a tokamak plasma (the pedestal) typically trigger eruptions called edge localised modes (ELMs). On the ITER scale, these have the potential to cause unacceptable erosion of materials. However, there exist scenarios, such as the quiescent H-mode (QH), where there are no ELMs. The ELITE code was originally developed to efficiently calculate the edge ideal MHD stability properties of tokamaks, optimised for the intermediate-high toroidal mode number, n, modes associated with ELMs. In QH-mode the limiting MHD is typically low n. Chapter 3 presents the extension of the ELITE code to arbitrary n. Chapter 4 presents successful benchmarks against the original ELITE code as well as GATO and MARG2D at low n. A first application of the new ELITE code was to study the stability of the QH-mode pedestal in DIII-D. Results from this study are presented in Chapter 5, which show the presence of low n phenomena.

Additionally, understanding the pedestal performance losses in JET ITER-like wall (ILW) plasmas is vital to the success of future JET and ITER experiments. Chapter 6 presents an inter-ELM pedestal stability study, which compares the pedestal evolution to the criteria of the pedestal structure model, EPED. These results suggest that maximising the region of plasma that has second stability access will lead to the highest pedestal heights and, therefore, best confinement - a key result for optimising the fusion performance of JET and future tokamaks, such as ITER.

Contents

List of Tables

List of Figures

Acknowledgements

Firstly, I would like to thank my supervisor, Howard Wilson, for all his advice, support and patience. He has been an inspiring and encouraging supervisor and I will be forever grateful for having been his PhD student.

There are many other people who I would like to thank for helping me in the last 4 years, whilst I have been working on this PhD. Firstly, Phil Snyder for all his advice and mentorship. Along with welcoming me as a visitor into the General Atomics theory group, he made sure that I learnt an invaluable amount from each visit, and that I was part of the DIII-D community. My trips to General Atomics were a real highlight of my PhD. Rich Groebner, for the time he spent teaching me about experimental reconstruction and QH-mode. Tom Osborne, for providing me with interesting QH-mode data and spending time helping me fully appreciate the experimental data in preparation for my EPS presentation. Keith Burrell and Xi Chen, for their interesting QH-mode insights. Richard Buttery, Wayne Solomon, George McKee, Andrea Garofalo, Jeff Candy, Gary Staebler and Alan Turnbull for making my visits to San Diego memorable.

Samuli Saarelma, for his advice and mentorship. Firstly, for providing me with access to his JET stability analysis tools, then spending the vast amount of time required for me to learn how to use them properly, both during my extended visit to Culham and whilst I was back at YPI. Also, for all his insights over the past year. Costanza Maggi and Lorenzo Frassinetti, for providing me with such an interesting JET dataset, and their input into the development of the analysis techniques. Matthew Leyland, for providing me with the initial JET data to analyse, and advising me on HRTS for this thesis. David Dickinson, for his input into my JET research.

Jarrod Leddy, for proof reading and helping me with the LaTeX learning curve that I experienced in writing this thesis. Koki Imada, for carefully reading chapters of this thesis. Chris Bowman, for all his interesting physics discussions which provided me with many a welcome break from writing up. Also, many thanks to Arka Bokshi, who has been my write up buddy! It has made the experience much more bearable, and his encouragement has been unwavering.

I would like to thank my friends. Without them, my PhD would have been a much lonelier experience! Laura and Lucy, who have been great to me over the last 4 years. Also my friends at YPI, where I have spent the last 5 years. Thank you for providing me with a working environment full of fun. I am sure I have made some friends for life! Finally, I would like to thank my family: first and foremost my husband

Will, for whole-heartedly supporting me even when I was away for months at a time, and then for putting up with me while I have been writing this thesis! Secondly, to my parents, Libby and Bob, I would not be where I am now without them. Finally, my brother Jimmy, for being supportive over the last 4 years.

Declaration

The work in this thesis was performed at York Plasma Institute, supervised by Prof. H. R. Wilson. Additionally, research was undertaken in extended research visits to General Atomics and Culham Centre for Fusion Energy. I declare that the work presented in this thesis has not been submitted previously for a degree in this or any other university. All sources are acknowledged as references. I declare that this work is my own except where indicated by appropriate citation and with the exceptions given below.

- The derivation and implementation of the extensions to the ELITE formalism and code, presented in Chapters 3 and 4, is the result of a collaboration between A. E. L. Lunniss and Prof. H. R. Wilson.
- The model equilibria used in Chapter 4, including the width scaling study equilibria, were provided by Dr P. B. Snyder.
- The GATO and MARG2D calculations in Chapter 4 were performed by Dr P. B. Snyder.
- The QH-mode EFIT reconstruction and VARYPED runs in Chapter 5 were performed by Dr T. H. Osborne.
- The JET stability analysis framework used in Chapter 6 has been developed and maintained by Dr S. Saarelma.
- The EFIT reconstructions and the ELM cycle window analysis for the JET-ILW pulses in Chapter 6 was performed by Dr L. Frassinetti, with input from Dr C. F. Maggi.
- The $s - \alpha$ diagrams in Chapter 6 were provided by Dr D. Dickinson.
- The ELM traces in Chapter 6 were produced by Dr A. Thornton, with input from Prof. H. R. Wilson.

This research has been presented at the following conferences:

- The research in Chapters 3, 4 and 5 were presented as an oral at the European Physical Society Plasma Physics Conference (2016). The contributed paper can be found here: http://ocs.ciemat.es/EPS2016PAP/pdf/O4.120.pdf

- The research in Chapter 6 was presented as an oral at the Institute of Physics Plasma Physics Conference (2016).
- The research in Chapters 3 and 4 were presented as a poster at the American Physical Society Division of Plasma Physics Conference (2015).

Chapter 1

Introduction

1.1 Global energy outlook

The 2015 UN Population Division estimated that total global population will increase from 7.35 billion to 11.21 billion by the year 2100 [1]. This increase in population will further increase demand for resources such as energy, with global energy demands expected to grow by 56% in just 30 years from 2010 to 2040 [2]. As the non-OECD countries further develop, their energy demands will also increase [3].

Furthermore, this trend is predicted to lead to a 46% increase in energy related carbon dioxide emissions, mostly from non-OECD countries and the continued reliance on fossil fuels [2]. The use of fossil fuels, i.e. oil, gas and coal, as the main global source of energy has distinct issues. Firstly, they are of limited supply and the oil and gas reserves are depleting; by various estimates, there are a few tens of years left at most [3].

The second, and arguably the most important issue, is that the burning of fossil fuels leads to the release of carbon dioxide into the atmosphere. It is widely accepted that this has lead to an increase in global temperatures through the greenhouse gas effect [4]. Rising temperatures have a number of unacceptable consequences for the global environment, such as the melting of the polar ice caps, more extreme weather events, the rising of sea levels, and the rising of ocean temperatures [4]. These can have a wide impact on global food supply, on both land with uncertainty in crop production [4], and in the ocean due to the rising sea temperatures changing the ocean chemistry. It also causing major threats to the world's coral reefs, which the ocean ecosystems depend on. For example, as reported in 2016, coral bleaching is greatly affecting 95% of the reefs that together form the Great Barrier Reef [5].

Broadly speaking, there are two issues with global energy production: the globe needs to be able to keep up with this ever increasing demand in energy supply, which is important in alleviating poverty [4], and secondly this needs to be done while ideally halting the ever increasing emission of carbon dioxide in the production of energy.

Therefore the globe needs energy sources that do not produce carbon dioxide emissions, and that can provide enough output to reach both the current and predicted surge in demand. Current possibilities include nuclear fission, solar, wind, tidal, biofuel and hydroelectric power. However, these all have significant limitations.

Nuclear fission has the ability to produce power on the scales that are required for significant global energy production. It also has the advantages of predictable costs in the long-term, as it is not affected by the fossil fuel market, and it can enhance energy security and provide climate-change mitigation, as it is carbon dioxide free [6]. However, there are significant disadvantages such as the disposal of long-lived radioactive waste produced in the process, political concerns from the production of nuclear material, and public opposition from the concerns for potential disasters, as seen in Chernobyl [3].

Clean energy solutions, such as wind and solar power, have significant issues due to their intermittent nature, efficiency, cost and energy density [3], which have to be addressed in order for them to be a solution to the world energy problem. All these technologies provide a valuable contribution to energy production, but it is very unlikely they could replace fossil fuels entirely.

Therefore, a new technology is needed to fill the void in energy demand and supply without the use of fossil fuels. Nuclear fusion is in development and is a very attractive option in the long term for global energy production. Its fuel production is secure and has long-term virtually unlimited availability, there is no carbon dioxide production, all waste is short-lived and there are inherent safety features in the process which do not allow for a run-away nuclear accident [7]. It is also crucially predicted to be commercially viable, which is critical in engaging industry to develop technologies associated with future power plants.

1.2 Fusion energy

Fusion is a nuclear process where light atoms combine exothermically, which results in an overall reduction in total mass of the resulting nucleus. The difference in mass is released in the form of kinetic energy [8, 9], as stated by Einstein's famous equation, $E = mc^2$. Fusion occurs naturally throughout the universe in stars, where hydrogen combines to form helium, releasing energy in the process. The basis for terrestrial fusion research is to harness this process on a smaller scale, such that fusion becomes a new economically viable energy source. The fusion reaction that occurs in the CNO process in the Sun does not have a large enough reaction cross-section to be viable on Earth. The reaction rate, R_{ij}, for a fusion reaction between two nuclei, i and j, assuming that the nuclei are hard spheres is given by:

$$R_{ij} = n_i n_j < \sigma v > V \tag{1.1}$$

where n_i and n_j are the density of the two nuclei, $< \sigma v >$ is the reactivity, V is the volume, σ is the reaction cross-section and v is the relative velocity of the nuclei [10]. The velocity-averaged cross-section as a function of temperature is shown for three possible fusion reactions with large reaction cross sections in figure 1.1.

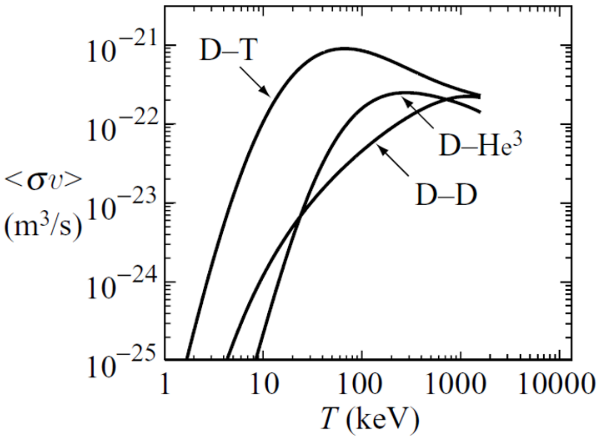

Figure 1.1: Velocity-averaged cross sections. $\sigma v = R_{ij}/n_i n_j$ (m ^{3}/s) for the D-T, D-D and D-He^3 fusion reactions as a function of temperature (keV). Reproduced from [10].

As figure 1.1 shows, the three most promising fusion reactions are deuterium-tritium (D-T), deuterium-deuterium (D-D) and deuterium-helium (D-He^3). The most favourable reaction, due to the significantly lower temperature (10keV) required to achieve a reactor-relevant cross-section, is the D-T reaction. This reaction releases 17.6 MeV of energy, and is given by [8]:

$$^2\text{D} +^3\text{T} \rightarrow^4\text{He}(3.5\text{MeV}) + \text{n}(14.1\text{MeV}) \tag{1.2}$$

where the He nuclei is also known as an α-particle.

1.3 Ignition

As the plasma is heated to 10 keV or above, the plasma becomes in a thermonuclear state. The fusion reaction given in equation 1.2 contains energy released from both the α-particle and the neutrons. The α-particles can heat the plasma using the 3.5 MeV of energy released [8]. As heating of the plasma occurs, the α-particle heating provides an increasing fraction of the total heating required by the plasma. When adequate confinement is obtained, a point is reached at which the plasma temperature can be maintained against the energy lost from the plasma, without the requirement for external heating [8]. This is known as ignition. This is summarised by the fusion triple product, which is a figure of merit used for fusion plasmas. It is related to the ignition condition, known as the Lawson criteria, but the fusion triple product has been modified to include the effects of α-particle heating [8]. For a typical D-T plasma with parabolic density (n) and temperature (T) profiles, this is given by [8]:

$$nT\tau_E > 5 \times 10^{21}\text{m}^{-3}\text{KeVs} \tag{1.3}$$

where τ_E is the energy confinement time. This equation shows the density, temperature and confinement time required to achieve ignition in a fusion plasma. Another useful figure of merit is Q, which is the measure of success in approaching the ignition conditions, also known as fusion gain [8]. Q is the ratio of thermonuclear power produced to the heating power supplied:

$$Q = \frac{P_{out} - P_{in}}{P_{in}} \tag{1.4}$$

where P_{out} is the total thermal power out of the plasma, and P_{in} is the heating power in [10]. At ignition there is no external heating and $Q \to \infty$ [8]. $Q = 1$ is known as break-even, and corresponds to an α particle heating which is 20% of the supplied heating power [8]. Note that ignition is not a requirement for a future reactor; only that Q is high.

1.4 Definition of a plasma

A plasma is a quasi-neutral gas of charged and neutral particles which exhibits collective behaviour [9], and is known as the fourth state of matter [11]. At reactor relevant temperatures, the D-T gas exists in the form of an ionised gas where the atoms are dissociated into ions and electrons [9]. There are three criteria that an ionised gas must satisfy to be called a plasma. These are given in terms of three plasma parameters: the characteristic length scale of the system, which is given by the Debye length (λ_D), the characteristic parameter for collisionality, which is given by the plasma parameter (Λ_D), and the characteristic inverse time-scale, which is given by the plasma frequency (ω_p) [10]. The Debye length is the characteristic length in the system which describes the finite distance over which a shielding of ions by electrons occurs in a plasma [8]. This happens for every ion, and the inverse occurs for every electron [8]. The three conditions for a system with length (L) are given by [9]:

$$\begin{aligned} &\lambda_D \ll L \\ &\Lambda_D \gg 1 \\ &\tau\omega_p > 1 \end{aligned} \tag{1.5}$$

where τ is the the mean time between collisions with neutral atoms [9]. The plasma parameter Λ_D represents the number of charged particles located within a Debye sphere, whose radius is given by the Debye length [10]. The quasi-neutrality condition is defined by the first condition and the collective behaviour arises from the second condition [9]. The third condition says the plasma behaves as a plasma rather than a neutral gas and is to do with collisions: the collisions occur infrequently enough with neutral atoms such that the motion is dominated by electromagnetic forces rather than hydrodynamic ones [9].

All methods of producing thermonuclear fusion require the plasma to be confined. There are currently two main routes that researchers are exploring: the first is inertial confinement fusion (ICF) and the second is magnetic confinement fusion (MCF). These two different approaches use very different regimes of n and τ_E. ICF uses large lasers to rapidly compress and heat a solid pellet of D-T fuel, which requires a very short confinement time in combination with high density and temperature [12]. MCF occurs on much longer time-scales, such that the τ_E is much greater, but occurs at much lower densities [8]. It exploits the ionisation of the atoms in a plasma such that their charge can be manipulated using magnetic fields. This is the type of fusion considered in this thesis.

1.5 Magnetic confinement fusion

Magnetic confinement fusion (MCF) begins with the equation of motion for a charged particle in a magnetic field. This is known as the Lorentz force [10]. When there is a finite magnetic field ($\mathbf{B}$) and zero electric field this is given by:

$$m\frac{d\mathbf{v}}{dt} = q\mathbf{v} \times \mathbf{B} \tag{1.6}$$

where m is the mass of the particle, $\mathbf{v}$ is the velocity of the particle and q is the charge of the particle [10]. When there is a uniform magnetic field, the components of this equation yield another characteristic plasma frequency, the cyclotron frequency (ω) [8, 9]:

$$\omega_c = \frac{qB}{m} \tag{1.7}$$

where there is a cyclotron frequency. Separation of variables and solutions of these equations yield the Larmour radius (ρ). This is the radius of circular motion of a charged particle in a magnetic field, and is given by [8, 9]:

$$\rho = \frac{mv_\perp}{qB} \tag{1.8}$$

where $v_\perp$ is the velocity of the particle perpendicular to the magnetic field. There is a different Larmour radius for the electrons and ion ($\rho_i \gg \rho_e$). Therefore, there is circular gyration of the charged particle about a fixed guiding centre, where the particle travels in a helical motion at a constant velocity in the direction of the magnetic field [8, 9]. In magnetic fusion there are non-uniform electromagnetic fields in the device and these lead to a number of different drifts: the $\underline{E} \times \underline{B}$ drift, the $\nabla \underline{B}$ drift, the curvature drift and the diamagnetic drift [8, 9, 10], which are important when considering the design of the device.

1.6 The tokamak

The tokamak is an axisymmetric toroidal magnetic confinement plasma device, first developed in the late 1950s [8, 10]. The tokamak contains field coils positioned around the plasma, which generate a toroidal field, and wind the long way around the torus. The resultant field is a non-uniform curved magnetic field. This causes charged particles to form an $\underline{E} \times \underline{B}$ drift due to charge separation and results in loss of confinement. Therefore a poloidal magnetic field is used, which is the short way around the torus. This is achieved by ramping the current in the solenoid which generates a loop voltage, which in turn generates a toroidal current which creates the poloidal field [8]. The two magnetic fields combine to form a helical magnetic field. A schematic of the tokamak is shown in figure 1.2 (a).

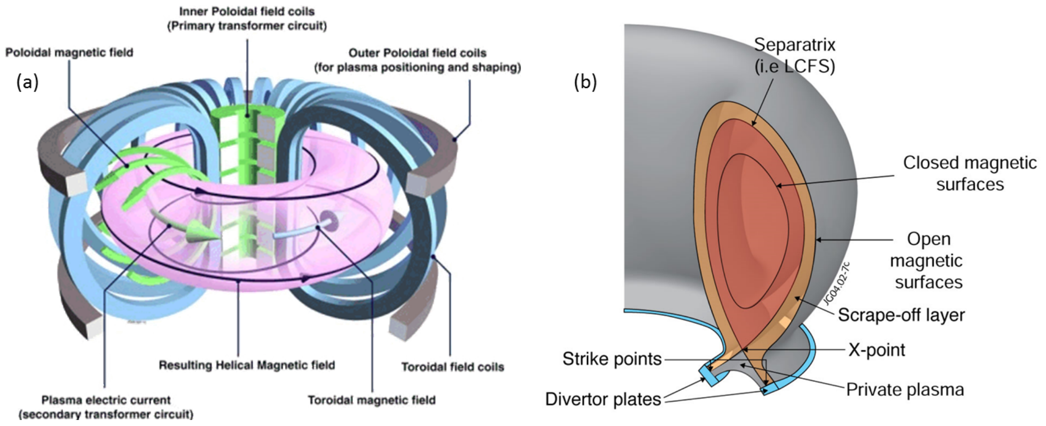

Figure 1.2: (a) Schematic of the tokamak, showing the toroidal and poloidal field coils, and the resulting helical magnetic field. Reproduced from [13]. (b) Schematic of the diverted tokamak cross section, showing the divertor and resulting plasma features: closed and open magnetic surfaces containing the separatrix (last closed flux surface (LCFS)), scrape-off layer (SOL), X-point, strike points and private plasma. Reproduced from [14].

Typical modern tokamaks have a divertor, which are toroidally symmetric plates that are typically at the bottom and sometimes at the top of the tokamak vessel [10]. The divertor was developed to address the technical challenges facing the development of tokamaks for fusion power: the proximity of the plasma to the wall of the tokamak and the build up of impurities from the plasma [15]. The divertor isolates the core plasma from the wall of the tokamak, minimising the impurity content of the plasma by keeping plasma surface interactions separate from the core plasma [8]. It is also designed to remove helium ash resulting from fusion reactions [8, 15]. A diverted plasma has a poloidal cross section as illustrated in figure 1.2 (b), where the core plasma is illustrated in red and the open magnetic surfaces in contact with the divertor in orange. The poloidal cross section shape is described as a combination of elongation (ϵ) and outward pointing triangularity (δ) [10], such that δ is a measure of the shape of the poloidal cross section of the last closed flux surface of a tokamak.

There are many tokamaks in operation around the world, including JET in the UK, DIII-D in the US, ASDEX-U in Germany and EAST in China. This thesis contains results from experiments in JET and DIII-D. JET is currently the world's largest operating tokamak, and in 1997 achieved a record $Q \approx 0.6$, corresponding to a maximum fusion power of 16.1MW, during D-T operation [16].

The next generation tokamak currently under construction is ITER, located in France. The aim of ITER is “to demonstrate the scientific and technological feasibility of fusion energy for peaceful purposes” [17] and is designed to be the step between present experimental devices and a demonstration fusion reactor. ITER will be approximately double the size of JET, with a major radius of 6.2m compared to JET’s 2.96m, and is aiming to achieve Q = 10, with a burn time of 300-500 seconds for a range of operating scenarios [8].

1.7 H-mode and the pedestal

As heating power is gradually increased to a certain threshold in a tokamak, a sudden transition from the low confinement state of operation (L-mode) to the high confinement state of operation (H-mode) can occur, and τ_E approximately doubles [18]. This is due to an increase in the density and temperature in the plasma [19]. This sharp transition suggests a bifurcation between two different plasma states [20], as shown in figure 1.3. H-mode was first discovered on the ASDEX tokamak in 1982 [21].

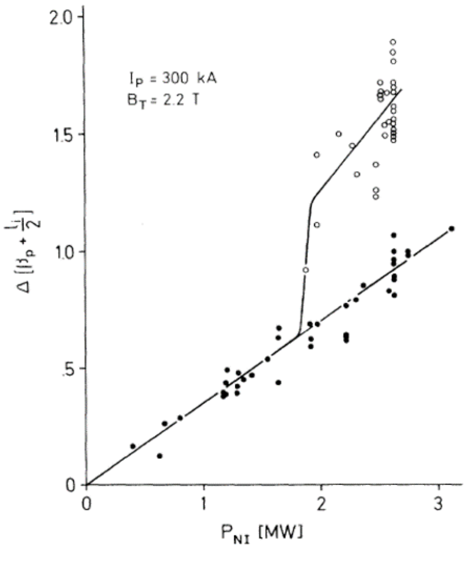

Figure 1.3: Bifurcation of performance from L-mode to H-mode, shown as β_p + $l_i/2$ vs. neutral beam injection power, where solid circles are L-mode, and open circles are H-mode. Reproduced from [21].

The improvement in H-mode confinement is characterised by an edge transport barrier in the last 5-10% of the minor radius of the plasma near the separatrix [22]. This is a region of suppressed turbulence where the density fluctuations are reduced by approximately 50% after the L-H mode transition [19]. The pressure rises steeply through the edge transport barrier and leads to a narrow region of steep pressure gradient, known as the pedestal [23]. The pressure profile is stiff: the core pressure profile sits on the pressure pedestal [24], and there is a broadly proportional dependence of the core pressure to the pressure at the top of the pedestal [25]. Therefore, the achieved pressure pedestal height determines the overall confinement [23, 26], and the pedestal has a critical impact on the performances of ITER, and the proposed D-T operation of JET. An illustration of the pedestal is shown in figure 1.4.

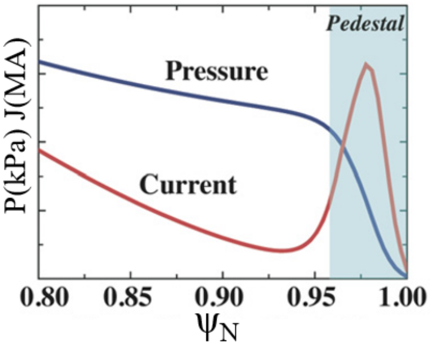

Figure 1.4: Illustration of the H-mode pressure pedestal (blue) and corresponding bootstrap current (red), where the pedestal region is indicated by the blue shaded region. Reproduced from [27].

The current shown in figure 1.4 is known as the bootstrap current. This is a self-induced current causing a peak in the current profile and results from the steep pressure gradient in the pedestal, such that the bootstrap current is approximately proportional to the pressure gradient [28, 29, 30]. This is a neoclassical current whose physical origin arises from collisional momentum passed from the particles trapped in banana orbits to the passing particles [10, 31], which is the reason a tokamak is a pulsed device. The bootstrap current is crucial to tokamak performance since, if it is of a significant enough magnitude, it may be able to maintain the plasma in steady state operation, with only a small amount of external current drive [10]. Therefore, it is seen as a critical element on the path to developing a viable fusion device [10].

Another plasma that it is useful to define is the collisionality (ν^*), which relates the frequency of the de-trapping collisions of the particles to the banana orbit frequency [30]. As collisionality increases, the ratio of the collisions to the frequency is such that the bootstrap current diminishes [30]. The calculation of bootstrap current and collisionality is complex, therefore numerical models are often used. One such highly used model is the Sauter formula [32, 33], which has also been more recently updated to become the Koh/Chang model [34].

1.8 Edge localised modes (ELMs)

The discovery of H-mode was coupled with the observation of a quasi-periodic bursting instabilities called edge localised modes (ELMs) [21], caused by the sharp pressure and current gradients in the pedestal region [35]. ELMs cause a rapid relaxation of pedestal, and sends a burst of energy and particles from the core plasma onto the open field lines, where they are rapidly transferred to the divertor target plates [35]. They occur on the ms time scale [35], and their quasi-periodic nature leads to the concept of the ELM cycle. The post-ELM relaxation of the pressure pedestal causes the pedestal to re-establish itself and build until the next ELM occurs [35]. ELMs have the benefit of transporting density and impurities from the plasma across the pedestal region, providing a way to control them [35, 36].

ELMs are observed in tokamaks as D_α emission [37]. Figure 1.5 from the MAST tokamak shows a visible image of an ELM. As this figure shows, ELMs are observed near the separatrix as radially propagating filamentary structures, as particles and energy are ejected from the pedestal region into the scrape off layer [22, 35].

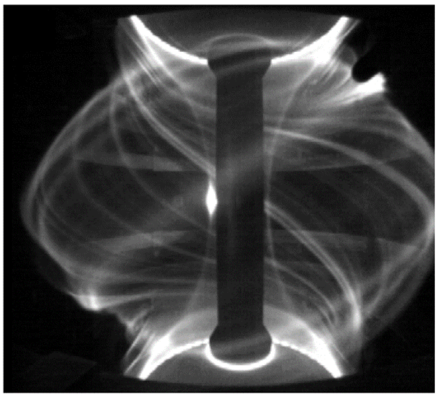

Figure 1.5: Visible image of an ELM in the MAST tokamak, from visible light. Reproduced from [22].

The ELM size is a measure of how much energy ejected during a single ELM event [23]. When an ELM is large and periodic it is known as a type I ELM [19], and this is known as ELMy H-mode. It has been previously found that individual ELMs decrease the plasma energy and particle content in the plasma by approximately 5-10% [38]. These transient events deposit a large particle and energy flux onto the divertor target plates, and over time this can lead to erosion of the divertor materials [39]. Therefore the size of the ELMs determines divertor target lifetimes [24].

The ITER baseline operating scenario is the standard ELMy H-mode [40]. On the ITER scale, large type I ELMs found in standard ELMy H-mode have the potential to transfer unacceptable heat loads onto the divertor, significantly limiting its lifetime [35, 41]. Therefore, ELMs and the pedestal are one of the key areas of research currently being undertaken by the International Tokamak Physics Activity (ITPA), which performs global research in support of ITER [42]. The underlying mechanisms that govern a full ELM cycle are still unknown. Therefore exploring the cause and behaviour of ELMs is a priority. The goal is to be able to mitigate or control ELMs [37], while still providing the plasma with essential density and impurity control [43].

1.9 ELM suppression and mitigation

The ITER baseline operating scenario is the standard ELMy H-mode, which is required for $Q = 10$ operation [40]. However, type I ELMs in ITER could lead to losses of up to 20% of the pedestal energy per ELM [44], placing unacceptably large heat loads on the divertor target plates [45]. Therefore, ELM suppression or mitigation while maintaining good confinement is required for the successful operation of ITER [46].

There are three specific approaches to ELM mitigation and control [35, 46]. The first is to obtain ELM control by triggering more frequent, smaller ELMs. Methods includes joggling the vertical plasma position, using oscillating applied magnetic fields, using supersonic molecular beam injection and using pellet injection [35]. Pellet injection is seen as the baseline control option for ITER [47] and been demonstrated on ASDEX-U and DIII-D [35]. The second, which is also an ITER baseline control system, is to apply resonant magnetic perturbations (RMPs) for ELM suppression and mitigation [35, 47, 48, 49, 50]. These are non-axisymmetric magnetic fields and their ability for ELM suppression has been demonstrated on multiple tokamaks, including JET and DIII-D [35]. However, this does require ELM control coils [47], which are not thought to be feasible in a demonstration reactor due to the radioactive environment.

Finally, ELM mitigation can be achieved through intrinsic small ELM or ELM-free regimes [35, 46, 51]. These have been identified in the exploration of tokamak parameter space to find new regimes where large type I ELMs are absent, and if ELMs that do exist they are tolerable [35]. These conditions are often found to be device dependent [46]. Some are not considered applicable to ITER due to their small operating regimes, so do not provide the required performance [35]. Small ELM regimes are discussed in section 1.9.1. Several ELM-free or very few ELM regimes have been discovered, where the density and impurity control is provided by other means [52]. These include: the EDA H-mode regime found on Alcator C-Mod [35, 52], which occurs at high collisionality and density, with a continuous mode proving additional particle transport [35]. The wall conditioning regimes on NSTX and EAST, where the wall is conditioned with lithium to change the ELM characteristics, which changes the pedestal by altering the pedestal density profile [35]. The next is the I-mode regime, which was discovered on the C-Mod tokamak [53, 54]. This is an enhanced confinement regime with a temperature pedestal, but no density pedestal which allows for straightforward density control through the L-mode like density profile [54]. The final ELM-free regime, which is studied in this thesis, is the quiescent H-mode. This is discussed in section 1.9.2.

1.9.1 ELM categorisation

As previously mentioned, there are different types of ELMs and their classification depends on their size and properties. An example of the D_α traces for different types of ELMs found in the JT-60U tokamak is shown in figure 1.6, which have a particular emphasis on a small ELM known as a grassy ELM [55]. This figure shows that the smaller grassy ELMs have significantly higher ELM frequencies and much smaller amplitude than type-I ELMs [55].

The various types of ELMs seen in various tokamaks are summarised in table 1.1. Note that they have only been observed in a limited range of pedestal conditions depending on each specific device, and therefore not all ELM types are seen in each

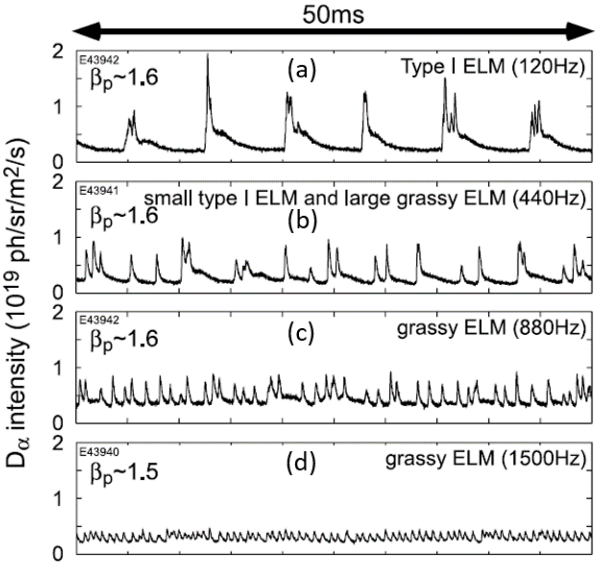

Figure 1.6: Time evolution of D_α emission for different types of ELMs in the JT-60U tokamak: (a) Type I ELM (b) Small type I ELM or large grassy ELM (c) lower frequency grassy ELM (d) grassy ELM at higher frequency. Reproduced from [55].

device [46]. Additionally, mixed ELM regimes have been observed [52, 56, 57].

1.9.2 QH-mode

The quiescent H-mode (QH) is a promising high performance ELM-free mode of operation which was first discovered on DIII-D [58]. The regime has similar confinement to ELMy H-mode, but avoids the energy losses found with type I ELMs [46]. It is a promising regime as it exists at low collisionality [59, 60] and with strong shaping, and has similar pedestal pressure profiles to ELMy H-mode [61]. QH-mode was originally discovered in DIII-D in discharges with the neutral beam injection in the direction opposite to the plasma current, which is known as counter-injection, as well as in plasma with high torque, although more recently neither of these have been found to be necessary [62, 63]. Since its discovery, QH-mode has now been observed in other tokamaks, including JET [64], ASDEX-U [59, 64] and JT-60U [65]. A typical set of traces for a QH-mode discharge in DIII-D is shown in figure 1.7.

As the D_α trace in figure 1.7 (d) shows, after an initial ELM-ing phase, the plasma enters the QH-mode phase and this is maintained for approximately 3.5 seconds [58]. This is coupled with the observation of density control, as shown in 1.7 (b) [58]. This is due to the presence of an edge harmonic oscillation (EHO) which limits the pedestal height and provides enhanced particle transport [58]. It has been found that this EHO is destabilised by rotational shear [60, 66]. Recently a second type of QH-mode has been discovered in DIII-D [43]. This is a low torque EHO-free QH-mode which also has density control [43]. A more in-depth description of both types of QH-mode is provided in chapter 5, where the analysis of a DIII-D QH-mode shot with both types of QH-mode is presented.

ELM type	ELM size	Properties
Type I	Large	Observed across devices. ELM frequency increases with heating power [38]. Sharp isolated bursts of D_α emission. High power required to obtain them, and relatively low frequency.
Type II	Small	Commonly observed in ASDEX-U and JET [46], but also observed in DIII-D [38]. No frequency dependence with heating power observed [38]. High plasma shaping and high collisionality required [35, 46]. They have a turbulent edge recycling signature [35]
Type III	Small	Well established in many tokamaks [46]. ELM frequency decreases with increasing heating power [19, 38, 46]. Very high frequency ELMs [35]. Requires high collisionality, and exhibits low pedestal pressures [35].
Type IV	Small	Not widely observed. A low collisionality branch of type III ELMs at low input power, which is also characterised by low pedestal pressure [35]
Type V	Small	Observed in the NSTX tokamak [46, 52]. High frequency (300-800 Hz) [52]. No observable drop in stored energy, with an $n = 1$ precursor observed [52].
Grassy	Small	Observed in the JT-60U tokamak. ELM frequency increases with heating power [55]. Very high frequency (800-1500 Hz) [55]. Requires low collisionality, high plasma shaping and high power [55].

Table 1.1: Summary of the different types of ELMs found on different tokamaks: type 1, type II, type III, type IV, type V and grassy

1.10 Thesis motivation and outline

The motivation of this thesis is to explore the physics of ELMs and the pedestal, an understanding of which is vital to the success of ITER. The ELITE code, which was originally developed to efficiently calculate the edge ideal magneto-hydrodynamic (MHD) stability properties of tokamaks, optimised for the intermediate-high toroidal mode number, n, modes associated with ELMs, has been extended. The motivation was to use the code to explore the stability properties of QH-mode. Further insight to ELM-free scenarios is important for determining suitable ELM mitigated regimes for ITER. Additionally, in 2011 JET finished installing a fully metal ITER-like-wall (ILW) with a beryllium first wall and tungsten divertor. This was performed to demonstrate: firstly to demonstrate the acceptable tritium retention, and secondly the ability to operate a large high power tokamak in within the limitations of the metal wall [67]. Understanding the mechanisms of the pedestal and the resulting ELMs in the presence of the JET-ILW is also highly important, since this will improve predictions of pedestal behaviour in ITER.

Chapter 2 presents the theory of ideal magnetohydrodynamics, instabilities that

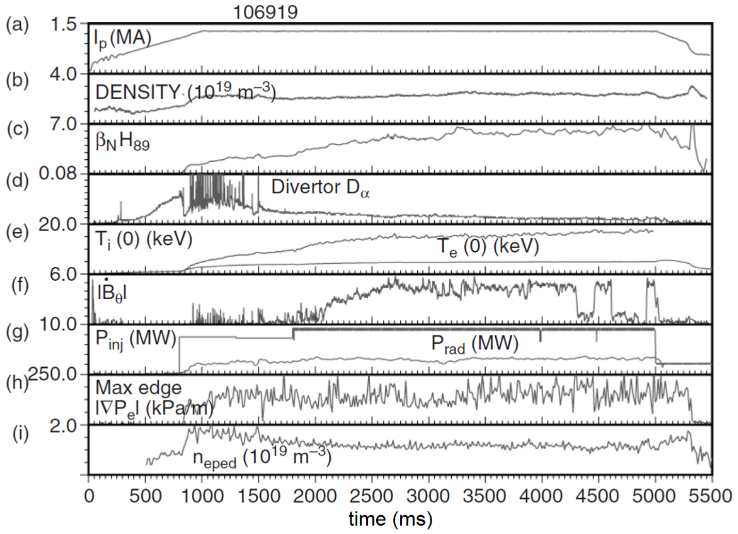

Figure 1.7: Time history traces from DIII-D QH-mode discharge 106919 where: (a) plasma current, (b) line-averaged density, (c) product of normalised beta and energy confinement enhancement factor, (d) divertor D_α emission, (e) central ion and electron temperature, (f) $|\dot{B}_\theta|$ from magnetic probe, (g) total injected neutral beam power and total radiated power, (h) maximum edge electron pressure gradient and (i) the pedestal electron density. (h) and (i) are determined from mtanh fits to the pedestal n and p from Thomson scattering [58]. Reproduced from [58].

arise and how they couple to form peeling-ballooning modes, which are thought to be the ELM triggering mechanism. The original formalism of the ELITE code is also presented to provide a theoretical basis for the formalism extension. Chapter 3 presents the extension of the ELITE formalism to arbitrary n. This was motivated by the low n dominated phenomena found in QH-mode. Chapter 4 presents benchmarks of the extended ELITE, to show that the formalism is valid. It also presents a diagnostic that has been implemented in the original ELITE version of the code to further explore the drive of the peeling-ballooning instability.

Chapter 5 presents the analysis of a DIII-D QH-mode discharge, which has both types of QH-mode. Applying the new ELITE formalism to the original QH-mode shows that it is able to obtain results that agree with previous work, which is important for code validation. Exploring the low n phenomena of the new QH-mode regime to explain observations is an important step in enhancing the understanding of this new mode of operation, and therefore whether it is applicable to ITER.

Chapter 6 presents the analysis of a database of JET-ILW pulses, which explores the inter-ELM pedestal evolution and compares this to stability analysis. This was a new way of exploring the performance loss that has been experienced since the installation of the JET-ILW. Understanding this is crucial for the success of the upcoming JET D-T campaign, and beyond to ITER.

Chapter 2

Magnetic Confinement Fusion Theory and the ELITE code

This chapter provides an introduction to MHD equilibrium and stability, a description of the original ELITE formalism, and an introduction to the Mercier-Luc formalism. Initially, the concept of ideal MHD and its assumptions are presented. Next introduced is the concept of MHD tokamak equilibria, and the equilibrium codes used to obtain equilibria for the results in this thesis, presented in chapters 4, 5 and 6. Next introduced is the concept of the MHD stability and peeling-ballooning (PB) modes. PB modes are thought to be the trigger for ELMs, and are the theoretical underpinning of the ELITE code. Finally the ELITE formalism is presented in its original form, to provide a basis for its extension presented in chapter 3. Also introduced is the Mericer-Luc formalism, which is used as part of the ELITE formalism framework.

2.1 Magnetohydrodynamics and ideal MHD

Magnetohydrodynamics (MHD) is a fluid model that describes the macroscopic equilibrium and stability properties of a plasma, such that the plasma is a moving conducting fluid in the presence of a magnetic field [68]. It does not require knowledge of the individual particles in the plasma. There are several versions MHD and the most simple version is ideal MHD. Ideal MHD has the following main initial assumptions: the ion gyro radius is zero, the plasma is a single fluid, has no viscosity and has infinite electrical conductivity [68]. This is the version of MHD used in this thesis, and therefore the version that will be discussed here. Another type of MHD is resistive MHD, which is defined by finite resistivity. There are also other extended versions of MHD which include two fluid effects, the Hall current term which is neglected in ideal MHD, and also kinetic effects [68]. Despite the simplicity, the ideal MHD equations are still too complex to be solved in their analytical form [68]. The ideal MHD equations are given by:

$$
\begin{aligned}
&\frac{\partial \rho}{\partial t} + \nabla \cdot \rho \mathbf{v} = 0 \\
&\rho \frac{d\mathbf{v}}{dt} = \mathbf{J} \times \mathbf{B} - \nabla p \\
&\frac{d}{dt}\left(\frac{p}{p^{\gamma}}\right) = 0 \\
&\mathbf{E} + \mathbf{v} \times \mathbf{B} = 0 \\
&\nabla \times \mathbf{E} = -\frac{\partial \mathbf{B}}{\partial t} \\
&\nabla \times \mathbf{B} = \mu_0 \mathbf{J} \\
&\nabla \cdot \mathbf{B} = 0
\end{aligned}
\tag{2.1}
$$

where $\mathbf{E}$ is the electric field, $\mathbf{B}$ is the magnetic field, $\mathbf{J}$ is the current density, ρ is mass density, $\mathbf{v}$ is the fluid velocity, p is the pressure, μ_0 is the vacuum permeability constant, $\gamma = 5/3$ which is the ratio of specific heats and is adiabatic, and the derivative $d/dt = \partial/\partial t + \mathbf{v} \cdot \nabla$ in the first equation is the convective derivative [68]. The first equation is for mass, known as the continuity equation. This equation implies that there is no dissipation of particles from the plasma, which is a reasonable assumption on the MHD time scale [68]. The second term is the momentum equation and describes the momentum of a fluid with three interacting forces: the pressure gradient force, the magnetic force and the inertial force. The third term is the energy equation, and this contains an adiabatic evolution of the plasma. The fourth term is Ohm's law, which shows the perfect conductivity assumption: that in a reference frame that moves with a plasma the electric field is zero [68]. The final three equations are Maxwell's equations.

Note that the last three equations are the low frequency form of Maxwell's equations, and the fourth Maxwell's equation is neglected. This is because deriving the ideal MHD equations requires taking moments of the kinetic equation corresponding to mass, momentum and energy. In the ordering process, further assumptions of ideal MHD are defined which are used to obtain closure of the equations. The first is quasi-neutrality, $n_i \simeq n_e$, which arises from the assumption that $\epsilon_0 \nabla \cdot \mathbf{E}$ can be neglected, so that locally the electrons respond fast enough to maintain this assumption [68]. This additionally leads to the displacement current being neglected, which is valid since the characteristic thermal ion velocity of the plasma , $v_{Ti} \ll c$. The second assumption is that there is no electron inertia in the electron momentum equation, such that $m_e \to 0$, giving electrons an infinitely fast response due to their very small mass [68]. After writing the equations in terms of a single fluid, more information is required to close the system. This is where an assumption of ideal MHD is used: is that the plasma has a high collision rate, making the plasma a collision dominated fluid. This arises from the assumption that higher order moments can be described using Braginskii's transport theory, which uses basic variables to describe higher order moments [68]. This leads to a set the of closed equations for ideal MHD.

The assumptions of ideal MHD set the characteristic time and length scales of the model, which defines the plasma phenomena the model can be used for. The characteristic length scale a is given as $a \sim 1m$. Therefore, the MHD length scale is much greater than the Debye length $a \gg \lambda_D$. Additionally, the MHD length scale is much greater than the electron gyro radius $a \gg r_e$ [31, 68]. The characteristic velocity scale is given by the thermal ion velocity $v_{Ti} = (2T_i/m_i)^{1/2}$, where T_i is the ion temperature, and m_i the ion mass [68]. This gives a characteristic MHD time, $\tau_M = a/v_{Ti}$: for deuterium and an ion temperature of 3keV this is approximately $\tau_M \approx 2\mu$sec. Therefore, the MHD time is much greater than the ion-electron equilibration time $\tau_M \gg \tau_{eq}$ [68]. Additionally, the MHD frequency is much less than the cyclotron frequency [31]. Therefore, MHD can be used to describe macroscopic equilibrium and stability: low frequency, large-scale phenomena. Combining this information leads to the conditions for validity of the ideal MHD model. These can be summarised as: high collisionality, zero viscosity, small ion gyro radius and small resistivity [68].

2.2 Tokamak equilibria

This section applies ideal MHD to the concept of tokamak equilibria. This is a vital tool for determining the MHD stability of a plasma, and therefore is used to analyse previous tokamak experiments. It can be also used to construct so-called model equilibria. In general, such model equilibria can be used to design future tokamak experiments [31].

There are two aspects of tokamak equilibria: the first is the internal balance of the pressure of the plasma and the electromagnetic forces from the magnetic field, and the second is the shape and position of the plasma, which is determined by currents produced in the external coils [8]. The concept of MHD macroscopic equilibria arises from how a magnetic field can produce forces that can hold a plasma in a stable configuration, allowing fusion reactions to take place [10]. Analysis of macroscopic equilibrium is determined using the ideal MHD equations, equation 2.1, with the basic assumption that as the plasma is in equilibrium and therefore all quantities are independent of time, such that $\partial/\partial t = 0$. A further simplification can often be made: that the plasma can be assumed to be stationary, $\mathbf{v} = 0$. This is a reasonable assumption as time independent flows do not usually influence the equilibria unless they are sonic [10]. Therefore in equilibrium the momentum equation is static, such that the $\mathbf{J} \times \mathbf{B}$ force balances the ∇p force [68]. This leaves the MHD equilibrium model to be given by:

$$\begin{aligned}
&\mathbf{J} \times \mathbf{B} = \nabla p \\
&\nabla \times \mathbf{B} = \mu_0 \mathbf{J} \\
&\nabla \cdot \mathbf{B} = 0
\end{aligned} \tag{2.2}$$

The first equation is known as the force balance equation. The equations allow the equilibrium properties of all magnetic fusion devices, including tokamaks, to be described [10].

2.2.1 Flux surfaces

A key property of MHD equilibrium is the concept of flux surfaces. In axisymmetric equilibria, such that the equilibrium is independent of toroidal angle, ϕ, the magnetic field lines lie on nested toroidal magnetic surfaces [8]. This is illustrated in figure 2.1.

Figure 2.1: Illustration of magnetic flux surfaces, which shows that the flux surfaces form a set of nested toroids, where magnetic field lines and current lines lie. Reproduced from [8].

The condition for equilibrium in the plasma is that the force on the plasma must be zero at all points such that the force balance equation, $\mathbf{J} \times \mathbf{B} = \nabla p$, must give the relation [8]:

$$\mathbf{B} \cdot \nabla p = 0 \tag{2.3}$$

Therefore, there is no pressure gradient parallel to the magnetic field lines, and the magnetic surfaces are surfaces of constant pressure [8]. In a tokamak the pressure is highest in the core and decreases to a minimum value at the edge. Furthermore, there is a similar relation for current density, combining the dot product of force balance with $\mathbf{J}$ [68]:

$$\mathbf{J} \cdot \nabla p = 0 \tag{2.4}$$

This implies that current density also lies in the magnetic surfaces [8]. These nested magnetic surfaces are well described by the introduction of a poloidal flux function ψ, which is given by:

$$\psi = \int \mathbf{B} \cdot d\mathbf{S} \tag{2.5}$$

where $d\mathbf{S}$ is the surface element of the flux surface [68]. This function defines the poloidal flux lying on each magnetic surface such that:

$$\mathbf{B} \cdot \nabla \psi = 0 \tag{2.6}$$

As this function ψ has a different value on each flux surface and is monotonic, it can be used as the radial coordinate [8]. In a tokamak the poloidal flux function, ψ, can be written in terms of major radius, R, and the vertical toroidal axis Z, so that $\psi = \psi(R, Z)$.

2.2.2 Grad-Shafranov equation

The equation that describes toroidal axisymmetric equilibrium is known as the Grad-Shafranov equation [69, 70]. This is a two-dimensional, non-linear, partial differential equation which is obtained from the reduction of the ideal MHD equations, which are the three equations shown in equation 2.2 [68]. The equation has two arbitrary flux functions, $f(\psi) = RB_\phi$, which is the toroidal field function, and $p(\psi)$ which defines the pressure. Also required are the functions that describe the poloidal magnetic field related to ψ [8, 68]:

$$\begin{aligned} B_R &= -\frac{1}{R}\frac{\partial \psi}{\partial Z} \\ B_Z &= \frac{1}{R}\frac{\partial \psi}{\partial R} \end{aligned} \tag{2.7}$$

Manipulation of equations 2.2, including taking the $\nabla\psi$ component of the force balance equation [31, 68], then using Ampére's law, leads to the Grad-Shafranov equation [8, 68]:

$$\Delta^* \equiv R^2 \nabla \cdot \left(\frac{\nabla \psi}{R^2} \right) = R \frac{\partial}{\partial R} \frac{1}{R} \frac{\partial \psi}{\partial R} + \frac{\partial^2 \psi}{\partial Z^2} = -\mu_0 R^2 p'(\psi) - {\mu_0}^2 f(\psi) f'(\psi) \tag{2.8}$$

where f' is a ψ-derivative of f, and similarly p' is the pressure gradient. In general this equation is too complex to solve analytically, and as such it needs to be solved numerically. This is discussed in section 2.2.5.

2.2.3 Safety factor, q

Another crucial concept to this thesis is that of the equilibrium parameter q, which is known as the safety factor. This is a key parameter in determining plasma stability [8], and the higher q is, generally the more safe from instability the plasma is [10]. To explain the concept, it is necessary to consider the helical magnetic field, as discussed in section 1.6. The magnetic field is produced by a combination of the toroidal and poloidal magnetic field, which travels in a helical trajectory around the torus. For every time the magnetic field goes around the torus toroidally, it is shifted by angle ι poloidally and this is known as the rotational transform [31] or the field line pitch. This leads to the definition of safety factor, which is the number of times the magnetic field lines goes around the tokamak toroidally for one full poloidal turn, given by [10, 31]:

$$q = \frac{2\pi}{\iota} \tag{2.9}$$

This can be a rational number, if $q = m/n$ where m and n are integers, with m the poloidal mode number, and n the toroidal mode number. The mode number is defined as the number of complete wavelengths in one poloidal or toroidal rotation respectively. Rational numbers of q are important for stability [8]. It is possible to calculate q, integrating around a single poloidal plane over a flux surface using the formula:

$$q(\psi) = \frac{1}{2\pi} \oint \frac{1}{R} \frac{B_\phi}{B_p} \mathrm{d}s \tag{2.10}$$

where B_ϕ is the toroidal magnetic field, B_p the poloidal magnetic field [8]. As there is a different value of q on each flux surface, collectively these form a q-profile.

2.2.4 Other important plasma parameters and typical plasma profiles

Other important factors to this thesis are introduced here. The first is the global magnetic shear, s, which is found from the radial minor radius coordinate, r, and the derivative of the safety factor, q. It is given by:

$$s = \frac{dq}{dr} \frac{r}{q} \tag{2.11}$$

In general, q is monotonic and shear is positive. However, shear can be negative, and can be found, for example, in the core of tokamaks associated with advanced tokamak operation where there is a minimum in the q-profile [10]. Another important parameter used throughout this thesis is α, the normalised pressure gradient, which is a dimensionless parameter. This is given by:

$$\alpha = \frac{-2\partial V/\partial\psi}{(2\pi)^2} \left(\frac{V}{2\pi^2 R_0}\right)^{\frac{1}{2}} \mu_0 \frac{\partial p}{\partial \psi} \tag{2.12}$$

where V is the plasma volume, R_0 is the major radius and p is the pressure [71, 72]. Note that there is a second definition of α used in this thesis, α_{HELENA}, which uses a different normalisation for the pressure gradient than the standard form for α. This is from the equilibrium code HELENA introduced in the next subsection 2.2.5. Next is the concept of plasma β which is the ratio of the plasma pressure to the magnetic pressure, and therefore is a measure of the efficiency of the confinement of the plasma pressure [8]. This is given by:

$$\beta = \frac{<p>}{<B^2>/2\mu_0} \tag{2.13}$$

where $<p>$ is the mean plasma pressure, and $<B^2>$ is the average square of total magnetic field strength [8]. The parameter β can be defined relative to the toroidal and poloidal field components. This leads to the related parameter called the poloidal β, β_p, and is given by:

$$\beta_p = \frac{<p>}{<B_p^2>/2\mu_0} \tag{2.14}$$

where $<B_p^2>$ is the average poloidal magnetic field strength. Also important is the normalised β, β_N, which is related to the Troyon β limit. The Troyon limit is a measure of the overall β limit of the plasma, the plasma has the required stability against all ideal MHD modes [10]. The limit was developed to optimise tokamak experiments, and it has been found that for an aspect ratio tokamak of $R/a = 2.5$, the maximum β in percent ($\%\beta$), the Troyon factor, is 2.8 [10]. Normalised beta, β_N, is given by:

$$\beta_N = \frac{\%\beta}{I_p/aB_\phi} \tag{2.15}$$

where I_p is the plasma current in MA, a is the minor radius, and B_ϕ is the toroidal magnetic field in T [8]. Note that a Troyon factor of 2.8 is not as high as desired for high performance fusion plasmas, thus motivating research into increasing the maximum β that can be achieved [10].

An example of some typical plasma profiles for pressure, q and shear ,s, are shown in figure 2.2. Note that, in comparison to figure 1.4, there is no characteristic pressure pedestal which is seen in H-mode. As it can be seen in the q-profile, q typically increases monotonically from the core of the plasma to the edge. Typically, q begins at approximately just above 1, to something around 5 to 10 at the plasma edge.

The q-profile is affected by current density. As current density increases locally, this leads to a local flattening of q. This causes a reduction and eventual zero in magnetic shear which will reduce field line bending. Furthermore, if current density keeps increasing this leads to a reversal of magnetic shear and non-monotonicity forming in the local part of the q-profile. This can occur at the edge of the plasma as well as in the core region of the q profile.

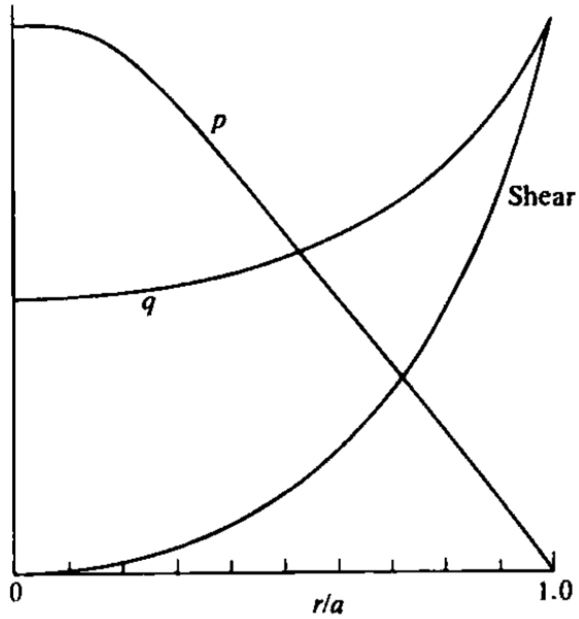

Figure 2.2: Illustration of typical pressure, q and shear profiles. r/a is the minor radius r normalised to the value of the minor radius at the edge a. Reproduced from [8].

2.2.5 Equilibrium codes: numerical calculation of tokamak equilibria

Numerical solutions to the Grad-Shafranov equation are sought to provide both experimental and model equilibria. There are two main types of codes that serve this purpose. The first are known as equilibrium solvers and the second are known as equilibrium fitting codes. Both have been used to produce results in this thesis.

Firstly consider the equilibrium solver codes. These take two plasma profiles as inputs, which are the $p(\psi)$ profile and typically the $f(\psi)$ profile (although this may be replaced with the $q(\psi)$ profile or the j_ϕ profile) along with the plasma boundary shape or the coil currents to numerically solve the Grad-Shafranov equation [31]. There are two different types of equilibrium solvers, depending on the plasma boundary specification. The first is a fixed boundary equilibrium solver where ψ is calculated within a predefined boundary, which is a closed flux surface [73]. The other type is a free boundary equilibrium solver where ψ is calculated throughout the vessel, including in the open field line scrape-off-layer region, and information about the current in the coils is required [74]. These codes are generally used in theory and modelling [31].

The two fixed boundary equilibrium solver codes that have been used in this thesis are the HELENA code [73, 75], and the TOQ code [76]. The HELENA code [73, 75] is a fixed boundary equilibrium solver that has been used extensively in the production of equilibria for the analysis of JET-ILW pedestal stability presented in chapter 6. HELENA represents ψ using isoparametric bi-cubic Hermite finite elements, and approximates the plasma boundary using a Fourier series, such that a global coordinate system is constructed using polar coordinates [73, 75]. The Grad-Shafranov equation is then solved using a the finite element Galerkin method [73, 75]. The HELENA code also has the ability to calculate the $n = \infty$ ballooning limit [73].

The TOQ code [76] is also a fixed boundary equilibrium solver. It uses an equal-arc-length, inverse equilibrium solver for the Grad-Shafranov equation. It was used to produce the majority of the benchmark equilibria presented in chapter 4, as well as the model equilibria for the pedestal width δW diagnostic analysis in chapter 4 section 4.10.

Now consider equilibrium fitting codes, which are a key tool for interpreting experimental data. These codes take experimental measurements from diagnostics, such as the Motional Stark Effect (MSE) and external magnetic probes, and translate these into useful information about the plasma, such as the current density distribution and the plasma geometry [74]. The code then solves the Grad-Shafranov equation to calculate the equilibrium [31, 74]. The example that is most widely used in tokamak plasma physics, and was used to produce equilibria from experimental data from both the JET and DIII-D tokamaks, is the EFIT (Equilibrium Fitting) code [74, 77, 78]. This was initially developed to study magnetic topology in the predecessor to DIII-D, Doublet III [78], and after turning diagnostic measurements into plasma information solves the Grad-Shafranov equation. EFIT solves this using the available measurements from diagnostics to provide a constraint on J_ϕ, the toroidal current density [74]. This is a non-linear problem, since the current density also depends on ψ, which is its solution. EFIT was used to produce experimental equilibria from DIII-D and JET for this thesis. It uses two one-dimensional stream functions to represent the 2D current density [74]. EFIT also contains a free and fixed boundary equilibrium solver [74].

2.3 MHD stability

This section details the concept of ideal MHD stability. An MHD equilibrium implies the total sum of the forces acting on the plasma is zero [68]. However, if a perturbation is applied to the plasma such that it is perturbed from its equilibrium state, there will be perturbation forces acting on the plasma. If these perturbation forces return the plasma to its equilibrium state, then the plasma is stable [68]. The so-called ball analogy for a stable equilibrium is shown in figure 2.3 (a): if the ball is moved a small distance away from its equilibrium point at the bottom of the well it will simply roll back to its equilibrium position, and therefore is stable. If the perturbation forces enhance the initial perturbation, then an instability will grow and the plasma is unstable [68]. This is illustrated in figure 2.3 (c): if the ball is moved a small distance away from its equilibrium position at the top of the hill, it will roll away from its equilibrium and is therefore unstable. Figure 2.3 (b) shows an analogy for the concept of marginal stability: this is a transition point where if the ball is moved, it will stay in its new position and neither become unstable nor return to the equilibrium position [68].

Figure 2.3 illustrates the concept of ideal MHD stability. Ideal MHD yields instabilities that would occur even if the plasma were perfectly conducting [8]. In tokamak plasmas, these tend to be the most violent and fastest occurring instabilities [31] and can lead to anything from serious degradation in performance to termination

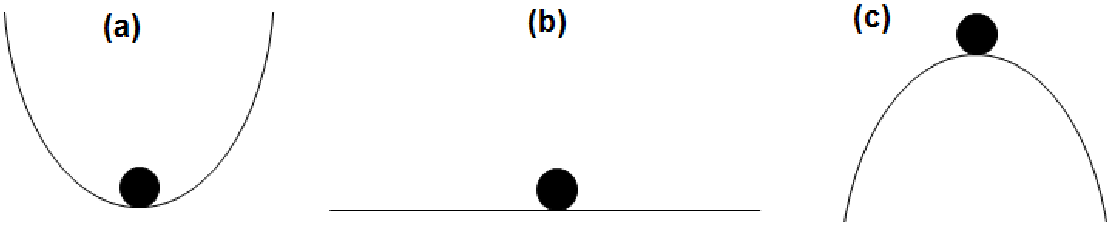

Figure 2.3: Illustration of MHD stability, using the ball analogy where: (a) is stable (b) is marginally stable and (c) is unstable.

of the plasma [68]. Understanding their mechanism is crucial to their avoidance or mitigation for future devices. In general, other physics effects such as resistivity, which yields resistive MHD and allows field line reconnection [31], are also associated with other tokamak instabilities. These are beyond the scope of this thesis.

The second classification is whether the mode is pressure or current driven. Pressure driven modes arise in the plasma due to pressure gradients and field-line curvature in the plasma. Field-line curvature can be classified as either good or bad, and depends on the direction of the radius of curvature vector with respect to the direction of the pressure gradient [10]. Instabilities can also be primarily driven by the pressure gradient, and these are usually categorised as either ballooning modes or interchange modes. These pressure driven instabilities are usually internal modes and provide a limit on the achievable plasma β [10]. Ballooning modes are discussed in section 2.4.1. Instabilities driven by parallel current are known as current driven modes. These can be present without a pressure driven mode being present at low β. These instabilities are known as kink modes as they deform the plasma into a kink shape [10]. They can be both internal and external modes and set a limit on the maximum toroidal current that can occur [10]. Kink instabilities are discussed in more detail in section 2.4.2. At high β the pressure gradient also contributes to the mode and it couples with the ballooning mode [8]. This is discussed in section 2.4.3.

The final classification is whether the mode occurs with or without a conducting wall present. When no wall is present, there is no wall to stabilise the coupled pressure-current driven modes, known as peeling-ballooning modes [10]. A conducting wall is stabilising, and a perfectly conducting wall, which is also known as an ideal wall, would cause a cessation in the presence of these modes [10]. However, in practice tokamak walls are resistive and therefore affected by the resistive wall mode. Resistive walls do not have the same stabilising effect as ideally conducting walls. They do not affect the stability boundary of the mode, which is the amount of pressure and current needed to destabilise the mode, and only effects the growth rate at which the mode grows once it has been initiated [10]. Finding regimes where the resistive wall mode is stabilised is an area of active research [10].

2.3.1 Linear analysis of stability and the energy principle

The process of linearising ideal MHD greatly reduces the complexity of performing stability analysis. This process takes an MHD equilibrium and perturbs this slightly away from the equilibrium point using linearised ideal MHD equations. The time dependence of the resulting small amplitude perturbation determines the linear stability of the system: whether the plasma returns to equilibrium, oscillates about the equilibrium, or becomes unstable [10]. If the system is unstable, the instability initially grows exponentially in time. In general real instabilities evolve out of this initial linear small amplitude oscillation to a large amplitude instability in a highly non-linear fashion, requiring non-linear 3D partial differential equations that are challenging to solve, even on today's computers [10] . However, using linear ideal MHD provides the stability of the system from this initial linear phase, and an indication of the growth rate of the small amplitude oscillation.

The mathematics of linear ideal MHD separates the time independent equilibrium quantities from the time dependent linear perturbed quantities. All dependent variables, $Q(\mathbf{r},t)$, are written in the form:

$$Q(\mathbf{r},t) = Q_0(\mathbf{r}) + \tilde{Q}_1(\mathbf{r},t) \tag{2.16}$$

where $Q_0(\mathbf{r})$ represents the equilibrium part of the solution and therefore is time independent, and $\tilde{Q}_1(\mathbf{r},t)$ represents the time dependent perturbation away from the equilibrium [10]. This in general can be written as:

$$\tilde{Q}_1(\mathbf{r},t) = Q_1(\mathbf{r})e^{-i\omega t} \tag{2.17}$$

where the complex mode frequency ω is determined as an eigenvalue of the system. This is the concept of exponential stability, such that the eigenvalues of the system correspond to the exponential growth of the instability if the system is unstable, where $\mathrm{Im}(\omega) > 0$. If not the system is stable, and this corresponds to $\mathrm{Im}(\omega) \leq 0$ [68]. The dependent variables are all written in this form.

The energy principle is a powerful concept, which determines if the MHD equilibrium is stable or unstable, without being significantly concerned with the exact growth rate or frequency of the mode oscillation [68]. This is an acceptable approximation for determining the nature of the instabilities and the configurations in which they occur, and the growth rates can easily be estimated [68]. It was first derived in 1958 by Bernstein et al. [79]. It allows the calculation of the stability of the system with a perfectly conducting wall or an isolating vacuum. The vacuum can be included to the formalism with the inclusion of a simple term.

The energy principle is based on the principle that if a perturbation of the equilibrium causes a reduction in the potential energy, then the equilibrium is unstable [8].

It is derived in several steps, too complex to fully reproduce here. The steps are: firstly formulate the stability problem into an initial value problem using general linearised equations of motion. Secondly the equations are formulated into a normal-mode eigenvalue problem. Thirdly this is transformed into a variational principle. Finally this is reduced to the energy principle [68]. There are, however, several important quantities to introduce from the derivation of the ideal MHD energy principle. It is also useful to have the initial equations for reference. The initial equations are given by:

$$\begin{aligned}
&\mathbf{J}_0 \times \mathbf{B}_0 = \nabla p_0\\
&\mu_0 \mathbf{J}_0 = \nabla \times \mathbf{B}_0\\
&\nabla \cdot \mathbf{B}_0 = 0\\
&\mathbf{v}_0 = 0
\end{aligned} \tag{2.18}$$

where $\mathbf{v}_0 = 0$ represents zero flow of the equilibrium [68]. Now all equations are linearised. When substituting into these equation is much more convenient to represent all the perturbed quantities in terms of a quantity known as the perturbation displacement. This is a vector, $\tilde{\xi}(\mathbf{r}, t)$, which represents the distance from the equilibrium position a plasma element is displaced [68]. When expanding the terms, any non-linear perturbations, which are terms with two or more perturbed quantities, are neglected as it is assumed these are small amplitude oscillations [10]. The perturbation displacement is three-dimensional, and is given by:

$$\mathbf{v}_1 = \frac{\partial \tilde{\boldsymbol{\xi}}}{\partial t} \tag{2.19}$$

After substitution, this leads to the force operator, which gives the force arising from the displacement [68]. This is given by:

$$\begin{aligned}
\mathbf{F}\left(\tilde{\boldsymbol{\xi}}\right) =& \rho \frac{\partial^2 \tilde{\boldsymbol{\xi}}}{\partial t^2}\\
=& \mathbf{J}_0 \times \tilde{\mathbf{B}}_1 + \tilde{\mathbf{J}}_1 \times \mathbf{B}_0 - \nabla \tilde{p}_1
\end{aligned} \tag{2.20}$$

Note that after this step most of the perturbed quantities are eliminated in the derivation in favour of expressing them in terms of the perturbation displacement and the equilibrium quantities [8, 10]. Therefore the $\tilde{\boldsymbol{\xi}}$ is written as $\boldsymbol{\xi}$ and the 0 subscript is dropped most equilibrium quantities. The perturbed momentum equation yields the eigenvalue of the system, ω^2:

$$-\omega^2 \rho \boldsymbol{\xi} = \mathbf{F}(\boldsymbol{\xi}) \tag{2.21}$$

Therefore this is an eigenvalue problem where ω^2 has to be real due to the Hermitian nature of $\mathbf{F}(\boldsymbol{\xi})$. Therefore stability transitions occur when ω^2 passes through zero [68]. The force operator is required to be a self-adjoint, the dot product can be taken with $\boldsymbol{\xi}^*$ and integrated over the plasma volume [68]. This yields:

$$\omega^2 = \frac{\delta W(\boldsymbol{\xi}^*, \boldsymbol{\xi})}{K(\boldsymbol{\xi}^*, \boldsymbol{\xi})} \tag{2.22}$$

where $\delta W$is the energy change that results from the perturbing the plasma by the perturbation displacement $\boldsymbol{\xi}$ [8]. This is given by:

$$\delta W(\boldsymbol{\xi}^*, \boldsymbol{\xi}) = -\frac{1}{2} \int \boldsymbol{\xi}^* \cdot \mathbf{F}(\boldsymbol{\xi}) d\mathbf{r} \tag{2.23}$$

where $\boldsymbol{\xi}^*$ is the complex conjugate [68]. K is the kinetic energy of the plasma and is given by:

$$K(\boldsymbol{\xi}^*, \boldsymbol{\xi}) = \frac{1}{2} \int \rho |\boldsymbol{\xi}|^2 \, d\mathbf{r} \tag{2.24}$$

The final form δW is the fluid energy, δW_f, and is given by:

$$\delta W_f = \frac{1}{2\mu_0} \int_{plas} \left[|\boldsymbol{B}_1|^2 - \boldsymbol{J} \cdot (\boldsymbol{B}_1 \times \boldsymbol{\xi}) + (\boldsymbol{\xi} \cdot \nabla p) (\nabla \cdot \boldsymbol{\xi}) + i\omega p \, (\nabla \cdot \boldsymbol{\xi})^2 \right] d\boldsymbol{V} \tag{2.25}$$

where $\boldsymbol{J}$ is the equilibrium current density, $\boldsymbol{B}_1$ is the perturbed magnetic field and p is the equilibrium pressure. This equation yields the stability of the plasma. As $K > 0$ for all displacements, if δW_f is greater than zero, this denotes that the plasma is stable, as this implies that ω^2 is positive for all modes [68]. This is given by:

$$\delta W_f(\boldsymbol{\xi}^*, \boldsymbol{\xi}) \geq 0 \tag{2.26}$$

If δW_f is found to be negative, this shows that the equilibrium is unstable. This is given by:

$$\delta W_f(\boldsymbol{\xi}^*, \boldsymbol{\xi}) < 0 \tag{2.27}$$

As the energy principle is a minimising principle, it is able to recover the exact stability boundary and approximate growth rates of the modes, by finding the most negative value of ω^2 and represents the minimum δW_f, using what is known as the trial function [68]. In this approach, rather than solving equation 2.21 for $\boldsymbol{\xi}$ a physically allowable form for $\boldsymbol{\xi}$ is used in equation 2.22 - the trial function. This approaches the solution from above, such that ω^2 becomes more negative the closer $\boldsymbol{\xi}$ is to the actual value derived from equation 2.22 [68]. Also note that in the extended energy principle, which is used in ELITE, there is a contribution to δW from the vacuum [68]. This is given by:

$$\delta W_v(\boldsymbol{\xi}^*, \boldsymbol{\xi}) = \frac{1}{2\mu_0} \int_{vac} |\mathbf{B}_1|^2 \, d\mathbf{r} \tag{2.28}$$

This is positive definite and therefore always stabilising. Finally, there are also surface terms in the full δW that form boundary conditions when there is a vacuum present [68]. This is given by:

$$\delta W_s(\boldsymbol{\xi}^*, \boldsymbol{\xi}) = \frac{1}{2\mu_0} \int_{surf} |\mathbf{n} \cdot \boldsymbol{\xi}_\perp|^2 \, \mathbf{n} \cdot \left[\nabla \left(\frac{B^2}{2} + \mu_0 p \right) \right] d\mathbf{S} \tag{2.29}$$

where $\mathbf{n}$ is a outward pointing normal vector [68]. These two additions modify this term somewhat such that the full δW equation consists of three contributions from the plasma, which are the fluid energy, surface and vacuum [68]:

$$\delta W(\boldsymbol{\xi}^*, \boldsymbol{\xi}) = \delta W_f + \delta W_s + \delta W_v \tag{2.30}$$

2.4 MHD instabilities

2.4.1 Ballooning modes

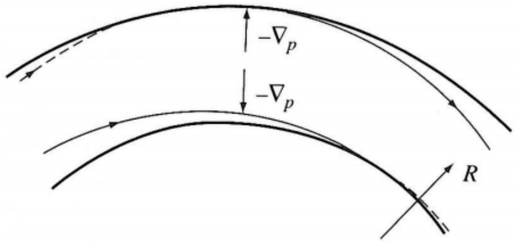

Figure 2.4: Illustration of curvature in a torus, where there is stabilising curvature on the inboard side and destabilising curvature on the outboard side. Reproduced from [8].

Ballooning modes are instabilities that arise on the outboard side of the plasma in a tokamak due to pressure gradients and field-line curvature [68]. They are internal modes, and are important since they provide a limit on the achievable plasma β [10]. As previously mentioned, field-line curvature can be classified as either favourable or unfavourable, and depends on the direction of the radius of curvature vector with respect to the direction of the pressure gradient [10]. This is illustrated in figure 2.4. The perturbation becomes concentrated in the region of destabilising curvature [8]. This causes a ballooning like distortion of the plasma flux surfaces, and the potential energy released is much greater than the stabilising forces from field-line bending [68].

This results in a ballooning mode. The modes localise to minimise field line bending, resulting in modes that are localised around rational surfaces [31]. The resulting modes have high toroidal mode number [68, 80].

Finite n ballooning modes are significantly stabilised by ion diamagnetic stabilisation, and the highest n modes are stabilised first [81]. Ion diamagnetic stabilisation is the finite gyro-radius stabilising effect of the ion diamagnetic drift frequency ω_{*i} [81]. The stabilisation leads to a peak in the growth rate vs. n as the higher n modes are suppressed and their growth rate is decreased. This effect was not included in the calculations in this thesis, except for the growth rates represented in figure 4.20, the use of these growth rates to determine threshold n in the δW KBM constrained study, and the $J - \alpha$ diagrams in chapter 5.

Ballooning modes differ to interchange modes, the other type of pressure-driven instabilities. Interchange modes can exist in both one-dimensional and tokamak geometries [68]. They represent plasma perturbations that are nearly constant along field lines, such that there is no field line bending, and the most unstable perturbations have very rapid variations perpendicular to the magnetic field [68]. This gives the modes a much shorter perpendicular wavelength compared to parallel wavelength and leads to the modes being highly localised in radius [68]. In general, they are stable in a tokamak provided that $q > 1$ described by a stability condition known as the Mercier criterion [31]. The Mercier criterion is given by:

$$D_M < 1/4 \tag{2.31}$$

where D_M is the Mercier coefficient which depends on equilibrium quantities [36, 82]. Therefore, localised interchange modes lead to necessary conditions for stability which can be expressed solely in terms of local values of equilibrium quantities [68].

Ballooning modes can also be studied in the $n = \infty$ limit, which simplifies their form to a 1D eigenmode equation [36, 83]. In general, ballooning modes can also be non-linear and can be used to explore the explosive nature of ELMs [84]. However, note that high n ballooning modes have been ruled out experimentally as the sole trigger of type I ELMs observed in tokamaks, as the ballooning limit in this case can be substantially exceeded [36].

At higher pressure gradient ballooning theory predicts that there is a second regime of stability is present, such that the pressure gradient can be much larger for the same amount of current density [85, 86, 87]. This occurs if magnetic shear is sufficiently low. A quantitative result of the solution of the ballooning mode equation at marginal stability can be visualised using $s - \alpha$ plots [68], where s is the magnetic shear and α is normalised pressure gradient, introduced in section 2.2.4. These plots have been used widely in previous research [25, 86, 83, 88, 89]. As example $s - \alpha$ diagram for ballooning modes is shown in figure 2.5.

Figure 2.5 shows that there are two branches in the diagram. The left branch

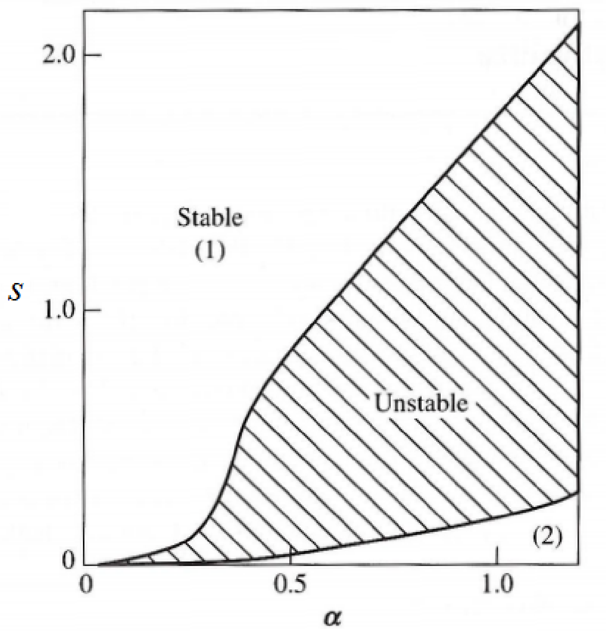

Figure 2.5: $s-\alpha$ marginal stability diagram for ballooning modes showing the first (1) and second (2) regions of stability, and the unstable region (cross-hatched region). Reproduced from [8].

separates the first stable region from the unstable region. Therefore, at a fixed value of shear the plasma is stable for sufficiently small pressure gradient [68]. As pressure gradient increases, the ballooning component overcomes shear and the plasma becomes unstable [68]. However, there is a second branch to the right, which separates the unstable region from a second region of stability [68, 85]. When shear is sufficiently low and the pressure gradient further increases such that $\alpha > s$ the shear becomes stabilising in the unfavourable curvature region, and a second region of stability to ballooning modes is produced [68].

As the pressure gradient increases, the shear will decrease creating a self-consistent path. If the pedestal reaches the unstable region, it will act as a barrier as the pressure gradient is clamped at its maximum for that value of shear and current density, and is unable to further increase without triggering the ideal ballooning mode. However, the current density will also increase as shear decreases. Therefore, this is a subtle and complex mechanism, which depends on transport processes, and predicting access to second stability is complex. The width of this second stable region, and how much current density is required to access it, depends on a number of associated factors in diverted tokamaks, including the triangularity (δ), q and β [90]. Kink modes restrict access to second stability [86].

2.4.2 Kink modes

As previously stated, instabilities driven by parallel current are known as current driven modes. These can be present without a pressure driven mode being present at low β. These instabilities are known as kink modes as they deform the plasma into a kink shape [10]. An illustration of a kink mode in a cylindrical piece of plasma, showing how the plasma kinks into a helix, causing the field lines to distort the magnetic field and further enhance the instability is shown in figure 2.6 [31].

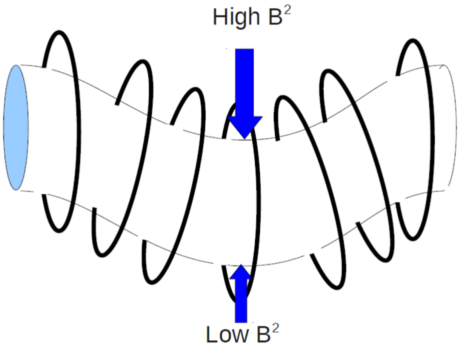

Figure 2.6: Illustration of the kink instability, showing how the plasma kinks, causing the field lines to bunch and spread, which then enhances the perturbation. Reproduced from [31].

They can be both internal and external modes and set a limit on the maximum toroidal current that can occur [10]. An internal kink is an instability that exists for $m = 1$ and $n = 1$ [8], and these therefore exist at the $q = 1$ surface, and produce an instability known as a sawtooth [68]. External kink modes are potentially the strongest of the ideal MHD instabilities [8]. At low β they are present without the pressure driven mode, and the main destabilising effect to high m modes is the radial variation of the parallel current [68]. At higher β the mode obtains a ballooning structure, but the harmonics are concentrated at the lower m values [68]. At high β external kink modes occur in the presence of pressure driven ballooning modes, and the kink mode can be present even with a low parallel current density. This coupled mode is known as the external ballooning-kink mode [91].

The peeling mode is an example of a limit of the external kink mode. It exists as the current gradient is indefinitely large at an infinitesimal region at the edge of the plasma [23], and is enhanced when there is a rational surface, where $q = m/n$, just outside the plasma [31]. The peeling mode taps into the free energy of the rational surface and causes the external current driven instability.

Diamagnetic stabilisation also provides significant stabilisation to low n kink (peeling) modes [81], and was only taken into account where stated in section 2.4.1 above.

2.4.3 Coupled peeling-ballooning modes

Coupling of the ballooning and kink modes occurs at high β, forming a coupled instability. In general if this occurs in the core region of the plasma, this is known as a kink-ballooning mode, which is driven by pressure and current gradients there [91]. However, at the edge barrier region these are conventionally called peeling-ballooning modes to distinguish that these are external ballooning-kink modes driven by the high current gradients located near the edge of the plasma [91]. Derived later in section

2.5.2, and reproduced here for reference, the peeling-ballooning equation is given by:

$$\begin{aligned}\delta W =&\pi \int_{-\infty}^{\psi_a} d\psi \oint d\chi \Bigg[\frac{JB^2}{R^2B_p^2}|k_\parallel X|^2 + \frac{R^2B_p^2}{JB^2}\left|\frac{1}{n}\frac{\partial Y}{\partial \psi}\right|^2 \\ &- \frac{2Jp'}{B^2}\left[|X|^2\frac{\partial}{\partial \psi}\left(p+\frac{B^2}{2}\right) - \frac{i}{2}\frac{f}{JB^2}\frac{\partial B^2}{\partial \chi}\frac{X^*}{n}\frac{\partial X}{\partial \psi}\right] \\ &- \frac{X^*}{n}JBk_\parallel\left(\sigma' X\right) + \frac{1}{n}\left[PJBk_\parallel^* Q^* + P^* JBk_\parallel Q\right] + \frac{\partial}{\partial \psi}\left[\frac{\sigma}{n}X^*Y\right]\Bigg]\end{aligned} \tag{2.32}$$

Note that there are in fact two terms relating to the current density in the peeling-ballooning equation, term 5 and term 7. Term 5 is known as the kink term, or current density gradient term, which is associated with the derivative of the parallel current density (σ') and acts across the plasma and edge barrier region [23]. The second is term 7 and is known as the peeling term, which contains the current density (σ) itself, and exists solely at the plasma surface as part of the δW_s boundary conditions. Thus the peeling part of the peeling-ballooning mode name refers to both the kink and peeling terms in the peeling-ballooning equation.

High pedestal current density reduces the edge magnetic shear, which stabilises high n ballooning modes, while concurrently providing drive for low - intermediate n peeling modes [36]. These modes couple to form intermediate n, typically $8 < n < 15$, peeling-ballooning (PB) modes [23, 35, 36]. These intermediate n PB modes are widely considered to be the trigger of type-I ELMs in tokamaks [35, 36, 92, 71].

The pedestal region at the edge of the plasma contains steep pressure and current gradients. These drive PB modes, initiating an ELM and causing a subsequent collapse in the pedestal, reducing the pedestal top pressure [71]. Therefore the stability boundary of the modes, which is how much pressure and current density in the pedestal that triggers the instability, sets a limit on the achievable pedestal height and limits H-mode performance [25, 35, 36]. This has been demonstrated on JET [93], DIII-D [94], JT-60U [95] and ASDEX-U [71, 93]. These studies have shown that the PB stability boundary was reached prior to a Type-I ELM crash [71]. ELMs are quasi-periodic eruptions, and therefore the pressure and current gradients in the pedestal must vary in a cyclical process: the ELM causes a loss of pedestal pressure height and bootstrap current from the edge barrier region. After the ELM, the pedestal is no longer constrained by the PB limit and the pedestal grows, and there is a corresponding increase in current density. This occurs until the PB limit is reached once more.

The PB boundary is very commonly illustrated in the two-dimensional parameter space of edge current density, J_{ped}, vs. pedestal pressure gradient, p', or normalised pressure gradient, α. These are known as $J-\alpha$ diagrams. Some examples are shown in [23, 25, 36, 43, 62, 71, 96, 97]. Firstly consider figure 2.7 (b). These plots are similar to $s-\alpha$ plots introduced in section 2.4.1, except shear decreases as current density increases. The stability boundary is shown as the solid line. At low pressure and current there is a region enclosed by the stability boundary, and this is known as the

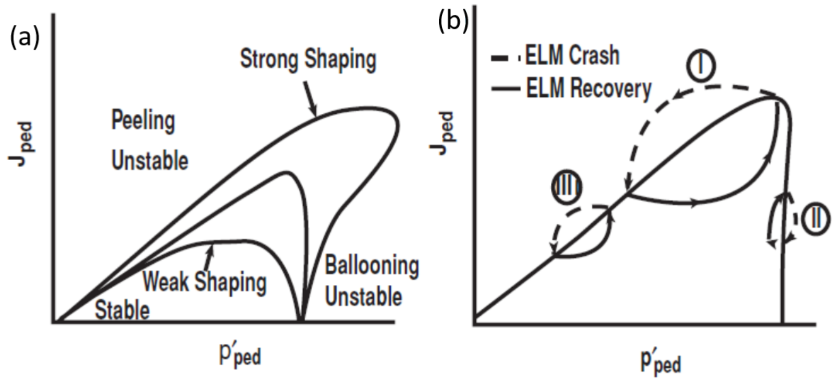

Figure 2.7: (a) An illustration of the peeling-ballooning stability boundaries for different plasma triangularity (b) A model of three types of ELM cycle, where I represents a type-I ELM, II represents ELMs that only cause a change in the pressure gradient, which are most likely Type-II ELMs and III represents a smaller ELM associated with the kink/peeling limit. The ELM crash is the dashed line, the recovery is the solid line. The other line is the peeling-ballooning stability boundary. The x-axis is pressure gradient, p', y-axis is current density in the pedestal, J_{ped}. Reproduced from [25].

stable region. Above the stability boundary is the unstable region. The ballooning unstable region is the region to the right of the vertical part of the stability boundary at high pressure gradient. The peeling unstable region is the region above the part of the stability boundary that starts at the current density axis. Figure 2.7 (b) is an illustration of the different types of ELM cycle, which consists of the initial ELM crash phase and subsequent recovery phase. Cycle I represents a type-I ELM, which causes a significant pedestal crash and recovery. Cycle II represents an ELM type which is pure ballooning, which could represent small type-I ELMs or type-II ELMs. Cycle III represents a lower power and density ELM, which is associated with striking the kink/peeling limit [94].

The PB stability boundary, and the journey towards the stability boundary, is affected by a number of different factors. The first is the plasma triangularity: the higher the triangularity, the more elongated the PB stability boundary [60, 94]. This is illustrated in figure 2.7 (a). This shows that high triangularity plasmas, depending on the pedestal evolution towards the stability boundary, are in general able to achieve higher pedestals due to this shaping. The PB stability boundary can be also elongated in a similar manner by increasing the power, and therefore the β, in the plasma and this particularly affects the ballooning region of the diagram [60]. These effects can be combined to achieve high performance.

The collisionality affects which part of the PB boundary the pedestal will reach. At low collisionality this is likely to be the kink/peeling boundary, whereas at high collisionality, where bootstrap current is suppressed, this is typically the ballooning boundary [27]. This is because the bootstrap current, although approximately proportional to the pressure gradient, is reduced by collisions [60]. The collisionality is related to the density, and therefore higher density pedestals follow a trajectory further towards the ballooning boundary [60, 62, 94]. This is illustrated on a realistic $J-\alpha$ diagram in figure 2.8. This also shows how the variation of the most unstable n associated with the PB mode changes depending on where the pedestal lies in the stability diagram, such that the intermediate n modes are at the highest achievable current and pressure gradient.

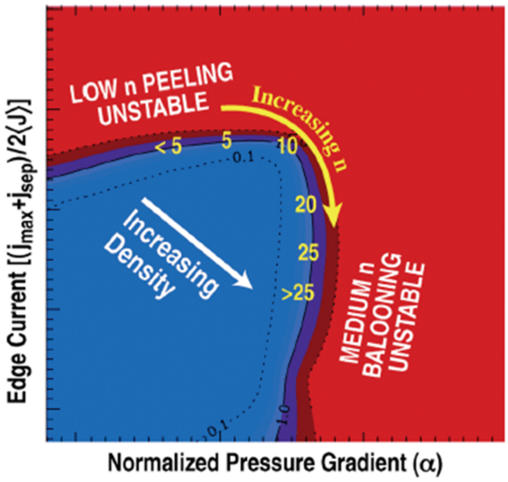

Figure 2.8: An example $J-\alpha$ diagram, where the y axis shows edge current density J and the x-axis shows normalised pressure gradient, α. Blue is the stable region, red is the unstable region, and the black line illustrates the stability boundary. This is illustrated with typical toroidal mode numbers for the modes that occur on that part of the stability boundary. Reproduced from [62].

2.4.4 Numerical codes for ideal MHD stability analysis

There were three codes used in this thesis to perform linear ideal MHD PB stability analysis. The first is the ELITE code [36, 98] which was both significantly extended and extensively used. This is formally introduced in the next section 2.5. This assumes a no wall, vacuum boundary condition. In general the growth rates given from the code are normalised to the Alfvén frequency, ω_A [99], such that the growth rate is given by γ/ω_A. In ELITE the Alfvén frequency used for normalisation of growth rate is the Alfvén frequency at the plasma edge, the last closed flux surface, which is given by:

$$\omega_A = \frac{B}{R\sqrt{\mu_0 \rho_a}} \tag{2.33}$$

where B is magnetic field, R is the major radius [99], ρ_a is the ion mass density at the edge, which the default is to use 2 for deuterium ions [100] and μ_0 is taken as 1. For major radius R the average of the innermost and outermost R values on the outer surface are used [99]. The magnetic field B is calculated by dividing $f = RB_\phi$ on the outer surface by the R value calculated [99], where f is the toroidal field function and B_ϕ is the toroidal magnetic field. In many cases, when a density profile is flat, as is often taken to be the case the value of ρ is the same everywhere. Furthermore, as the ELITE eigenvalue is $\gamma^2 4\pi\rho$, means that ρ is only needed to calculate the growth rate if ρ is varying [99]. When ρ is varying, only the relative variations of mass density are really needed, an overall value, for which only the outermost value is used, normalises out [99]. Note that if using equilibria with x-points these values will be where the flux cut-off point is taken to be [100].

The other two codes were used in benchmarks of the new, arbitrary n version of the ELITE code. These are the GATO code [101, 102], which is a low-intermediate n code. It is based on the variational principle of reference [79]. The second is the MARG2D code [103, 104]. This uses the 2D Newcomb method to solve the eigenvalue problem.

2.5 The ELITE and Mercier-Luc formalisms

ELITE [36, 98] is a linear edge ideal MHD stability code that is optimised for the study of intermediate-high toroidal mode number, n, modes associated with ELMs, using peeling-ballooning theory. This section details the ELITE formalism as described principally in [98]. It is detailed here show how the new arbitrary n ELITE formalism differs from the original ELITE formalism.

2.5.1 The Euler equation

Before the formalism of ELITE is formally introduced, it is helpful to introduce the Euler equation, also known as the Euler-Lagrange equation, for minimisation. The calculus of variations is employed, where problems are stated by saying a certain quantity is to be minimised [105]. This is in fact undertaken by saying that there is a quantity to be made stationary, and that quantity is an integral [105], given by:

$$I = \int_{x_1}^{x_2} F\left(x, y, y'\right) dx \tag{2.34}$$

where $y' = \frac{dy}{dx}$ [105]. Given the points (x_1, y_1) and (x_2, y_2) and the form of the function, F, the curve to be found, $y = y(x)$, is the curve which makes the integral I the smallest possible value [105]. The $y(x)$ that does this is the extremal. Letting $\eta(x)$ represent a function of x which is zero at x_1 and x_2 and has a continuous second derivative between these points but is otherwise arbitrary [105], the function $Y(x)$ is defined by:

$$Y(x) = y(x) + \epsilon\eta(x) \tag{2.35}$$

where ϵ is a parameter, therefore making $Y(x)$ any single-valued curve [105]. Differentiating equation 2.35 with respect to x gives the form for $Y'(x)$:

$$Y'(x) = y'(x) + \epsilon\eta'(x) \tag{2.36}$$

The solution is the curve that makes the integral I a minimum. Therefore, making the integral a function of ϵ:

$$I(\epsilon) = \int_{x_1}^{x_2} F\left(x, Y, Y'\right) dx \tag{2.37}$$

It is then desired for $I\left(\epsilon\right)$ take its minimum value $\left(\frac{d}{d\epsilon}\right) I\left(\epsilon\right) = 0$ when $\epsilon = 0$ [105]. Differentiating the integral with respect to ϵ gives:

$$\frac{dI}{d\epsilon} = \int_{x_1}^{x_2} \left(\frac{\partial F}{\partial Y}\frac{dY}{d\epsilon} + \frac{\partial F}{\partial Y'}\frac{dY'}{d\epsilon}\right) dx \tag{2.38}$$

Substituting equations 2.35 and 2.36 into equation 2.38 gives [105]:

$$\frac{dI}{d\epsilon} = \int_{x_1}^{x_2} \left(\frac{\partial F}{\partial Y}\eta\left(x\right) + \frac{\partial F}{\partial Y'}\eta'\left(x\right)\right) dx \tag{2.39}$$

It is required that $\frac{dI}{d\epsilon} = 0$ at $\epsilon = 0$, and equation 2.35 gives that $\epsilon = 0$ gives $Y = y$ [105]. Therefore, equation 2.39 becomes:

$$\left(\frac{dI}{d\epsilon}\right)_{\epsilon=0} = \int_{x_1}^{x_2} \left(\frac{\partial F}{\partial y}\eta\left(x\right) + \frac{\partial F}{\partial y'}\eta'\left(x\right)\right) dx = 0 \tag{2.40}$$

Using the assumption that y'' is also continuous, the second term can be integrated using integration by parts [105], giving:

$$\int_{x_1}^{x_2} \frac{\partial F}{\partial y'}\eta'\left(x\right) dx = \frac{\partial F}{\partial y'}\eta\left(x\right)\Big|_{x_1}^{x_2} - \int_{x_1}^{x_2} \frac{d}{dx}\left(\frac{\partial F}{\partial y'}\right)\eta\left(x\right) dx \tag{2.41}$$

As the integrated term is zero, as $\eta\left(x\right) = 0$ at both x_1 and x_2 [105], this gives:

$$\left(\frac{dI}{d\epsilon}\right)_{\epsilon=0} = \int_{x_1}^{x_2} \left(\frac{\partial F}{\partial y} - \frac{d}{dx}\frac{\partial F}{\partial y'}\right)\eta\left(x\right) dx = 0 \tag{2.42}$$

As $\eta\left(x\right)$ is arbitrary this yields the Euler equation [105], given by:

$$\frac{d}{dx}\frac{\partial F}{\partial y'} - \frac{\partial F}{\partial y} = 0 \tag{2.43}$$

Therefore, any problem in the calculus of variations, such as in the ELITE formalism, can be solved by setting up the integral which is to be stationary, writing what the function F is, substituting it into the Euler equation, and solving the resulting differential equation [105].

2.5.2 The δW equation

This formalism extends that of Connor-Hastie-Taylor [106], but the orthogonal coordinate system, given by (ψ, χ, ϕ), changes the definition of poloidal flux such that $[\psi] \rightarrow [-\psi]$. This is due to the fact that in ELITE the gauge for ψ is chosen such that $\psi = 0$ at the plasma edge, and takes a negative value everywhere in the core of the plasma [98]. Firstly, start with the ideal MHD energy principle, which is given by equation 2.25 [106]. The perturbation displacement ($\boldsymbol{\xi}$) can be written in terms of its three components, in three directions, X, U and Z. These are illustrated in the plane of a flux surface with the magnetic field B, in figure 2.9.

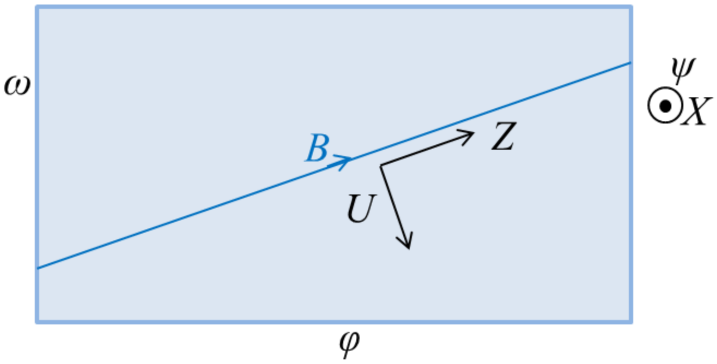

Figure 2.9: Three components, X, U and Z, of the perturbation displacement $\boldsymbol{\xi}$ shown in the plane of a single flux surface with a magnetic field line, $\boldsymbol{B}$, in the plane of the flux surface where: the x-axis is the toroidal, ϕ, direction, the y-axis is the poloidal, ω, direction and the radial, ψ direction is perpendicular to the x-y plane. The three perturbations in this 3D geometry are: X is perpendicular to the flux surface in the ψ direction, U is in the plane of the flux surface and perpendicular to the magnetic field line, and Z is in the plane of the flux surface and parallel to the magnetic field line.

As figure 2.9 shows, X is perpendicular to the flux surface, and is in the radial direction. U is in the plane of the flux surface, but perpendicular to the field line, and Z is parallel to the magnetic field. The incompressible limit is characterised by $\nabla \cdot \boldsymbol{\xi} = 0$ and therefore the parallel perturbation displacement, Z, is trivially eliminated (neglecting its contribution to inertia) [106]. Therefore, the ideal MHD energy principle becomes:

$$\begin{aligned} \delta W = \pi \int d\psi \oint d\chi \Bigg[& \frac{JB^2}{R^2 B_p^2} |k_\parallel X|^2 + \frac{R^2}{J} \left| \frac{\partial U}{\partial \chi} - f \frac{\partial}{\partial \psi} \left(\frac{JX}{R^2} \right) \right|^2 \\ & + JB_p^2 \left| inU + \frac{\partial X}{\partial \psi} - \frac{J_\phi}{RB_P^2} X \right|^2 - 2JK|X|^2 \Bigg] \end{aligned} \tag{2.44}$$

where

$$K = \frac{ff'}{R^2} \frac{\partial \ln(R)}{\partial \psi} + \frac{J_\phi}{R} \frac{\partial \ln(JB_p)}{\partial \psi} \tag{2.45}$$

where ψ is the poloidal magnetic flux, a prime denotes a derivative with respect to ψ,

χ is the poloidal angle related to ω, B is the total magnetic field, J is the Jacobian defined as $Jd\chi = dl/B_p$ where dl is the poloidal arc length element along a flux surface, B_p is the poloidal magnetic field, R is the major radius, and $k_\parallel$ represents the parallel gradient operator [98, 106], given by:

$$JBk_\parallel = -i\frac{\partial}{\partial\chi} + n\nu \tag{2.46}$$

where the pitch ν is given by:

$$\nu = \frac{fJ}{R^2} \tag{2.47}$$

The equilibrium magnetic field, $\mathbf{B}$ [98, 106], is given by:

$$\mathbf{B} = f\nabla\phi + \nabla\phi \times \nabla\psi \tag{2.48}$$

so that ψ is an increasing function of the minor radius of flux surfaces, and ϕ is the toroidal angle, [98], and finally J_ϕ is the toroidal current [98, 106], which is given by:

$$J_\phi = -Rp' - \frac{ff'}{R} = \frac{R}{J}\frac{\partial}{\partial\psi}\left(JB_p^2\right) \tag{2.49}$$

In the intermediate-high n limit, the perturbation displacement, U, can also be eliminated, employ the Euler equation for U to order n^{-1}:

$$U = \frac{i}{n}\frac{\partial X}{\partial\psi} + \frac{ip'}{nB^2}X + \frac{f}{n^2JB^2}\frac{\partial\left(JBk_\parallel X\right)}{\partial\psi} \tag{2.50}$$

where the presence of the $\frac{\partial}{\partial\psi}$ operating on X raises the order of the term by n, making the first term the leading order term in the expansion, and hence making the final term n^{-1}. Currently neglecting the contribution due to inertia, the change in energy to the first two orders (n^{-1}) is given by the equation [98, 106];

$$\begin{aligned}\delta W =& \pi\int_{-\infty}^{\psi_a} d\psi \oint d\chi\Bigg[\frac{JB^2}{R^2B_p^2}|k_\parallel X|^2 + \frac{R^2B_p^2}{JB^2}\left|\frac{1}{n}\frac{\partial Y}{\partial\psi}\right|^2 \\ &- \frac{2Jp'}{B^2}\left[|X|^2\frac{\partial}{\partial\psi}\left(p + \frac{B^2}{2}\right) - \frac{i}{2}\frac{f}{JB^2}\frac{\partial B^2}{\partial\chi}\frac{X^*}{n}\frac{\partial X}{\partial\psi}\right] \\ &- \frac{X^*}{n}JBk_\parallel\left(\sigma' X\right) + \frac{1}{n}\left[PJBk_\parallel^* Q^* + P^*JBk_\parallel Q\right] + \frac{\partial}{\partial\psi}\left[\frac{\sigma}{n}X^*Y\right]\Bigg]\end{aligned} \tag{2.51}$$

where a star denotes a complex conjugate and where Y is given by:

$$Y = JBk_{\parallel}X \tag{2.52}$$

and σ is the parallel current density, which is defined by:

$$\sigma = -\frac{fp'}{B^2} - f' \tag{2.53}$$

Finally P and Q are given by [98, 106]:

$$\begin{aligned} P =& \sigma X + \frac{fB_p^2}{n\nu B^2}\frac{\partial Y}{\partial\psi} \\ Q =& \frac{p'}{B^2}X + \frac{f}{nJB^2}\frac{\partial Y}{\partial\psi} \end{aligned} \tag{2.54}$$

As the modes are edge localised, and the perturbation $X \to 0$ in the core, this gives $-\infty$ as the lower limit of integration, and ψ_a is the poloidal flux at the plasma edge. In equation 2.51 the terms are as follows: the first two terms are the field-line bending terms, and these are always stabilising. The next two terms are the curvature/ballooning terms, the part in brackets being the curvature terms, and overall the ballooning terms which are stabilising in the inboard, and destabilising on the outboard. They can be identified as the ballooning terms due to the pressure gradient, p' term. The 5th term is the kink term, which is evident from the presence of the current density gradient (σ') in the term. The 6th term is the finite n term, and is of the order $1/n$. The 7th and final term is the peeling term, which becomes a surface term following the ψ integration. There is no peeling term in Connor-Hastie-Taylor because it was assumed that the mode amplitude at the plasma-vacuum interface is negligible. This is not the case in ELITE, where the edge-vacuum interaction is vital to edge kink/peeling modes, which are an integral component of the phenomena the code is designed to study [98].

2.5.3 Inertia contribution to δW

Here the inertia terms that form part of the full ELITE δW are detailed. This follows from a method originally in [106]. The δW in equation 2.51 provides the marginal stability of the equilibrium, while the inertia contribution provides an indication of the growth rate. The contribution to inertia arising from the parallel component of the displacement, Z, is also neglected here, which is valid at marginal stability [98]. The equation for inertia, which gives the kinetic energy of the transverse motion [106], is given by:

$$\delta W_{inertia} = \pi\gamma^2 \int_{-\infty}^{\psi_a} d\psi \oint d\chi J\rho \left[\frac{|X|^2}{R^2 B_p^2} + \frac{R^2 B_p^2}{B^2} |U|^2 \right] \tag{2.55}$$

where $\rho(\psi)$ is the mass density and γ^2 is the eigenvalue of the system, equal to the growth rate squared [98]. This equation is shown in reference [106] to leading order. However, here higher orders in n^{-1} are retained. Therefore, after eliminating U, the equation for the δW contribution from inertia is given by:

$$\begin{aligned}\delta W_{inertia} =& \pi\gamma^2 \int_{-\infty}^{0} d\psi \oint d\chi \left[\frac{\rho J}{R^2 B_p^2} |X|^2 + \frac{\rho J R^2 B_p^2}{n^2 B^2} \left| \frac{\partial X}{\partial \psi} \right|^2 \right. \\ & + \frac{G}{n^2} \left(X \frac{\partial X^*}{\partial \psi} + X^* \frac{\partial X}{\partial \psi} \right) \\ & \left. + \frac{H}{n^3} \left(\frac{\partial X^*}{\partial \psi} J B k_\parallel \left(\frac{\partial X}{\partial \psi} \right) + \frac{\partial X}{\partial \psi} J B k_\parallel^* \left(\frac{\partial X^*}{\partial \psi} \right) \right) \right]\end{aligned} \tag{2.56}$$

where

$$\begin{aligned} G &= \frac{\rho R^2 J B_p^2}{B^2} \left(\frac{p'}{B^2} + \frac{\nu'}{\nu} \frac{f^2}{R^2 B^2} \right) \\ H &= \frac{\rho f R^2 B_p^2}{B^4} \end{aligned} \tag{2.57}$$

Also note that the ordering of n is performed such that the Hermitian property of ideal MHD is exactly preserved, which is vital to the numerical results produced by ELITE [98].

2.5.4 Integration by parts

To determine the final form of the Euler equations from δW, integration by parts on radial ψ derivatives that act on complex conjugates, X^*, is performed. Deriving the Euler equations for X that minimise δW is then trivial. An example, using term 2 of

2.51, is illustrated here, where Y is given in equation 2.52.

$$\begin{aligned}
\delta W_2 =& \pi \int_{-\infty}^{\psi_a} d\psi \oint d\chi \frac{R^2 B_p^2}{JB^2} \left| \frac{1}{n} \frac{\partial Y}{\partial \psi} \right|^2 \\
=& \pi \int_{-\infty}^{\psi_a} d\psi \oint d\chi \frac{R^2 B_p^2}{JB^2} \frac{1}{n^2} \frac{\partial Y}{\partial \psi} \frac{\partial Y^*}{\partial \psi} \\
=& \pi \int_{-\infty}^{\psi_a} d\psi \oint d\chi \Bigg[\frac{\partial}{\partial \psi} \left(\frac{R^2 B_p^2}{JB^2} \frac{1}{n^2} \frac{\partial Y}{\partial \psi} Y^* \right) \\
& - \frac{Y^*}{n^2} \left(\frac{\partial}{\partial \psi} \left(\frac{R^2 B_p^2}{JB^2} \right) \frac{\partial Y}{\partial \psi} - \frac{R^2 B_p^2}{JB^2} \frac{\partial^2 Y}{\partial \psi^2} \right) \Bigg] \\
=& S_2 + \pi \int_{-\infty}^{\psi_a} d\psi \oint d\chi \left[- \frac{Y^*}{n^2} \left(\frac{\partial}{\partial \psi} \left(\frac{R^2 B_p^2}{JB^2} \right) \frac{\partial Y}{\partial \psi} - \frac{R^2 B_p^2}{JB^2} \frac{\partial^2 Y}{\partial \psi^2} \right) \right] \\
S_2 =& \pi \int_{-\infty}^{\psi_a} d\psi \oint d\chi \frac{\partial}{\partial \psi} \left(\frac{R^2 B_p^2}{JB^2} \frac{1}{n^2} \frac{\partial Y}{\partial \psi} Y^* \right)
\end{aligned} \tag{2.58}$$

where S_2 is the surface term for term 2, and the other two terms form the contributions to the Euler equations in the plasma for Y. Now this term can be Fourier decomposed, to find the final form for the terms in the Euler equations that ELITE must solve.

2.5.5 Fourier decomposition and coupled equations

The associated Euler equation now undergoes Fourier decomposition of the poloidal variation of the perturbation X in terms of the straight field line poloidal angle, ω, to find the final form of the δW equation. The straight field line poloidal angle takes the form [98]:

$$\omega = \frac{1}{q} \int^{\chi} \nu d\chi \tag{2.59}$$

where the safety factor, q, takes the form [98]:

$$q = \frac{1}{2\pi} \oint \nu d\chi \tag{2.60}$$

Therefore the perturbation X, takes the form [98]:

$$X = \sum_m u_m(x) e^{-im\omega} \tag{2.61}$$

where x is the fast radial variable, related to poloidal flux ψ by scaling, and m are the poloidal mode numbers, and its complex conjugate, X^*, takes the form:

$$X^* = \sum_k u_k^*(x) e^{ik\omega} \tag{2.62}$$

where k represents a Fourier mode. Then Y, from equation 2.52, takes the form:

$$Y = \sum_m \frac{-\nu}{q} (m - nq)\, u_m (x)\, e^{-im\omega} \tag{2.63}$$

with a similar form for Y^*. This form for Y demonstrates that the parallel derivatives go to zero at rational surfaces, as $m = nq$ at the rational surfaces, which is key to minimising field line bending. For high m modes field line bending will have a significant influence and this means that the $u_m (x)$ are restricted and highly localised around rational surfaces. Therefore this introduces the fast radial variable, $x = (m_0 - nq)$, determining the length scale for which $u_m (x)$ varies, where m_0 is the poloidal mode number of some reference rational surface [98], and is chosen such that the first rational surface in the vacuum is given by :

$$m_0 = \mathrm{Int}\,[nq_a] + 1 \tag{2.64}$$

where q_a is the safety factor at the plasma edge. Note that therefore x takes integer values at the rational surfaces, increasing from the edge to the core [98]. This is one of the three key features of the ELITE code, which allow the significant increase in code performance: at any single radial position, only a subset of the many harmonics that form the full mode structure are required. Therefore, at that single radial position only a small number of harmonics are significant, and the rest can therefore be set to zero [98].

Using the forms for X, X^*, Y and Y^*, after performing integration by parts if necessary will lead to the eventual derivation of the form for δW which provides the Euler equations to be solved by ELITE. The total δW is given by:

$$\delta W = \delta W_p + \delta W_s \tag{2.65}$$

where δW_p is the contribution from the core plasma, including inertia terms. δW_s is the contribution from the surface terms, from the peeling term and integration by parts which also has inertia contributions [98]. As ELITE is designed to address peeling modes, which interact with the vacuum, a vacuum model is necessary. This becomes a contribution, δW_v, to the surface δW_s, which only exists at the plasma-vacuum interface. This exploits the assumption that the plasma wall is far from the plasma edge, allowing the vacuum contribution to be simplified to an infinite vacuum on all sides [98]. This a good approximation for the localised modes ELITE is designed to consider.

The final resulting full expressions for δW can be seen in the appendix of reference [98]. ELITE is optimised to solve the set of coupled equations for $u_m (x)$ that minimise δW. Note that this is not an energy principle method, but solves a full set of Euler equations for the radial variations of the of the Fourier mode amplitudes [98]. Also note that the plasma and surface contributions, δW_p and δW_s respectively, are minimised separately. After Euler minimisation with respect to u_k^* for each Fourier mode, k, they take the form:

$$A''_{km}\frac{d^2u_m}{d\psi^2} + A'_{km}\frac{du_m}{d\psi} + A_{km}u_m = 0 \tag{2.66}$$

where a prime denotes the radial (ψ) derivative(s) of the u_m, not a derivative of the matrix elements themselves. The A_{km} are the matrix elements, and they take the form, for example for the coefficients of u_m:

$$\begin{aligned} A_{km} &= E_{2mk}(m-nq)^2(k-nq) + E_{m2k}(m-nq)(k-nq)^2 + E_{mk}(m-nq)(k-nq) \\ &\quad + E_{2m}(m-nq)^2 + E_{2k}(k-nq)^2 + [E_m - \gamma^2 I_m](m-nq) + \\ &\quad [E_k - \gamma^2 I_k](k-nq) + E - \gamma^2 I \end{aligned} \tag{2.67}$$

where E_i are flux surface averages of equilibrium quantities, comprised of individual matrix elements, T_i, given by:

$$T_i(\psi) = \oint K_i(\psi,\omega)\, e^{i(k-m)\omega} d\omega \tag{2.68}$$

where the kernels, K_i, are derived analytically in terms of equilibrium quantities. The full set of matrix elements and kernels, as well as the Euler minimised full final equations are published in reference [98]. If there are a total number of Fourier harmonics, M, required to fully describe the mode being analysed, then there are M coupled differential equations in the form of equation 2.66 for the mode amplitudes u_m [98].

The formalism is completed with the following boundary conditions. Firstly, is that the modes tend to zero in the plasma core, which is a reasonable assumption since ELITE was designed for edge localised modes. This boundary condition is given by [98]:

$$\lim_{x\to\infty} u_m(x) = 0 \tag{2.69}$$

The next condition is the surface contribution to the total energy is zero, representing the jump in $p + B^2/2$ across the plasma-vacuum interface is zero [98]. The final condition for the matching of the plasma-vacuum interface is that the radial component of the magnetic field is continuous across this interface. This condition is used to express the vacuum magnetic field perturbation in terms of the u_m at the plasma surface, which forms part of the surface terms [98]. These surface terms provide the second boundary condition required for a full solution. These boundary conditions for each Fourier mode, k, are applied at the plasma boundary, where $\psi = \psi_a$, so that the fast radial variable, x, takes the form:

$$x = \Delta = m_0 - nq_a \tag{2.70}$$

where $0 \leq \Delta \leq 1$ [98], and q_a is the safety factor at the plasma boundary [98]. The surface terms, as with the core plasma terms, contain surface terms from the plasma terms, S, as well as surface terms from the inertia, J, there is also the contribution from the vacuum, δW_v. The terms are fully detailed in [98]. Here an example Fourier decomposition to produce a matrix element and coefficient matrix for a core plasma term is shown here for term 1 of 2.51:

$$\begin{aligned}
\delta W &= \pi \int_{-\infty}^{\psi_a} d\psi \oint d\chi \frac{JB^2}{R^2 B_p^2} |k_\| X|^2 \\
&= \pi \int_{-\infty}^{\psi_a} d\psi \oint d\chi \frac{1}{JR^2 B_p^2} |Y|^2 \\
&= \pi \int_{-\infty}^{\psi_a} d\psi \sum_{m,k} \oint d\omega \frac{q}{\nu} \frac{f}{\nu R^4 B_p^2} \frac{\nu^2}{q^2} (m - nq)(k - nq)\, u_m u_k^* e^{i(k-m)\omega} \\
&= \pi \int_{-\infty}^{\psi_a} d\psi \sum_{m,k} \oint d\omega \frac{f}{R^4 B_p^2} \frac{1}{q} (m - nq)(k - nq)\, u_m u_k^* e^{i(k-m)\omega} \\
&= \pi \int_{-\infty}^{\psi_a} d\psi \sum_{m,k} u_k^* \left[\frac{(m - nq)(k - nq)}{q} T_1 u_m \right]
\end{aligned} \tag{2.71}$$

where T_1 is the matrix element for term 1, given by:

$$\begin{aligned}
T_1(\psi) &= \oint \frac{f}{R^4 B_p^2} (\psi, \omega)\, e^{i(k-m)\omega} d\omega \\
&= \oint K_1(\psi, \omega)\, e^{i(k-m)\omega} d\omega
\end{aligned} \tag{2.72}$$

T_1 will form part of the full set of matrix elements for A_{km}. The use of kernels allows for the creation of two radial length scales.

2.5.6 Radial length scales separation

The separation of length scales, the equilibrium length scale, represented by the equilibrium terms, E_i, and the length scale consisting of the distance between the rational surfaces, $(m_0 - nq)$, on which the u_m is calculated, is the second key feature of ELITE. An illustration of these two length scales is shown in figure 2.10.

The distance between the rational surfaces is $1/nq'$, and tends to zero at large n. As field-line bending restricts $u_m(x)$ to be radially localised to within a few rational surfaces. Therefore, the $u_m(x)$ must be solved on a much finer radial mesh, denoted by the $(m_0 - nq)$ length scale to obtain an accurate result. In contrast, the equilib-

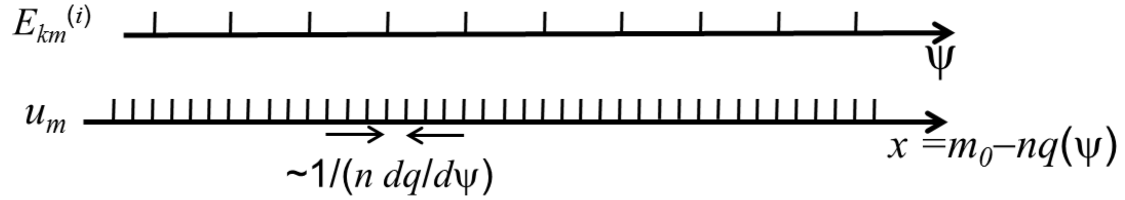

Figure 2.10: Illustration of the radial length scales in ELITE, where (a) is the length scale of the equilibrium terms, $E_i^{k,m}$, on a ψ scale and (b) the mode amplitude, u_m, is determined on the length scale comprised of the distance between the rational surfaces, $x = (m_0 - nq)$. The distance between the rational surfaces tends to zero at large n.

rium quantities vary slowly when considered on this rational surface length scale at intermediate-high n. This allows the matrix elements to be evaluated and tabulated on the coarser radial (ψ) grid [98]. Therefore to solve for $u_m(x)$ requires interpolation of the equilibrium quantities from the coarser radial equilibrium length scale mesh, to the finer mesh. However, as seen in term 1 in equation 2.71, the equilibrium terms, E_i, contain derivatives of equilibrium quantities. Calculating these using numerical derivatives across the coarse mesh introduces inaccuracies. Therefore, they are calculated by deriving analytic derivatives.

2.5.7 Mercier-Luc formalism

The third and final feature of ELITE is that it is designed to evaluate the radial derivatives of equilibrium quantities using an expansion about a flux surface, following the formalism of Mercier-Luc [72]. These could in principle be calculated numerically if the equilibrium is fully described on all flux surfaces. However, a more accurate approach is to derive analytic derivatives by expansion of the Grad-Shafranov equation, equation 2.8, about a flux surface, ($\psi = \psi_0$), using quantities only on that flux surface. This has the obvious advantage that deriving analytic derivatives on the coarse mesh and then interpolating to the fine mesh is far more accurate than numerical derivatives being interpolated. It also has the additional advantage that it ensures that each flux surface is an accurate solution of the Grad-Shafranov equation. Specifically required for the calculation are: the flux surface shape, $R_s(l)$, $Z_s(l)$, the poloidal field variation on the flux surface, $B_{ps}(l)$; and the components of the toroidal current $p(\psi_0)$ and $ff'(\psi)$, where R and Z are the usual cylindrical coordinates and l is the poloidal distance along the flux surface. This is known as the Mercier-Luc formalism [98, 72]. As previously, a prime denotes a poloidal flux, ψ, derivative and the magnetic field is given by equation 2.48.

Using this information, as well as a piece of information to determine q and the toroidal field ($f(\psi_0) = RB_\phi$), [72] a local expansion of the Grad-Shafranov equation about the flux surface ($\psi = \psi_0$) can be performed: for a close flux surface, a small distance ρ away, the quantities can be derived on that flux surface. Taking the limit $\rho \to 0$ provides analytic derivatives. This is illustrated in figure 2.11 (a). To employ this method, a co-ordinate system needs to be defined. This is illustrated in figure 2.11

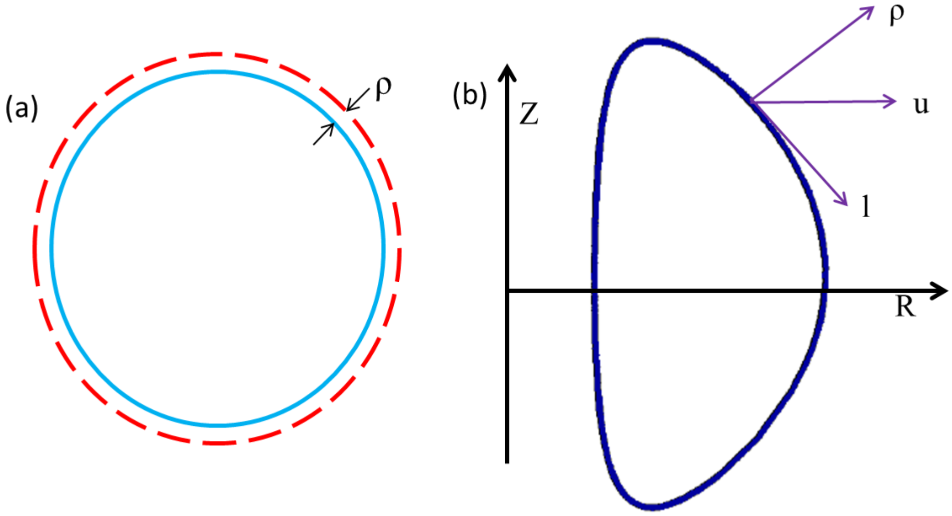

Figure 2.11: Illustration of the Mercier-Luc formalism where (a) illustrates the small distance, ρ, from the blue flux surface $\psi = \psi_0$, forming the red dashed surface (b) illustrates the Mercier-Luc orthogonal co-ordinate system, (ρ, l, ϕ), where ρ is the normal distance from the flux surface $\psi = \psi_0$, l is the poloidal distance along the flux surface and ϕ is the toroidal angle; u is an additional angle that is useful.

(b). This co-ordinate system is orthogonal, defined as (ρ, l, ϕ), where ρ is the normal distance from the flux surface $(\psi = \psi_0)$, also illustrated in (a) and ϕ is the toroidal angle [72]. Also shown in figure 2.11 (b) is angle u, which is given by [72]:

$$\begin{aligned} \frac{dR_s}{dl} &= \cos u \\ \frac{dZ_s}{dl} &= -\sin u \end{aligned} \tag{2.73}$$

This provides a relation of u to the radius of curvature of the flux surface $\psi = \psi_0$, $R_c(l)$, given by [72]:

$$\frac{du}{dl} = -\frac{1}{R_c} \tag{2.74}$$

The cylindrical co-ordinates at a neighbouring surface, R and Z, may then be written [72]:

$$\begin{aligned} R(\rho, l) &= R_s(l) + \rho \sin u(l) \\ Z(\rho, l) &= Z_s(l) + \rho \cos u(l) \end{aligned} \tag{2.75}$$

and the Jacobian is given by [72]:

$$J = \left(1 - \frac{\rho}{R_c}\right) R \tag{2.76}$$

Now ψ can be expressed as an expansion:

$$\psi = \psi_0 + \rho\psi_1(l) + \rho^2\psi_2(l) + \rho^3\psi_3(l) + ... \tag{2.77}$$

Note that in [72] this expansion is only used up to $\psi_2(l)$. However, ELITE requires second derivatives, solution shown in [98], and therefore the expansion is undertaken to the $\psi_3(l)$ ordering, to allow for this. Now $\psi_1(l)$, $\psi_2(l)$ and $\psi_3(l)$ need to be calculated. The details of this for $\psi_1(l)$ and $\psi_2(l)$ can be seen in [72]. The $\psi_1(l)$ term can be calculated from the expression for B_p from 2.48. This takes the resulting expression for B_p^2, then considers the solution at $\psi = \psi_0$, i.e. $\rho \to 0$, and therefore consequentially $B_p \to B_{ps}$ and $R \to R_s$, yielding [98, 72]:

$$\psi_1(l) = R_s(l)B_{ps}(l) \tag{2.78}$$

Calculating $\psi_2(l)$ is more complex. This uses the ψ expansion in the Grad-Shafranov equation. Taking the resulting expression, using the solution at $\rho \to 0$, and using 2.78 to eliminate $\psi_1(l)$ yields $\psi_2(l)$ [98, 72]:

$$\psi_2(l) = \frac{1}{2}\left[\left(\sin u + \frac{R_s}{R_c}\right)B_{ps} - R_s^2 p'(\psi_0) - ff'(\psi_0)\right] \tag{2.79}$$

where μ_0 is assumed to be 1, as in ELITE. Finally, the expression for $\psi_3(l)$ is also calculated from the Grad-Shafranov equation. The expression is derived by matching the 1st order ρ terms, which is equivalent to taking the derivative $\partial/\partial\rho$ and matching the resulting terms as $\rho \to 0$. The parameters are also all evaluated on the flux surface, yielding [98]:

$$\begin{aligned}\psi_3(l) = \frac{1}{6}\Bigg[& -2B_{ps}\sin u\left(\frac{1}{R_c} + \frac{\sin u}{R_s}\right) + 4\psi_2\left(\frac{1}{R_c} + \frac{\sin u}{R_s}\right) - R_s\frac{\partial}{\partial l}\left(\frac{1}{R_s}\frac{\partial\psi_1}{\partial l}\right) \\ & + R_s^2 p'\left(\frac{1}{R_c} - \frac{\sin u}{R_s}\right) + ff'\left(\frac{1}{R_c} + \frac{\sin u}{R_s}\right) - R_sB_{ps}\left(R_s^2 p'' + (ff')'\right)\Bigg]\end{aligned} \tag{2.80}$$

Now all the analytic first derivatives of the equilibrium quantities can be obtained. For example the equation for RB_p, which has been evaluated to $O(\rho^2)$ [98]:

$$RB_p = R_sB_{ps}\left[1 + 2\rho\frac{\psi_2}{\psi_1} + \frac{\rho^2}{2}\left[\frac{6\psi_3}{\psi_1} + \frac{1}{\psi_1^2}\left(\frac{\partial\psi_1}{\partial l}\right)^2\right]\right] \tag{2.81}$$

Ordering to ρ^2 is required to allow the derivation of second derivatives which ELITE requires. Applying this procedure to all the equilibrium quantities provides all the differentials required.

2.5.8 The eigenvalue condition

Once the equation 2.66 with all the boundary conditions has been derived, it is solved to find the eigenfunction and corresponding eigenvalue for the system. This is performed using a shooting algorithm. Detailed description of the ELITE shooting algorithm is provided in the appendix, in section A.1. Here a summary of the eigenvalue condition is provided, for which the eigenvalue, and therefore the growth rate of the system can be determined. $u_m(x)$ can be written as an expansion in a set of M linearly independent solutions, v_m, for each of the M Fourier harmonics, given by:

$$u_m(x) = \sum_{k=1}^{M} a_k v_{mk}(x) \tag{2.82}$$

After the shooting algorithm has been performed, a matching condition can be imposed at the plasma-boundary interface, which provides an eigenvalue equation for the eigenvector a_k and the growth rate, γ, given by:

$$\sum_{k=1}^{M} T_{mk}(\gamma^2) a_k = 0 \tag{2.83}$$

where $T_{mk}(\gamma^2)$ is an $M \times M$ matrix which depends on v_m at the surface, and includes the edge boundary condition. It is defined in equation A.13 in section A.1 in the appendix. The true growth rate satisfies this condition. However, the initial γ^2, may not be the true growth rate. Therefore a fictitious eigenvalue λ is introduced, such that:

$$\sum_{k=1}^{M} T_{mk}(\gamma^2) a_k = \lambda(\gamma^2) a_m \tag{2.84}$$

The growth rate then satisfies $\lambda(\gamma^2) = 0$. This fictitious eigenvalue can be used as a check of the stability of the system: if $(\gamma^2 = 0) < 0$, then the system is unstable. If the actual growth rate is required, an iteration on γ^2 must be performed, until $\lambda(\gamma^2) = 0$.

2.5.9 Example results from ELITE

This subsection shows an example ELITE output calculated for a model equilibrium. ELITE calculates the growth rate, γ, normalised to the Alfvén frequency, ω_A. ELITE also has routines that allow the radial profiles of Fourier harmonics $u_m(x)$ to be visualised [94, 98]. The mode structure can also be plotted as a contour plot of the eigenfunction $X(\psi, \chi)$ in R and Z space, which is the normalised radial displacement of the mode [99]. Using an up-down asymmetric D-shaped test case, described in more detail in section 4.5, an example of each plot has been produced for $n = 15$. The result is shown in figure 2.12, where (a) is the eigenfunction $u_m(x)$ in normalised ψ space and

(b) is the contour plot, in the poloidal plane.

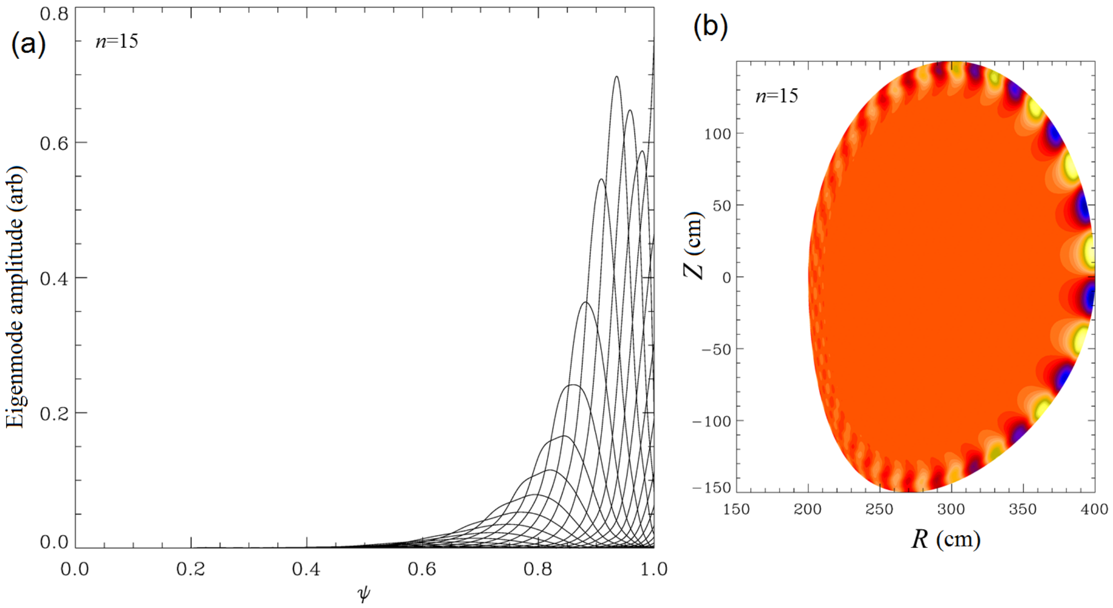

Figure 2.12: Example results produced by ELITE for a up-down asymmetric D-shaped test case for $n = 15$ where (a) shows the radial profiles of the Fourier harmonics, $u_m(x)$, where each harmonic corresponds to a single poloidal mode structure and (b) is a contour plot of the normalised radial displacement of the eigenfunction $X(\psi, \chi)$, in the poloidal plane with filled contours

As figure 2.12 (a) shows, each poloidal harmonic is radially localised about its rational surface [98], and illustrates the importance of the separation of length scales, where the equilibrium values vary relatively slowly over the envelope of all the individual Fourier mode structures. The structure shows a typical peeling-ballooning mode with the ballooning mode structure coupling many harmonics across a relatively wide range of ψ, and the edge kink/peeling component as a single poloidal harmonic with the highest amplitude at the edge, which is therefore interacting with the vacuum region, as illustrated in [94]. Figure 2.12 (b) shows the contour plot of the same eigenfunction, where there are lighter and darker shades represent large positive and negative perturbations respectively [98]. This shows how far the mode structure extends in from the edge to the plasma core.

2.6 Kinetic ballooning modes and the EPED model

The kinetic ballooning mode (KBM) is a highly radially localised high n ballooning mode with kinetic effects. This provides a soft limit on the pedestal as it clamps the local pressure gradient, but still allows the pedestal height and width to increase. Calculating the full stability of the KBM requires the use of challenging gyro-kinetics [107, 108, 109, 110].

The EPED model was designed to predict the pedestal height with the premise that there are two key properties that influence the pedestal height [27, 91, 111]. The first property is the width of the pedestal, and the second is the gradient that the pedestal achieves. The EPED model has been shown to successfully reproduce the experimental pedestal height across a wide range of parameter space on multiple tokamaks [111].

The EPED model is comprised of two key instabilities which provide two constraints on the pedestal. Initially the pedestal is able to grow unconstrained, until it reaches the first limit, which is due to the KBM. The KBM causes a highly radially localised, also known as soft, local limit. The KBM provides a constraint on the pedestal pressure gradient, which becomes clamped when the KBM limit is reached. The pedestal height and width then evolves with the gradient constrained by the KBM until the second limit is reached, which is provided by PB mode. This is a hard limit which usually extends right across the pedestal, and is sensitive to the pedestal gradient and the pedestal width. These two constraints therefore allow the determination of the pedestal height, and therefore the pedestal structure. The model has can be used to compare to experimental results, as well as to make pedestal predictions, such as for ITER [111]. An illustration of the EPED model is shown in figure 2.13.

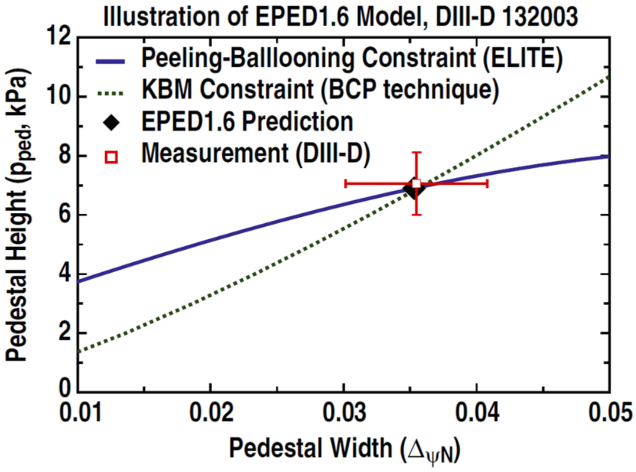

Figure 2.13: Illustration of the EPED pedestal structure model. This shows KBM (dashed) and PB (solid) boundaries. Where the boundaries intersect is the prediction of the pedestal height. The experimentally measured value, for this case on DIII-D, is shown as the red square. This shows that the EPED model predicted the experimentally observed pedestal height and width. Reproduced from [111].

.

The description of the model using figure 2.13, is as follows: the pedestal initially grows unconstrained until it reaches the KBM boundary. The pedestal then grows monotonically by widening and then moving along the KBM boundary at fixed gradient. This occurs until the pedestal reaches the PB boundary, where the two boundaries intersect, and then an ELM occurs. Multiple tokamaks including MAST [107, 112], DIII-D [113, 114], C-Mod [27, 115] and NSTX [55] support this premise that the pedestal width (Δ_{ped}) increases as the pedestal height increases at a fixed gradient. An example from MAST, which shows the clamping of the density pedestal through one ELM cycle can be seen in figure 2.14.

A complete model of the underlying physics of the pedestal width evolution is still unknown. There is evidence that micro-tearing modes may play a role in pedestal

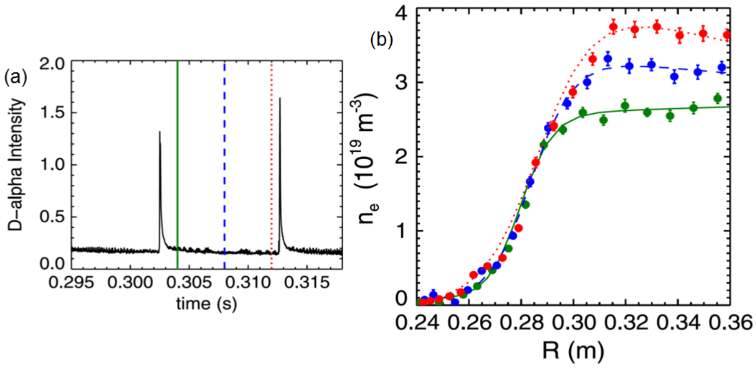

Figure 2.14: Data from the MAST tokamak showing clamping of the gradient in the density pedestal through one ELM cycle. Reproduced from [112].

dynamics [71, 112, 116]. A full calculation of KBM stability requires the use of gyro-kinetics, which is challenging. Studies on ASDEX Upgrade used the gyro-kinetic code GENE [143] which showed that the pressure gradient is held fixed and near to the KBM limit [143], as expected by the EPED model. Further gyro-kinetic studies of ASDEX Upgrade inter-ELM pedestal profile evolution [144] have shown later inter-ELM phases appear to be simultaneously constrained by electron temperature gradient (ETG) and KBM turbulence [144]. The nominal profiles were shown to lie just below the KBM limit in the outer half of the pedestal during the last two-thirds of the ELM cycle [144].

EPED avoids the difficulty of gyro-kinetics by adopting one of the two known proxies for the KBM. First is the proxy used by the EPED model detailed in 2.6.1, and second is another proxy used in this thesis, detailed in 2.6.2.

2.6.1 Width scaling proxy for the KBM

The first proxy to be discussed is the $\sqrt{\beta_{p,ped}}$ width scaling proxy for the KBM, which is the proxy used for the KBM in the EPED1 and EPED1.6 models [27, 91, 111]. In addition to the observation on multiple tokamaks that the pedestal width (Δ_{ped}) grows as the height grows for a fixed gradient, [107, 112, 114] there is also significant experimental evidence from a wide range of different tokamaks, including DIII-D [117, 118], MAST [27, 119, 120], C-Mod [27, 115, 121], JT-60U [55, 122] and ASDEX-U [27, 123] that Δ_{ped} scales as the square root of $\beta_{p,ped}$, $\sqrt{\beta_{p,ped}}$ [27, 91]. The equation for the scaling of $\Delta_{p,ped}$ is therefore taken to be:

$$\Delta_{p,ped} = c_1\sqrt{\beta_{p,ped}} \tag{2.85}$$

where c_1 is a constant [27, 57, 91, 111, 124]. In EPED1 this was calculated using a wide range of different pulses in DIII-D encompassing over 4000 individual time slices, the method is detailed in [91], and is calculated to be 0.076. In the more sophisticated EPED1.6 model this constant is taken to be a weakly varying function, G, of plasma parameters including collisionality, ν^*, and aspect ratio, ϵ [57, 91]. The KBM constraint uses a ballooning critical pedestal (BCP) technique, where an edge barrier profile is taken to be ballooning critical when the central half of it is beyond the first local ballooning threshold [91]. This leads to a typical value when it is calculated for standard aspect ratio tokamaks, such as JET, of $c_1 = 0.07 - 0.1$ [91].

2.6.2 n=∞ ballooning proxy for the KBM

The second proxy for the KBM is the $n = \infty$ ideal MHD ballooning mode. Gyrokinetic and electromagnetic gyrofluid analysis has shown that as the $n = \infty$ ideal ballooning boundary is approached the KBM growth rates increase rapidly [108, 109, 110, 125, 126]. Additionally, collisionless KBMs and $n = \infty$ ideal ballooning modes have previously been shown to have similar character and are described by related equations [107, 127]. Furthermore, in the low frequency limit the kinetic result reduces to the ideal ballooning result [71, 127]. Therefore, this suggests the ideal MHD ballooning mode can be used as a proxy for the onset of the KBM instability, the clamping of the pressure gradient and the associated stiff transport response [91, 71, 128].

The $n = \infty$ ideal ballooning stability can be calculated with the HELENA code [75], introduced in subsection 2.2.5, using the method published in [129]. Using HELENA for this purpose has been employed for the MAST tokamak and was compared to the local gyrokinetic GS2 code, which was used to calculate the KBM stability to assess the suitability of the proxy [107]. This shows that the $n = \infty$ ideal ballooning unstable region matches closely to the region where KBMs are the dominant modes [107, 112]. This is despite the kinetic finite Larmour radius (FLR) effect, which is stabilising and expected to be important, being neglected in the $n = \infty$ ideal ballooning model [107, 127]. Therefore, $n = \infty$ ideal ballooning stability is a reasonable proxy for the KBM [107].

An example from JET showing the normalised pressure gradient α, which shows the pedestal (blue), and the corresponding $n = \infty$ ballooning limit (red) can be seen in figure 2.15. It can be seen in figure 2.15 that the pedestal is constrained by the $n = \infty$ ballooning limit as the peak in α in the pedestal region is up against the $n = \infty$ ballooning limit.

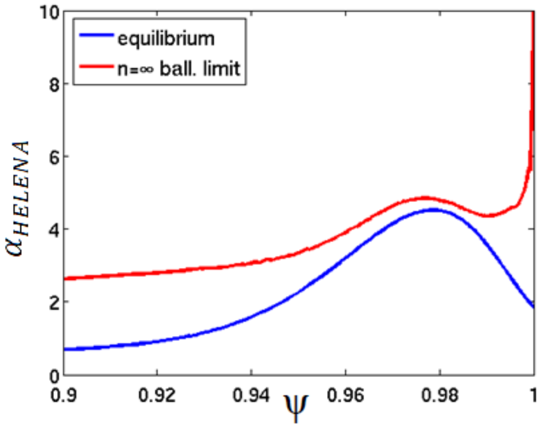

Figure 2.15: Example output from JET of the $n = \infty$ ballooning limit which is shown in red, and the normalised pressure gradient α, which is shown in blue, as a function of normalised flux ψ.

Chapter 3

Extension of the ELITE code to arbitrary toroidal mode number

3.1 Introduction and Motivation

The ELITE code, whose original formalism is described in the previous chapter, was previously optimised to explore intermediate-to-high toroidal mode number (n) ideal MHD modes. The initial motivation for the code was to test the peeling-ballooning (PB) theory of ELMs. This has been very successful and key to validating PB as the trigger for type I ELMs. ELITE is also a key component of the EPED model which, as described in the previous chapter, predicts the pressure pedestal width and height. The efficient nature of the ELITE code, due to the efficiencies described in the previous chapter, allows for many stability calculations to be performed in a relatively small amount of time. This is key to the EPED model which can run on the order of 100s-1000 individual ELITE calculations in a single EPED run. Due to the n^{-1} expansion performed, the ELITE code is typically accurate down to $n \approx 4-5$. However, there are tokamak regimes where the pedestal is limited by low n activity (QH Mode, for example). To study these regimes with ELITE, it was required that the formalism be extended to arbitrary n. The extension of the ELITE formalism to arbitrary n is justified because, at the edge of a tokamak plasma where q' gets large, the distance between rational surfaces becomes small, even at low n. The ELITE formalism, which employs the separation of radial length scales, is still useful even when n is low. Details of the mathematical formalism that was developed for arbitrary n is presented in this chapter. The entire solution for the arbitrary n δW equation is detailed in full in appendix B.

3.2 Extension of the δW equation

The derivation of the arbitrary n δW equation initially follows that of the original ELITE formalism, yielding equation 2.44. In the high n limit, a second component, U, is eliminated using its Euler equation, correct to $O(n^{-2})$, such that the perturbation is purely in terms of the radial displacement X. This is given by equation 2.50. However, in the arbitrary n limit, all orders of U need to be retained and the following expansion of U is used:

$$U = \frac{i}{n}\frac{\partial X}{\partial \psi} + \frac{ip'}{nB^2}X + \frac{iW}{n} \tag{3.1}$$

This is a modified version of 2.50 without the second $O(n^{-1})$ term, which is absorbed into the W term, and all the orders of U are retained in the W term. This expansion is performed so that the δW equation that is derived has a similar form for the X terms, particularly to leading order. However, the second $O(n^{-1})$ term is absorbed into the W term to allow the simplification of the number of kernels produced, since the ψ derivative in the term leads to many different kernels. As will be shown, despite the significantly more complex δW from the two components, the number of final kernels decreases from 66 in the original formalism, seen in [98], to 46 in the new arbitrary n formalism, which are shown in appendix section B.4. This also changes the equilibrium coefficients on some of the original terms, such that the original terms are formed numerically in the new arbitrary n version of ELITE from these modified original terms, and some of the new terms. Therefore, when benchmarking the new and original ELITE codes at higher n, the growth rates are calculated from distinctly different terms.

Equation 3.1 for U is now substituted into equation 2.44. Also required to determine the form for δW, are equations for σ (2.53), J_ϕ (2.49), the parallel gradient operator (2.46), where ν is given by equation 2.47, and the form for K, shown in equation 2.45. First substitute the form for U inside the modulus of term 3 in equation 2.44. After manipulation this yields:

$$\frac{\partial X}{\partial \psi} + inU - \frac{J_\phi}{RB_p^2}X = -\left[W + \frac{f\sigma}{R^2B_p^2}X\right] \tag{3.2}$$

Secondly, substituting the form for U inside the modulus of term 2 and this after manipulation yields:

$$\frac{\partial U}{\partial \chi} - f\frac{\partial}{\partial \psi}\left(\frac{JX}{R^2}\right) = -\left[\frac{1}{n}\frac{\partial Y}{\partial \psi} + \frac{\sigma J}{R^2}X + \frac{p'}{n}JBk_\parallel\left(\frac{X}{B^2}\right) - \nu W + \frac{1}{n}JBk_\parallel W\right] \tag{3.3}$$

where Y is given by equation 2.52. This yields δW in this intermediate form;

$$\begin{aligned}\delta W =\pi \int_{-\infty}^{\psi_a} d\psi \oint d\chi\Bigg[&\frac{JB^2}{R^2B_p^2}\left|k_\parallel X\right|^2 + \frac{R^2}{J}\left|\frac{1}{n}\frac{\partial Y}{\partial \psi} + \frac{\sigma J}{R^2}X + \frac{p'}{n}JBk_\parallel\left(\frac{X}{B^2}\right)\right.\\ &\left. - \nu W + \frac{1}{n}JBk_\parallel W\right|^2 + JB_p^2\left|W + \frac{f\sigma}{R^2B_p^2}X\right|^2 - 2KJ\left|X\right|^2\Bigg]\end{aligned} \tag{3.4}$$

Now a significant amount of algebra is performed: firstly, the manipulation of terms that include W is performed, including terms that contain both W and X. Next, manipulation of terms involving only X is performed, including the use of the following determined relations:

$$\begin{aligned}
&\pi\int_{-\infty}^{\psi_a} d\psi \oint d\chi\left[\frac{\sigma}{n}\left[X\frac{\partial Y^*}{\partial\psi}+X^*\frac{\partial Y}{\partial\psi}\right]\right] \\
=&\pi\int_{-\infty}^{\psi_a} d\psi \oint d\chi\frac{\partial}{\partial\psi}\left[\frac{\sigma}{n}XY^*\right] \\
&+\pi\int_{-\infty}^{\psi_a} d\psi \oint d\chi\left[\sigma\nu'|X|^2-\frac{\sigma'}{n}XY^*+\frac{ifp'}{B^4}\frac{\partial B^2}{\partial\chi}\frac{X^*}{n}\frac{\partial X}{\partial\psi}\right]
\end{aligned} \tag{3.5}$$

and, using the manipulation of equation 2.49 to give:

$$\frac{JB^2\sigma^2}{R^2B_p^2}-2KJ+\sigma\nu'=-\frac{2Jp'}{B^2}\frac{\partial}{\partial\psi}\left(p+\frac{B^2}{2}\right) \tag{3.6}$$

Using the manipulation of equations 3.5 and 3.6 provides the new arbitrary n δW equation, given by:

$$\begin{aligned}
\delta W =&\pi\int_{-\infty}^{\psi_a} d\psi \oint d\chi\Bigg[\underbrace{\frac{JB^2}{R^2B_p^2}|k_\parallel X|^2}_{1}+\underbrace{\frac{R^2}{n^2J}\left|\frac{\partial Y}{\partial\psi}\right|^2}_{2} \\
&-\frac{2Jp\prime}{B^2}\left[\underbrace{\frac{\partial}{\partial\psi}\left(p+\frac{B^2}{2}\right)|X|^2}_{3}-\underbrace{\frac{if}{2JB^2}\frac{\partial B^2}{\partial\chi}\frac{X^*}{n}\frac{\partial X}{\partial\psi}}_{4}\right] \\
&\underbrace{-\frac{X^*}{n}JBk_\parallel\left(\sigma'X\right)}_{5}+\underbrace{\frac{p'}{n}\left[PJBk_\parallel^*\left(\frac{X^*}{B^2}\right)+P^*JBk_\parallel\left(\frac{X}{B^2}\right)\right]}_{6} \\
&+\underbrace{\frac{\partial}{\partial\psi}\left[\frac{1}{n}\sigma XY^*\right]}_{7}+\underbrace{\frac{R^2p'^2}{n^2J}\left|JBk_\parallel\left(\frac{X}{B^2}\right)\right|^2}_{8} \\
&+\underbrace{JB^2|W|^2}_{9}+\underbrace{\frac{R^2}{n^2J}|JBk_\parallel W|^2}_{10}-\underbrace{\frac{f}{n}\left[W^*JBk_\parallel W+WJBk_\parallel^*W^*\right]}_{11} \\
&\underbrace{-\frac{f}{n}\left[W^*\left(\frac{\partial Y}{\partial\psi}+p'JBk_\parallel\left(\frac{X}{B^2}\right)\right)+W\left(\frac{\partial Y^*}{\partial\psi}+p'JBk_\parallel^*\left(\frac{X^*}{B^2}\right)\right)\right]}_{12} \\
&+\underbrace{\frac{1}{n}\Bigg[JBk_\parallel^*W^*\left(P+\frac{R^2p'}{nJ}JBk_\parallel\left(\frac{X}{B^2}\right)\right)}_{13} \\
&\underbrace{+JBk_\parallel W\left(P^*+\frac{R^2p'}{nJ}JBk_\parallel^*\left(\frac{X^*}{B^2}\right)\right)\Bigg]}_{13}\Bigg]
\end{aligned} \tag{3.7}$$

where P has been modified compared to equation 2.54 such that there is no longer a factor of B_p^2/B^2, and additionally there is no factor Q in the new equation. The modified P is given by:

$$P = \sigma X + \frac{R^2}{nJ}\frac{\partial Y}{\partial \psi} \tag{3.8}$$

The terms in the new δW equation are as follows, comparing to the original δW equation 2.51. Terms 1 and 2 on the first line of equation 3.7 are equivalent to the field line bending terms, (terms 1 and 2, in 2.51) but now the equilibrium coefficients in term 2 are modified, and there is no longer a factor of B_p^2/B^2. Terms 3 and 4 in equation 3.7 are identical to terms 3 and 4 in equation 2.51, and correspond to the curvature/ballooning terms. Term 5, on the third line, is also identical to term 5 in equation 2.51, which is the kink term. Term 6, also on the third line, is the significantly modified version of the finite n term 6 in equation 2.51. There is no longer Q, and P is modified such that it also does not have a factor of B_p^2/B^2. Other parts of the finite n term are therefore contained in new terms in equation 3.7 . Term 7, on the beginning of the 4th line, is the same as term 7 in equation 2.51, and is the peeling term. The remaining terms, 8-13 are all new terms. Apart from term 8, all contain the new perturbation, W, either exclusively or combined with perturbation X. It should be noted some of the parts of the previous equation are inherently contained within these terms due to the modified equilibrium coefficients.

3.2.1 Integration by parts

To determine the final form for δW, integration by parts on radial ψ derivatives that act on both of the complex conjugates, X^* and W^*, is performed: when the equations are Euler-minimised, this is greatly simplified when there are no derivatives on complex conjugate terms, as detailed in subsection 2.5.4. For term 13 this yields:

$$\begin{aligned}
\delta W_{13} =& \pi \int_{-\infty}^{\psi_a} d\psi \oint d\chi \frac{1}{n}\Bigg[JBk_{\parallel}^{*}W^{*}\left(P + \frac{R^2p'}{nJ}JBk_{\parallel}\left(\frac{X}{B^2}\right)\right) \\
&+ JBk_{\parallel}W\left(P^{*} + \frac{R^2p'}{nJ}JBk_{\parallel}^{*}\left(\frac{X^{*}}{B^2}\right)\right)\Bigg] \\
=& \pi \int_{-\infty}^{\psi_a} d\psi \oint d\chi \frac{1}{n}\Bigg[JBk_{\parallel}^{*}W^{*}\left(\sigma X + \frac{R^2}{nJ}\frac{\partial Y}{\partial \psi} + \frac{R^2p'}{nJ}JBk_{\parallel}\left(\frac{X}{B^2}\right)\right) \\
&+ JBk_{\parallel}W\left(\sigma X^{*} + \frac{R^2}{nJ}\frac{\partial Y^{*}}{\partial \psi} + \frac{R^2p'}{nJ}JBk_{\parallel}^{*}\left(\frac{X^{*}}{B^2}\right)\right)\Bigg] \\
=& \pi \int_{-\infty}^{\psi_a} d\psi \oint d\chi \Bigg[\frac{\partial}{\partial \psi}\left[\frac{1}{n^2}\frac{R^2}{J}JBk_{\parallel}WY^{*}\right] + \frac{1}{n}JBk_{\parallel}^{*}W^{*}\Bigg(\sigma X + \frac{R^2}{nJ}\frac{\partial Y}{\partial \psi} + \\
&\frac{iR^2p'}{nJB^4}\frac{\partial B^2}{\partial \chi}X + \frac{R^2p'}{nJB^2}Y\Bigg) + \frac{1}{n}JBk_{\parallel}W\Bigg(\sigma X^{*} - \frac{iR^2p'}{nJB^4}\frac{\partial B^2}{\partial \chi}X^{*} + \frac{R^2p'}{nJB^2}Y^{*}\Bigg) \\
&- \frac{1}{n^2}Y^{*}\Bigg[\frac{\partial}{\partial \psi}\left(\frac{R^2}{J}\right)JBk_{\parallel}W + \frac{R^2}{J}\frac{\partial}{\partial \psi}\left(JBk_{\parallel}W\right)\Bigg]\Bigg] \\
S_{u13} =& \pi \int_{-\infty}^{\psi_a} d\psi \oint d\chi \frac{\partial}{\partial \psi}\left[\frac{1}{n^2}\frac{R^2}{J}JBk_{\parallel}WY^{*}\right]
\end{aligned} \tag{3.9}$$

where the first of the terms is the surface term for term 13, S_{u13}, and the other terms form the plasma terms for term 13. Now this term is ready for the Fourier decomposition, to find the final form for δW for the term. This can also be used on the χ derivatives to simplify the solution. The full integration by parts calculations for all terms that require it are shown in the B.1 section of the appendix.

3.3 Extension of inertia terms

This section details the extension of the inertia terms, introduced in section 2.5.3, to provide an indication of the growth rate at low n. As with the original ELITE inertia, the contribution from the parallel Z component of the inertia is neglected, and Z is determined by incompressibility. This is valid at marginal stability, and is therefore an approximation when the growth rate is small. Derivation of the equation for arbitrary n inertia begins with $\delta W_{inertia}$ for X and U, given by equation 2.55. Next, using equation 3.1 to write U in terms of X and W, and substituting this into 2.55, gives the following equation for inertia:

$$\begin{aligned}
\delta W_{inertia} =& \pi\gamma^2 \int_{-\infty}^{\psi_a} d\psi \oint d\chi J\rho\Bigg[\left(\frac{1}{R^2B_p^2} + \frac{R^2B_p^2p'^2}{n^2B^6}\right)|X|^2 + \frac{R^2B_p^2}{n^2B^2}\left|\frac{\partial X}{\partial \psi}\right|^2 \\
&+ \frac{R^2B_p^2}{n^2B^2}|W|^2 + \frac{R^2B_p^2}{n^2B^2}\left[W^{*}\frac{\partial X}{\partial \psi} + \frac{\partial X^{*}}{\partial \psi}W\right] \\
&+ \frac{R^2B_p^2p'}{n^2B^4}\left[X^{*}\frac{\partial X}{\partial \psi} + \frac{\partial X^{*}}{\partial \psi}X\right] + \frac{R^2B_p^2p'}{n^2B^4}\left[X^{*}W + W^{*}X\right]\Bigg]
\end{aligned} \tag{3.10}$$

where, as with the original ELITE formalism, $\rho(\psi)$ is the mass density and γ^2 the eigenvalue of the system, equal to the growth rate squared. Integration by parts is then required on terms 2, 4 and 5, and this is detailed in appendix section B.2.

3.4 Fourier decomposition and two coupled equations

3.4.1 Fourier decomposition

In the original ELITE formalism, detailed in section 2.5.5, Fourier decomposition of the poloidal variation of the perturbation X is written in terms of the straight field line poloidal angle, ω, to find the final form for the δW equation. In the new arbitrary n ELITE formalism the same process is used, but now there are two perturbation displacements to Fourier decompose, X and W. The forms for X and X^* is given by equations 2.61 and 2.62 respectively, ω is given by equation 2.59 and q is given by equation 2.60. In addition, the forms for the W and W^* perturbation displacements are:

$$W = \sum_m w_m(x)\, e^{-im\omega} \tag{3.11}$$

and

$$W^* = \sum_k w_k^*(x)\, e^{ik\omega} \tag{3.12}$$

where x again is the fast radial variable, $x = m_0 - nq$. Then Y is given by equation 2.63, with a similar form for Y^*. Parallel derivatives acted on W and W^* additionally take a similar form to equation 2.63. In order to calculate the matrix elements, the following definitions are also crucial. These are the same form as original ELITE. Any W derivatives take a similar form. First is the ψ derivative of X. This takes the form:

$$\frac{\partial X}{\partial \psi} = \sum_m \left[-im\omega' u_m + \frac{du_m}{d\psi} \right] e^{-im\omega} \tag{3.13}$$

Also required is the second ψ derivative of X. This is given by:

$$\frac{\partial^2 X}{\partial \psi^2} = \sum_m \left[\left(-m^2\omega'^2 - im\omega''\right) u_m - 2im\omega' \frac{du_m}{d\psi} + \frac{d^2 u_m}{d\psi^2} \right] e^{-im\omega} \tag{3.14}$$

Also required is the ψ derivative of Y. This takes the form:

$$\frac{\partial Y}{\partial \psi} = \sum_m n\nu \left[\left[\frac{(m - nq)}{nq} \left(im\omega' - \frac{\nu'}{\nu} \right) + \frac{mq'}{nq^2} \right] u_m - \frac{(m - nq)}{nq} \frac{du_m}{d\psi} \right] e^{-im\omega} \tag{3.15}$$

Finally, also required is the second derivative of Y. This is given by:

$$\begin{aligned} \frac{\partial^2 Y}{\partial \psi^2} = \sum_m n^2\nu \Bigg[\Bigg[& \frac{(m - nq)}{n^2 q} \left(m^2\omega'^2 + 2im\omega'\frac{\nu'}{\nu} + im\omega'' - \frac{\nu''}{\nu} \right) \\ & + \frac{2mq'}{n^2q^2} \left(\frac{\nu'}{\nu} - im\omega' - \frac{q'}{q} \right) + \frac{mq''}{n^2q^2} \Bigg] u_m \\ & + 2 \left[\frac{(m - nq)}{n^2 q} \left(im\omega' - \frac{\nu'}{\nu} \right) + \frac{mq'}{n^2q^2} \right] \frac{du_m}{d\psi} - \frac{(m - nq)}{n^2 q} \frac{d^2 u_m}{d\psi^2} \Bigg] e^{-im\omega} \end{aligned} \tag{3.16}$$

Now, recall the form for the flux surface averages of equilibrium quantities, E_i, given by equation 2.68. This equation is re-defined such that the arbitrary n ELITE kernels, are given by $L_i(\psi, \omega)$, and the flux surface averages of equilibrium quantities are given by S_i:

$$S_i(\psi) = \oint L_i(\psi, \omega)\, e^{i(k-m)\omega} d\omega \tag{3.17}$$

This is to distinguish them from the original ELITE kernels and they are detailed in appendix section B.4. The terms in the arbitrary n δW equation are Fourier decomposed to determine the matrix elements and the kernels. Using term 13 as an example, firstly the plasma terms of δW_{13} are Fourier decomposed. This is given by:

$$
\begin{aligned}
\delta W_{13} =& \pi \int_{-\infty}^{\psi_a} d\psi \oint d\chi \Bigg[\frac{1}{n} JBk_{\parallel}^{*} W^{*} \Bigg(\sigma X + \frac{R^2}{nJ} \frac{\partial Y}{\partial \psi} \\
& + \frac{iR^2 p'}{nJB^4} \frac{\partial B^2}{\partial \chi} X + \frac{R^2 p'}{nJB^2} Y \Bigg) + \frac{1}{n} JBk_{\parallel} W \Bigg(\sigma X^{*} - \frac{iR^2 p'}{nJB^4} \frac{\partial B^2}{\partial \chi} X^{*} \\
& + \frac{R^2 p'}{nJB^2} Y^{*} \Bigg) - \frac{1}{n^2} Y^{*} \Bigg[\frac{\partial}{\partial \psi} \left(\frac{R^2}{J} \right) JBk_{\parallel} W + \frac{R^2}{J} \frac{\partial}{\partial \psi} \left(JBk_{\parallel} W \right) \Bigg] \Bigg] \\
=& \pi \int_{-\infty}^{\psi_a} d\psi \oint d\omega \sum_{m,k} \frac{q}{\nu} \Bigg[w_k^{*} \Bigg[\left(\frac{-\nu}{q} \right) \frac{(k-nq)}{n} \sigma u_m + \left(\frac{-\nu}{q} \right) \frac{R^2}{n^2 J} (k-nq) n\nu \Bigg[\\
& \Bigg(\frac{(m-nq)}{nq} \left(im\omega' - \frac{\nu'}{\nu} \right) - \frac{mq'}{nq^2} \Bigg) u_m - \frac{(m-nq)}{nq} \frac{du_m}{d\psi} \Bigg] \\
& + \left(\frac{-\nu}{q} \right) \frac{(k-nq)}{n^2} \Bigg[\frac{iR^2 p'}{JB^4} \frac{\partial B^2}{\partial \chi} + \left(\frac{-\nu}{q} \right) \frac{R^2 p'}{JB^2} (m-nq) \Bigg] u_m \Bigg] \\
& + u_k^{*} \Bigg[\left(\frac{-\nu}{q} \right) \frac{(m-nq)}{n} \Bigg[\sigma - \frac{iR^2 p'}{nJB^4} \frac{\partial B^2}{\partial \chi} + \frac{R^2 p'}{nJB^2} \left(\frac{-\nu}{q} \right) (k-nq) \Bigg] w_m \\
& - \frac{1}{n^2} \left(\frac{-\nu}{q} \right) (k-nq) \Bigg[\frac{\partial}{\partial \psi} \left(\frac{R^2}{J} \right) \left(\frac{-\nu}{q} \right) (m-nq) w_m \\
& + \frac{R^2}{J} n\nu \Bigg[\Bigg(\frac{(m-nq)}{nq} \left(im\omega' - \frac{\nu'}{\nu} \right) + \frac{mq'}{nq^2} \Bigg) w_m - \frac{(m-nq)}{nq} \frac{dw_m}{d\psi} \Bigg] \Bigg] \Bigg] \Bigg] e^{i(k-m)\omega} \qquad (3.18) \\
=& \pi \int_{-\infty}^{\psi_a} d\psi \sum_{m,k} \Bigg[u_k^{*} \Bigg[\Bigg[\frac{fp'}{n} S_{13} (m-nq) + \frac{f'}{n} S_{12} (m-nq) \\
& + \frac{ip'}{n^2} S_{10} (m-nq) + \frac{fp'}{n^2 q} S_{13} (m-nq)(k-nq) - \frac{1}{n^2 q} S_{16} (m-nq)(k-nq) \\
& + \frac{im}{n^2 q} S_6 (m-nq)(k-nq) - \frac{1}{n^2 q} S_3 (m-nq)(k-nq) \\
& + \frac{mfq'}{n^2 q^2} S_{12} (k-nq) \Bigg] w_m - \frac{f}{n^2 q} (m-nq)(k-nq) S_{12} \frac{dw_m}{d\psi} \Bigg] \\
& + w_k^{*} \Bigg[\Bigg[\frac{fp'}{n} S_{13} (k-nq) + \frac{f'}{n} S_{12} (k-nq) - \frac{ip'}{n^2} S_{10} (k-nq) \\
& + \frac{fp'}{n^2 q} S_{13} (k-nq)(m-nq) - \frac{im}{n^2 q} S_6 (m-nq)(k-nq) \\
& + \frac{1}{n^2 q} S_3 (m-nq)(k-nq) - \frac{mfq'}{n^2 q^2} S_{12} (k-nq) \Bigg] u_m \\
& + \frac{f}{n^2 q} (m-nq)(k-nq) S_{12} \frac{du_m}{d\psi} \Bigg] \Bigg]
\end{aligned}
$$

where S_i are the matrix elements and the subscript, i, refers to the kernel number such that S_i is the flux surface average of kernels, L_i, given by equation 2.68, which are completely listed in the appendix 3.17. Note that these were previously labelled T_i, with kernels, K_i [98], and S_i here does not refer to the surface terms, as in reference [98]. Also note that the following factors are independent of χ: m, k, n, q and its ψ derivatives, p and its ψ derivatives and toroidal field function, f, and its ψ derivatives.

Now the surface term for term 13, S_{u13}, is Fourier decomposed, which is given by:

$$\begin{aligned} S_{u13} =&\pi \int_{-\infty}^{\psi_a} d\psi \oint d\chi \frac{\partial}{\partial\psi}\left[\frac{1}{n^2}\frac{R^2}{J}JBk_{\parallel}WY^*\right] \\ =&\pi \oint d\omega \sum_{k,m} \frac{R^2}{n^2 J}\left(\frac{-\nu}{q}\right)^2 \frac{q}{\nu}(m-nq)(k-nq)u_k^* w_m e^{i(k-m)\omega} \\ =&\pi \sum_{m,k} u_k^* \frac{f}{n^2 q} S_{12}(m-nq)(k-nq)w_m \end{aligned} \tag{3.19}$$

The collective contribution of the surface terms, including the ones for inertia, form part of the boundary conditions for each Fourier mode k applied at the plasma-vacuum interface, along with the vacuum contribution, δW_v. Appendix section B.1 contains the full Fourier decomposition calculations for all the plasma and surface terms in the full arbitrary n δW equation, given by equation 3.7. Fourier decomposition of the inertia and surface inertia terms, is undertaken in the exact same manner. The full Fourier decomposition of all of the inertia terms is detailed in the appendix in section B.2.

3.4.2 Matrix elements and two sets of coupled Euler equations

Once all of the terms in the δW equation, including the inertia terms, have been Fourier decomposed to determine their matrix elements, which are both plasma and surface matrix elements, the δW equation is in a form suitable to read off the set of minimising equations solved by ELITE. The Fourier decomposition of the plasma contributions to the δW equation, including the inertia terms, form two sets of Euler equations. One is minimised with respect to u_k^*, which forms the so-called X equation, and the other minimised with respect to w_k^*, which forms the so-called W equation. The boundary conditions for the Euler equations come from the surface terms, which are minimised with respect to u_k^*. These are minimised separately and have to be zero in their own right. The Euler equations for X and W and the boundary conditions are written in terms of the Fourier mode amplitudes, defined in equations, 2.61, 2.62, 3.11 and 3.12.The X equation for the plasma contribution takes the form:

$$\begin{aligned} \delta W_{p,X} = \pi \int_{-\infty}^{\psi_a} d\psi \sum_{m,k} u_k^* \Bigg[&\left[A''_{mk}(m-nq)(k-nq) - \gamma^2 A''_I\right]\frac{d^2 u_m}{d\psi^2} \\ &+ \Big[A'_{mk}(m-nq)(k-nq) + A'_m(m-nq) + A'_k(k-nq) + A' \\ &- \gamma^2 A'_I\Big]\frac{du_m}{d\psi} + \Big[A_{mk}(m-nq)(k-nq) + A_m(m-nq) + A_k(k-nq) \\ &+ A - \gamma^2 A_I\Big]u_m + \left[B'_{mk}(m-nq)(k-nq) + B'_k(k-nq) - \gamma^2 B'_I\right]\frac{dw_m}{d\psi} \\ &+ \left[B_{mk}(m-nq)(k-nq) + B_m(m-nq) + B_k(k-nq) - \gamma^2 B_I\right]w_m \Bigg] \end{aligned} \tag{3.20}$$

where A, A' and A'' are the matrix elements that act on the u_m Fourier amplitudes, and the first and second radial ψ derivatives of the Fourier mode amplitudes respectively. Note the prime is not indicative of a radial derivatives on the matrix elements themselves. A_I, A'_I and A''_I are the matrix elements that act on u_m and its radial derivatives due to the inertia. B and B' are the matrix elements that act on the w_m Fourier amplitudes and its radial derivatives, and similarly B_I and B'_I are the matrix elements of the inertia terms that act on w_m. These terms are all fully documented in appendix section B.3. Secondly for the W equation for the plasma contribution:

$$
\begin{aligned}
\delta W_{p,W} = \pi \int_{-\infty}^{\psi_a} d\psi \sum_{m,k} w_k^* \Bigg[\Bigg[& C_{mk}(m - nq)(k - nq) + C_m(m - nq) + C_k(k - nq) \\
& + C - \gamma^2 C_I \Bigg] w_m + \Bigg[D'_{mk}(m - nq)(k - nq) + D'_m(m - nq) \\
& - \gamma^2 D'_I \Bigg] \frac{du_m}{d\psi} + \Bigg[D_{mk}(m - nq)(k - nq) + D_m(m - nq) + D_k(k - nq) \\
& + D - \gamma^2 D_I \Bigg] u_m \Bigg]
\end{aligned}
\tag{3.21}
$$

where C are the matrix elements that act on the w_m Fourier amplitudes, and C_I the matrix elements due to inertia that act on w_m. D and D' are the matrix elements that act on the u_m Fourier mode amplitude and its radial derivatives respectively, D_I and D'_I are similarly the inertia matrix elements. These terms are also fully documented in appendix section B.3. Finally, the following gives the boundary conditions from the surface contribution, including the vacuum contribution W_v:

$$
\begin{aligned}
\delta W_s = \frac{\pi}{n} \sum_{m,k} u_k^* \Bigg[\Bigg[& A'_{Smk}(m - nq)(k - nq) - \gamma^2 A'_{SI} \Bigg] \frac{du_m}{d\psi} \\
& + \Bigg[A_{Smk}(m - nq)(k - nq) + A_{Sk}(k - nq) - \gamma^2 A_{SI} \Bigg] u_m + \\
& \Bigg[B_{Smk}(m - nq)(k - nq) + B_{Sk}(k - nq) - \gamma^2 B_{SI} \Bigg] w_m + \delta W_v(u_m) \Bigg]
\end{aligned}
\tag{3.22}
$$

where A_S A'_S are the matrix elements due to the surface terms that act on the u_m Fourier amplitudes and its radial derivatives respectively, A_{SI} and A'_{SI} are similarly the surface inertia terms matrix elements. B_S are the matrix elements due to the surface terms that act on the w_m Fourier amplitudes, and similarly B_{SI} for matrix elements of the surface inertia terms. These are also all detailed in full in the appendix section B.3. The two full sets of coupled Euler equations for the radial variations of the Fourier mode amplitudes solved by ELITE can be trivially obtained using Euler minimisation. These are for each Fourier mode, k, and they are given by, firstly for the X equation:

$$\begin{aligned}\sum_m \Bigg[& \Bigg[A''_{mk}(m-nq)(k-nq) - \gamma^2 A''_I\Bigg]\frac{d^2u_m}{d\psi^2} + \Bigg[A'_{mk}(m-nq)(k-nq) \\ & + A'_m(m-nq) + A'_k(k-nq) + A' - \gamma^2 A'_I\Bigg]\frac{du_m}{d\psi} \\ & + \Bigg[A_{mk}(m-nq)(k-nq) + A_m(m-nq) + A_k(k-nq) + A - \gamma^2 A_I\Bigg]u_m \\ & + \Bigg[B'_{mk}(m-nq)(k-nq) + B'_k(k-nq) - \gamma^2 B'_I\Bigg]\frac{dw_m}{d\psi} + \Bigg[B_{mk}(m-nq)(k-nq) \\ & + B_m(m-nq) + B_k(k-nq) - \gamma^2 B_I\Bigg]w_m\Bigg] = 0\end{aligned} \tag{3.23}$$

and for the W equation:

$$\begin{aligned}\sum_m \Bigg[& \Bigg[C_{mk}(m-nq)(k-nq) + C_m(m-nq) + C_k(k-nq) \\ & + C - \gamma^2 C_I\Bigg]w_m + \Bigg[D'_{mk}(m-nq)(k-nq) + D'_m(m-nq) \\ & - \gamma^2 D'_I\Bigg]\frac{du_m}{d\psi} + \Bigg[D_{mk}(m-nq)(k-nq) + D_m(m-nq) + D_k(k-nq) \\ & + D - \gamma^2 D_I\Bigg]u_m\Bigg] = 0\end{aligned} \tag{3.24}$$

Finally, Euler minimisation of the full set of boundary conditions for each Fourier mode, k, can be applied at the plasma boundary, ψ_a, defined in the previous chapter in equation 2.70. This is given by:

$$\begin{aligned}\sum_m \Bigg[& \Bigg[A'_{Smk}(m-nq)(k-nq) - \gamma^2 A'_{SI}\Bigg]\frac{du_m}{d\psi} + \Bigg[A_{Smk}(m-nq)(k-nq) \\ & + A_{Sk}(k-nq) - \gamma^2 A_{SI}\Bigg]u_m + \Bigg[B_{Smk}(m-nq)(k-nq) + B_{Sk}(k-nq) \\ & - \gamma^2 B_{SI}\Bigg]w_m + \delta W_v(u_m)\Bigg]_{x=\Delta} = 0\end{aligned} \tag{3.25}$$

where δW_v is the vacuum contribution, which is unchanged from original ELITE and, as it will be shown as w_m is eliminated, this acts on u_m. The matching conditions for the edge and the core, given in equations 2.69 and 2.70, are the same for arbitrary n ELITE. For the next part of the process, it is important to define a simplified form for the full set of coupled equations. These are summed over repeated indices, and for X

this is given by:

$$A''_{km}\frac{d^2u_m}{d\psi^2} + A'_{km}\frac{du_m}{d\psi} + A_{km}u_m + B'_{km}\frac{dw_m}{d\psi} + B_{km}w_m = 0 \tag{3.26}$$

and for W this is given by:

$$C_{km}w_m + D'_{km}\frac{du_m}{d\psi} + D_{km}u_m = 0 \tag{3.27}$$

where A_{km} contains all of the A terms: A_{km}, A, A_k and A, as well as all the A_I terms, including any $(k - nq)$ and $(m - nq)$ factors for included in the individual terms. This is similar for all the rest of the B, C and D terms.

3.5 Creating a single modified set of Euler equations

The next part of the process is to obtain a single original ELITE-like set of Euler equations, which is given in the original ELITE by equation 2.66, from the two coupled sets of Euler equations in X and W in arbitrary n ELITE. This allows the equations to be solved using many of the same routines already in ELITE and eliminates $\underline{w}$, where $\underline{w}$ is a vector which represents w_m. Similarly, $\underline{u}$ is a vector which represents u_m and the matrices $\underline{\underline{A}}$ represent A_{km}.

3.5.1 Matrix manipulation

The matrix manipulations begin with equation 3.27. Firstly, re-arrange this equation such that an equation for $\underline{w}$ is obtained:

$$\underline{\underline{C}} \cdot \underline{w} = -\underline{\underline{D}}' \cdot \frac{d\underline{u}}{d\psi} - \underline{\underline{D}} \cdot \underline{u} \tag{3.28}$$

which gives the equation for $\underline{w}$:

$$\underline{w} = -\underline{\underline{C}}^{-1} \cdot \underline{\underline{D}}' \cdot \frac{d\underline{u}}{d\psi} - \underline{\underline{C}}^{-1} \cdot \underline{\underline{D}} \cdot \underline{u} \tag{3.29}$$

An equation for $\frac{d\underline{w}}{d\psi}$ is also required to fully eliminate $\underline{w}$, as seen in equation 3.26. To obtain the equation the matrix elements need to be differentiated with respect to ψ.

Therefore define new matrices, $\underline{\underline{E}}$, $\underline{\underline{F}}$ and $\underline{\underline{G}}$ for these such that they are given by:

$$\begin{aligned}
\underline{\underline{E}} &= \frac{d\underline{\underline{C}}}{d\psi} \\
\underline{\underline{F}} &= \frac{d\underline{\underline{D}}'}{d\psi} \\
\underline{\underline{G}} &= \frac{d\underline{\underline{D}}}{d\psi}
\end{aligned} \tag{3.30}$$

Now the $\underline{w}$ equation needs to be differentiated. Starting with 3.28, and differentiating:

$$\begin{aligned}
\underline{\underline{C}} \cdot \frac{d\underline{w}}{d\psi} &= -\underline{\underline{D}}' \cdot \frac{d^2\underline{u}}{d\psi^2} - \left(\underline{\underline{F}} + \underline{\underline{D}}\right) \cdot \frac{d\underline{u}}{d\psi} - \underline{\underline{G}} \cdot \underline{u} - \underline{\underline{E}} \cdot \underline{w} \\
&= -\underline{\underline{D}}' \cdot \frac{d^2\underline{u}}{d\psi^2} - \left(\underline{\underline{F}} + \underline{\underline{D}} - \underline{\underline{E}} \cdot \underline{\underline{C}}^{-1} \cdot \underline{\underline{D}}'\right) \cdot \frac{d\underline{u}}{d\psi} - \left(\underline{\underline{G}} - \underline{\underline{E}} \cdot \underline{\underline{C}}^{-1} \cdot \underline{\underline{D}}\right) \cdot \underline{u}
\end{aligned} \tag{3.31}$$

Therefore the equation for $\frac{d\underline{w}}{d\psi}$ can be obtained:

$$\frac{d\underline{w}}{d\psi} = -\underline{\underline{C}}^{-1} \cdot \underline{\underline{D}}' \cdot \frac{d^2\underline{u}}{d\psi^2} - \underline{\underline{C}}^{-1} \cdot \underline{\underline{M}} \cdot \frac{d\underline{u}}{d\psi} - \underline{\underline{C}}^{-1} \cdot \underline{\underline{N}} \cdot \underline{u} \tag{3.32}$$

where $\underline{\underline{M}}$ and $\underline{\underline{N}}$ are given by:

$$\begin{aligned}
\underline{\underline{M}} &= \underline{\underline{F}} + \underline{\underline{D}} - \underline{\underline{E}} \cdot \underline{\underline{C}}^{-1} \cdot \underline{\underline{D}}' \\
\underline{\underline{N}} &= \underline{\underline{G}} - \underline{\underline{E}} \cdot \underline{\underline{C}}^{-1} \cdot \underline{\underline{D}}
\end{aligned} \tag{3.33}$$

Now the original ELITE-like equation can be obtained, with modified coefficient matrices:

$$\underline{\underline{\hat{A}}}'' \cdot \frac{d^2\underline{u}}{d\psi^2} + \underline{\underline{\hat{A}}}' \cdot \frac{d\underline{u}}{d\psi} + \underline{\underline{\hat{A}}} \cdot \underline{u} = 0 \tag{3.34}$$

where $\underline{\underline{\hat{A}}}''$, $\underline{\underline{\hat{A}}}'$ and $\underline{\underline{\hat{A}}}$ are given by:

$$\begin{aligned}
\underline{\underline{\hat{A}}}'' &= \underline{\underline{A}}'' - \underline{\underline{B}}' \cdot \underline{\underline{C}}^{-1} \cdot \underline{\underline{D}}' \\
\underline{\underline{\hat{A}}}' &= \underline{\underline{A}}' - \underline{\underline{B}}' \cdot \underline{\underline{C}}^{-1} \cdot \underline{\underline{M}} - \underline{\underline{B}} \cdot \underline{\underline{C}}^{-1} \cdot \underline{\underline{D}}' \\
\underline{\underline{\hat{A}}} &= \underline{\underline{A}} - \underline{\underline{B}}' \cdot \underline{\underline{C}}^{-1} \cdot \underline{\underline{N}} - \underline{\underline{B}} \cdot \underline{\underline{C}}^{-1} \cdot \underline{\underline{D}}
\end{aligned} \tag{3.35}$$

Thus the Euler equations can be solved using many of the same routines that already exist in ELITE. It is also necessary to transform equation 3.34 onto the x-mesh used by ELITE. This requires using the definition for x, given by $x = (m_0 - nq(\psi))$, which allows the transformation of the derivatives of ψ into x derivatives, which are given by:

$$
\begin{aligned}
\frac{d}{d\psi} &= -nq'\frac{d}{dx} \\
\frac{d^2}{d\psi^2} &= n^2q'^2\frac{d^2}{dx^2} - nq''\frac{d}{dx}
\end{aligned}
\tag{3.36}
$$

Equation 3.34 in terms of x becomes:

$$
\underline{\underline{a}}'' \cdot \frac{d^2\underline{u}}{dx^2} + \underline{\underline{a}}' \cdot \frac{d\underline{u}}{dx} + \underline{\underline{a}} \cdot \underline{u} = 0
\tag{3.37}
$$

Note that this manipulation is also performed in original ELITE. However, now that the coefficient matrices are modified, this requires additional manipulation of the matrices. The modified coefficient matrices with respect to x, $\underline{\underline{a}}$, need to be related back to the original matrices, $\underline{\underline{A}}$, that can be calculated. Starting with $\underline{\underline{a}}''$:

$$
\begin{aligned}
\underline{\underline{a}}'' &= n^2q'^2\underline{\underline{\hat{A}}}'' \\
&= n^2q'^2\underline{\underline{A}}'' - n^2q'^2\underline{\underline{B}}' \cdot \underline{\underline{C}}^{-1} \cdot \underline{\underline{D}}'
\end{aligned}
\tag{3.38}
$$

Then for $\underline{\underline{a}}'$:

$$
\begin{aligned}
\underline{\underline{a}}' &= -nq''\underline{\underline{\hat{A}}}'' - nq'\underline{\underline{\hat{A}}}' \\
&= \left[-nq''\underline{\underline{A}}'' - nq'\underline{\underline{A}}'\right] + nq''\underline{\underline{B}}' \cdot \underline{\underline{C}}^{-1} \cdot \underline{\underline{D}}' + nq'\left[\underline{\underline{B}}' \cdot \underline{\underline{C}}^{-1} \cdot \underline{\underline{M}} + \underline{\underline{B}} \cdot \underline{\underline{C}}^{-1} \cdot \underline{\underline{D}}'\right]
\end{aligned}
\tag{3.39}
$$

Finally for $\underline{\underline{a}}$:

$$
\begin{aligned}
\underline{\underline{a}} &= \underline{\underline{\hat{A}}} \\
&= \underline{\underline{A}} - \underline{\underline{B}}' \cdot \underline{\underline{C}}^{-1} \cdot \underline{\underline{N}} - \underline{\underline{B}} \cdot \underline{\underline{C}}^{-1} \cdot \underline{\underline{D}}
\end{aligned}
\tag{3.40}
$$

The modification of the coefficients therefore produce shifts due to the additional terms in the transformation of the coefficient matrices to the x mesh from the ψ mesh when compared to their forms in the original ELITE. In the original ELITE, these transformations are simply given by the $\underline{\underline{A}}$ parts in the transformation, taking into account that the $\underline{\underline{A}}$s are different in original ELITE. Thus, the shifts $\underline{\underline{\Delta}}$ can be defined. The shift in $\underline{\underline{a}}''$, $\underline{\underline{\Delta}}''$, is given by:

$$
\underline{\underline{\Delta}}'' = n^2q'^2\underline{\underline{B}}' \cdot \underline{\underline{M_1}}
\tag{3.41}
$$

The shift in $\underline{\underline{a}}'$, $\underline{\underline{\underline{\Delta}}}'$, is given by:

$$\begin{aligned}\underline{\underline{\underline{\Delta}}}' &= -nq''\underline{\underline{\underline{B}}}'\cdot\underline{\underline{\underline{M_1}}} - nq'\left[B'\cdot\underline{\underline{\underline{C}}}^{-1}\cdot\underline{\underline{\underline{M}}} + \underline{\underline{\underline{B}}}\cdot\underline{\underline{\underline{C}}}^{-1}\cdot\underline{\underline{\underline{D}}}'\right]\\ &= -nq''\underline{\underline{\underline{B}}}'\cdot\underline{\underline{\underline{M_1}}} - nq'\left[\underline{\underline{\underline{M_3}}}\cdot\left(\underline{\underline{\underline{F}}}+\underline{\underline{\underline{D}}}\right) + \underline{\underline{\underline{M_4}}}\cdot\underline{\underline{\underline{M_1}}}\right]\end{aligned} \tag{3.42}$$

Finally shift in $\underline{\underline{a}}$, $\underline{\underline{\underline{\Delta}}}$, is given by:

$$\underline{\underline{\underline{\Delta}}} = \underline{\underline{\underline{M_3}}}\cdot\underline{\underline{\underline{G}}} + \underline{\underline{\underline{M_4}}}\cdot\underline{\underline{\underline{M_2}}} \tag{3.43}$$

where new combination of matrix multiplications have been defined, $\underline{\underline{\underline{M_1}}}$, $\underline{\underline{\underline{M_2}}}$, $\underline{\underline{\underline{M_3}}}$ and $\underline{\underline{\underline{M_4}}}$, which are given by:

$$\begin{aligned}\underline{\underline{\underline{M_1}}} &= \underline{\underline{\underline{C}}}^{-1}\cdot\underline{\underline{\underline{D}}}'\\ \underline{\underline{\underline{M_2}}} &= \underline{\underline{\underline{C}}}^{-1}\cdot\underline{\underline{\underline{D}}}\\ \underline{\underline{\underline{M_3}}} &= \underline{\underline{\underline{B}}}'\cdot\underline{\underline{\underline{C}}}^{-1}\\ \underline{\underline{\underline{M_4}}} &= \underline{\underline{\underline{B}}} - \underline{\underline{\underline{M_3}}}\cdot\underline{\underline{\underline{E}}}\end{aligned} \tag{3.44}$$

Note that these all also contain matrix elements due to the inertia terms.

3.5.2 Differentiation of the matrix elements

The final part of the calculations is to obtain analytic forms for $\underline{\underline{\underline{E}}}$, $\underline{\underline{\underline{F}}}$ and $\underline{\underline{\underline{G}}}$, defined in equation 3.30, as numerical derivation of the matrix elements on the ψ mesh is inaccurate. Therefore this requires that the matrix elements, S_i, that are collectively contained in the $\underline{\underline{\underline{C}}}$, $\underline{\underline{\underline{D}}}'$ and $\underline{\underline{\underline{D}}}$ coefficients be individually differentiated with respect to ψ, to give $\frac{dS_i}{d\psi}$ and to collectively give $\underline{\underline{\underline{E}}}$, $\underline{\underline{\underline{F}}}$ and $\underline{\underline{\underline{G}}}$ respectively. This begins with the form for the matrix elements given in equation 3.17, which can also be written in terms of χ, given by:

$$\begin{aligned}S_i(\psi) &= \oint L_i^{i(k-m)\omega}d\omega\\ &= \oint \frac{\nu}{q}L_i e^{i(k-m)\omega}d\chi\end{aligned} \tag{3.45}$$

where L_i is the kernel containing the equilibrium quantities. Also required is the following derivatives of ω, calculated using 2.59:

$$\begin{aligned}\frac{\partial\omega}{\partial\chi} &= \frac{\nu}{q}\\ \frac{\partial^2\omega}{\partial\psi\partial\chi} &= \frac{\partial\omega'}{\partial\chi} = \frac{\nu'}{q} - \frac{q'\nu}{q^2}\end{aligned} \tag{3.46}$$

Now $\frac{dS_i}{d\psi}$ can be calculated. This is given by

$$\begin{aligned}\frac{dS_i}{d\psi} &= \oint \frac{\partial L_i}{\partial\psi} e^{i(k-m)\omega} d\omega + \oint L_i \left[\frac{\nu'}{q} - \frac{q'\nu}{q^2} + \frac{i\nu}{q}(k-m)\omega'\right] e^{i(k-m)\omega} d\chi\\ &= \oint \frac{\partial L_i}{\partial\psi} e^{i(k-m)\omega} d\omega + \oint L_i \frac{i\nu}{q}(k-m)\omega' e^{i(k-m)\omega} d\chi + \oint L_i \frac{\partial\omega'}{\partial\chi} e^{i(k-m)\omega} d\chi\\ &= \oint \frac{\partial L_i}{\partial\psi} e^{i(k-m)\omega} d\omega + \oint L_i \frac{i\nu}{q}(k-m)\omega' e^{i(k-m)\omega} d\chi\\ &\quad - \oint L_i \frac{i\nu}{q}(k-m)\omega' e^{i(k-m)\omega} d\chi - \oint \frac{\partial L_i}{\partial\chi}\omega' e^{i(k-m)\omega} d\chi\\ &= \oint \frac{\partial L_i}{\partial\psi} e^{i(k-m)\omega} d\omega - \oint \frac{\partial L_i}{\partial\chi}\omega' e^{i(k-m)\omega} d\chi\end{aligned} \tag{3.47}$$

where there is no surface term associated with the integration by parts of χ. Therefore, transforming the second term back into an integral with respect to $d\omega$, the final form for $\frac{dS_i}{d\psi}$ is given by:

$$\frac{dS_i}{d\psi} = \oint \left[\frac{\partial L_i}{\partial\psi} - \frac{q\omega'}{\nu}\frac{\partial L_i}{\partial\chi}\right] e^{i(k-m)\omega} d\omega \tag{3.48}$$

Here is an example of a full ψ derivative of a matrix element. The matrix element $\frac{q}{f}S_{25}$, is used as the example, with L_{25}, L_{26} and L_{27} defined in appendix section B.4. Its derivative with respect to ψ is given by:

$$\begin{aligned}\frac{\partial}{\partial\psi}\left(\frac{q}{f}S_{25}\right) &= \frac{q}{f}\left(\frac{q'}{q} - \frac{f'}{f}\right)S_{25} + \frac{\partial S_{25}}{\partial\psi}\\ &= \frac{q}{f}\left(\frac{q'}{q} - \frac{f'}{f}\right)S_{25} + \oint \left[\frac{\partial L_{25}}{\partial\psi} - \frac{q\omega'}{\nu}\frac{\partial L_{25}}{\partial\chi}\right] e^{i(k-m)\omega} d\omega\\ &= \frac{q}{f}\left(\frac{q'}{q} - \frac{f'}{f}\right)S_{25} + \frac{q}{f}\oint \left[\frac{\partial}{\partial\psi}\left(R^2B^2\right) - \frac{q\omega' R^2}{fJ}\frac{\partial}{\partial\chi}\left(R^2B^2\right)\right] e^{i(k-m)\omega} d\omega\\ &= \frac{q}{f}\left(\frac{q'}{q} - \frac{f'}{f}\right)S_{25} + \frac{q}{f}S_{26} - \left(\frac{q}{f}\right)^2 S_{27}\end{aligned} \tag{3.49}$$

The differentiation of all the required kernels associated with $\underline{\underline{E}}$, $\underline{\underline{F}}$ and $\underline{\underline{G}}$ including inertia matrix elements is shown in the appendix, in section B.5. The final forms of all of the $\underline{\underline{E}}$, $\underline{\underline{F}}$ and $\underline{\underline{G}}$ matrix elements is also shown appendix section B.5. This therefore is the final piece of the arbitrary n ELITE formalism.

3.6 Conclusions and further work

In conclusion the ELITE formalism has been successfully extended to arbitrary n, to allow the study of low n dominated phenomena with the ELITE code. Firstly the derivation for the arbitrary n δW equation begins with the ideal MHD energy principle. A new expansion for the second component U of the perturbation ξ was used, where one $1/n$ term from its Euler equation was absorbed, along with all other orders of U, into a W term. Then, after algebraic manipulation, this expansion leads to the new arbitrary n δW equation, given by equation 3.7. The method of integration by parts to ease the Euler minimisation process was then illustrated. Next the extension of the inertia terms to arbitrary n was shown, using the same expansion for U.

The next section details the Fourier decomposition process for both perturbations, X and W, to produce matrix elements, containing kernels. This preserves the separation of radial length scales from the original ELITE formalism, such that the Fourier mode amplitude is on a finer length scale dictated by the distance between the rational surfaces, and the equilibrium length scale on the ψ mesh. This was shown to produce two sets of coupled equations for the plasma terms after Euler minimisation with respect to u_k^* and w_k^*. Finally, discussion on the process by which a single original ELITE-like set of Euler equations are obtained was presented. This process eliminates the Fourier amplitude w_m and allows the new arbitrary n ELITE equations to be solved with many of the same routines already in ELITE. This requires matrix manipulation and differentiation of the matrix elements to form three new groups of matrix elements.

This formalism has been successfully implemented in the ELITE code. The further work from this chapter is detailed in subsequent chapters. The results of benchmarks using the new arbitrary n ELITE formalism are detailed in chapter 4. A study of QH-mode in DIII-D using the new arbitrary n ELITE is in chapter 5. Further work beyond this is detailed in subsequent chapters.

Chapter 4

Benchmarks and further extensions to arbitrary n ELITE, and the δW diagnostic

4.1 Introduction and motivations

This chapter details the extensive benchmarking of the new arbitrary n ELITE, which is crucial for verifying the new arbitrary n ELITE formalism, both against original ELITE as well as other codes. The implementation of the arbitrary n ELITE formalism required intermediate steps. These were to use the high n inertia as an approximation, and also implementing an ideal wall edge boundary condition to test the plasma terms in the absence of the surface and vacuum contributions. Also required was to implement both the up-down symmetric and non-up-down symmetric versions of arbitrary n ELITE. Next, the code was benchmarked using increasingly complex test cases: where all the test cases were previously produced in the verification of the original ELITE formalism. Both the eigenfunctions, and the growth rates (γ/ω_A) are directly compared. All benchmarks needed their own parameter convergence tests, which is detailed in section 4.8. In appendix section C.1 are example converged input files for all of the test cases. Further benchmarks are then shown which detail the effects of calculating and inverting C, which are the matrix elements in the W equation that act on the w_m Fourier amplitudes on both the fine and coarse meshes. This is to improve the efficiency of the code.

The second major part of this chapter is the discussion of the new δW diagnostic which has been implemented into the original ELITE code. This takes equation 2.51 and calculates the relative amplitude of all the terms in the equation individually, providing further insight into the peeling-ballooning (PB) drive mechanism. This has the advantage of only needing to be run on the equilibrium, without having to perform a full scan in $J-\alpha$ space.

4.2 Formalism implementation

4.2.1 High n inertia approximation

The arbitrary n ELITE formalism was implemented in stages; this was imperative to the success in the implementation, allowing the terms to be systematically tested. The first stage was to implement the solutions to the terms in equation 3.7 without implementing the arbitrary n inertia terms. Therefore, the solution to equation 2.56 was originally used for the inertia before the arbitrary n inertia terms were implemented. This was valid since the implementation was tested using an intermediate n and comparing the eigenfunctions and growth rates to the original ELITE outputs, where the original form for inertia is also valid. Surprisingly, however, it was found that the high n inertia approximation performs remarkably well even at low n, except for $n = 1$ where it often fails to converge. Therefore this approximation is illustrated in all of the following benchmarks, as a further intermediate verification of the new arbitrary n formalism.

4.2.2 Ideal wall edge boundary condition

Another intermediate step in the process of implementing the arbitrary n was to implement a new shooting algorithm which allowed the edge boundary condition of the plasma to be changed. This was also imperative in the success of the implementation of the new arbitrary n ELITE formalism: this allowed the testing of the plasma terms, without the surface and the vacuum contributions present, using an ideal wall edge boundary condition. This was implemented using an extension of the shooting algorithm, detailed in appendix A.1, to become a double shooting algorithm. This allows the edge boundary condition to be changed. The algorithm uses a chosen position in the plasma, ψ_{shoot}, which is placed in the region where the eigenfunction exists and shoots in both directions. The algorithm then, in the ideal wall case, uses both a zero core and zero edge boundary conditions, modifying equation 2.70 for the edge, and keeping equation 2.69 for the core. The independent solutions of the eigenfunction from each side of ψ_{shoot} are then matched in three points: ψ_{shoot} and the two mesh points either side, as described in [29]. This algorithm has an additional purpose: as the shooting algorithm is no longer confined to the edge, core localised modes, for example from internal transport barriers, can be studied. Here, it is used simply for the purpose of benchmarking the plasma terms of the arbitrary n ELITE formalism.

4.2.3 ELITE: up-down symmetric and non-up-down symmetric

The arbitrary n ELITE formalism was first implemented in the simpler up-down symmetric version of ELITE. This version has matrix elements that are solely real. The matrix elements in ELITE are described in terms of cosine and sine components in the poloidal plane at each radial ψ position. The parity of the function determines if the component is written in terms of cosine or sin: if the matrix element is an even function this has its component in terms of cosine, and if the matrix element is an odd function this has its component described in terms of sine. The non-up-down symmetric version of ELITE, implemented second, has matrix elements that are complex. This requires the matrix elements to have both a real and an imaginary component, where the imaginary component is the opposite of its corresponding real component. The matrix elements are then stored in arrays, where the array is complex for non-up-down symmetric ELITE. Non-up-down symmetric version is essential for experimental analysis as in general real tokamak equilibria are non-up-down symmetric. The δW diagnostic is also implemented in both versions.

4.3 Circular test case benchmark

The first test case, the “circa” test case, is the simplest test case used and is the one which was used to implement the arbitrary n ELITE formalism. This has a circular cross section, as illustrated in figure 4.1, with $q(95) = 1.8043$, normalised beta $\beta_n = 1.88$, and the average effective atomic charge $Z_{eff} = 2$. The density and temperature pedestals are tanh-shaped. The test case was produced by the TOQ equilibrium code [99]. Figure 4.1 shows an $n = 10$ mode reconstructed in the poloidal plane, calculated with the full arbitrary n ELITE for this circular cross section test case. There have been two benchmarks performed with this test case: one with an ideal wall present, and the other with the vacuum and surface terms present.

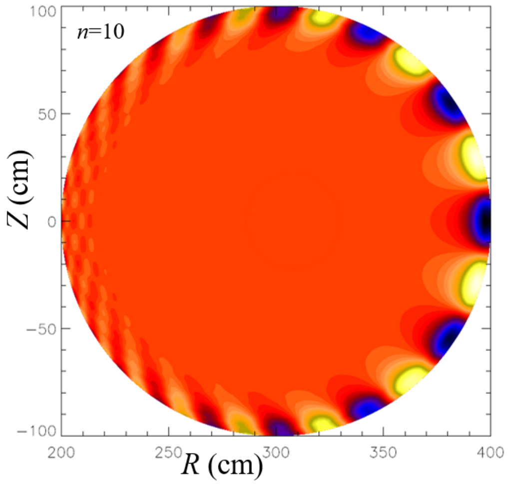

Figure 4.1: Shape of the circular cross section benchmark with an $n = 10$ mode calculated with arbitrary n ELITE with the full arbitrary n inertia.

4.3.1 Benchmark of circular test case with an ideal wall

This section details the benchmark of the circular test case with an ideal wall. This benchmark has been performed for the full arbitrary n ELITE code, the arbitrary n

ELITE code with the high n inertia terms, and the original ELITE code. Due to the stabilising effect of the ideal wall on PB modes, this test case is stable for $1 \leq n \leq 12$. The result of the benchmark for $12 \leq n \leq 30$ is shown in figure 4.2.

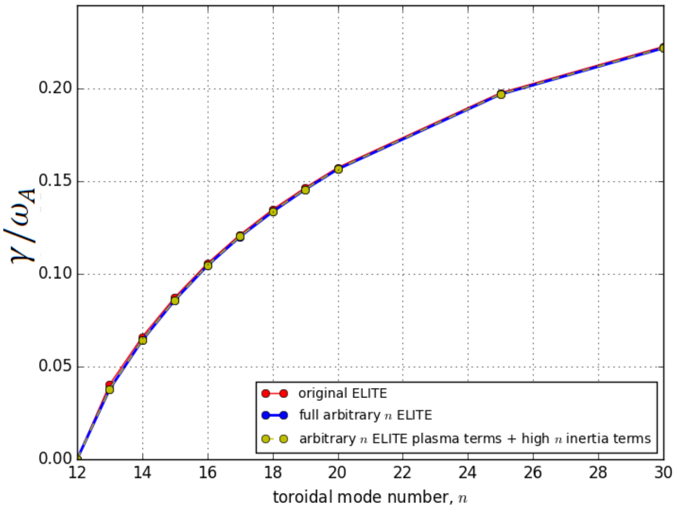

Figure 4.2: Benchmark of the arbitrary n ELITE code for the circular cross section test case in the presence of an ideal wall with: the full arbitrary n ELITE (blue dots and line), the arbitrary n ELITE with the high n inertia approximation (yellow dots and dashed line) and the original ELITE code (red dots and line), for $n = 12$ to $n = 30$.

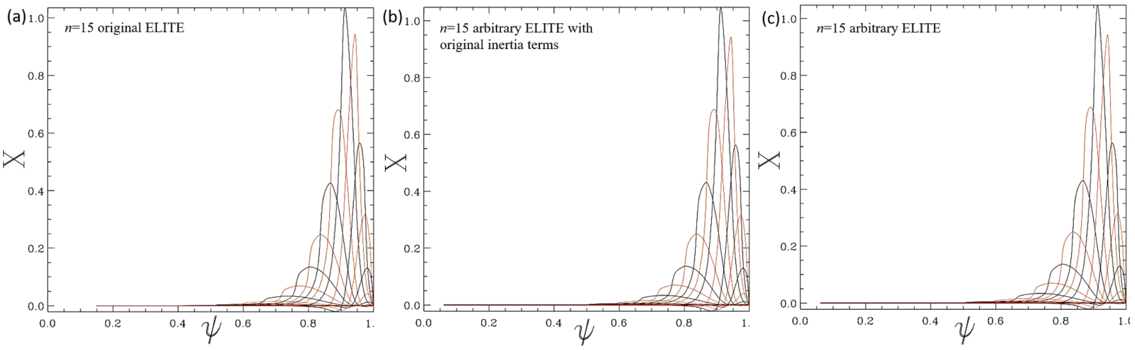

Figure 4.3: $n = 15$ eigenfunctions for the circular cross section benchmark in the presence of an ideal wall where: (a) is calculated by original ELITE, (b) is calculated by the arbitrary n ELITE with the high n inertia approximation and (c) is calculated by the full arbitrary n ELITE.

Figure 4.2 shows excellent agreement between the original ELITE code and the arbitrary n ELITE code with both the full arbitrary n inertia, and the high n inertia approximation. There is also excellent agreement between the eigenfunctions, as illustrated for $n = 15$ in figure 4.3. Notice how the eigenfunction does not show any coupling to the edge, as expected by the ideal wall.

4.3.2 Benchmark of circular test case

This section details the benchmark of the circular test case in the presence of a vacuum. This benchmark has been performed for the full arbitrary n ELITE code, the arbitrary n ELITE code with the high n inertia terms from $3 \leq n \leq 20$ and the original ELITE code from $5 \leq n \leq 20$. The $n = 1$ and $n = 2$ are easily calculated by arbitrary n ELITE; but the eigenfunctions for these modes show that the modes extend right across the plasma and therefore, are not zero when the core boundary condition is reached. As the core boundary condition assumes that the modes have zero amplitude at the core, this assumption for the $n = 1$ and $n = 2$ modes is inaccurate, thus rendering the results for these two mode numbers unreliable. The result of the benchmark is shown in figure 4.2.

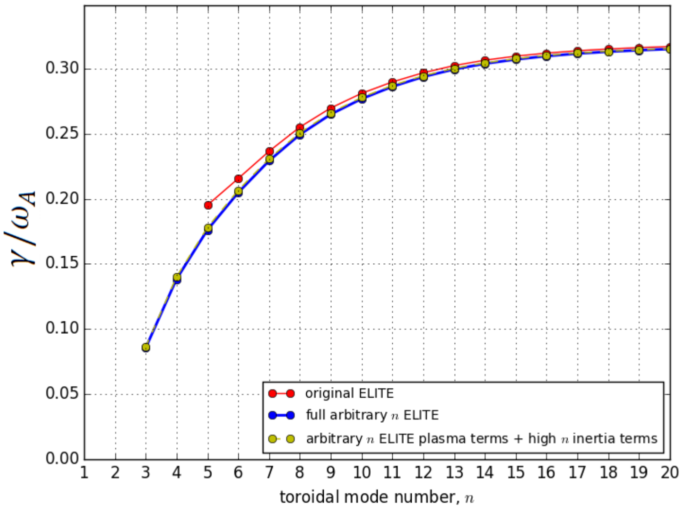

Figure 4.4: Benchmark of the arbitrary n ELITE code for the circular cross section test case with:the full arbitrary n ELITE (blue dots and line), the arbitrary n ELITE with the high n inertia approximation (yellow dots and dashed line) and the original ELITE code (red dots and line), for $n = 3$ to $n = 20$ (arbitrary n ELITE) and $n = 5$ to $n = 20$ (original ELITE).

Figure 4.4 shows that there is excellent agreement between arbitrary n ELITE and original ELITE at intermediate-high n, $n \approx\geq 7$ and above, and from $5 \leq n \leq 7$ there is good agreement with a small, but perhaps expected discrepancy between original and arbitrary n ELITE. There is excellent agreement between the eigenfunctions, as shown for $n = 10$ in figure 4.5. Note from the eigenfunctions the effect of the vacuum on the eigenfunction: the modes are now non-zero at the edge.

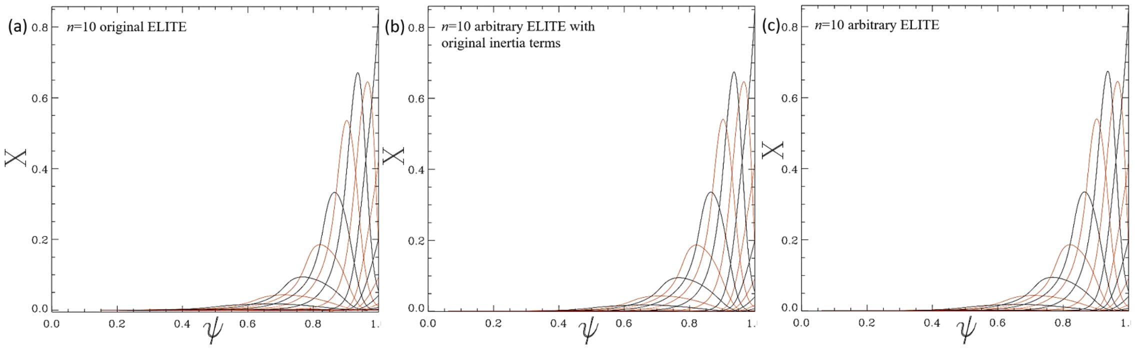

Figure 4.5: $n = 10$ eigenfunctions for the circular cross section benchmark where: (a) is calculated by original ELITE, (b) is calculated by the arbitrary n ELITE with the high n inertia approximation and (c) is calculated by the full arbitrary n ELITE.

4.4 Up-down-symmetric D-shaped benchmark

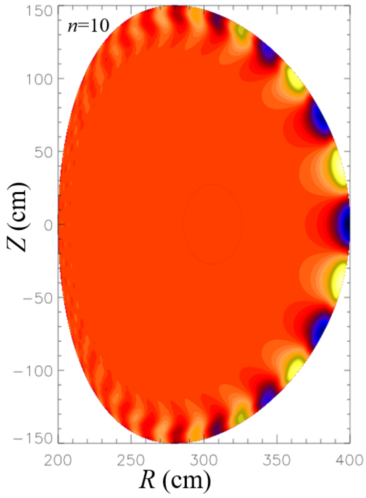

Figure 4.6: Shape of the D-shaped up-down-symmetric test case with an $n = 10$ mode calculated with arbitrary n ELITE with the full arbitrary n inertia.

This section details the up-down-symmetric D-shaped test case, “dbm9”. This test case has also been produced by TOQ, and was originally produced to benchmark the original ELITE code [99] against the low n code GATO [101]. This successful benchmark can be seen in figure 4.18, discussed later in this chapter. Therefore, the original ELITE code can be used to benchmark the arbitrary n ELITE. This test case has tanh-shaped wide density and temperature pedestals, and self-consistent Sauter bootstrap current [99]. It was designed to be significantly unstable to all n and has an aspect ratio $A = 3$, elongation of 1.5, a triangularity of 0.2 [99], as well as $q(95) = 2.3753$ and normalised beta $\beta_n = 2.83$. Figure 4.6 shows an $n = 10$ mode reconstructed in the poloidal plane calculated with the full arbitrary n ELITE.

This benchmark has been performed for the full arbitrary n ELITE code, the arbitrary n ELITE code with the high n inertia terms from $3 \le n \le 20$ and the original ELITE code from $7 \le n \le 20$. Again the $n = 1$ and $n = 2$ cases are easily calculated by arbitrary n ELITE, but the eigenfunctions are non-zero when the core boundary condition is reached. The result of this benchmark is shown in figure 4.7. This figure shows that there is again excellent agreement between original ELITE, and the full arbitrary n ELITE, which improves as n increases. The arbitrary n ELITE with the high n inertia terms gives growth rates between the original ELITE and the full arbitrary n ELITE. There is also excellent agreement between the eigenfunctions, illustrated in figure 4.8 for $n = 10$.

4.5 Non-up-down symmetric D-shaped benchmark

This section details the non-up-down symmetric D-shaped benchmark, “dbm8”. As with the previous benchmark, “dbm9”, the equilibrium was also produced by TOQ, and was originally produced to benchmark the original ELITE code against the low n

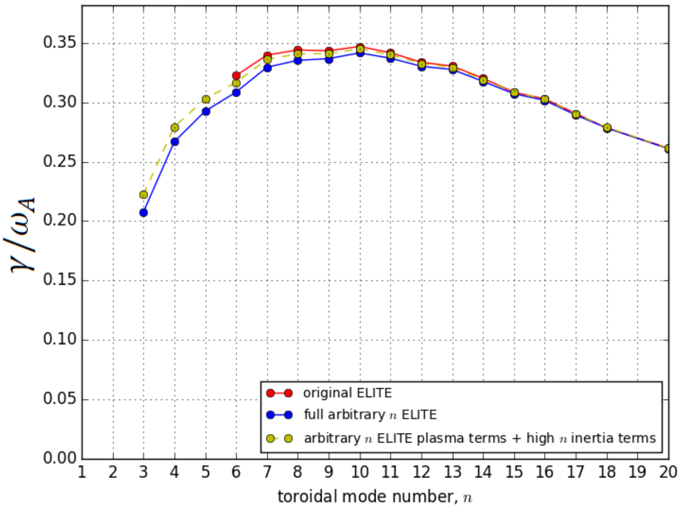

Figure 4.7: Benchmark of the arbitrary n ELITE code for the D-shaped up-down-symmetric test case with:the full arbitrary n ELITE (blue dots and line), the arbitrary n ELITE with the high n inertia approximation (yellow dots and dashed line) and the original ELITE code (red dots and line), for $n = 3$ to $n = 20$ (arbitrary n ELITE) and $n = 6$ to $n = 20$ (original ELITE).

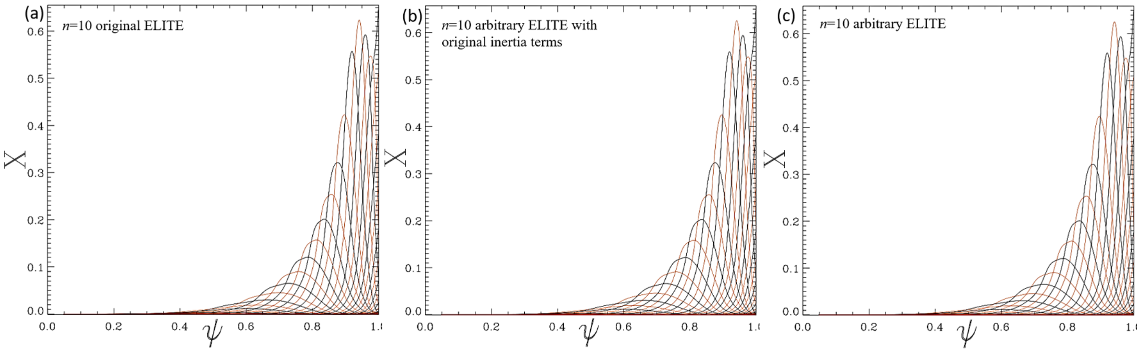

Figure 4.8: $n = 10$ eigenfunctions for the D-shaped up-down-symmetric test case where: (a) is calculated by original ELITE, (b) is calculated by the arbitrary n ELITE with the high n inertia approximation and (c) is calculated by the full arbitrary n ELITE.

code GATO [99]. This test case also has tanh-shaped wide density and temperature pedestals, and self-consistent Sauter bootstrap current [99]. It was designed to be significantly unstable to all n. It also has an aspect ratio $A = 3$, elongation of 1.5, with an upper triangularity of 0.0 and a lower triangularity of 0.3 [99]. Figure 4.9 shows an $n = 10$ mode reconstructed in the poloidal plane calculated with the full arbitrary n ELITE.

This benchmark has been performed for the full arbitrary n ELITE code and the arbitrary n ELITE code with the high n inertia terms from $2 \leq n \leq 20$, the low n code GATO from $1 \leq n \leq 8$, and the original ELITE code from $4 \leq n \leq 20$. Again, the $n = 1$ mode is calculated by arbitrary n ELITE, but the eigenfunction is non zero when the core boundary condition is reached. The result of this benchmark is shown in figure 4.10, showing overall excellent agreement. The figure shows that at low n there is good agreement between arbitrary n ELITE and GATO, and that as n increases, the agreement improves. As n increases, the original and arbitrary n versions of ELITE

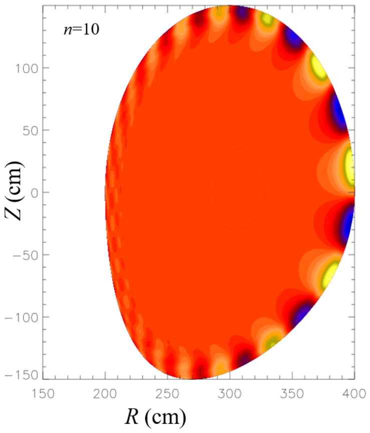

Figure 4.9: Shape of the D-shaped non-up-down-symmetric test case with an $n = 10$ mode calculated with arbitrary n ELITE with the full arbitrary n inertia.

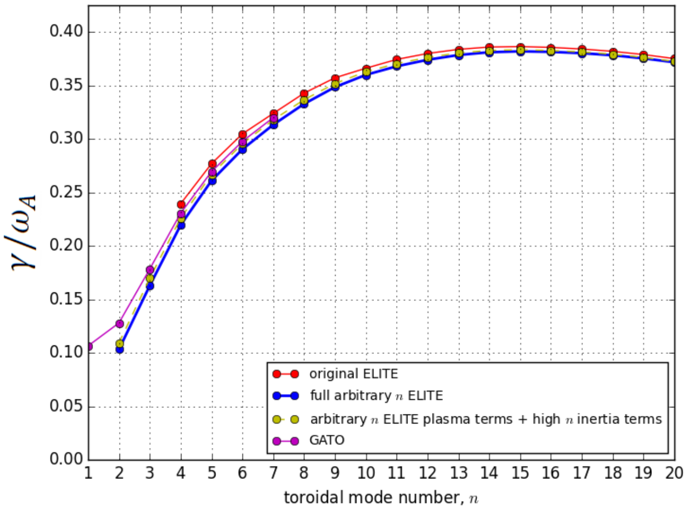

Figure 4.10: Benchmark of the arbitrary n ELITE code for the D-shaped non-up-down-symmetric test case with: the full arbitrary n ELITE (blue dots and line), the arbitrary n ELITE with the high n inertia approximation (yellow dots and dashed line), the original ELITE code (red dots and line) and the GATO code (magenta), for $n = 2$ to $n = 20$ (arbitrary n ELITE), $n = 4 - 20$ (original ELITE) and $n = 1$ to $n = 8$ (GATO).

also converge, as with the previous benchmarks. Note that GATO runs in an hour or so, but arbitrary n ELITE runs in minutes. There is also excellent agreement between the eigenfunctions, illustrated in figure 4.11 for $n = 10$.

4.6 High resolution EFIT-style benchmark

The final benchmark is a very high resolution EFIT-type g-file benchmark “meudas1025”, which has a $R - Z$ grid resolution of 1025×1025, compared to the usual $R - Z$ resolution of an experimental EFIT of 129×129 [100]. Figure 4.12 shows an $n = 5$ mode reconstructed in the poloidal plane, calculated with the full arbitrary n ELITE, which shows that the shape is highly non-up-down symmetric. A cut-off of 99.6% was used, which removes the separatrix and therefore the x-point.

This benchmark has been performed for the full arbitrary n ELITE code and the

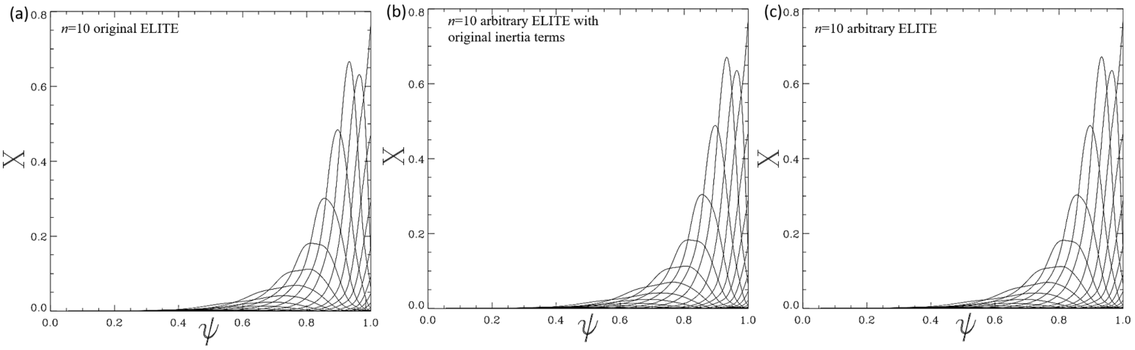

Figure 4.11: $n = 10$ eigenfunctions for the D-shaped non-up-down-symmetric test case where: (a) is calculated by original ELITE, (b) is calculated by the arbitrary n ELITE with the high n inertia approximation and (c) is calculated by the full arbitrary n ELITE.

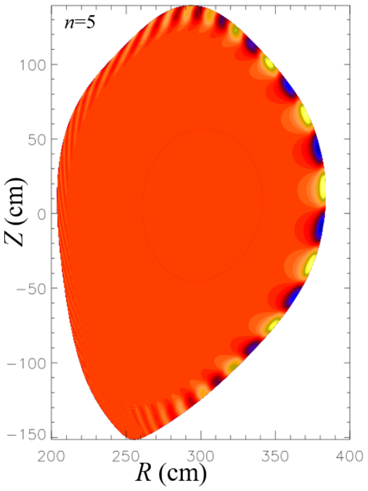

Figure 4.12: Shape of the high resolution EFIT style test case with an $n = 5$ mode calculated with arbitrary n ELITE with the full arbitrary n inertia.

arbitrary n ELITE code with the high n inertia terms from $2 \le n \le 9$, the ideal MHD code MARG2D [103, 104] from $n = 1 - 9$, and the original ELITE code from $5 \le n \le 9$. The $n = 1$ mode was calculated as being likely to be stable by arbitrary n ELITE. The result of this benchmark is shown in figure 4.13, showing overall excellent agreement. The small systematic difference between ELITE and MARG2D was previously observed in an earlier benchmark of this test case [100]. There is also excellent agreement between the eigenfunctions from original and arbitrary n ELITE, illustrated in figure 4.14 for $n = 5$.

Also illustrated are the $n = 2$, $n = 3$ and $n = 9$ eigenfunctions produced using full arbitrary n ELITE, and shown in figure 4.15. Notice how the number of poloidal harmonics increases as n increases. Also note how the mode becomes more radially localised towards the edge as n increases. Both these properties are seen in all the benchmarks tested, and begins to show how the low n modes could extend to the axis of the plasma. The main ballooning envelope can be seen in all the mode structures, as can the peeling component, seen right at the edge of the plasma. Therefore all 4 benchmarks verify the results produced by the arbitrary n ELITE formalism. Hence, the formalism can be used on experimental cases, the first example of which is seen in

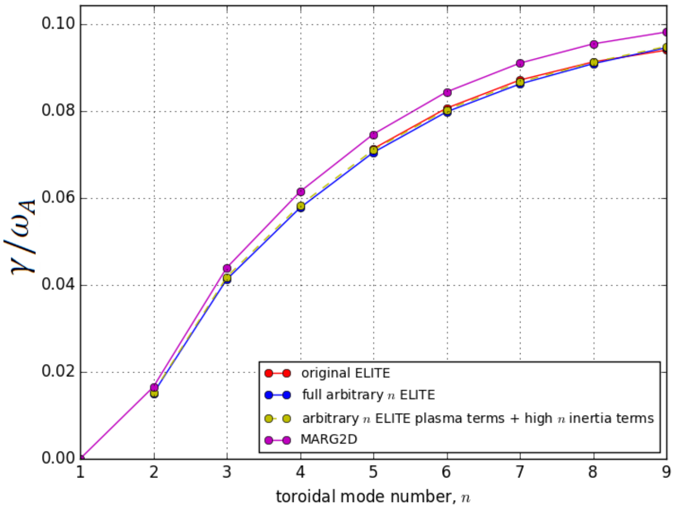

Figure 4.13: Benchmark of the arbitrary n ELITE code for the high resolution EFIT-style test case with: the full arbitrary n ELITE (blue dots and line), the arbitrary n ELITE with the high n inertia approximation (yellow dots and dashed line), the original ELITE code (red dots and line) and the MARG2D code (magenta), for n = 2 to n = 9 (arbitrary n ELITE), n = 5 to n = 9 (original ELITE) and n = 1 to n = 8 (MARG2D).

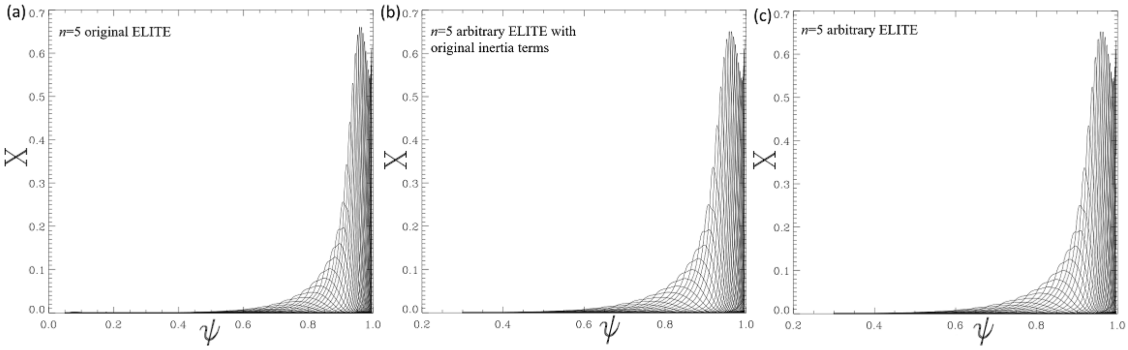

Figure 4.14: n = 10 eigenfunctions for the high resolution EFIT-style test case where: (a) is calculated by original ELITE, (b) is calculated by the arbitrary n ELITE with the high n inertia approximation and (c) is calculated by the full arbitrary n ELITE.

chapter 5.

4.7 ELITE - calculating the C matrix

The ELITE code has two different mesh scales: the coarse x mesh on which the equilibrium quantities are evaluated and a fine x mesh on which the eigenfunction calculation occurs. The arbitrary n ELITE code has to perform matrix multiplications and invert the C matrix, which is not part of original ELITE. This calculation of the C matrix and its subsequent inversion, is costly computationally. The first version of arbitrary n ELITE inverts and calculates the C matrix on the fine mesh, where the w_m matrix is generated, since this is where the calculation of the matrices takes place in the original ELITE formalism. All the benchmarks of the arbitrary n ELITE code presented in this chapter so far have used this first version. However, it is computationally beneficial to calculate and invert C on the coarse mesh. This is possible since when all the terms are

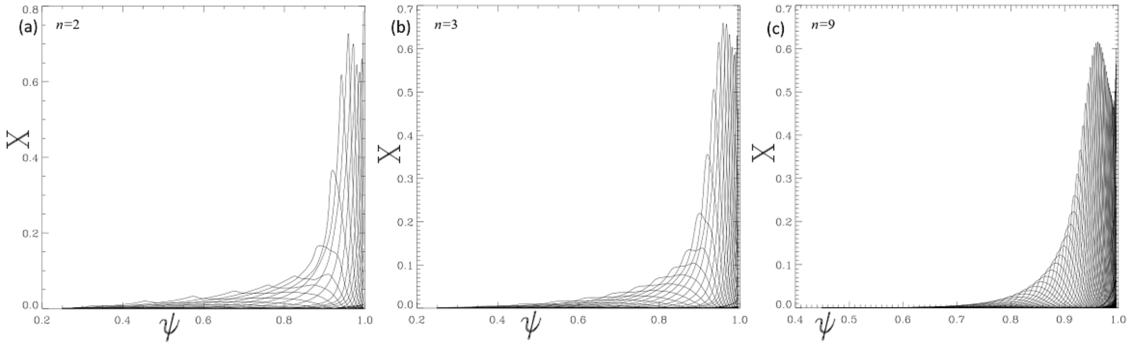

Figure 4.15: (a) $n = 2$, (b) $n = 3$ and (c) $n = 9$ eigenfunctions for the high resolution EFIT-style test case calculated with arbitrary n ELITE with full arbitrary n inertia.

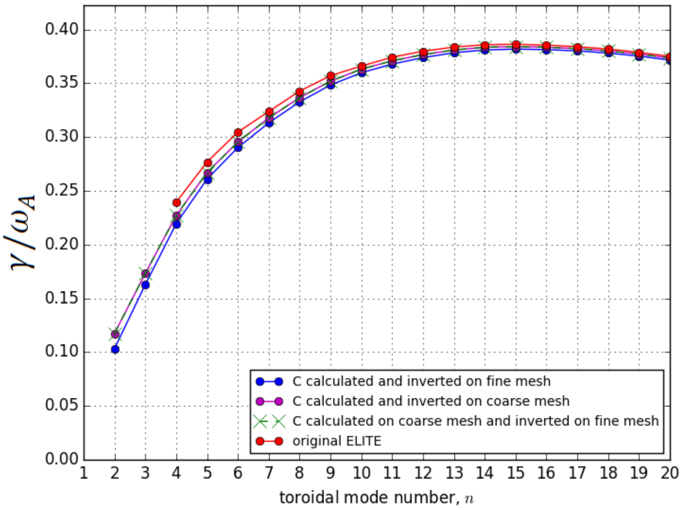

Figure 4.16: Benchmark of the D-shaped non-up-down symmetric test case where in the arbitrary n ELITE with full arbitrary n inertia but where C is calculated and inverted on different meshes. Different meshes shown against the original ELITE code result where: C is calculated and inverted on the fine mesh (used for previous benchmarks) (blue dots and line), C is calculated on the coarse mesh but inverted on the fine mesh (green crosses and dashed line), C is calculated and inverted on the coarse mesh (magenta dots and line) the original ELITE code (red dots and line), for $n = 2$ to $n = 20$ (arbitrary n ELITE), $n = 4 - 20$ (original ELITE).

combined there is no fast varying terms in the C matrix. This has been implemented in both up-down symmetric and non-up-down symmetric versions of ELITE. There is also an intermediate version in non-up-down symmetric ELITE, which is useful for testing, which calculated on the coarse mesh but inverted on the fine mesh. The names of all the versions are detailed in the appendix, section C.1.

The benchmarking of both the up-down-symmetric and non-up-down symmetric versions for C calculated on the coarse mesh has been performed, which show excellent agreement. Two examples are included here. The first uses the non-up-down symmetric D-shaped test case “dbm8”, and the second uses the EFIT-style test case “meudas1025”. These benchmarks have all used the full arbitrary n inertia, such that the calculation and inversion of C on the fine mesh results shown in blue, are the same blue results from the previous benchmarks. Similarly in red are the same original

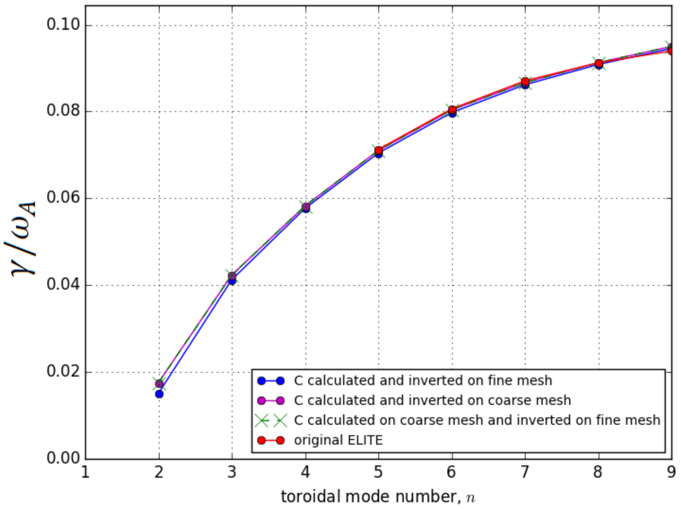

Figure 4.17: Benchmark of the EFIT style test case where in the arbitrary n ELITE with full arbitrary n inertia but where C is calculated and inverted on different meshes. Different meshes shown against the original ELITE code result where: C is calculated and inverted on the fine mesh (used for previous benchmarks) (blue dots and line), C is calculated on the coarse mesh but inverted on the fine mesh (green crosses and dashed line), C is calculated and inverted on the coarse mesh (magenta dots and line) the original ELITE code (red dots and line), for $n = 2$ to $n = 9$ (arbitrary n ELITE), $n = 5 - 9$ (original ELITE).

ELITE results. The first benchmark is for "dbm8", and the results for $2 \leq n \leq 20$ are shown in figure 4.16. As the figure shows, the growth rates calculated with the three types of C calculation and inversion agree excellently. These results suggest that the simplification is valid.

The second benchmark is for "meudas1025", and the results for $2 \leq n \leq 9$ are shown in figure 4.17. As the figure shows, the growth rates calculated with the three types of C calculation and inversion also agree excellently. Both benchmarks provide validity to improving the efficiency of the arbitrary n ELITE code in this manner. The difference between the three different ways C is calculated and inverted in arbitrary n ELITE is negligible.

4.8 ELITE: parameter convergence discussion

The arbitrary n ELITE code has quite different convergence properties to the original ELITE code, especially in the complex EFIT-type cases. The arbitrary n ELITE code requires the following, compared to the default set up for original ELITE:

- Increased poloidal resolution in the plasma part of the code, ns, which is used for solving the eigenfunction. If using an EFIT equilibrium, npts, which is the number of poloidal mesh points that the EFIT will be mapped onto in the equilibrium part of ELITE should also match ns.
- A significantly increased number of poloidal modes resonant in the vacuum, nmvac. This is the most striking difference between the two formalisms.

- Also required is higher number of additional poloidal harmonics retained in the plasma, nmlow.

- An increased number of equilibrium surfaces to be interpolated to from EFIT when the grid is created, nxinterp. This does not apply to other equilibrium types.

- Increased resolution of the fine x mesh points over a given range, ndist.

- The arbitrary n ELITE code works much better with "mesh type 2", which uses an even grid for the x points [99].

The arbitrary n ELITE code requires a significantly increased number of vacuum modes, as well as an increased number of extra modes in the plasma as there is a stronger coupling of poloidal modes, m, for a given lower n. The reason for this could be that this increases the number of modes in the Fourier amplitudes of both perturbations, which are not needed when there is sufficient number of modes [130]. However, despite needing extra modes, the arbitrary n ELITE formalism has an advantage as it is easier to converge these nmvac and nmlow than in the original ELITE code at $4 \leq n \leq 8$. Therefore, the two ELITE formalisms need their own default parameters and input files, and to compare the two formalisms, requires independent convergence tests. The input files used to run arbitrary n ELITE for the four test cases are shown in appendix section C.1. This includes a description of each of the input file parameters.

4.9 Development of a δW diagnostic

This section details an additional extension to the original ELITE code. This is the development of a so-called "δW diagnostic". The solution of the eigenmode, X, can be used to calculate the individual contributions of terms to the δW equation, given by equation 2.51, and so identify the dominant drive for the instability at any given n. This provides a much more effective measure than mapping out the full $J-\alpha$ diagram. The contribution at each n is a relative value. This has been implemented in both the up-down symmetric and non-up-down symmetric versions of ELITE. As an example of the new δW diagnostic, the reasons for the peak in the growth rate seen in the up-down symmetric D-shaped test case, "dbm9", shown in figure 4.18, is explored.

The result of the diagnostic performed on "dbm9" test case is shown in figure 4.19, in the range $6 < n < 100$. A positive contribution is stabilising, and negative is destabilising. Contributions are normalised to the coefficient of growth rate in the inertial term.

The terms in the δW equation 2.51 are grouped as follows: field-line bending terms are terms 1 and 2, as well as the finite n correction term, term 6. This is because at lower n two of the terms, 2 and 6, become very large and cancel out, so this grouping avoids large spikes in the relative amplitudes. Aside from this the term 6 is usually stabilising, and becomes small at high n as it is an $O(n^{-1})$ term. The curvature terms,

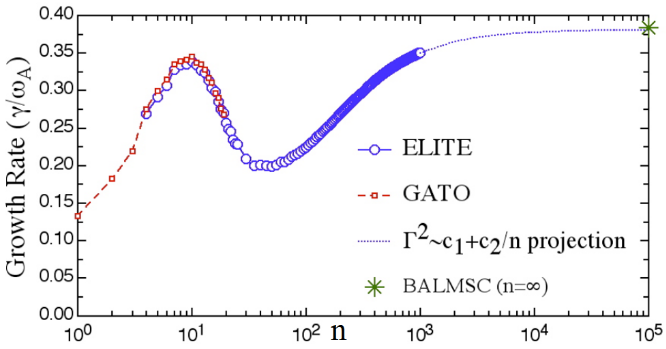

Figure 4.18: Growth rate (γ/ω_A) vs. n for the D-shaped up-down symmetric test case calculated with original ELITE, benchmarked against GATO and BALMSC ($n = \infty$). Reproduced from [99].

also known as the ballooning terms, are terms 3 and 4. The kink term is term 5, which is an $O(n^{-1})$ term which contains the current density gradient. The peeling term, which is a surface term containing the current density, is term 7.

Figure 4.19 shows that the peak in the growth rate at intermediate n arises mainly from the kink term, and that there is also a significant contribution from the curvature terms, and a small contribution from the peeling term. Therefore, this is a coupled PB mode as expected from PB theory. At high n, the dominant drive is from the curvature, which balances with the field line bending. However, an interesting result of this study is that the kink term is the dominant drive up until $n = 40$, and is still present and contributes to the drive at $n = 100$. The kink term is $O(n^{-1})$, and therefore was not expected to dominate out to $n = 40$. This is due to large current density gradients in the pedestal region, and this result supports the non-monotonicity seen in the growth rate in figure 4.18. This has significant implications for pedestal gyro-kinetics: the kink term is not currently retained in gyro-kinetics, where it is assumed that the drive is ballooning, for example in high n kinetic ballooning modes. This result shows that the assumption in gyrokinetic codes that at high n the kink term is insignificant is not an accurate assumption, and may be important for a reliable prediction of the KBM stability in realistic low collisionality tokamak pedestals.

4.10 Width KBM constrained study using the δW diagnostic

This section details an additional study that was performed with the δW diagnostic to study the drive. In this study, up-down symmetric model tokamak equilibria, broadly based on “dbm9”, were produced at different widths using the TOQ code. The height of the pedestal was then increased so that the pedestal gradients are constrained by the KBM. This was performed at high collisionality, where the pedestal density is $n = 8 \times 10^{19} m^{-3}$. Four different width equilibria were produced, where their widths are given in terms of percentage of minor radius: for example, wid2 has a pedestal width of 2% of the minor radius. Their growth rate is shown vs. n in figure 4.20. The growth

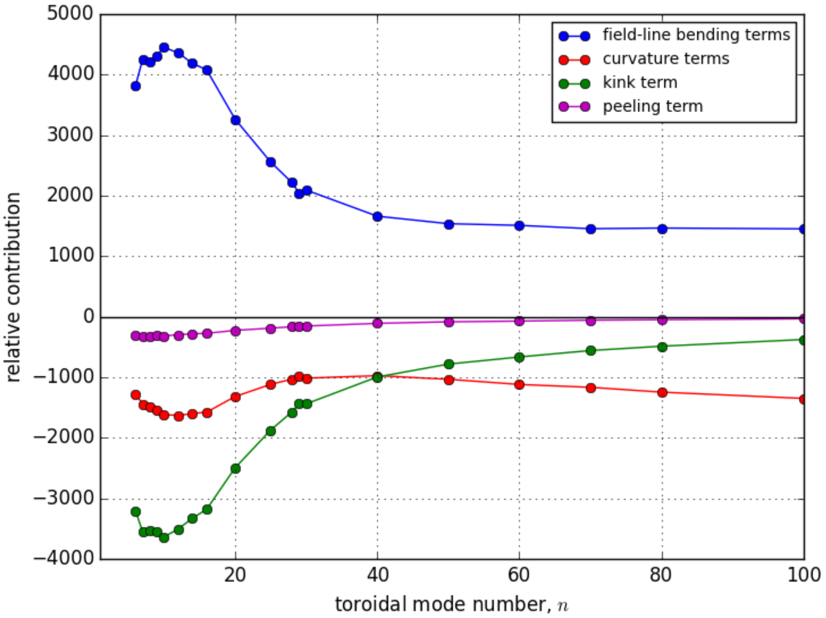

Figure 4.19: Original ELITE δW diagnostic output for the D-shaped up-down symmetric test case, showing the relative amplitude of the drive terms. Positive contribution is stabilising, negative is destabilising. Separate drives are as follows: the field-line bending, including the finite $1/n$ term (blue line and dots), the curvature/ballooning terms (red line and dots), the kink term (green line and dots) and the peeling term (magenta line and dots).

rate $(\gamma/(\omega^*/2))$ here is normalised to the diamagnetic frequency, which is commonly used in the EPED model [111]. The PB threshold is taken to be when the growth rate is $\gamma/(\omega^*/2) = 1$.

Figure 4.20 shows that the narrowest width, which is 2% of the minor radius and corresponds to early in the ELM cycle, is stable to PB modes. However, at a later time when the pedestal has reached a width of 3% of the minor radius, the critical width of the pedestal is realised and an intermediate n PB mode is destabilised. The PB threshold in this case is reached at $n = 26$. This is intermediate n destabilisation as the ELM trigger is expected by EPED and PB theory. The wider widths, at 5% and 7% of the minor radius, would not occur since the pedestal has reached the PB threshold at the narrower width and this results in the pedestal collapse at the end of the ELM cycle. Therefore, the δW diagnostic was used to determine the drive in the 3% width case. The result is shown in figure 4.21.

As figure 4.21 shows, at the critical n, $n = 26$, the drive is dominated by the curvature, and is also substantially contributed to by the kink term. Also here, it can be seen that the kink term also survives to large n, due to steep current density gradients in the pedestal. It is expected that this case would have a stronger drive from the curvature than the kink drive. This is because the case is at high collisionality, and therefore the modes would be less kink-like and have a higher n most unstable mode. This is seen in the difference in the most unstable intermediate n: in the previous case this was at $n = 10$, as shown in figure 4.18, and in this case the peak in the growth rate as shown in figure 4.20 occurs at $n = 31$, and the growth rate normalised to the

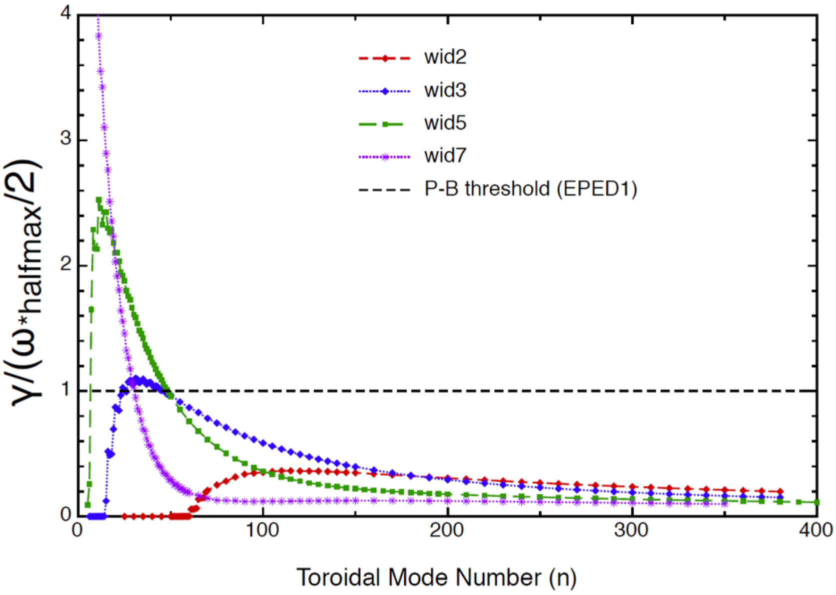

Figure 4.20: Growth rate, $\gamma/(\omega^*/2)$, vs. n for up-down symmetric model equilibria with different width pedestals: from 2% (wid2 - red), 3% (wid3 - blue), 5% (wid5 - green) and 7% (wid7 - purple) of the minor radius, and the diamagnetic peeling-ballooning (PB) threshold is shown in black. Pedestal height such that the pedestals are critical to the EPED KBM criterion.

Alfvén frequency (γ/ω_A) is still increasing at the highest n the diagnostic was run to. This case also shows that, even in cases where the curvature dominates, the kink term is therefore significant, and is still important to accurately calculate the stability.

4.11 Conclusions and further work

In conclusion this chapter has shown the systematic verification of the results produced by the new arbitrary n ELITE for both up-down symmetric and non-up-down symmetric equilibria. Four benchmarks have been performed using four test cases: a circular cross section test case, an up-down symmetric D-shaped test case, a non-up-down symmetric D-shaped test case and a high resolution EFIT-type test case. The benchmarks have shown that there is excellent agreement in the growth rates produced by the arbitrary n ELITE compared with the original ELITE and well as compared to the GATO and MARG2D codes. It has also been shown that the high n approximation for inertia in the arbitrary n ELITE code is a surprisingly accurate approximation, except at $n = 1$. However, presently $n = 1$ always extends to the on-axis boundary condition and as such cannot be included in the results shown here. There is also excellent agreement in the eigenfunctions produced by the two ELITE formalisms.

It has also been illustrated that the arbitrary n ELITE code can be optimised by performing the calculation and subsequent inversion of the C matrix on the coarse mesh. This allows the arbitrary n code to be more computationally efficient. Benchmarks have shown that this is valid and produces results with excellent agreement. The parameter convergence of ELITE has been briefly discussed, which shows that arbitrary n ELITE requires more modes and additional resolution for convergence than

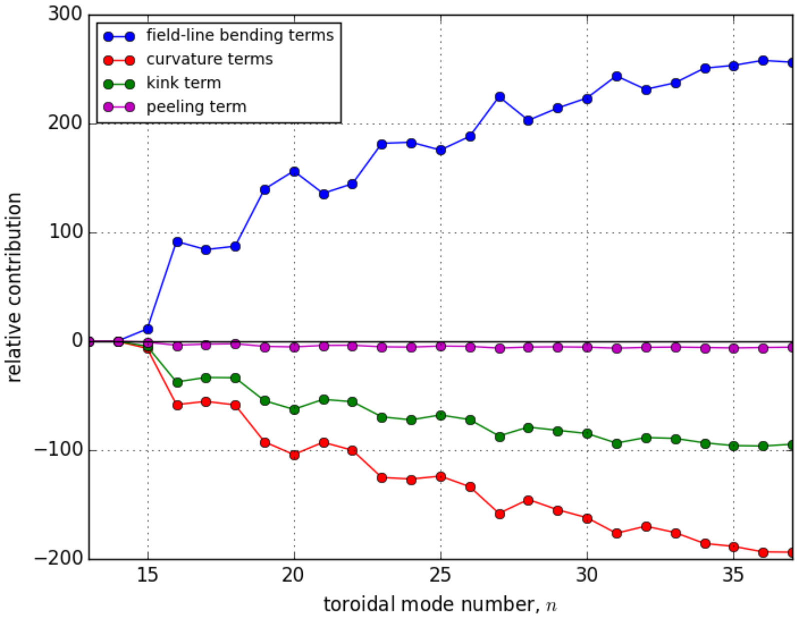

Figure 4.21: ELITE δW diagnostic output for the 3% width KBM constrained pedestal, showing the relative contribution of the drive terms. Positive contribution is stabilising, negative is destabilising. Separate drives are as follows: the field-line bending, including the finite $1/n$ term (blue line and dots), the curvature/ballooning terms (red line and dots), the kink term (green line and dots) and the peeling term (magenta line and dots).

original ELITE. While this does slow the speed of the code, as it will in practice only be run for low n, and at low-intermediate n as an overlap with the original ELITE code as n is increased, this is not such an issue.

A δW diagnostic has been implemented in the original ELITE code. The diagnostic allows the exact relative amplitude of all the drive terms in the δW equation to be determined, without the need for a 2D parameter scan of $J - \alpha$ space to determine the drive. Analysis using the diagnostic has shown that, although the kink term is $O(n^{-1})$, it survives to very large n because of steep current density gradients in the pedestal. The kink term is not presently retained in gyro-kinetic codes, which questions the validity of the use of gyro-kinetic codes in the pedestal, and it may be important for an accurate prediction of the KBM stability criterion in realistic tokamak pedestals.

There is much further work to be done. Firstly, arbitrary n ELITE needs to be made ready for release to the ELITE users community. This requires choosing which version of arbitrary n ELITE to use; this would be preferably the version where C is calculated and inverted on the coarse mesh as this is the least expensive computationally, and whether the full or high n inertia should be used. Also to be decided is default values of the input parameters to be used for experimental cases. An experimental DIII-D analysis using arbitrary n ELITE, where C is calculated and inverted on the fine mesh, and the full arbitrary n inertia is used, is presented in the next chapter. Another crucial extension is to implement a non-zero core boundary condition, so that all low n modes can be studied, in particular $n = 1$. Also important is the implementation a different radial coordinate: using x as the radial coordinate requires that q is monotonic: in low collisionality pedestals at low n, which are often current dominated, this is often not the case and this extension will help ELITE, including the original ELITE formalism, to become a more general code. Equally important for the accurate study of analysis of low n dominated phenomena is to derive an additional arbitrary n ELITE formalism that includes flow shear, which is non trivial. This is important since, for example in QH-mode, flow shear is destabilising at low n, and stabilising at intermediate to high n, as discussed in the next chapter. Yet another extension is to implement the δW diagnostic in the arbitrary n ELITE such that the drive can be determined across a full range of n. This is also non-trivial since the different expansion of the U perturbation leaves the terms in the original ELITE δW equation to be present across the 13 terms of the new arbitrary n δW. Another interesting extension would be to include a more complex and realistic vacuum model to account for a real wall in the plasma. Finally, it would beneficial to incorporate arbitrary n ELITE into the EPED model to help resolve the kink/peeling boundary.

Chapter 5

QH-mode in DIII-D: a study using arbitrary n ELITE

5.1 Introduction and motivation

As introduced in subsection 1.9.2 in chapter 1, the quiescent H-mode (QH) is a high-performance edge localised mode (ELM) free mode of operation which was discovered on DIII-D [58]. There are now two types of known QH-modes [43]. In the standard QH-mode [58] the pedestal is limited by an MHD edge harmonic oscillation (EHO) with a low toroidal mode number (n), which is typically $n \sim 1-3$. This EHO has been found to be a saturated kink-type mode, which is destabilised by flow shear, and provides density control [60, 131]. This mode requires large edge rotational shear [60, 62] and therefore high torque is required, and in DIII-D this is provided using neutral beam injection (NBI) [43]. There have also been demonstrations of EHO QH-mode in a near zero toroidal rotation and near zero net NBI torque regime where the electromagnetic torque is obtained from 3D static, non-axisymmetric, non-resonant magnetic fields (NMRFs) [63].

Very recently a wide-pedestal QH-mode was discovered in double-null plasmas on DIII-D, when experiments designed to test the effects of rotation on the EHO were performed [43]. This new QH-mode is stationary and has overall high confinement with: increased pedestal width, pedestal height and thermal energy confinement [43]. This is achieved at no net external torque, without the need for 3D NMRFs [43]. There is generally an absence of an EHO: however the EHO can exist initially just after the transition to wide-pedestal QH-mode if the rotation is high enough [132]. Wide-pedestal QH-mode achieves this performance by modifying the edge turbulence when rotation shear at the edge is lowered; allowing for an increase in the broadband electromagnetic turbulence (broadband MHD) [43]. This broadband MHD provides the necessary density and impurity control, which previously was provided by the EHO. This increased turbulence lowers the pedestal pressure gradient and therefore allowing the pedestal to widen and increase in height, leading to approximately a 40% improvement in thermal energy confinement [43]. Furthermore these plasmas have been produced for up to two seconds, and were only limited by hardware constraints [43]. This regime provides stationary operation, which is ELM free with zero torque, and improved pedestal confinement which is highly important for future devices, including ITER. Future devices will require ELM free operation at low torque with good confinement, which is crucial for future energy production [43].

Comparisons of $J-\alpha$ diagrams from EHO QH-mode and wide-pedestal QH-mode published in [43] show that the experimental points sit in different locations in parameter space. In EHO QH-mode the experimental point lies on the kink/peeling boundary [60]. However, in wide-pedestal QH-mode the experimental point lies below the kink/peeling boundary [43].

In EHO QH-mode as previously discussed, a low n saturated kink-type MHD mode known as the EHO, which has multiple harmonics, is present [133] which is destabilised by flow shear [60, 131]. Numerical studies published in [133] indicate that the low n EHO-like solutions found in studies of EHO-QH mode are destabilised by rotation and/or rotational shear while the high n modes are stabilised [133]. In an EHO QH-mode pulse with a dominant $n = 2$ EHO, stabilisation by rotation or by rotation and rotational shear was found to occur for all the modes where $n \geq 3$ [133]. Furthermore, destabilisation of the $n = 2$ mode was found with rotation or rotation and rotational shear [133]. The effect of suppression of modes where $n \geq 3$ and destabilisation of the $n = 2$ modes was found to be enhanced by the increasing of rotation [133]. The growth rate for $n = 1$ was found to be almost unaffected by rotation [133]. These observations are consistent with experimental observations of EHO QH-mode which show that ELMs return when rotation is reduced [133], and wide-pedestal QH-mode is not entered. These results agree with previous results that show that the EHO is observed as a low n saturated kink-type mode [60]. The results also agree with experimental observations which show that the EHO enhanced with increased rotation and/or rotational shear and the EHO allows the suppression of intermediate-high n modes associated with ELMs.

The $J-\alpha$ diagrams shown for shot 163520 in this chapter were produced using ELITE from $n = 5$ to $n = 25$, except the last time interval analysed, which was calculated from $n = 5$ to $n = 40$. This chapter shows a study using arbitrary n ELITE to study low n modes in QH-mode shot 163520 in DIII-D. The first motivation for this work was to see whether it could be determined, using ideal MHD, what phenomena causes the ELMs to return in wide-pedestal QH-mode. In EHO QH-mode ELMs do not return, as the EHO provides a limit on the pedestal which prevents peeling-ballooning modes becoming unstable. However, the broadband MHD in wide-pedestal QH-mode does not provide this limit, and when density is increased to a high enough level ELMs are able to return [134]. Determining the nature of the MHD which leads to the return of ELMs is very important for the application of wide-pedestal QH-mode to future devices.

A secondary motivation was to see how the arbitrary n ELITE performed in regimes dominated by low n phenomena. Before this analysis was performed the arbitrary n ELITE had only previously been used with benchmarks, presented in the previous chapter. This required careful convergence tests to be performed using the real data: an example input file is included in the appendix section C.1. The study of EHO QH-mode shows that experimental results from the arbitrary n ELITE agree with previously published results [60, 131, 133].

5.2 Introduction to data: DIII-D discharge 163520

The arbitrary n version of ELITE was used to study low n modes in DIII-D QH-mode shot 163520. This shot has both wide-pedestal and EHO QH-modes, and was performed in August 2015. It is a double-null discharge with the toroidal magnetic field $B_T = 2.06T$, the plasma current $I_P = 1.107MA$ in the toroidal direction, collisionality at the pedestal top of approximately $\nu^* \approx 0.4 - 0.5$, elongation $\kappa = 1.87075$, upper and lower triangularities $\delta_u = 0.546$ and $\delta_l = 0.681$ respectively. The traces for the discharge are shown in figure 5.1.

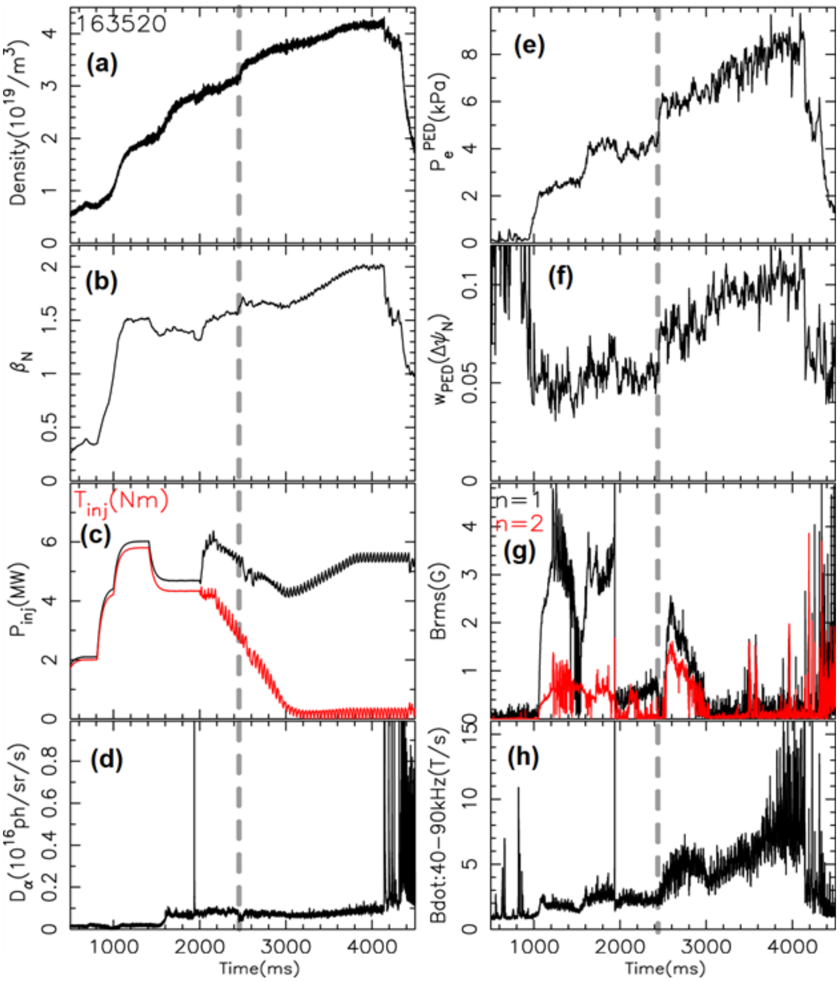

Figure 5.1: This figure shows the traces for DIII-D pulse 163520. The grey dotted line is the transition from EHO QH-mode to wide-pedestal QH-mode where (a) line averaged electron density, (b) normalised beta, (c) red: injected neutral beam injection (NBI) torque, black: injected NBI power, (d) divertor D_α emission, (e) pedestal electron pressure, (f) width of edge electron pressure pedestal, (g) magnetics showing n=1 and n=2 modes from the EHO, (h) magnetic flux through coil showing the broad band MHD magnetic fluctuations.

The evolution of the discharge is as follows: firstly the plasma starts in L-mode, then transitions from L to H-mode at 940ms. Next, it transitions into EHO QH-mode at 1060ms, and finally into wide-pedestal QH-mode at 2430ms. The transition from EHO to wide-pedestal QH-mode is indicated by the grey dotted line in figure 5.1. The transition can be seen as a sudden increase in electron pressure pedestal width, shown in 5.1 (f), coupled with the appearance of broad band magnetic fluctuations, shown in 5.1 (h). It can also be seen that this transition occurs as the NBI torque is being reduced, shown in red 5.1 (c). Initially whilst in the first type of QH-mode the EHO, shown in 5.1 (g), is present in the discharge. The EHO then turns off briefly at the time of the EHO QH-mode to wide-pedestal QH-mode transition, near 2500ms, but then returns. The EHO then continues with the broadband fluctuations as the torque is gradually reduced to zero at 3000ms, at which time the EHO turns off completely. In other cases in DIII-D after the transition to wide-pedestal QH-mode the EHO has not re-appeared [135]. At 3000ms the broadband amplitude also decreases, but remains active. These two changes can be seen in the traces, 5.1 (g) and (h). Next, just after 3000ms, the injected NBI power is ramped up at constant torque, shown in black 5.1 (c), and the broadband amplitude also increases. This increase in power is also seen additionally with the increase in the normalised beta in the pedestal, shown in 5.1 (b), and the increase in electron pedestal pressure width, 5.1 (f). Finally, at the end of the power ramp, just after 4000ms, as shown in 5.1 (d), wide-pedestal QH-mode is lost as the ELMs return.

It is important to note the apparent co-linearity shown here: as the power ramp is occurring the density also increases, shown in 5.1 (a). When [43] was published, it was believed that the power ramp was responsible for the return in ELMs. However, in January 2016, it was demonstrated in shot 164880 that this co-linearity can be broken: the NBI injected power can be increased without increasing the density, and ELMs do not return [134]. Therefore, it can be deduced that the increase in density is responsible for the return in ELMs. Also note that in a near identical shot 163518, see [43] for the trace, there was no power ramp, the density was controlled successfully by the broadband MHD and ELMs did not return.

It was speculated before the analysis that the increase in pedestal width was perhaps destabilising a mode of $n < 5$. Unusually an $n = 1$ or $n = 2$ mode, more likely $n = 2$, is seen on the magnetics data less than $100\mu s$ before the return of ELMs. This is of note as it is unusually low for an ELM precursor, which is usually $n \approx 4 - 6$ [135]. It was speculated that if the pedestal expansion rather than a gradient increase was triggering the return of ELMs, this might produce a different perspective on whether the wide pedestal state would be useful for future tokamaks [135]. Therefore, one objective was to see if this mode is detected using arbitrary n ELITE. Previous analysis shown in the $J - \alpha$ diagrams below for each point in the discharge analysed, show that the experimental point just before the ELM, see figure 5.17, is stable down to $n < 5$; and therefore does not explain why this discharge had the ELMs return.

The analysis of this discharge was undertaken for five separate times. These are illustrated on the D_α trace in figure 5.2. The first time is at 2200ms, shown in figure 5.2

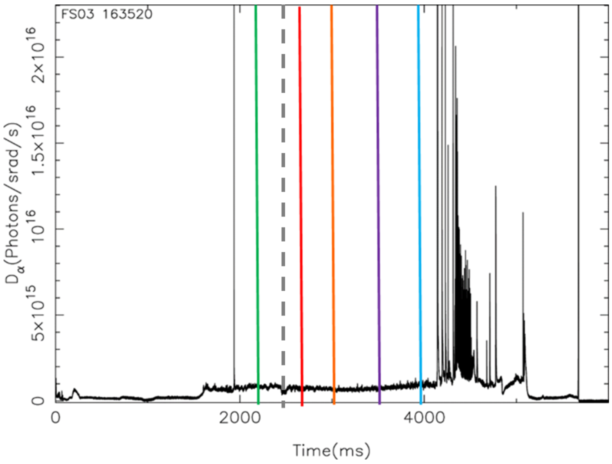

Figure 5.2: D_α trace for DIII-D discharge 163520 including the EHO to wide-pedestal transition (grey dotted line). The colours show the times in the discharge that were analysed: 2200ms (green), 2650ms (red), 3000ms (orange), 3500ms (purple) and 3985ms (blue). The transition from EHO to wide-pedestal QH-mode is just after 2400ms.

as green. This is in the coherent EHO phase at high torque (4.4Ntm), $\beta_N = 1.5$, before the wide-pedestal transition. The second time analysed is 2650ms, shown in figure 5.2 as red. This is just after the transition to the wide-pedestal phase while the pedestal width is relatively small and torque is still significant (2.4Ntm), $\beta_N = 1.65$. The third time analysed is 3000ms, shown in figure 5.2 as orange. This is in the middle of the wide-pedestal phase just after reaching zero torque, before the power, and therefore the β_N ramp, and $\beta_N = 1.64$. The forth time is 3500ms, shown in figure 5.2 as purple. This is also in the middle of the wide-pedestal phase at zero torque, but is during the power ramp and $\beta_N = 1.85$. Finally, the fifth time analysed is just before ELMs return at zero torque and $\beta_N = 2.0$.

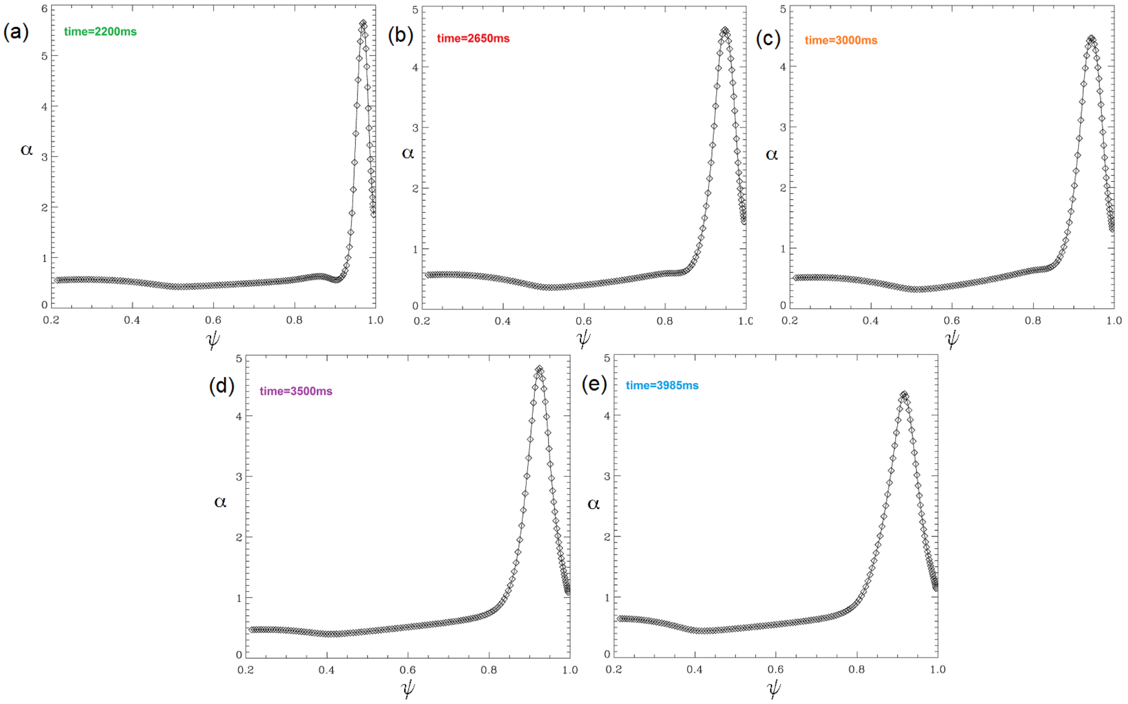

Figure 5.3: Normalised pressure gradient, α, profiles for 5 times analysed in DIII-D discharge 163520: (a) 2200ms, (b) 2650ms, (c) 3000ms, (d) 3500ms and (e) 3985ms

The normalised pressure gradient, α, profiles for each of the five times analysed in the discharge are illustrated in figure 5.3. These show how the pressure pedestal width, denoted by the width of the peak in α, increases throughout the times analysed, as previously shown in figure 5.1. It also shows how the most significant change in the width of the pedestal occurs between the first two times analysed, where the transition to wide-pedestal QH-mode from EHO QH-mode occurs.

5.3 Analysis methods

This section details the analysis methods used in this chapter. The details of arbitrary n ELITE are given in previous chapters 3 and 4. Used additionally to arbitrary n ELITE was the δW diagnostic which is also detailed in chapter 3. The stability boundary in all the analysis has been taken as $\gamma/\omega_A = 0.02$ to take non-ideal diamagnetic effects into account. Detailed convergence tests across all the varying parameters were undertaken in order to obtain accurate results from both arbitrary n ELITE, as well as original ELITE for the δW diagnostic. See the example arbitrary n ELITE input file for this discharge and parameter details in appendix section C.1.

After the convergence tests all five experimental time points were studied for low to intermediate n. Only the first experimental time point was found to be unstable to all n's tested, the other four experimental time points were found to either be marginally stable or stable. Therefore, to study the proximity to marginal stability the amount of current density in the equilibrium was increased in incremental steps, usually 10%, in the calculations. This allowed the exploration of the experimental point's sensitivity to current density. This would firstly show which modes, low or intermediate n, were destabilised first and the order which the modes are destabilised. Secondly, by comparing this to a $J-\alpha$ diagram calculated using original ELITE, it can be deduced if the stability boundary has been moved significantly. This was particularly of interest in the last time, just before the ELMs returned. The four time points all lie directly below the kink/peeling boundary, far from the ballooning boundary, therefore it was decided that the pressure gradient profile would be kept fixed, to ease the analysis. This was also motivated by previous work showing QH-modes are typically related to the kink/peeling boundary [60].

The current density in the EFITs for the experimental time points was modified using T.H. Osborne's VARYPED tool. Note that the pressure gradient profile remained fixed, so this was not calculated self consistently. This is in contrast to producing a $J-\alpha$ diagram, where both the pressure gradient and current profiles are varied across 2D parameter space. When changing the current density distribution at the edge in VARYPED, the new value (J_{new}) is obtained by essentially multiplying from its original value (J_{old}) by:

$$J_{new} = J_{old}\frac{s}{cosh\left(2\left(\psi_N - S_{cur}\right)/W_{cur}\right)^2} \tag{5.1}$$

where s is the scale factor, S_{cur} is the location of the current peak in the edge and W_{cur} is the width of the original current peak in the edge. An adjustment and iteration is done to keep the total plasma current fixed, and also the current density on axis is kept fixed at its initial value by flattening the current profile near the axis [135]. Note asymmetries in the fictitious eigenvalues occur when adding more than 20% extra current density were significant due to the equilibrium no longer being a good solution for the Grad-Shafranov equation. Also, as expected, it was not possible to achieve perfect symmetry in the experimental solution due to limitations on the experimental equilibrium quality. It is also important to note there are no $n = 1$ modes studied in this discharge, as the $n = 1$ mode structures were found to extend to the magnetic axis.

5.4 Results of analysis of 163520

5.4.1 EHO QH-mode phase: time 2200ms

As previously explained the first time slice that was analysed is 2200ms, which is shown in figure 5.2 as green. This is in the coherent EHO phase at high torque (4.4Ntm), $\beta_N = 1.5$, before the wide-pedestal transition. The EHO is still present, along with the broadband MHD fluctuations. A $J - \alpha$ diagram produced for this time is shown in figure 5.4. This was created using VARYPED to vary the pressure gradient and current density, then run through ELITE down to $n = 5$ to assess the stability at each point in parameter space.

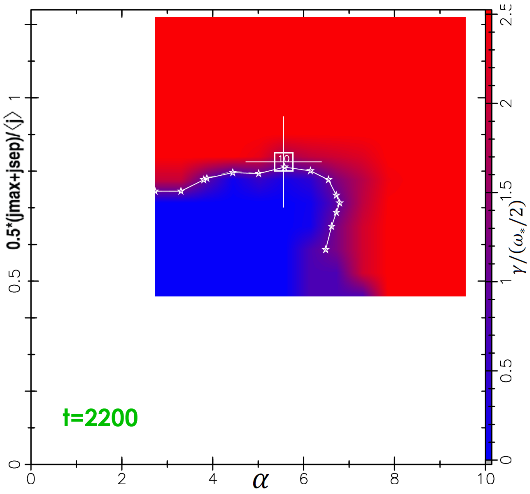

Figure 5.4: $J - \alpha$ diagram for time=2200ms with $5 < n < 25$ which indicates that the experimental point, which is the white box with error bars, lies on the kink/peeling boundary which is taken to be $\gamma/\omega_A = 0.02$ and is indicated by the white line. Blue region is stable and the red region is unstable.

As can be seen in figure 5.4, the experimental point lies on the kink/peeling boundary, which agrees with previous analysis for QH-mode plasmas with coherent EHO [60, 43]. Using the new arbitrary n ELITE, modes from $n = 2 - 10$ have been calculated and the results can be seen in figure 5.5, which shows growth rate γ/ω_A vs.

n. As the figure shows, all the low-intermediate n modes have non-zero growth rate and at $n = 8$, the growth rate peaks very close to the stability boundary.

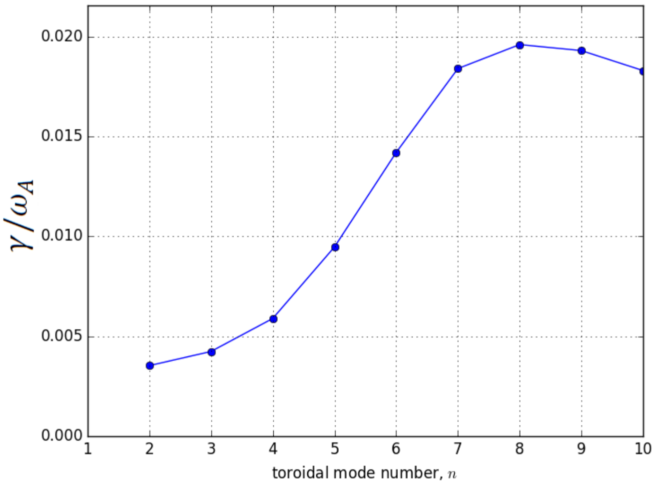

Figure 5.5: Growth rate γ/ω_A vs. n for time=2200ms.

From studying figure 5.5 an ELM might be expected to occur, as the most unstable mode number is intermediate n and this is at the kink/peeling limit. However, it is clear that an ELM does not occur due to the EHO. In this shot the experimentally observed dominant EHO is $n = 1$, and it also has harmonics in the low n's. In a similar EHO QH-mode discharge published in [133], it was shown that when flow and therefore rotation shear is included in the calculation of the growth rate for different values of n, the intermediate n modes are stabilised and the low n modes are further destabilised. It is expected from this shot that the rotation would have a similar effect and amplify the low n modes, whilst stabilising the intermediate n modes [132].

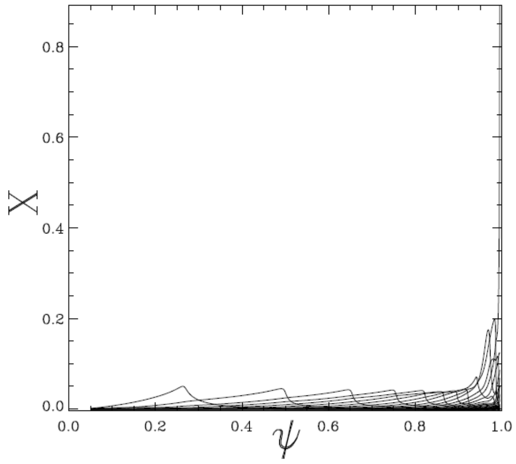

Figure 5.6: $n = 2$ mode structure for time 2200ms which shows that the mode is kink/peeling in structure, due to the single dominant poloidal mode at the edge, and the largest amplitude modes being situated in the pedestal region.

It is also interesting to analyse the low n mode structures produced by arbitrary n ELITE. An example mode structure, which is for the $n = 2$ mode, is shown in figure 5.6. This is characteristically a kink/peeling mode as when looking at the Fourier poloidal harmonics the largest amplitude modes are concentrated in the pedestal region, and in addition to this there is single very dominant poloidal harmonic at the edge. The observation of this kink/peeling mode structure is consistent with the observation of coherent EHO, which has previously been shown to be a saturated kink-type mode [60, 131]. To further determine the drive for these modes, additional analysis was performed using the δW diagnostic in original ELITE. Here the relative contributions are normalised to the first field-line bending term in the δW equation.

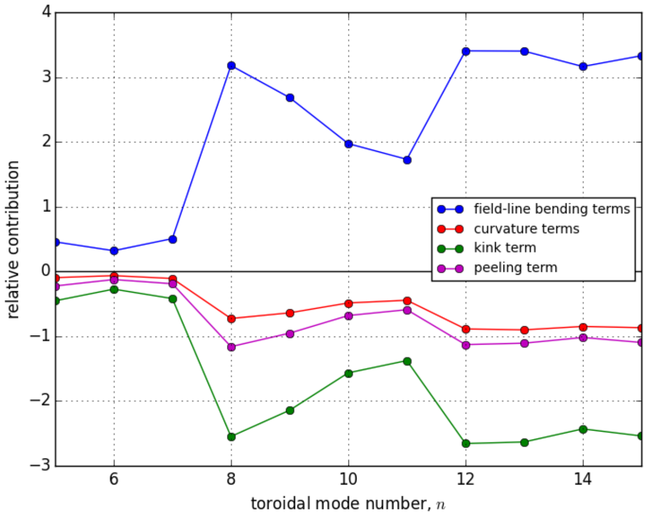

Figure 5.7: ELITE δW diagnostic output for the amplitude of the drive terms for $n = 5-15$ at time=2200ms. Positive contribution is stabilising, negative is destabilising. Field-line bending terms are indicated by the blue line, curvature/ballooning terms by the red line, the kink term by the green line and the peeling term by the magenta line.

The relative amplitude of the terms from the δW equation are shown in figure 5.7. Any terms that are positive are stabilising, and any terms that are negative are destabilising, as explained in chapter 4. The terms are grouped as follows: the field-line bending terms, including the finite n term, is indicated in blue, the curvature/ballooning terms in red, the kink term in green and peeling term in magenta. The terms have been calculated for $n = 5-15$, and are not calculated for low n since it is only implemented in the original ELITE code. However, the amplitude at intermediate-high n clearly shows that the dominant drive is the kink term, and the second drive is the peeling term. The curvature/ballooning terms are much smaller in magnitude when compared to the field line bending terms and kink+peeling terms.

The results from the δW diagnostic confirm the findings from the $J-\alpha$ diagrams, which shows the experimental point lying on the kink/peeling boundary. The low n mode structures found with arbitrary n ELITE are kink/peeling in nature, and this is consistent with the observation of the coherent EHO.

5.4.2 Wide-pedestal QH-mode phase: time 2650ms

Next, the first wide-pedestal phase at 2650ms was analysed, which is shown in figure 5.2 as red. This immediately follows the transition to the wide-pedestal phase while the pedestal width is relatively small and torque is still significant (2.4Ntm), $\beta_N = 1.65$.

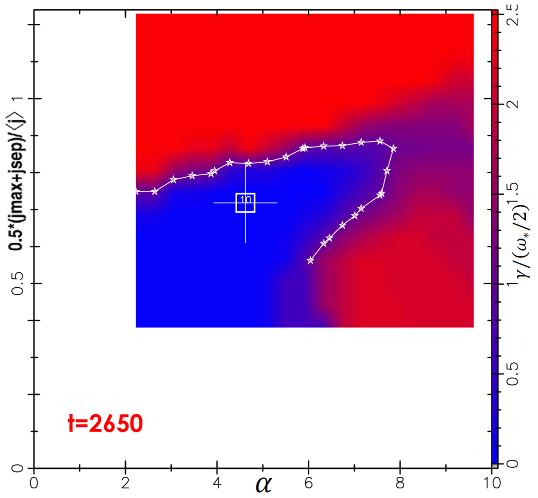

Figure 5.8: $J - \alpha$ diagram for time=2650ms with $5 < n < 25$ which indicates that the experimental point, which is the white box with error bars, lies below the kink/peeling boundary which is taken to be $\gamma/\omega_A = 0.02$ and is indicated by the white line. Blue region is stable and the red region is unstable.

The $J - \alpha$ diagram for this time is shown in figure 5.8. This figure shows that the experimental point lies below the kink/peeling boundary. This agrees with previous work on wide-pedestal QH-mode, published in [43]. Running the new arbitrary n ELITE for this case on the experimental point finds that most mode numbers are stable and some are marginally stable.

Therefore, as described in section 5.3, current density was increased to see if including the low n modes in this case altered the position of the stability boundary. The results are shown in figure 5.9 which show that when current is increased by 20%, this destabilises the $3 < n < 6$ modes across the stability boundary. Note this is when the EHO is still present, but this does not appear to influence where this experimental point sits in stability space when compared to other wide-pedestal time slices at 3000ms, 3500ms and 3985ms. The inclusion of these low n modes in this time in the discharge does not significantly alter the position of the stability boundary.

The mode structures of these destabilised modes were also studied. An example for $n = 4$ is given in figure 5.10, which shows it is much broader and more global than the pedestal region dominated kink/peeling type mode shown in figure 5.6. The stability of this time point is characteristically different to the EHO QH-mode phase.

5.4.3 Wide-pedestal QH-mode phase: time 3000ms

The third time slice analysed is 3000ms, shown in figure 5.2 as orange. This is in the middle of the wide-pedestal phase just after reaching zero torque, before the power, and therefore β_N, ramp, and $\beta_N = 1.64$. The EHO has turned off, and the broadband fluctuation amplitude also decreases, but remains on. The $J - \alpha$ diagram for this time is shown in figure 5.11.

As figure 5.11 shows as with the previous time slice at 2650ms, the experimental point lies below the kink/peeling boundary. This again agrees with previous work

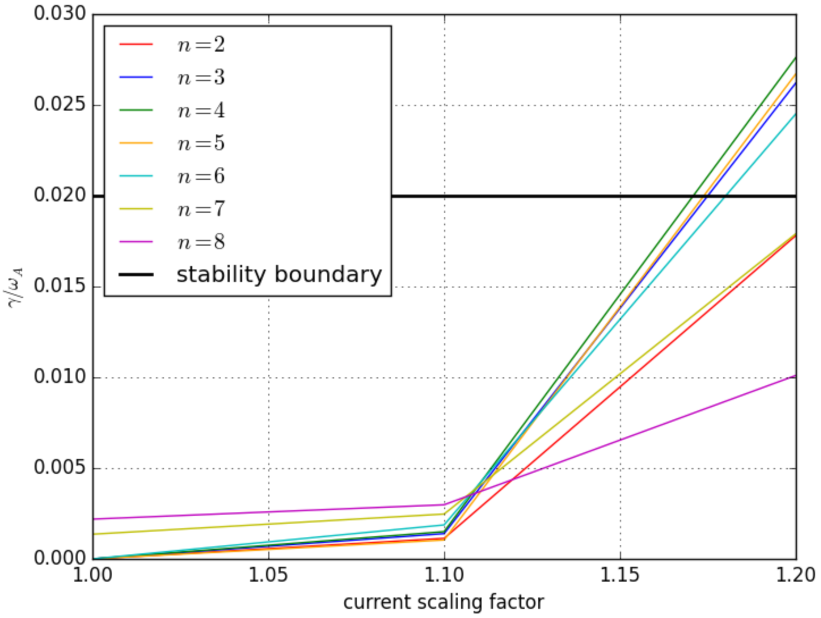

Figure 5.9: Time 2650ms growth rate (γ/ω_A) vs. current scaling factor, where 1=100% and 1.1=110%, for $n = 2 - 8$. Stability boundary=0.02.

on wide-pedestal QH-mode, published in [43]. Running the new arbitrary n ELITE for this case on the experimental point finds all the low n mode numbers are stable. Therefore, calculated current density was again increased to see if including the low n modes in this case moved the stability boundary. The results are shown in figure 5.12.

Figure 5.12 shows, that when current is increased by 30%, this destabilises all of low n modes across the stability boundary. This was the most stable time in the discharge, with respect to the amount of extra current density needed to destabilise the modes. Again the first modes to be destabilised are $3 < n < 5$. The inclusion of these low n modes in this time in the discharge again does not significantly alter the position of the stability boundary. The mode structures of these destabilised modes again were also studied. An example for $n = 4$ with 30% extra current density is shown in figure 5.13, which is also a much broader/global mode, and characteristically similar to the previous figure for $n = 4$ with 20% extra current density for time 2650 ms shown in figure 5.10.

5.4.4 Wide-pedestal QH-mode phase: time 3500ms

The forth time slice is at 3500ms, shown in figure 5.2 as purple. This is also in the middle of the wide-pedestal phase at zero torque, but is during the power ramp and $\beta_N = 1.85$. The broadband fluctuation amplitude is increasing. The $J - \alpha$ diagram for this time is shown in figure 5.14, which shows that the experimental point also lies below the kink/peeling boundary. This again agrees with previous work [43]. However, note that this is the closest of any of the wide-pedestal times in the discharge.

Running the new arbitrary n ELITE for this case on the experimental point finds that all the lower n mode numbers are stable, so calculated current density

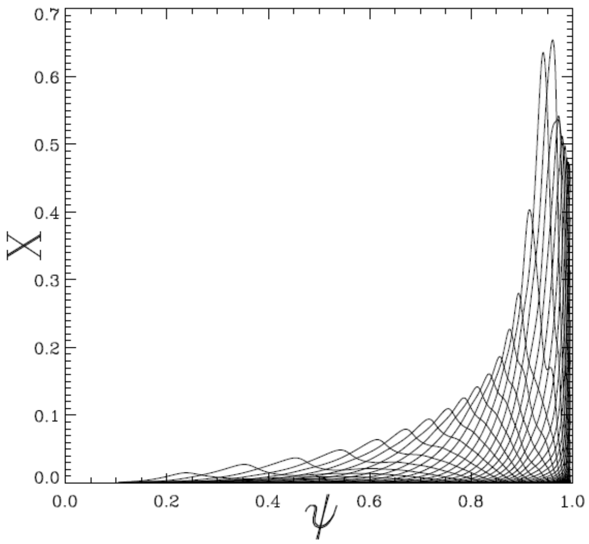

Figure 5.10: $n = 4$ mode structure for time 2650ms and 20% additional current density which shows that the mode is a broad/global mode

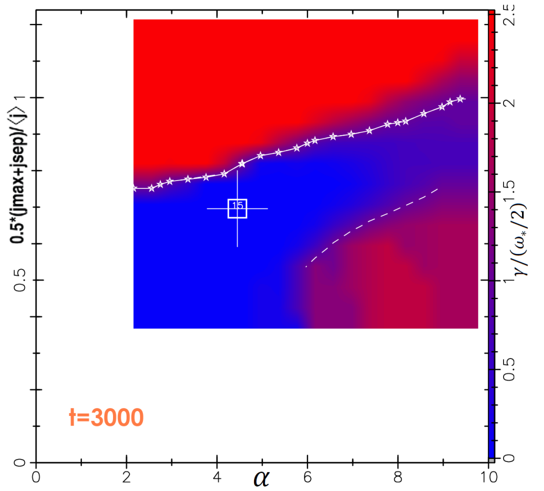

Figure 5.11: $J - \alpha$ diagram for time=3000ms with $5 < n < 25$ which indicates that the experimental point, which is the white box with error bars, lies below the kink/peeling boundary which is taken to be $\gamma/\omega_A = 0.02$ and is indicated by the white line. Blue region is stable and the red region is unstable.

was increased. The results are given in figure 5.15, which show that when current is increased by 10%, this destabilises all of low n modes across the stability boundary. This was least stable of the wide-pedestal phases in the discharge, with respect to the amount of extra current density needed to destabilise the modes. The first modes to be destabilised are $3 < n < 4$. The inclusion of these low n modes in this time in the discharge again does not significantly alter the position of the stability boundary: figure 5.14 shows that it is below, but close to the stability boundary. The mode structures of these destabilised modes again were also studied, and the $n = 4$ mode with 10% extra current density is shown in figure 5.13 as an example. Again this is a much broader/global mode, which is characteristically similar to the two previous figures for $n = 4$ with the additional current density.

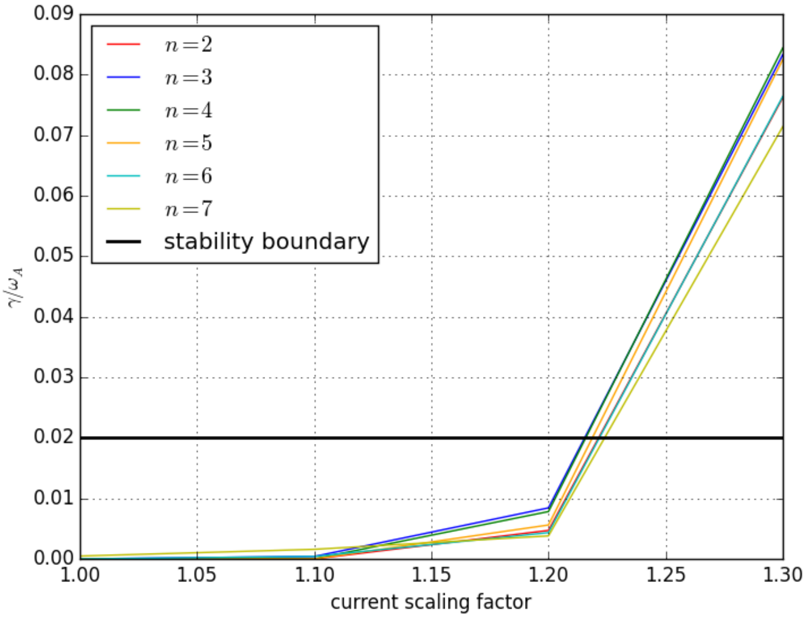

Figure 5.12: Time 3000ms growth rate (γ/ω_A) vs. current scaling factor, where 1=100% and 1.1=110%, for $n = 2-7$. Stability boundary=0.02.

5.4.5 Wide-pedestal QH-mode phase: time 3985ms

The final time in the shot to be analysed is at 3985ms, shown in figure 5.2 as blue. This is at the end of the power and density ramp, at zero torque and $\beta_N = 2.0$, just before the ELMs return. The $J-\alpha$ diagram for this time is given in figure 5.17, which shows the experimental point again lies below the kink/peeling boundary, agreeing with previous work [43]. However, note at this time in the discharge that this is perhaps an unexpected result. This time is just before the ELMs return, so it could be expected that for the experimental point would move towards the stability boundary, as peeling-ballooning modes are widely thought to be the cause of the onset of ELMs. As stated in section 5.2, it was speculated before this analysis that the increase in pedestal width was perhaps destabilising a mode of $n < 5$. This is due to the observation of an $n = 1$ or $n = 2$ MHD mode, more likely $n = 2$, seen on the magnetics data less than 100μs before the return of ELMs.

Therefore a final scan of increasing current density was performed to explore the sensitivity. This was undertaken using a finer current scaling scan, as this time in the discharge was of particular importance for improving the understanding of wide-pedestal QH-mode. The result can be seen in figure 5.18, which shows as in all the other wide-pedestal phases, the low n modes are destabilised first. The first mode destabilised is $n = 3$, just at the stability boundary at 20% . Adding an additional 1% current causes the $n = 2$ and $n = 4$ modes, along with $n = 3$ to cross the stability boundary. An additional 1% current then destabilises the $n = 5$ mode. Hence there is no significant change in the stability boundary here either and no significantly more unstable low n mode is observed to explain the return of ELMs here. Unfortunately, the code does not seem to detect the ELM precursor seen on the magnetics. The $n = 3$

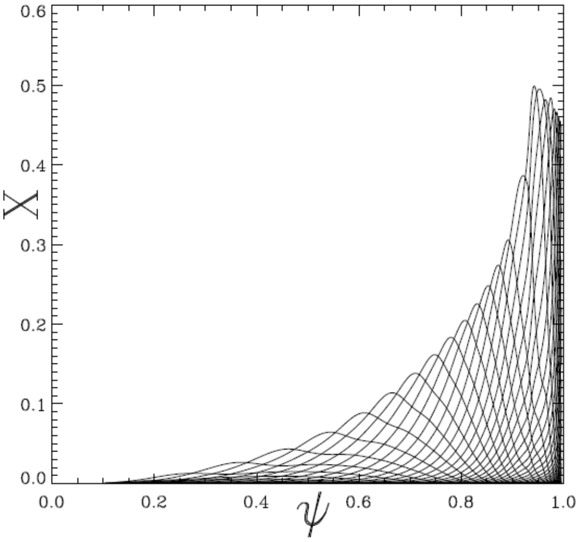

Figure 5.13: n = 4 mode structure for time 3000ms and 30% additional current density which shows that the mode is a broad/global mode.

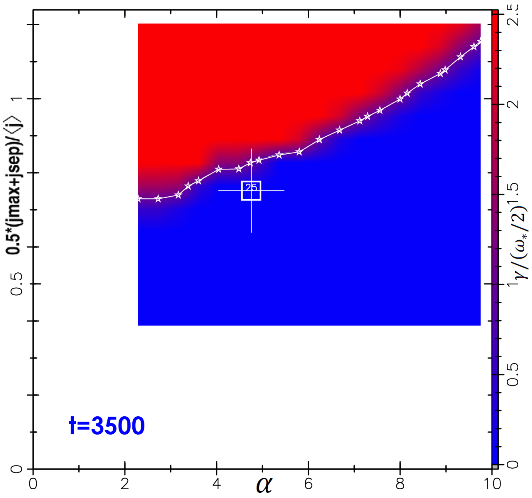

Figure 5.14: $J - \alpha$ diagram for time=3500ms with $5 < n < 25$ which indicates that the experimental point, which is the white box with error bars, lies below the kink/peeling boundary which is taken to be $\gamma/\omega_A = 0.02$ and is indicated by the white line. Blue region is stable and the red region is unstable.

mode for 20% additional current density is shown in figure 5.19. This mode is a much broader global mode, consistent with all the other wide-pedestal phases.

Therefore, there is nothing significantly different about this time in the discharge compared to the other three wide-pedestal phases. All four phases find that the low n modes are destabilised first, but this does not significantly alter the stability boundary in any case. Ideal MHD is therefore unable to explain the return of ELMs in this case. It is important to note that there is still flow shear present in this time slice in the discharge, even in the absence of external applied torque from the NBI [134]. In previous EHO QH-mode studies, including the recently published [133], flow shear is found to significantly destabilise low n modes. So it could be that with the inclusion of flow shear into the ideal MHD model in wide-pedestal QH-mode is crucial for assessing the stability of the experimental point. Further shots have been done in January 2016 [134], and more investigation of the return of ELMs in wide-pedestal QH-mode

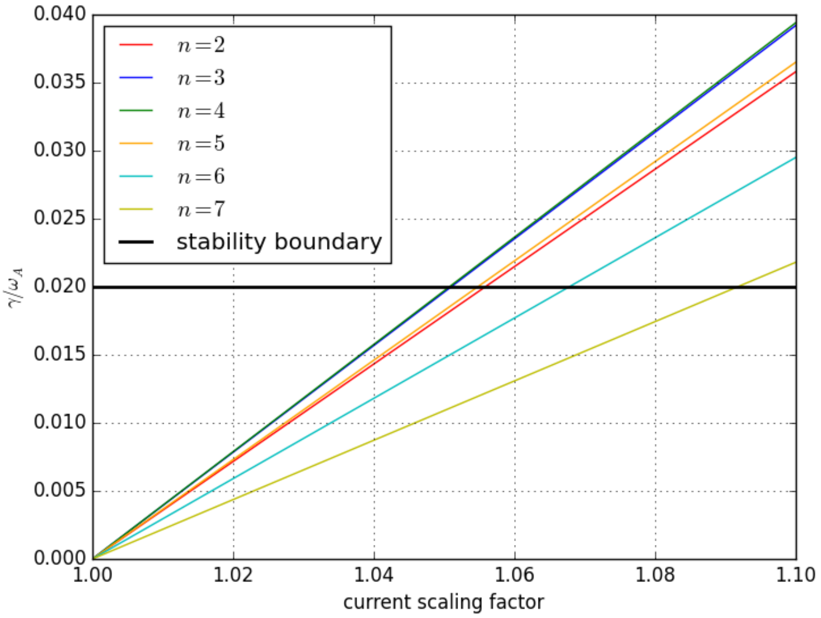

Figure 5.15: Time 3500ms growth rate (γ/ω_A) vs. current scaling factor, where 1=100% and 1.1=110%, for $n = 2 - 7$. Stability boundary=0.02.

is planned at DIII-D. Therefore, more information is needed before conclusions can be made regarding the peeling-ballooning stability in cases where the ELMs return. It is reassuring that the new arbitrary n ELITE reproduces previous results on EHO QH-mode, and is consistent with all findings in the new wide-pedestal QH-mode.

5.4.6 Kinetic ballooning mode constraint

As stated in [43], the increase in pedestal pressure height and width in wide-pedestal QH-mode can be illustrated by considering the kinetic ballooning mode (KBM) and peeling-ballooning (PB) mode constraints that are the foundation the EPED model [27, 111], which was introduced in section 2.6. An illustration of this model modified for wide-pedestal QH-mode can be seen in figure 5.20. In wide-pedestal QH-mode there is enhanced edge transport provided by the broadband MHD. This moves the KBM boundary to allow for wider pedestals for a given pedestal pressure height, illustrated in figure 5.20 as the red line. Therefore the intersection point of the KBM boundary with the PB boundary occurs at higher pressure, allowing for a greater pressure pedestal height and width before instability occurs [43]. Using this model therefore explains that despite an initial premise that the increased transport given by the broadband fluctuations would degrade the pedestal, it actually allows for improved stability [43]. It is therefore likely that the KBM does not limit the pressure gradient in wide-pedestal QH-mode, and suggests a route to creating improved pedestal pressures in tokamaks [135].

To investigate whether the KBM is limiting the pressure pedestal in both the EHO QH-mode (2200ms) and the wide-pedestal QH-mode (3985ms), the $n = \infty$ ballooning limit was calculated. This has previously been shown to be a good proxy for the KBM,

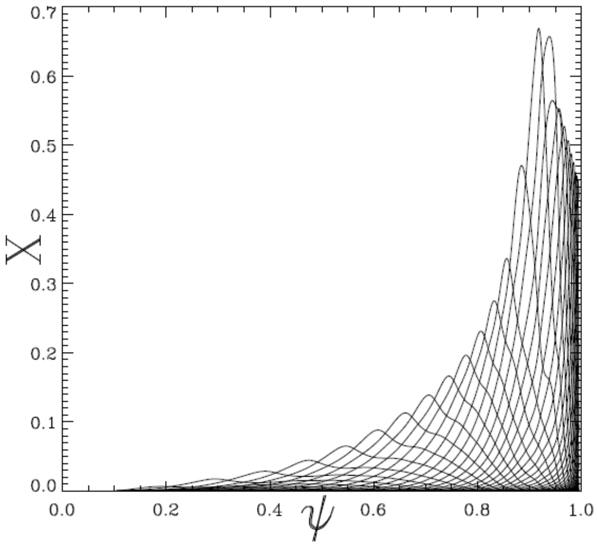

Figure 5.16: n = 4 mode structure for time 3500ms and 10% additional current density which shows that the mode is a broad/global mode.

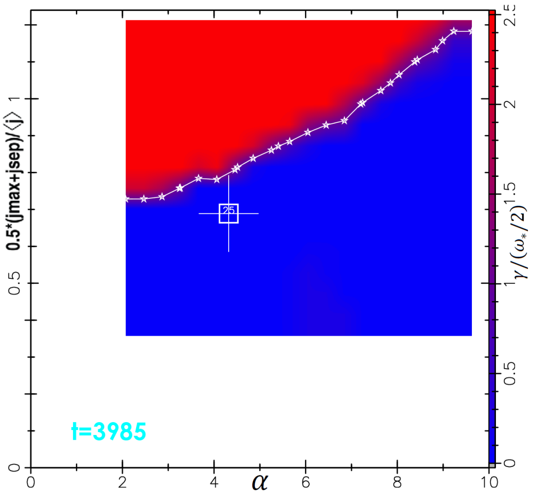

Figure 5.17: $J - \alpha$ diagram for time=3985ms with $5 < n < 40$ which indicates that the experimental point, which is the white box with error bars, lies below the kink/peeling boundary which is taken to be $\gamma/\omega_A = 0.02$ and is indicated by the white line. Blue region is stable and the red region is unstable.

as discussed in section 2.6 [71, 107]. The result for 2200ms is shown in figure 5.21. This figure 5.21 shows that there is second stability access, which was introduced in section 2.4.1. This can be seen here because the $n = \infty$ ballooning limit is significantly higher than the equilibrium α in the peaked pedestal region, while the edge of the pedestal appears to be at broadly contained at the bottom of the pedestal, approximately ψ = 0.99, and at the top of the pedestal at approximately ψ = 0.94. This contrasts with figure 2.15, which has the peak in α constrained by the $n = \infty$ ballooning limit. The pressure pedestal is far below the $n = \infty$ ballooning limit, and therefore from this result it appears that the pressure gradient is not constrained. However, it should be noted that the pedestal may still be constrained, just not by the KBM.

The limit has also been calculated for wide-pedestal QH-mode at 3985ms. The result is shown in figure 5.22. Note the different scales of the x-axis in the two figures. As figure 5.22 shows the wide-pedestal QH-mode, clearly has a wider pedestal. This

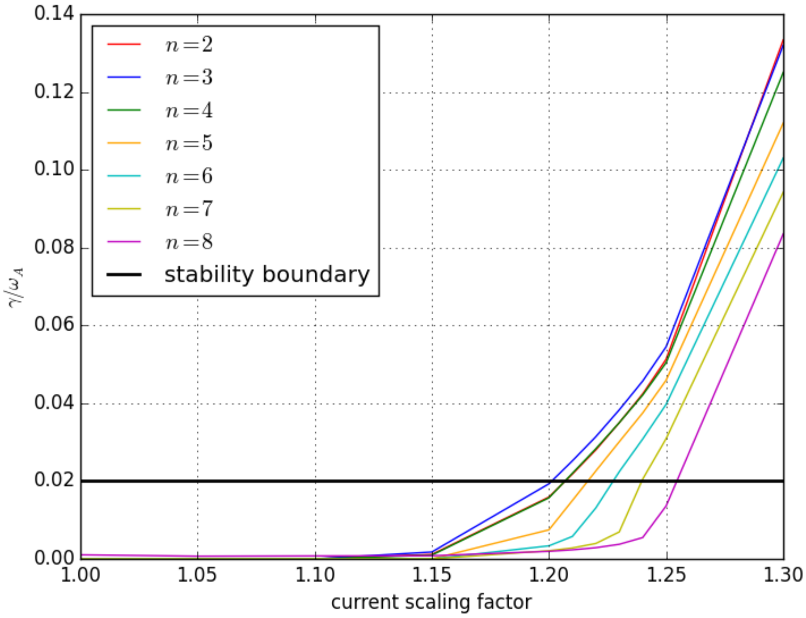

Figure 5.18: Time 3985 growth rate (γ/ω_A) vs. current scaling factor, where 1=100% and 1.1=110%, for $n = 2-8$. Stability boundary=0.02.

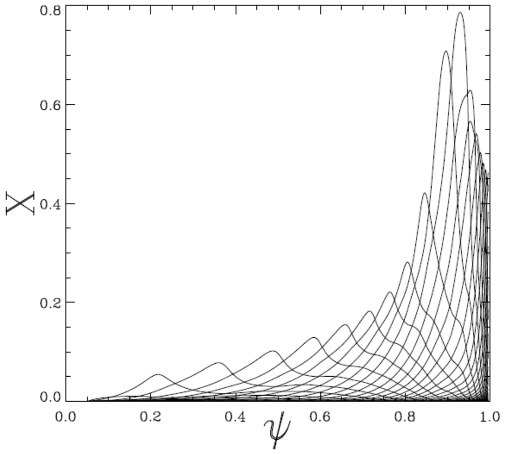

Figure 5.19: $n = 3$ mode structure for time 3985ms and 20% additional current density which shows that the mode is a broad/global mode.

also similarly has clear second stability access, where the $n = \infty$ ballooning limit is far above the pressure gradient, and therefore it appears that the pressure gradient is not constrained by the KBM. This agrees with the picture for the pedestal in wide-pedestal QH-mode published in [43], which states the enhanced edge transport allows for a shift of the KBM stability curve to allow a higher pedestal for a given width. Note that the additional transport from the broadband MHD is shifting the constraint here, and not a change in the KBM itself.

However, what also needs to be considered is the lack of inclusion of the kink term in this model: QH-mode phenomena is generally kink/peeling dominated. It has been shown in previous work that the inclusion of the kink term tends to restrict access to second stability [86], so this could also be that this access has been closed off, and this could explain why in both figures the peak in the pressure gradient is significantly

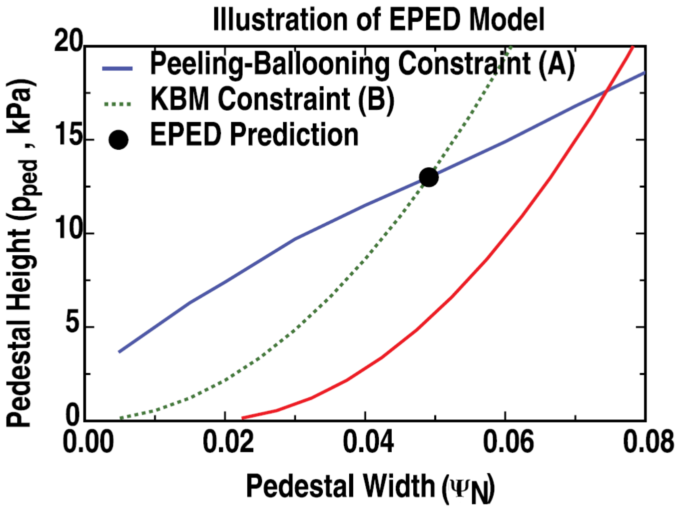

Figure 5.20: Standard EPED model illustration with EPED prediction for pedestal height and width occurring at the intersection of the peeling-ballooning and the kinetic ballooning constraints. The red curve shows what would happen if an additional source of edge transport in the pedestal, such as in wide-pedestal QH-mode, increases the pedestal width for a given pressure. Reproduced from [43].

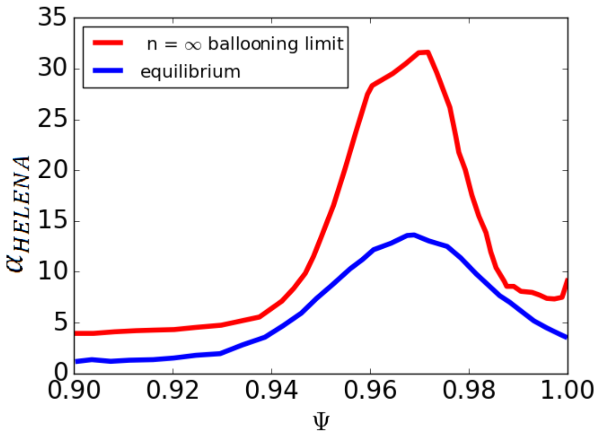

Figure 5.21: $n = \infty$ ballooning limit vs. normalised pressure gradient for 163520 2200ms, where blue is the equilibrium normalised pressure gradient in the pedestal region and red is the $n = \infty$ ballooning limit which shows second stability access for the pedestal in EHO QH-mode.

below the $n = \infty$ ballooning limit: the pedestal width is defined by the $n = \infty$ ballooning limit, but the peak in the pressure gradients for both pedestals is significantly lower than the $n = \infty$ ballooning limit. Therefore, without the inclusion of the kink term in the KBM model, which would require gyro-kinetics, it cannot be known exactly how constrained the pressure gradient is in these cases. These results do agree with previous research which shows that the wide-pedestal QH-mode allows for broader pedestals. It also shows that therefore pure ballooning-type modes are unlikely to be the cause of the return of ELMs here, using $n = \infty$ ballooning as an approximation for very high ballooning modes, which agrees with the findings in the $J - \alpha$ diagrams.

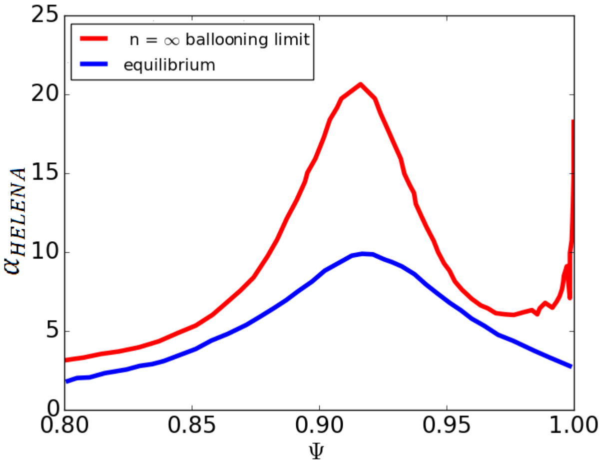

Figure 5.22: $n = \infty$ ballooning limit vs. normalised pressure gradient for 163520 3985ms, where blue is the equilibrium normalised pressure gradient in the pedestal region and red is the $n = \infty$ ballooning limit which shows second stability access for the pedestal in wide-pedestal QH-mode.

5.5 Conclusions and further work

To conclude an analysis of DIII-D shot 163520 has also been performed, which allows comparison between the standard EHO and wide-pedestal regimes. Ideal MHD has been used to analyse the newly discovered wide-pedestal QH-mode, which is not yet fully understood. It has allowed the new arbitrary n ELITE to be used for experimental pedestal stability studies, and further verification of the code to be obtained. This analysis has also that shown in the better but still not fully understood EHO QH-mode that the new arbitrary n ELITE produces results that agree with previous studies [60, 131, 133].

In the EHO QH-mode phase, at 2200ms, modes from $n = 2-10$ were studied and all these modes were found to be unstable. The peak in the growth rate was found to be $n = 8$. However, this shot is at high torque. It has been recently shown in depth in [133] that both the low n modes are destabilised and the intermediate n modes are stabilised by flow shear in a shot with similar plasma parameters. So it is expected that this effect would also be seen here and enhance the low n modes. All the low n modes are kink/peeling like in structure, as illustrated by $n = 2$ in figure 5.6. This is consistent with the observation of coherent EHO at this time in the discharge. Using the new δW diagnostic in ELITE confirms that the drive at 2200ms is predominately kink/peeling, which also agrees with previous findings [60, 131]. Looking at the $n = \infty$ ballooning limit as a proxy for the KBM at this time shows that the pedestal is likely not constrained by the KBM as there is clear second stability access. However, note that as has been shown in this thesis, the high n kink/peeling terms are still significant and the kink term is known to restrict access to second stability [86]. This could be important for an accurate model of the KBM in this case, and further gyro-kinetic analysis would be needed to fully determine the KBM stability in this discharge.

All the wide-pedestal QH mode phases at: 2650ms just after the transition, 3000ms at zero torque, 3500ms during the power ramp and 3985ms at the end of the power ramp just before ELMs return are shown to be stable. This agrees with the $J - \alpha$ diagrams for these times in the discharge. When calculated current density is increased to explore the sensitivity of the stability boundary all the times have low n modes destabilised first. However, this does not significantly alter the stability boundary which was calculated with intermediate-high n modes. All the low n modes, once current is added, interestingly are very different to the low n mode structures seen in the EHO QH-mode. Flow shear in the wide pedestal phase is still significant even without any torque from the NBI system. Therefore the role of flow shear could be important in accurately determining the stability in this phase, and may move the stability boundary. The time 3985ms just before the ELMs return has second stability access when looking at the $n = \infty$ ballooning limit at this time shows that the pedestal is likely not constrained by the KBM, which is consistent with the picture of wide-pedestal QH-mode, but equally does not explain the ELMs returning and the low $n = 1$ or $n = 2$ mode seen on the magnetics at this time.

There is clearly further work to be done on this topic. This study should be extended to many more wide-pedestal QH-mode shots using arbitrary n ELITE so that more information can be used to draw significant conclusions about the PB stability as ELMs return. From a scientific perspective is it important to determine the mechanism that leads to the return of ELMs in wide-pedestal QH-mode. This needs to be both a computational and experimental endeavour, and more experiments on DIII-D are planned [134]. Including further work with the arbitrary n ELITE to study more discharges, there are more efforts that need to be undertaken on the code itself. The first is to include an on-axis boundary condition and wall physics for wall and global modes, which is of integral importance for accurately modelling $n = 1$ modes in particular. In addition to this, a new formalism for ELITE is planned which incorporates flow shear into arbitrary n ELITE, since flow shear has been found to be destabilising to low n modes in QH-mode [133]. It would also be of merit to include the arbitrary n ELITE into EPED to help resolve the kink/peeling boundary where low n modes dominate.

Chapter 6

Evolution of the pedestal during the ELM cycle in JET-ILW plasmas: comparisons with the EPED model

6.1 Introduction and motivation

Since the installation of the JET-ILW, replacing carbon (JET-C) with tungsten (W) and beryllium (Be), a decrease in the pedestal confinement has been observed primarily due to a drop in the pedestal temperature [96, 145, 146]. There are two reasons for this: firstly, the wall materials affect the plasma parameters through wall recycling and plasma composition [146]. Secondly, as the divertor is now tungsten, JET must operate with increased D_2 gas rates in order to avoid impurity influxes from it [145] and protect plasma first wall materials [96]. Additionally, the ability to achieve high performance H-mode plasmas at high triangularity has not been recovered since the installation of the JET-ILW. The temperature pedestal height that were seen with the JET-C wall can be partially recovered in the JET-ILW using nitrogen seeding, initially used for divertor heat load mitigation [96, 145, 147]. However, this reduction in performance and of H-mode operation space available for good ELMy H-mode confinement [96] has serious consequences for both planned JET D-T experiments and ITER, which will have the same configuration, so understanding the cause is a priority.

Similarly to JET, ASDEX Upgrade has replaced the previous carbon wall and had a metal tungsten (W) wall installed [142]. Studies of ASDEX Upgrade have shown at low triangularity there is no significant differences in plasma performance without gas puffing between the two wall materials [142]. Other studies of ASDEX Upgrade have shown that during nitrogen seeding, which improves the confinement as in the JET-ILW, the increased pressure gradient also increases the current density as expected. However, this occurs concurrently with the increased Z_{eff} in the pedestal acting to reduce the current density [136].

The results for pedestal stability in the JET-ILW have so far focussed on the time immediately before the ELM, known as the pre-ELM phase of the ELM cycle

[96, 145]. These studies have shown that instead of the pre-ELM pedestal being close to the peeling-ballooning (PB) boundary as it was in the JET-C experiments with type-I ELMy H-mode plasmas, many of the new pedestals, which are at low beta (β_N) and high gas rate, appear to be deep in the stable region of PB stability space [96] due to the lower pedestal temperature.

This chapter discusses the development of analysis that explores the full ELM cycle, looking specifically at the inter-ELM evolution. The full ELM cycle evolution is compared to the kinetic ballooning mode (KBM) and PB mode criteria, the EPED framework, and the dynamics of the EPED model. The motivation of this work was to develop an improved understanding of the physics that influences the evolution of the pedestal in the JET-ILW between the ELMs. This may help identify a route to optimising the pedestal height, and therefore the plasma confinement.

The chapter is laid out as follows: firstly a detailed description and framework of the JET data analysis is discussed, which includes High Resolution Thomson Scattering (HRTS) and profile fitting. Next is the detailed description of stability analysis, including the equilibrium reconstruction process. Next is the development of analysis techniques to study the inter-ELM pedestal evolution, which allows the ELM cycle to be studied and compared to the EPED model framework. An introduction to the dataset is provided and the results are presented with their interpretation. Finally, there is a summary of the chapter and further work is discussed.

6.2 JET equilibrium reconstruction and stability analysis framework

In order to perform stability analysis on any tokamak, an accurate reconstruction of the equilibrium is required. This is a highly complex process, so here an overview of the process is given to provide understanding of both the origin of the analysed data and the limitations. A flow chart of the equilibrium reconstruction procedure is shown in figure 6.1.

6.2.1 Equilibrium reconstruction: production of profiles from HRTS

More detail of each step in figure 6.1 is described here. Firstly, the stationary phase in the pulse is chosen and the timing of the ELMs is selected. The stationary phase is the length of time over which the ELMs in a pulse are chosen to be analysed [148], and is ideally between 1.5 – 2.0 seconds. This requires the consideration of a range of plasma parameters, see reference [148]. The aim of this process is to determine an unvarying phase in the plasma pulse, with a regular ELM frequency [148]. Next the calibrated HRTS diagnostic [149, 150] provides the electron temperature, T_e, and electron density, n_e, profiles in time slices as a function of radius along a line of sight [149].

Figure 6.1: Overview flow chart of JET equilibrium reconstruction procedure

It is worth noting that the timings of the ELMs are determined by considering a threshold intensity of a specific spectral line [148]. In the previous chapter, this was the D_α line, but in the JET-ILW this is not a good signal for ELM traces, especially at high D_2 gas injection, as it detects all the recycling flux [151]. Therefore the intensity of the $Be-II$ spectral line from the inner divertor is used. After the timings of the ELMs have been determined, the ELM cycle is divided into percentage interval windows in the ELM cycle across the multiple ELMs. For example, the standard JET pre-ELM window is the 70-99% interval. A discussion of the chosen intervals for this analysis is in the next section. Next, the T_e and n_e profiles are binned according to which interval in the ELM cycle they fall into [71, 148]. The multiple profiles are then overlaid in a process known as ELM synchronisation [150]. The T_e and n_e profiles in the bin for each ELM interval are then combined to form a composite profile [71, 148], effectively averaging the profiles.

Next, the instrument function is calculated to obtain a reliable estimation of the actual plasma pedestal width [149]. The instrument function is only calculated once and then applied separately to both the T_e and n_e. It includes effects due to the geometrical layout of the laser beam, the collection optics and the orientation of the magnetic flux surfaces in the pedestal [148, 149]. Next, it is necessary to introduce the modified mtanh-function which is used to fit the profiles [107, 148, 152, 153, 154]. This is given by:

$$\mathrm{edge}(r;\vec{a}) = \frac{a_{ped} - a_{sol}}{2} \times \left[\mathrm{mtanh}\left(\frac{a_{etb} - r}{2a_{\Delta}}, a_{slope}\right) + 1\right] + a_{sol} \tag{6.1}$$

where

$$\mathrm{mtanh}(r', a_{slope}) = \left(\frac{(1 + a_{slope}r')\, e^{r'} - e^{-r'}}{e^{r'} + e^{-r'}}\right) \tag{6.2}$$

and a_{ped} is the pedestal height, a_{sol} is the scrape off layer height, a_{etb} is the transport barrier position, a_{Δ} is the transport barrier width and a_{slope} is the core slope [153].

Now the deconvolution process, which uses a forward convolution technique, is as follows [150]. Starting with the n_e profile an initial mtanh is guessed and convolved with the instrument function. The least squares of the forward convolution is then calculated, and an iterative process to find the minimum is undertaken to obtain the best fit and the final mtanh for the n_e profile [148, 149, 153]. The same process is repeated for the T_e profile, which requires weighting by the n_e profile as the number of scattered electrons varies with the density across the scattering volume [148, 150, 153]. This is known as weighted deconvolution [150, 153]. These resulting fits can then be mapped onto other coordinate systems, most likely poloidal flux, as the profiles are still as a function of radius along a line of sight.

6.2.2 Equilibrium reconstruction: the profile tool

The profile fitting tool, which is the yellow box of figure 6.1, takes the deconvolved fit and produces an output file containing the parametrisation of the profiles [155]. This intermediate step is essential for obtaining any successful equilibrium out of HELENA. As indicated in figure 6.1 the profile fitting tool has three functions.

The first function is to smooth the core profiles. The deconvolved fits near the edge are already smooth and therefore do not require any additional smoothing to be used in stability analysis. However, there are often discontinuities or sharp sudden un-physical changes in gradients in the core of either the n_e or T_e profiles. The second function of the profile tool is to create a parametrisation for the core profile, since only the pedestal is parametrised in the previous steps of the profile fitting process [156]. This creates a fully parametrised fit for both the n_e and T_e profiles. This is achieved using 9 parametrisations, p, for each of the full n_e and T_e profiles [155]. The electron pressure, p_e, is also parametrised but not used in the analysis since it is recalculated by HELENA. The formula for the pedestal fit, f, is a type of modified mtanh [154] where ψ is parametrised by $(\psi > p(6))$, are given by;

$$\begin{aligned} f(\psi) &= 0.5\left(p(1) - p(2)\right)\left(\frac{\left(1 + p(3)\psi\right)e^{z} - e^{-z}}{e^{z} - e^{-z}} + 1\right) + p(2) \\ z &= \frac{(p(4) - \psi)}{2p(5)} \end{aligned} \tag{6.3}$$

The formulas for the core fit, f, where $(\psi < p(6))$, are given by:

$$\begin{aligned} f(\psi) &= C\left(\frac{(p(7)\psi + 1 - p(7))}{p(6)^{p(8)}\left(1 + p(8)\right)}\psi^{p(8)+1}\right) + D \\ f(\psi) &= C\left(\frac{\left(\frac{(\frac{2}{3})p(7)\psi}{p(6)^{1.5}} + \frac{1}{2}p(8)\left(\frac{\psi}{p(6)}\right)^{2}\right)}{p(7) + p(8)} + p(9)\left(\frac{\psi}{p(6)} - \frac{1}{2}\left(\frac{\psi}{p(6)}\right)^{2}\right)\right)p(6) + D \end{aligned} \tag{6.4}$$

where the first is used for n_e and the second is used for T_e [156]. This is because the core T_e profile normally has a non-linear form, and requires more complex parametrisation than the density profile, which usually only requires flattening [156]. C and D are calculated to match core and edge values and derivatives at the cut off $(p(6))$ [155], which is specified in the input file. Determining accurate parametrisation fits for the pedestal is the most important part of the parametrisation, as the pedestal is the dominant determination of edge stability. The third function is to shift the radial position of the profiles to make sure that the separatrix temperature is physically sensible, since there is no measurement of separatrix position [156]. This is achieved by shifting the profile position radially so that the separatrix temperature is $T_{e,sep} = 100eV$. Alternatively, the two point model [71, 157] is implemented to calculate the separatrix temperature $T_{e,sep}$, matching the separatrix temperature with the two-point power balance model, given by:

$$T_{e,sep}(eV) = \left(T_{div}^{\frac{7}{2}} + \frac{7}{2}\left(P_{heat} - P_{rad}\right)\frac{L_{\parallel}}{\lambda_q 2\pi R_{OMP} k_0}\right)^{\frac{2}{7}} \tag{6.5}$$

where T_{div} is the temperature (in eV) at the divertor, P_{heat} is the total heating power (in MW), $L_{\parallel} = \pi R_0 q_{95}$ is the parallel connection length (in m), λ_q is the radial power decay length (in m), R_{OMP} is the major radius (in m) of the outer mid-plane, and k_0 is the heat conduction [71, 157].

An example fit from the profile tool for the 60-80% ELM interval of pulse 87346 is shown in figure 6.2. This figure illustrates the importance of re-fitting the outputs from the deconvolution in order to smooth the T_e and n_e profile fit functions, shown in (a) and (b) respectively. Looking at figure 6.2 (a) there is a significant rise of the T_e profile in the core, which would immediately crash the HELENA equilibrium code. Additionally, in the n_e profile there are sharp un-physical changes in gradient, which

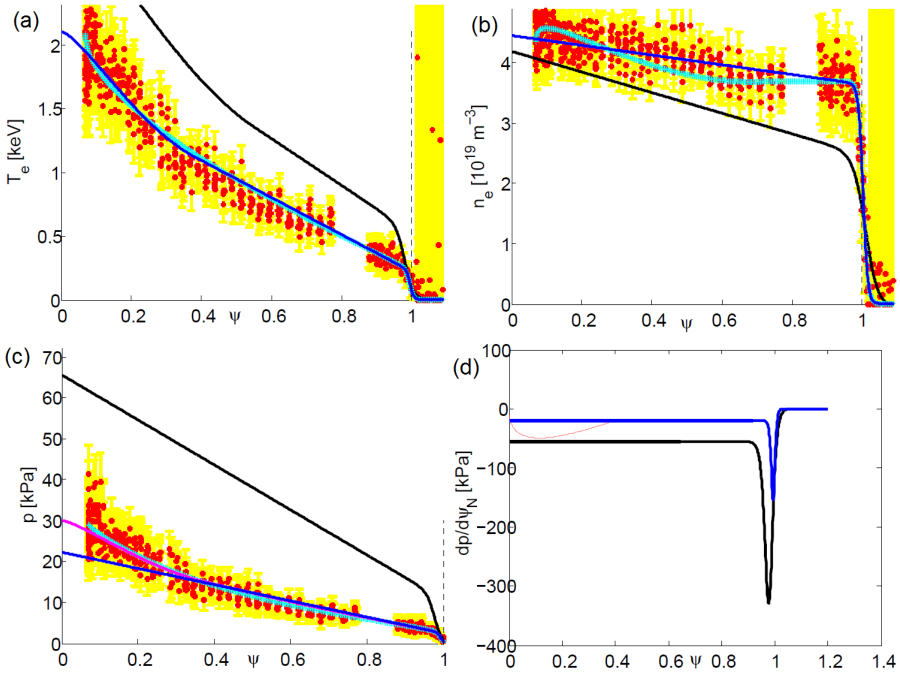

Figure 6.2: Example output of the profile tool for the 60-80% interval of pulse 87346 where (a) is the T_e profile fit, (b) is the n_e profile fit, (c) is the p_e profile fit and (d) is the pressure gradient, $p_e{}'$ fit. In the diagrams: red dots are the data with yellow error bars, cyan is the deconvolved fit data from initial reconstruction, black is the initial guess for the parametrisations by profile tool for the fit and blue is the final parametrisation fit. The final electron pressure p_e profile fit in (c) is in pink as it does not use its parametrisation fit (blue and black) and is instead calculated from combining the n_e and T_e profiles. In (d) red is the calculated p' corresponding to the derivative of the pink curve in (c)

would also be highly problematic. Details of how to make a good physical fit are in reference [155].

6.2.3 Equilibrium reconstruction for full JET equilibrium with HELENA

This subsection details the final part of the equilibrium reconstruction, shown as the last 5 steps in figure 6.1. This is accomplished using the fixed boundary equilibrium code HELENA, described in section 2.2. This is run as part of a script, as described in the next subsection. HELENA reads the fully parametrised fits from the profile tool for n_e and T_e, then obtains the plasma boundary and other plasma parameters, such as the toroidal magnetic field, B_t (in T), and the total plasma current, I_p (in MA), at the specified time in the pulse that the fit was performed from EFIT [71]. Next the formula for p_e is used, and a number of assumptions are made, which include the assumption that beryllium, $Z = 4$, is the main impurity:

$$\begin{aligned}
&T_i = T_e \\
&Z_{eff} = const \\
&n_i = n_e((5 - Z_{eff})/4) \\
&p_e = 1.6022 n_e T_e \\
&p = p_e(9 - Z_{eff})/4
\end{aligned} \tag{6.6}$$

where Z_{eff} is the average effective atomic charge. Next HELENA calculates the current profile, which is assumed to be a combination of the bootstrap current density, J_{BS}, and an inductively driven current density, J_I. J_I is assumed to be a relaxed neoclassical current profile [71] and its profile shape is assumed to be the same as the conductivity profile, which is calculated using neoclassical resistivity [156]. The amplitude of this current is then adjusted so that the total current matches with the input value. In the absence of current measurements, which is the case for this analysis, J_{BS} can either be calculated using the Sauter model, which is detailed in [32, 33], or the Koh/Chang model, which is detailed in [34]. This analysis uses the Koh/Chang model because this new simple modification to the Sauter formula, brings the results into better agreement with the edge kinetic simulation results [34]. Another way to calculate the J_{BS} is to use the NEO code, detailed in [158]. Once the rest of the equilibrium reconstruction is finalised, α, the normalised pressure gradient, is calculated. This is the end of the equilibrium reconstruction and a full JET equilibrium is obtained.

6.2.4 Stability analysis techniques: 2D and self-consistent stability analysis scans with the HELENA and ELITE codes

The JET stability analysis process to determine PB stability is described in this section. This includes the HELENA calculations as detailed in section 6.2.4. Figure 6.3 shows an overview flowchart of the process, where the operational point (OP) is the experimental point for which equilibrium reconstruction is undertaken.

After the profile fits have been produced using the profile tool, as described in 6.2.2, next a script is used to explore the finite n PB stability. The script uses two codes: firstly, the fixed boundary equilibrium solver HELENA, described in section 2.2, is used to generate equilibria and finish the equilibrium construction process as described in subsection 6.2.3. Next ELITE is used to calculate the stability of each equilibrium. Note that JET stability analysis is also set up to use the MISHKA code [159], but this analysis exclusively uses the ELITE code. The threshold for stability is taken to be $\gamma/\omega_A = 0.03$, because it has been found to be a suitable compromise between eliminating un-physical modes with very low growth rates while still keeping the growing physical PB modes. The $n = \infty$ ballooning as a proxy for KBM stability is discussed in later section 6.4.

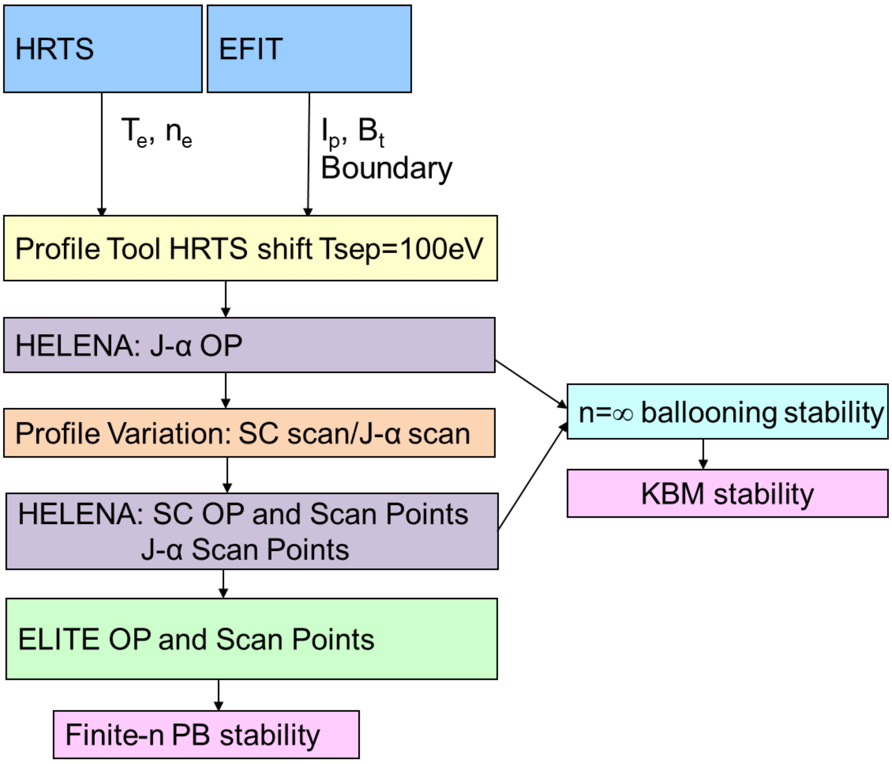

Figure 6.3: Flow chart of JET stability analysis, from reconstruction to result; where OP is the operational/experimental point, $J-\alpha$ refers to a 2D parameter scan in current density J_ϕ and normalised pressure gradient, α, space. SC refers to a self-consistent scan along the self-consistent path in $J-\alpha$ space. The blue boxes, profile tool yellow box and the HELENA boxes form part of the equilibrium reconstruction.

The exact order of the calculations depend on whether a 2D or self-consistent scan in $J-\alpha$ space is being undertaken. Firstly the production of a 2D scan will be described, which is given as $J-\alpha$ in figure 6.3. This is because these scans produce the characteristic 2D $J-\alpha$ diagrams, which are a visualisation of where the OP sits in $J-\alpha$ space, also seen in the previous chapter. An illustration of the output of a 2D $J-\alpha$ diagram can be seen in figure 6.4, where the y-axis is the maximum edge current density, J, and the x-axis is the maximum normalised pressure gradient, α. The arrows in figure 6.4 represent how J_ϕ and α are varied from the OP, while blue indicates the stable region, and red the unstable region. The boundary is between the two regions as is taken at the threshold for stability, $\gamma/\omega_A = 0.03$. In a 2D scan the procedure is as follows:

- Input files for all the ELITE runs for different toroidal mode numbers, n, are created.
- A HELENA input file for the OP is created.
- HELENA is run to calculate the equilibrium of the OP.
- ELITE is launched for the OP.
- Using the HELENA run for the OP, profiles are varied not self-consistently so that the variation of J and α creates a 2D map of parameter space. This produces

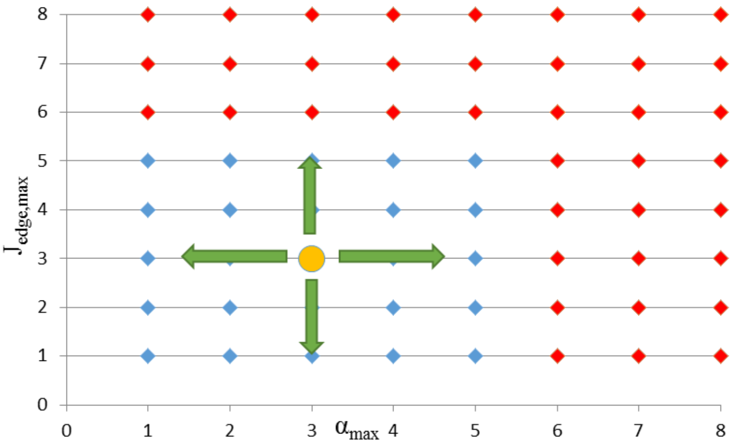

Figure 6.4: Illustration of a 2D $J - \alpha$ scan where the y-axis is the maximum edge current density, J, and the x-axis is the maximum normalised pressure gradient, α. The yellow circle is the operational point (OP), blue diamonds are scan points stable to PB modes, and red diamonds are scan points unstable to PB modes. The arrows represent how J and α are varied, not self-consistently, from the OP to produce a 2D map of parameter space. The threshold for stability is taken to be $\gamma/\omega_A = 0.03$.

HELENA inputs for all the scan points. The OP has a profiles of p' and j_ϕ. These are multiplied by a function: $1 + Ce^{-\left(\frac{(\psi - pos)}{width}\right)^2}$ where: C is the multiplier that changes from point to point, *pos* and *width* are given in the input file and should match with the position of the maximum pressure gradient and the width of the pedestal.

- Input files for HELENA for all the profiles are created.
- HELENA is run on all the scan points.
- ELITE is run on all the scan points.
- Scan is finished and results are then processed into an output file.

The output file contains the scan, the equilibrium parameters for all the points, the stability parameters from ELITE and the most unstable n at each point. It also contains the input parameters and the n numbers used in the run [155]. An example real output of a 2D scan is shown in figure 6.5, ignoring the green arrow.

A self-consistent scan is a procedure by which α is raised using either a change in n_e or T_e, in this analysis T_e was used, and for the new value of α the bootstrap current is then self-consistently re-calculated. The total current is kept fixed so this leads to a re-distribution of current, as described in section 5.3. The core pressure is kept constant for JET [156]. This is done for different values, which produces a self-consistent path which the OP would travel along if J and α were raised. An illustration of a self-consistent scan can be seen in figure 6.6. This path, consisting of the individually calculated points, is shown in blue. Typically the parameters start at the OP and then increase to calculate the self-consistent distance to the stability boundary [155], but this is not always the case. The production of a self-consistent scan is shown in figure 6.3 as SC, and the procedure is as follows:

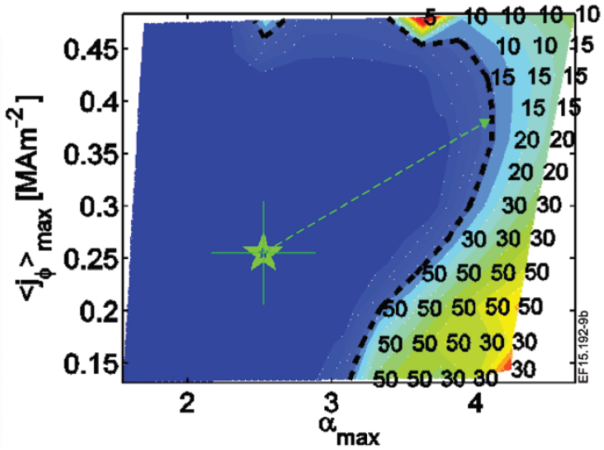

Figure 6.5: $J-\alpha$ diagram for pulse 87341 which shows the experimental point (OP) as the green star, and the 2D scan as the background. The y-axis is the maximum edge current density, $J_{edge,max}$, and the x-axis is the maximum normalised pressure gradient, α_{max}. The blue region is the stable region, where the OP lies, and the stability boundary (black dashes) is taken to be $\gamma/\omega_A = 0.03$. In the unstable region, the colours represent how unstable the most unstable mode number n is, and the most unstable n at that point is illustrated by the number. The green arrow is from the self-consistent scan and shows the distance of the OP to the stability boundary. Reproduced from [96].

- Input files for all the ELITE runs for different toroidal mode numbers, n, are created.
- Self-consistent profile variation is undertaken producing inputs for each individual points in the path. As this is self-consistent the OP equilibrium is not varied and everything is re-calculated at each point self-consistently.
- Next the HELENA input files are created for both the OP and the scan points.
- HELENA is run for the OP and the scan points.
- ELITE is run on the OP and the scan points.
- Scan is finished and results are then processed into an output file.

An example output of a self-consistent scan is illustrated in figure 6.6 as the green arrow, showing the self-consistent path. An experimental self-consistent calculation is shown in figure 6.5, also as the green arrow.

6.3 Development of analysis technique for studying the inter-ELM evolution

6.3.1 EPED model for JET pedestals and current understanding of JET pedestal dynamics

The development of this analysis begins with the EPED model [27, 111], introduced in section 2.6. The EPED model has been shown to successfully reproduce the experimental pedestal height on JET [111]. The theoretical applicability of EPED model to

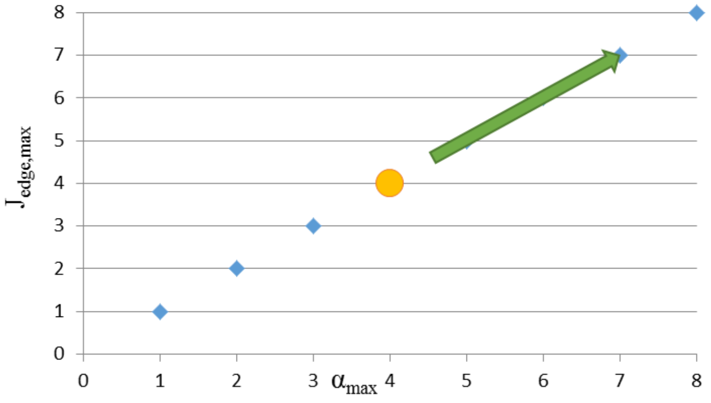

Figure 6.6: Illustration of a self-consistent $J - \alpha$ scan where the y-axis is the edge current density, $J_{edge,max}$, and the x-axis is the maximum normalised pressure gradient, α_{max}. The yellow circle is the operational point (OP), and the blue diamonds are the self-consistently calculated points forming the path. The arrow shows the direction of the calculation, as α and J are raised.

JET has been shown in [71]. Using the KBM and PB constraints on the JET pedestal has shown to be accurate to within ±20% [111]. However, the evolution of the JET pedestal has been shown to be different than the other tokamaks, such as MAST. In a study on JET-C, the pedestal has been shown to narrow [57, 148], and there is a difference in the pedestal trends of height with density [57]. An illustration of this is shown for the p_e pedestal in JET-C pulse 79498 in figure 6.7.

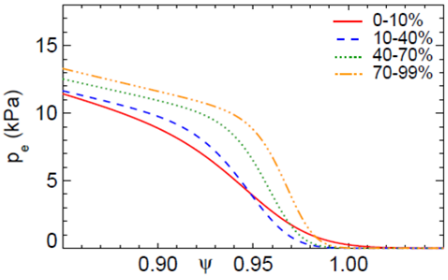

Figure 6.7: Evolution of the JET-C p_e pedestal in pulse 79498 through the ELM cycle. Reproduced from [57, 148].

In the new JET-ILW the PB boundary is most commonly not reached at the ELM onset in high D_2 gas fuelling/injection rate plasmas [96]. Furthermore, in the JET-ILW the pedestal is often observed to narrow between ELMs as the pedestal height increases. Both of these observations in JET-ILW experiments are seemingly inconsistent with the EPED model paradigm. Therefore, the aim of this research was to develop an improved understanding of the physics underpinning the evolution of the pedestal in JET-ILW plasmas: potentially identifying ways of improving the pedestal height in JET-ILW, and therefore ways to optimise confinement.

Recent studies of ASDEX Upgrade pedestals [143] have shown that inter-ELM pedestal recovery studied with the ideal PB limit show that the stability boundary moves closer to the operational point (OP) as the pedestal becomes wider. This would be expected from the EPED model, as described in section 2.6. However, these ASDEX

Upgrade studies have also found that the final ELM trigger condition in some cases cannot be determined by ideal PB MHD stability as the pre-ELM pressure gradient was found to be 30% lower than the PB boundary [143]. This suggests that this is not just a phenomenon seen in JET-ILW plasmas.

6.3.2 Discussion of ELM cycle windows

This subsection details the process by which the ELM cycle windows for the HRTS data were chosen, allowing the inter-ELM pedestal evolution to be assessed. Once the timings of the ELMs has been determined, the ELM cycle can then be divided into percentage interval windows in the ELM cycle. An example, which shows the bins which were chosen for this analysis is shown in figure 6.8.

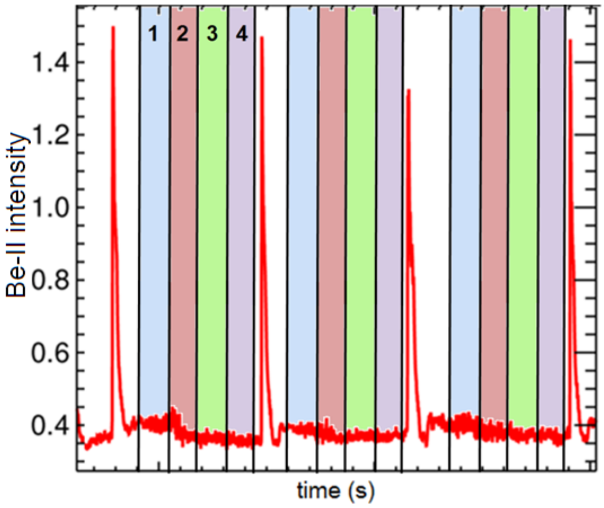

Figure 6.8: ELM interval bins 1=20-40%, 2=40-60%, 3=60-80% and 4=80-99% shown on part of the $Be-II$ emission trace for JET-ILW pulse 84795.

The ELM cycle is divided into four phases: 20-40%, 40-60%, 60-80% and 80-99%. The 0-20% interval is neglected and this is the space after the ELM just before bin 1. It is neglected as in when the fast Electron Cyclotron Emission (ECE) data was compared against the evolution of the T_e pedestal in the dataset, it showed that the first 10% of the ELM cycle contains the MHD part of the ELM crash. This is not part of the pedestal recovery, and therefore should be excluded from the analysis as part of the previous ELM [151]. The 99-100% interval is also neglected because the ELM starts before the peak is seen in the spectral line, as the energetic particles have to leave the plasma and enter the SOL for the spectral emission to be seen [148].

Once the intervals which do not contain the ELM crash have been selected, the number of bins for the ELM cycle needs to be determined. Initially, this was chosen as 10-40%, 40-70% and 70-99%, as 70-99% is the pre-ELM window that has been used in the previous analysis of this dataset [96]. However, it cannot be assumed that this is the optimum number of intervals, so the data was binned from 0-99% into 10%, 20% and 30% windows. Then for each window size, all the T_e and n_e profiles are combined to form a composite profile [71, 148]. From mtanh fits, the height and width of the n_e and T_e pedestals can be obtained for each composite profile in each window. Therefore, the variation of height and width of the n_e and T_e pedestals through the ELM cycle using each window size can be visualised. This process was undertaken for all the pulses in the dataset presented in this chapter. An example result from the process for pulse 87342 is shown in figure 6.9, where the 10% windows are brown, the 20% windows are cyan and the 30% windows are red. The variation bars shown are not the errors used in the analysis.

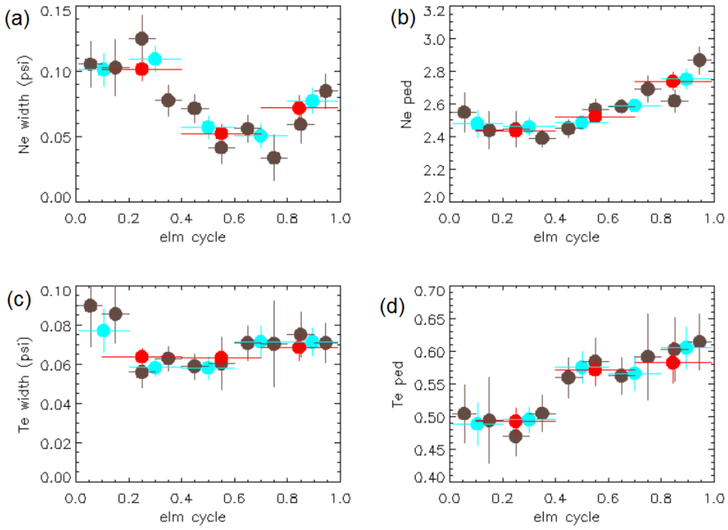

Figure 6.9: Inter-ELM evolution of the T_e and n_e pedestals using different intervals, brown=10% blue=20% red=30%, for pulse 87342 through the normalised ELM cycle (where e.g. 0.2 is 20% through the ELM cycle). Where (a) is the n_e pedestal width in $\%\psi$, (b) is n_e pedestal height in $10^{19}m^{-3}$ (c) is the T_e pedestal width in $\%\psi$ and (d) is the T_e pedestal height in keV. The bars on the 10% parameters are the uncertainty on the fit. The bars on the 20% and 30% bins capture the variation of the 10% parameters that fall within that bin.

Figure 6.9 shows that the bins for the initial 20% of the ELM cycle contain part of the ELM crash, as the pedestal height has not reached a minimum value in the ELM cycle. This provides further evidence that this initial 20% window is affected by physics of the ELM crash. Therefore, there is a balance between improved visualisation of the evolution, and there being enough individual HRTS profiles in the interval bin to provide confidence in the pedestal parameters. It was found that in general the 10% ELM interval should not be used, as illustrated in this case by the significant variations in the 10% obtained values the n_e width shown in (a) in figure 6.9. This broad variation is un-physical, and most likely a consequence of too few profiles in the bin: with some 10% ELM intervals only containing a single profile. Therefore, the 10% window is not reliable enough to study the inter-ELM evolution. Additionally, the 30% window is in general too large and resulted in a loss of detail and smoothing of the data, which may lead to the loss of information about the inter-ELM behaviour. Therefore, in the majority of cases the 20% windows were chosen for the analysis.

6.3.3 Operational points

In order to study the pressure pedestal evolution, the so-called operational points (OP) for each interval have to be calculated. These are the combination of the total pressure pedestal height, p_{ped} (in kPa), and width, $\Delta_{p,ped}$ (in $\%\psi$). These are calculated from the final mtanh fits of the n_e and T_e data. The electron pressure height, p_e (in kPa) is calculated from n_e (in $10^{19}m^{-3}$) and T_e (in keV). Results from an analysis of a pedestal database of ASDEX Upgrade, DIII-D and JET pedestals show that in general the pedestal width, Δ, has a similar dependence with pedestal electron density and temperature [140]. The p_e allows the total pressure pedestal height p_{ped} (in keV) to be calculated, assuming beryllium, $Z = 4$, is the main impurity. The two equations are given by:

$$\begin{aligned} p_e &= 1.6022 n_e T_e \\ p_{ped} &= p_e(9 - Z_{eff})/4 \end{aligned} \tag{6.7}$$

The electron pressure pedestal width, $\Delta_{pe,ped}$ (in $\%\psi$) is calculated using the EPED definition which is an average of the n_e and T_e pedestal widths (both in ψ) [57, 91, 124]. It is then assumed, due to a lack of ion pressure pedestal width $\Delta_{pi,ped}$ measurement, that the total pressure pedestal width $\Delta_{p,ped}$ (in $\%\psi$) is the same as the electron pressure pedestal width $\Delta_{Pe,ped}$ [151]. $\Delta_{p,ped}$ is multiplied by a factor of 100 to become in terms of $\%\psi$. Therefore their equations are:

$$\begin{aligned} \Delta_{pe,ped} &= \frac{1}{2}(\Delta_{ne,ped} + \Delta_{Te,ped}) \\ \Delta_{p,ped} &= 100\Delta_{Pe,ped} \end{aligned} \tag{6.8}$$

The operational points for each phase in the ELM cycle can be seen in figure 6.10. This also shows the KBM and PB boundaries.

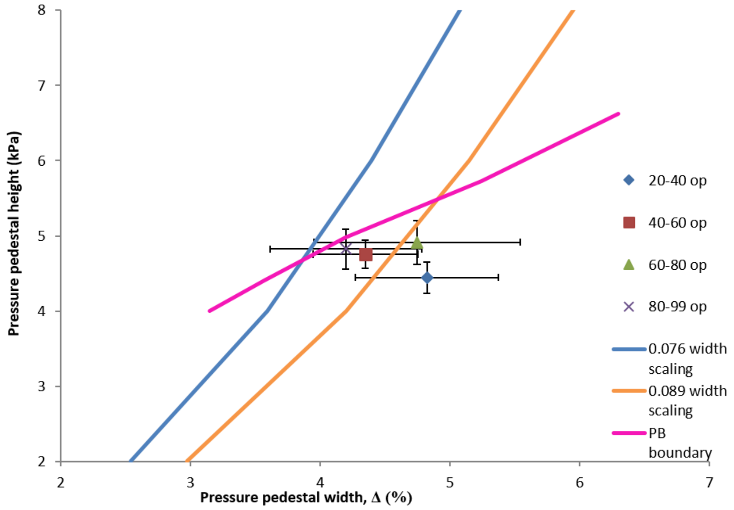

Figure 6.10: Example output for pulse 84795 showing the KBM and PB boundaries and OPs. The operational points are: 20-40% OP is the blue diamond, 40-60% OP is the red square, 60-80% OP is the green triangle and 80-99% OP is the purple cross. The PB boundary is in pink. The KBM boundaries calculated with two different width scaling constants: 0.079 and 0.089 and these are blue and yellow respectively. The x-axis is the total pressure pedestal width, in $\%\psi$, and the y-axis is the total pressure pedestal height, in kPa.

6.3.4 Discussion of errors on the operational points

The uncertainties on the pressure pedestal height and width, are displayed as the error bars on the operational points (OP) in figure 6.10. These are calculated in the following way: firstly, the fitting errors on the n_e and T_e pedestal heights and widths are obtained from the HRTS n_e and T_e profile fitting deconvolution process. The majority of this fitting error comes from the statistical error, which consists of the error on the fit due to the scatter of the data and the error on the data points [160, 161]. However, it should be noted that the uncertainties on the pedestal heights and widths are also affected by other systematic errors. These are, the systematic errors from the deconvolution process [149], the uncertainty in the profile position due to the systematic error from the ELM synchronisation process [150], the uncertainty in the calibration of the HRTS and the uncertainty in the ELM detection procedure [160]. The only systematic error taken into account in the fitting error is from the deconvolution process. The deconvolution process leads to an increase in the uncertainty of the pedestal width and position, but has a negligible effect on the uncertainty on the pedestal height [149, 161]. This effect is usually small compared to the statistical error, unless the pedestal is of a similar width to the instrument function [149]. The small systematic error from ELM synchronisation [150] is not taken into account. The HRTS is regularly calibrated and the calibrations are then implemented to remove systematic uncertainty, but some residual uncertainty is always left [160]. When the profiles are fitted this is always done to the latest calibration. There is no addition to the fitting error from the uncertainty in this calibration. The uncertainty in the ELM detection procedure is small and also difficult to quantify and therefore not considered. Therefore, the overall fitting error is a combination of the statistical error, which is the largest uncertainty, and the smaller systematic error due to deconvolution [149]. This has the consequence that a ELM synchronised pedestal profile consisting of more individual HRTS profiles will have a smaller statistical error, and therefore error bars. However, it should be appreciated that this leads to a larger, albeit smaller scale, systematic error due to the larger stationary phase, and the assumptions underpinning the stationary phase which is not considered in the errors in this analysis [150].

Once the errors on the height and width of the n_e and T_e profiles have been obtained from the fitting that occurs before the profiles enter the profile tool, these are combined to obtain the error on the electron pressure pedestal, p_e. For this the equation 6.7 for p_e is required. Using propagation of fractional errors the error of the height of p_e, δp_e, is given by:

$$\delta p_e = p_e \sqrt{\left(\frac{\delta n_e}{n_e}\right)^2 + \left(\frac{\delta T_e}{T_e}\right)^2} \tag{6.9}$$

To calculate the error on the total pedestal pressure height equation 6.7 for the total pedestal pressure height, p_{ped}, is required and it is also assumed beryllium, $Z = 4$, is the main impurity. An additional assumption for the uncertainty in the Z_{eff} measurement is required, and this is taken to be $\delta Z_{eff} = 15\%$ [151]. Therefore, again using error propagation yields the following equation for the error on p_{ped}, δp_{ped}, given by:

$$\delta p_{ped} = p_{ped}\sqrt{\left(\frac{\delta p_e}{p_e}\right)^2 + \left(\frac{\delta Z_{eff}}{9 - Z_{eff}}\right)^2} \tag{6.10}$$

Next, the error of the electron pedestal pressure width, $\delta\Delta_{pe,ped}$, needs to be obtained. This is calculated from the equation 6.8 for $\Delta_{pe,ped}$ using propagation of addition errors. This yields the equation for $\delta\Delta_{pe,ped}$, given by:

$$\begin{aligned} \delta\Delta_{pe,ped} &= \frac{1}{2}\sqrt{(\delta\Delta_{ne,ped})^2 + (\delta\Delta_{Te,ped})^2} \\ \delta\Delta_{p,ped} &= 100\delta\Delta_{pe,ped} \end{aligned} \tag{6.11}$$

The operational point assumes that the electron pedestal pressure width is equal to the total pedestal pressure width, due to a lack of ion pressure pedestal measurement. Therefore, it is also assumed that the error on the total pressure pedestal width is equal to the error on the electron pressure width.

6.3.5 Peeling-ballooning boundary

This section details the calculation of the PB boundary. The method used is employed in the references [25, 91] for model equilibria, and can also be used for reconstructions of equilibria from previous tokamak experiments. In this method PB stability calculations can be performed on sets of equilibria, with the same plasma shape and parameters but different pedestal widths, while the pedestal height is increased until a threshold growth rate is reached and the PB boundary is found [25, 91]. In this analysis, the reconstructed n_e and T_e profiles from the profile tool were used for each pre-ELM 80-99% interval for each individual pulse.

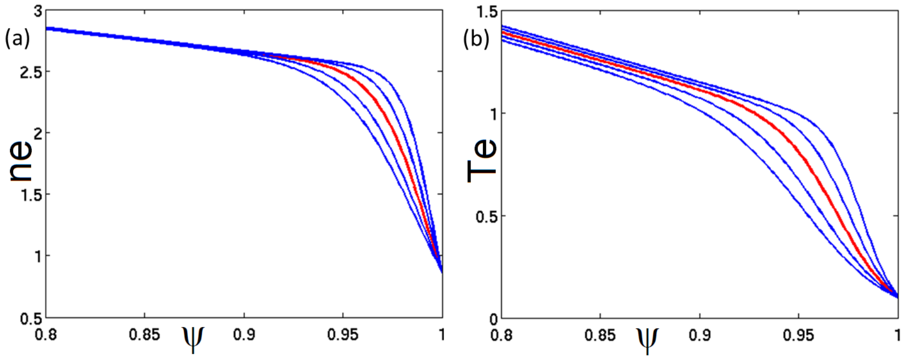

Figure 6.11: Variation of the width of the 80-99% (a) n_e pedestal and (b) T_e pedestal for pulse 84794, to produce narrower and wider pedestals for the production of the peeling-ballooning boundary. The original profile is red, and the additional “artificial” profiles are in blue.

This was undertaken using a profile width tool that takes the parametrised n_e and T_e profiles from the output of the original profile tool and artificially varies the width of the T_e and n_e profiles individually, for a specified number of additional profiles. The bottom position of each pedestal, and the height of the pedestal is fixed. Note that the position of the pedestal moves inwards as the pedestal is made wider as a result. The number of extra profiles and the exact width of the profiles that are required can be specified. An example output for the 80-99% interval of pulse 84794 is shown in figure 6.11. This figure shows that in this case four additional "artificial" profiles are produced, two that are narrower and two wider than the original. The experimental plasma shape and parameters from EFIT are kept fixed.

The critical height for each of the 5 profiles needs to be determined to calculate the PB stability boundary across the range of widths. This is obtained by employing a self-consistent scan up to n = 70 on each of the 5 different sets of profiles. This self-consistently raises the pedestal height for each set of profiles and finds the critical height of the pedestal, which is the height of the pedestal when the PB mode has a growth rate of γ/ω_A = 0.03. An illustration of this process is shown in figure 6.12.

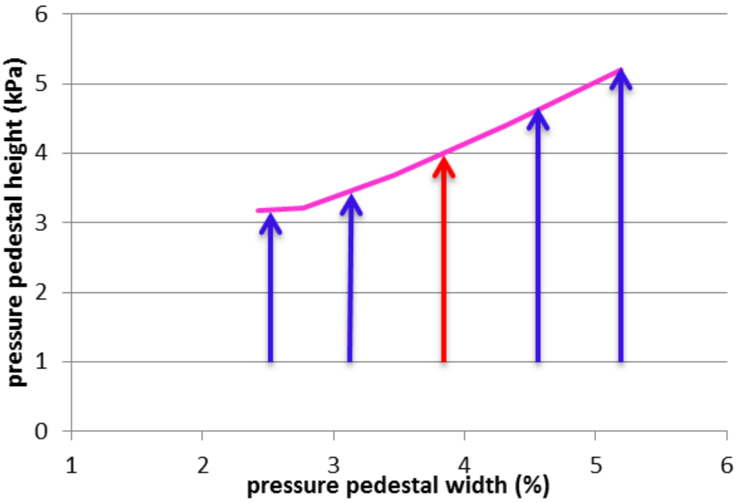

Figure 6.12: Illustration of the production of the peeling-ballooning boundary, shown in pink, using a self-consistent scan for each of the 5 different pedestal widths, blue are artificial width and red the equilibrium width of the 80-99% ELM interval produced using the width tool. The stability boundary is taken to be at γ/ω_A = 0.03.

Note that each of the five different width pedestals will have a different current density, J_ϕ profile. This is because, although the total current stays the same, the current distribution changes with each width as the gradients of the n_e and T_e profiles change and the bootstrap current J_{BS} is calculated from each set of n_e and T_e pedestals individually. As the scan takes place, the pedestal height is self-consistently increased and passes through the critical height at γ/ω_A = 0.03. This will be through two different scan points, one above and one below the critical height. Therefore these need to be linearly interpolated to find the exact critical value. This interpolation formula to obtain the critical total pedestal pressure pedestal height, $p_{3\%}$, is given by:

$$p_{3\%} = p_{low} + \frac{0.03 - \gamma_{low}}{\gamma_{high} - \gamma_{low}} \left(p_{high} - p_{low}\right) \tag{6.12}$$

where p_{low} is the total pressure pedestal height of the scan point below the critical total pressure height, p_{high} is the total pressure pedestal height of the scan point above the critical total pressure height, 0.03 is the value of the normalised growth rate, γ/ω_A, at the threshold for instability, γ_{low} is the growth rate at p_{low} and γ_{high} is the growth rate at p_{high}. Applying this for each individual scan yields the five points on the peeling-ballooning stability boundary.

6.4 Kinetic ballooning mode proxies and second stability on JET

As discussed in section 2.6, there are two proxies for KBM stability. The first is the proxy used by the EPED model detailed in 2.6.1, and second is the $n = \infty$ ideal ballooning mode proxy used in this analysis, detailed in 2.6.2. Also discussed in this section are $s-\alpha$ diagrams for further assessing second stability, as introduced in section 2.4.1.

The first proxy is the $\sqrt{\beta_{p,ped}}$ width scaling proxy for the KBM, which is the proxy used for the KBM in the EPED1 and EPED1.6 models [27, 91, 111]. The poloidal pedestal beta, $\beta_{p,ped}$, can be calculated for each pulse and is given by:

$$\beta_{p,ped} = \frac{p_{ped}}{{B_p}^2/2\mu_0} = \frac{p_{ped}}{\left(\mu_0 I_p/C\right)^2/2\mu_0} = \frac{2C^2 p_{ped}}{\mu_0 I_P^2} \tag{6.13}$$

where p_{ped} is the plasma pedestal pressure height (in Pa), B_p is the averaged poloidal magnetic field (in T), I_P is the total plasma current (in A), and C is the plasma circumference (in m) [57, 124]. Arbitrary values for p_{ped} can be used with values of the plasma parameters to create two curves with two different values of c_1: 0.076 [91] and 0.089 [111]. This gives 2 KBM width scaling curves, shown in figure 6.10. However, these curves are not presented in the results of the analysis, because they did not enable an improved understanding of the pulses and the second proxy, the $n = \infty$ ballooning limit proxy, was found to provide a clearer picture of the underlying physics.

The second proxy for the KBM, used extensively in this analysis, is the $n = \infty$ ideal MHD ballooning mode. The applicability of using the $n = \infty$ ideal ballooning stability as an accurate proxy in JET has been illustrated in JET-C pedestals [71]. Good agreement has been shown between the threshold pressure gradient for the $n = \infty$ ideal ballooning mode and the KBM threshold, which was also calculated using the local gyrokinetic GS2 code. [71]. Also demonstrated is that the most unstable regions in the pedestal for the $n = \infty$ ideal ballooning mode also have the highest local growth rates for KBMs. Furthermore, the regions which were unstable to local KBMs agree very well with the regions unstable to $n = \infty$ ideal ballooning modes [71].

In this analysis the HELENA code was also used to calculate the $n = \infty$ ideal ballooning limit. An example result is shown in figure 6.13. This figure shows the $n = \infty$ ballooning limit for the (a) 20-40% and (b) 40-60% intervals of JET-ILW pulse 84795, which shows that the region of the pedestal is constrained by the $n = \infty$ ballooning limit as the equilibrium pedestal fills the peak in $n = \infty$ ballooning limit, and is below but close to this limit. The beginning of second stability access, described in section 2.4.1, is seen in 6.13 (b).

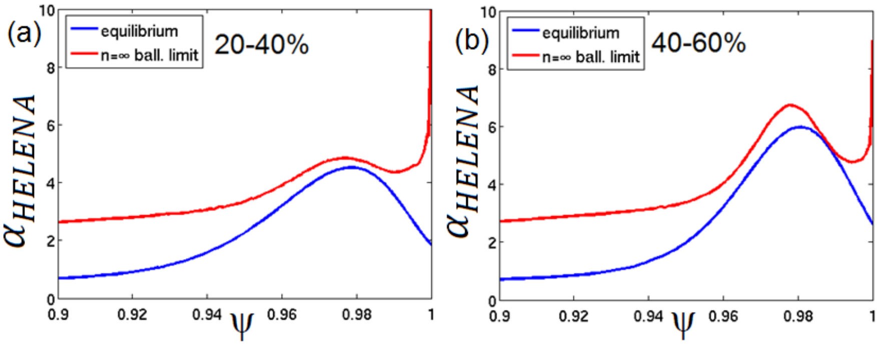

Figure 6.13: Example output for the ideal $n = \infty$ ballooning limit which is shown in red, and the normalised pressure gradient, α, which is shown in blue, as a function of normalised flux, for the 20-40% and 40-60% intervals of pulse 84795. The x-axis is normalised ψ, and the y-axis is α, the normalised pressure gradient.

To further study the rapid increase in the $n = \infty$ ballooning limit present in some of the discharges in this analysis, a further technique for studying the ideal ballooning stability was employed using $s - \alpha$ plots, introduced in section 2.4.1. These were produced in this analysis by using the ideal ballooning routine "ideal_ball" that is part of the GS2 code package [162, 163]. The routine reads in the equilibrium output from HELENA, which includes the calculation of shear. The code treats the equilibrium about a single field line surface using the Bishop's formalism [164], and integrates geometrically related quantities to calculate them along this single field line surface. If this function crosses the axis then the mode is unstable [163]. Also needed to produce the 2D $s - \alpha$ plot is to use the formalism which is detailed in Greene et al 1981 [85] for perturbing the local equilibrium. In the plots produced by the code the pressure gradient is given by $\beta' = \beta \frac{1}{p}\frac{dp}{dr}$, which is normalised pressure gradient, related to α. This perturbation of shear and pressure gradient allows the production of a graph in a 2D shear and pressure gradient space.

An example $s - \alpha$ plot for JET can be seen in figure 6.14 (a), which is taken at $\psi = 0.98$ as this is close to the maximum pressure gradient. This is compared in the same figure with its $n = \infty$ ballooning diagram in (b) where the $\psi = 0.98$ surface is marked by the yellow line. This is for pulse 84795 and at the 20-40% interval.

Figure 6.14 (a) shows the region stable to ballooning modes in blue and the region unstable to ballooning modes in orange. As previously stated in section 2.4.3 this plot is similar to a $J - \alpha$ plot, but current density increases as shear (s) decreases,

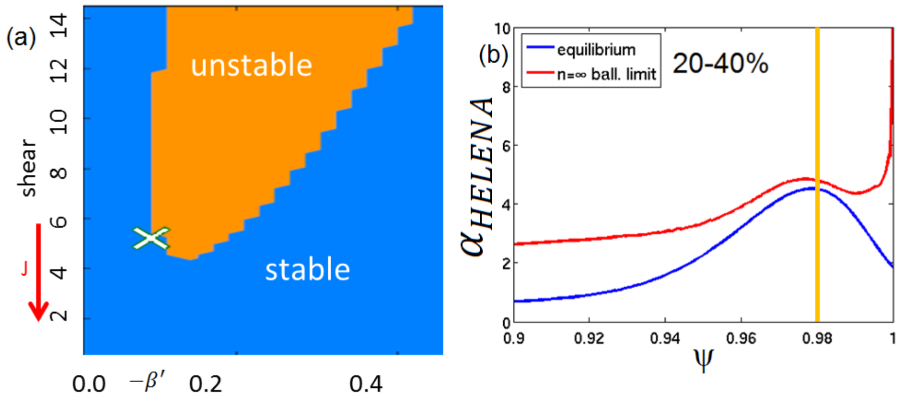

Figure 6.14: (a) $s-\alpha$ diagram for $\psi = 0.98$ where the white cross is the OP, blue is the stable region and orange is the unstable region to ballooning modes, and the red arrow illustrates that current density, J increases as shear decreases. The x-axis is β', which is a normalised pressure gradient, proportional to α, and the y-axis is shear, s (b) $n = \infty$ ballooning plot with red as the $n = \infty$ ballooning limit and blue as the equilibrium α, yellow marking the ψ chosen for the $s - \alpha$ diagram, for 20-40% interval of pulse 84795.

as illustrated by the red arrow.

As shown in figure 6.13 (a), the pressure gradient is clamped at its maximum pressure gradient due to the $n = \infty$ ballooning limit. This is also illustrated in 6.14 (a) as the OP is right up against the unstable region. However, as the previous figure 6.13 (b) shows, the $n = \infty$ ballooning limit has increased due to a small increase in current density, allowing a significant increase in the pressure gradient. This significant increase in pressure gradient is known as second stability, as introduced in section 2.4.1, and here the two stable regions are able to join and the OP is able to travel under the unstable region barrier and has second stable access. The plasma is then stable to $n = \infty$ ballooning modes at all values of pressure gradient [87]. This gaining of second stability access is illustrated in figure 6.15, which is for the same pulse and intervals as figure 6.13, the 20-40% and 40-60% intervals of pulse 84795.

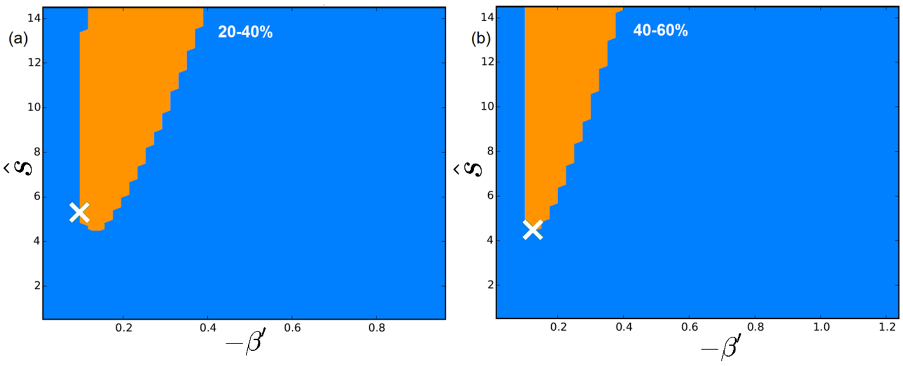

Figure 6.15: $s - \alpha$ diagrams for the first two phases, (a) 20-40% and (b) 40-60% ,of pulse 84795. White cross is the OP, orange and blue are the regions unstable and stable to the ideal ballooning modes respectively. (b) shows that the equilibrium has second stability access as it is under the unstable region. The x-axis is β', which is a normalised pressure gradient, and the y-axis is shear, s.

As figure 6.15 shows, initially in (a) there is not sufficient current density to get into the second stability regime and therefore the pressure gradient is clamped.

However, as the current density increases to (b) the shear reduces, and the equilibrium starts to have access to the second stable region. The pressure gradient is then able to increase rapidly when in this region. Note that the two different plots in figure 6.14 (a) and (b) are inconsistent with each other. The $n = \infty$ ballooning limit in figure 6.14 (b) does not go to infinity, and it appears that there is still a limit. This is in contrast to the $s - \alpha$ diagram in figure 6.14 (a), where it appears that there is no limit to the pressure gradient. This is because the diagrams are not calculated in the same manner. In the $s - \alpha$ diagram shear and pressure gradient are independent, and the equilibrium is not re-calculated when perturbed, and this becomes less valid further from the equilibrium point [163]. In the $n = \infty$ ballooning plot there is no perturbation in 2D space, and shear is not independent of the pressure gradient.

6.5 Introduction to the JET-ILW dataset

The dataset considered in this chapter is a set of JET-ILW pulses from the 2013-14 campaign. These were produced operating at a fixed magnetic field, $B_T = 1.7$ T, and fixed current, $I_P = 1.4$ MA, and are the result of power scans to provide a range of normalised beta, β_N. These were first performed at low and high triangularity, $\delta = 0.2$ and $\delta = 0.4$ respectively, with a low D_2 gas injection rate, $\Gamma_D = 2.8 \times 10^{21} es^{-1}$ [96]. Additionally, the power scans were repeated at low δ at two higher gas rates, providing a medium gas injection rate, $\Gamma_D = 8.4 \times 10^{21} es^{-1}$, and a high gas injection rate, $\Gamma_D = 18 \times 10^{21} es^{-1}$ [96]. More in depth information about these pulses is described in reference [96]. All the pulses from the low δ dataset are represented in figure 6.16, where the low gas pulses are blue, the medium gas pulses are green and the high gas pulses are pink.

As figure 6.16 (a) shows, as the gas rate is increased the maximum achievable β_N at the highest input power, here given as the net power across the separatrix, P_{sep}, falls from $\beta_N = 2.76$ at low gas to $\beta_N = 1.95$ at high gas. Therefore, this illustrates how the achieved β_N is a combination of input power, P, and gas rate [96]. Figure 6.16 (b) shows that at all gas rates the frequency of the ELMs increases with power, which implies all these pulses have type I ELMs, as defined in Zohm et al. 1996 [38, 96]. Figure 6.16 (c), which is calculated using the 70-99% pre-ELM window and HRTS ELM-synchronised profiles, shows that as gas rate increases the pedestal pressure reduces across the entire injected power range [96]. This data agrees with previous data published in [137] shows that pedestal pressure in general increases with power for a given gas rate. This was illustrated across multiple tokamaks, including ASDEX Upgrade, DIII-D, JET and JT-60U [137]. Finally, figure 6.16 (d) shows that the collisionality at the pedestal top, which is again calculated using the 70-99% pre-ELM window and HRTS ELM-synchronised profiles, is sensitive to gas injection rate reduces as $\beta_{pol,ped}$ increases [96].

The previous pedestal stability study for this dataset, published in [96], analysed the 70-99% ELM-synchronised pre-ELM interval. This ideal MHD stability analysis performed on this pre-ELM interval shows that at the low gas injection rate, the PB

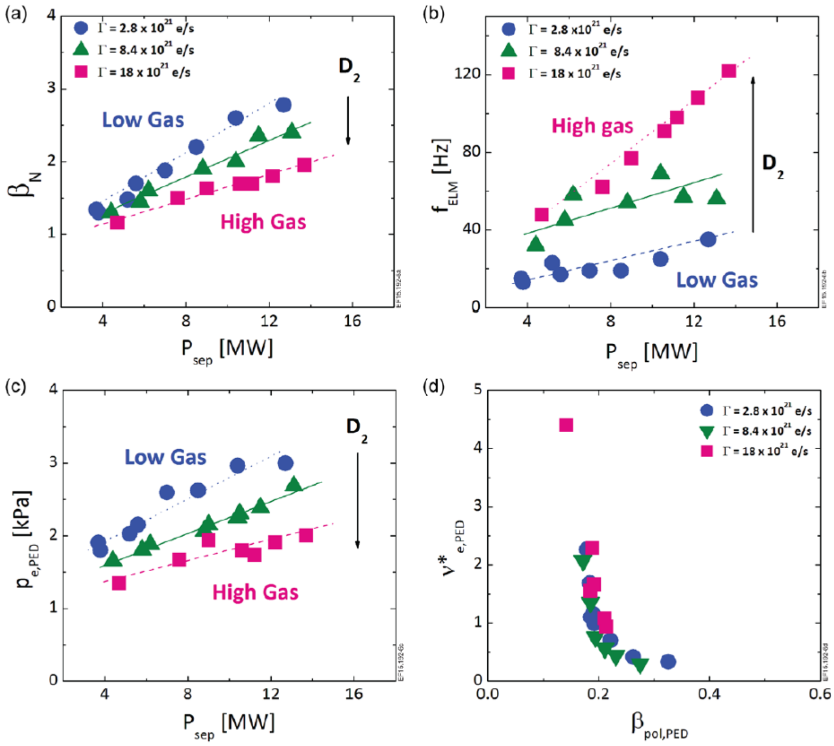

Figure 6.16: Low triangularity JET dataset for three power scans at three different gas injection rates, blue is low gas, green is medium gas and pink is high gas. (a) normalised beta, β_N, vs. P_{sep} (b) ELM frequency, f_{ELM}, vs. P_{sep} (c) ELM-averaged for 70-99% interval electron pedestal pressure, $p_{e,ped}$, vs. P_{sep} where P_{sep} is net power across the separatrix, given by: $P_{sep} = P_{heat} - dW/dt - P_{rad,bulk}$. (d) Pedestal top collisionality, $\nu^*_{e,ped}$, vs. pedestal poloidal beta, $\beta_{pol,ped}$. These are 70-99% window values from HRTS. Reproduced from [96].

mode is marginally stable or unstable across the range of β_N. However, for the high gas injection rate pulses, the PB boundary is typically not reached, and this is particularly pronounced at high β_N, initially suggesting that using only ideal MHD PB theory does not explain the ELMs in these discharges [96].

This analysis explores the inter-ELM evolution of the pedestal structure along with the PB and KBM stability of the pedestal to explore how the ELM trigger is approached, and the underlying physics of the dynamics. Thirteen pulses form the dataset for this analysis which were chosen across β_N ranges for low δ at the three different gas injection rates, and also for high δ at low gas injection rate. Firstly, the low δ dataset is explored, which consists of ten pulses. There are four low gas fuelling pulses, three medium gas fuelling pulses and three higher gas fuelling pulses, and pulses at each gas injection rate are across a range of β_N values. Finally, three high δ low gas fuelling pulses are analysed across a range of β_N values. Additionally, the nature of the ELM traces for the low and high gas injection rates pulses at low δ are considered.

6.6 Analysis of dataset: low deuterium gas injection rate and low triangularity

This section details the results from the JET-ILW pulses 84797, 84795, 84796 and 84794, which are all at low triangularity, $\delta = 0.2$, and low D_2 gas injection rate, $\Gamma_D = 2.8 \times 10^{21} es^{-1}$. These four pulses have a range of normalised beta, β_N, from 1.28 to 2.76. Firstly the analysis of the evolution of the pressure pedestal height and width will be discussed, next the KBM proxy $n = \infty$ ballooning stability will be discussed and finally a summary of the analysis will be presented.

6.6.1 Pressure pedestal height and width evolution

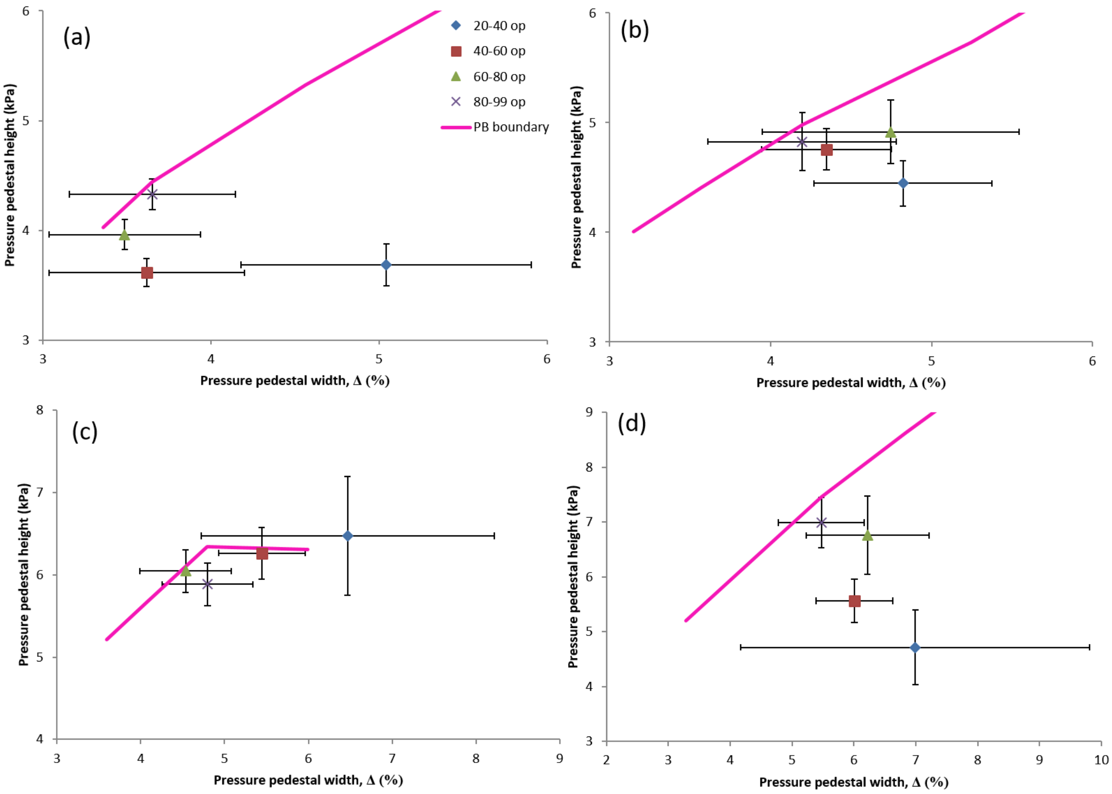

Figure 6.17: Evolution of the total pressure pedestal height and width for low gas, low triangularity pulses (a) 84797, $\beta_N = 1.28$, (b) 84795, $\beta_N = 1.7$, (c) 84796, $\beta_N = 2.2$ and (d) 84794, $\beta_N = 2.76$, with the peeling-ballooning (PB) boundary. The operational points (OPs) are: 20-40% OP is the blue diamond, 40-60% OP is the red square, 60-80% OP is the green triangle and 80-99% OP is the purple cross. The PB boundary is in pink. The x-axis is the total pressure pedestal width, in $\%\psi$, and the y-axis is the total pressure pedestal height, in kPa.

This section considers the evolution of the ELM cycle for the ELM-synchronised 20-40%, 40-60%, 60-80% and 80-99% OPs. The PB boundary is also considered to obtain the proximity of the OPs to the PB boundary. The results of this study for the four low D_2 gas injection rate (low gas) pulses are shown in figure 6.17. Figure 6.17 (a) shows the PB boundary and the OPs for pulse 84797. This is the lowest β_N pulse of the considered low gas dataset with $\beta_N = 1.28$, $Z_{eff} = 1.1$ and the ELM frequency in the stationary phase of the pulse is f_{ELM} = 13Hz. As the figure (a) shows, firstly the pedestal narrows between the 20-40% and 40-60% phases, then the pedestal increases in height with a narrowing between 40-60% and 60-80%. Finally the pedestal broadens between the 60-80% and 80-99% pre-ELM phases as the ELM is approached, and the PB boundary is reached at the the 80-99% pre-ELM window. This therefore follows the EPED paradigm that there is widening of the pedestal before the ELM and the PB boundary is reached.

Figure 6.17 (b) shows the PB boundary and the OPs for pulse 84795. This is the second lowest β_N pulse with β_N = 1.7, Z_{eff} = 1.22 and the ELM frequency in the stationary phase is f_{ELM} = 17Hz. As the figure (b) shows, contrary to pulse 84797, this pulse does not show a clear trend in the width evolution. Firstly, the pedestal increases in height between the first two phases and then all the 40-60%, 60-80% and 80-99% OPs have similar heights and widths, with no obvious evolution. As with the previous pulse, the PB boundary is reached at the pre-ELM 80-99% interval. This pulse therefore does not appear to follow the EPED paradigm that there is widening of the pedestal before the ELM, but the PB boundary is reached which satisfies the PB criteria.

Figure 6.17 (c) shows the PB boundary and the OPs for pulse 84796. This is the second highest β_N pulse with β_N = 2.2, Z_{eff} = 1.24 and the ELM frequency in the stationary phase is f_{ELM} = 19Hz. As figure (c) shows, this pulse does not show a clear trend in the width evolution. Note the large error bars on the initial 20-40% phase which shows that it is difficult to accurately determine where this OP should be. There is little change in the pedestal height and width between the 60-80% and the pre-ELM 80-99% OPs. The evolution shows that the pedestal height decreases throughout the ELM cycle, with mostly narrowing of the width, which suggests a reduction in the pedestal through the ELM cycle. This evolution, within the error bars, could either be a saturation of the pedestal or the onset of a saturated mode which causes a reduction in the pedestal top. Again the PB boundary is reached at the 80-99% pre-ELM phase. The kink in the PB boundary is unlikely to be physical: there is no ELM in the earlier 40-60% and 60-80% phases. Therefore, this does not appear to follow the EPED paradigm for width evolution, but the PB boundary is reached.

Figure 6.17 (d) shows the PB boundary and the OPs for pulse 84794. This is the highest β_N pulse with β_N = 2.76, Z_{eff} = 1.7 and the ELM frequency in the stationary phase is f_{ELM} = 35Hz. As the figure (d) shows, this pulse has a clearer trend in the width evolution. However, there is no characteristic widening of the pulse between the 60-80% and 80-99% OPs before the ELM, but there is widening in the middle of the ELM cycle between the 40-60% and 60-80% OPs. It is difficult to deduce the true evolution between the first two phases of the ELM cycle, 20-40% and 40-60%, because of the very large error bar on the 20-40% OP. As with all the other low gas fuelling pulses the PB boundary is reached at the ELM onset, the 80-99% pre-ELM interval. However, this pulse does not appear to follow the EPED paradigm for width evolution.

Therefore all 4 low gas injection pulses satisfy the PB criteria of the EPED model, that the PB boundary is reached just before the ELM, which is consistent with previous pre-ELM 70-99% results published in [96]. However, only one pulse has characteristic EPED pedestal widening between the last two phases before the ELM occurs. Therefore, does this rule out the KBM playing a role in the JET-ILW? The next subsection considers this question more carefully, using the $n = \infty$ ideal MHD ballooning proxy for the KBM.

6.6.2 KBM proxy: n=∞ ballooning stability

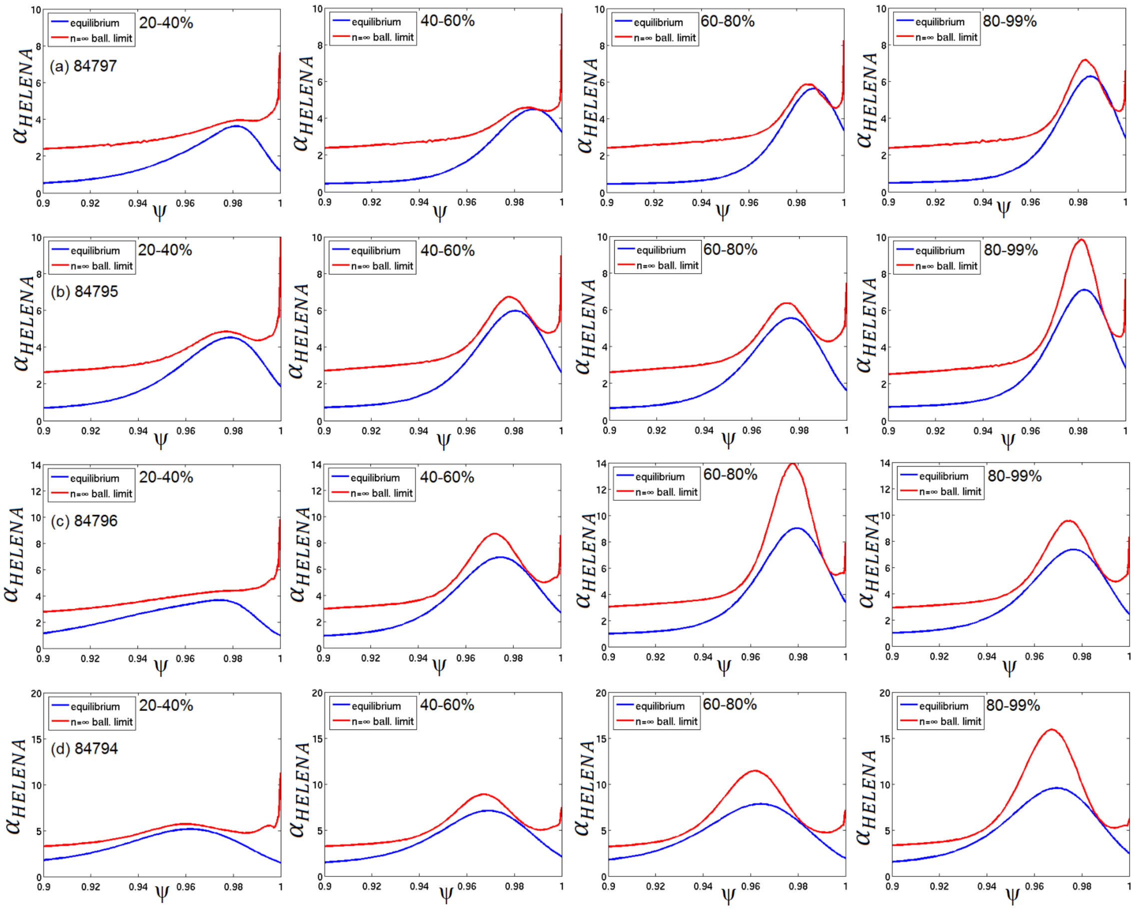

Figure 6.18: $n = \infty$ ballooning diagrams for low triangularity low gas pulses (a) 84797, $\beta_N = 1.28$, (b) 84795, $\beta_N = 1.7$, (c) 84796, $\beta_N = 2.2$ and (d) 84794, $\beta_N = 2.76$. The ideal $n = \infty$ ballooning limit is shown in red, and the normalised pressure gradient, α, is shown in blue, as a function of normalised flux. There are 4 plots for each pulse corresponding to the 20-40%, 40-60%, 60-80% and 80-99% intervals of the ELM cycle. The x-axis is normalised flux, ψ, and the y-axis is α, the normalised pressure gradient.

In this section the KBM constraint is considered in more detail using HELENA to calculate the ideal $n = \infty$ ballooning limit. These are for the same four ELM-synchronised windows as the pedestal evolution diagrams. The results for the four low D_2 gas injection pulses, (a) 84797, (b) 84795, (c) 84796 and (d) 84794, are shown in figure 6.18.

Firstly, consider pulse 84797, shown in figure 6.18 (a). This pulse reaches the PB boundary, as illustrated in 6.17 (a). Note that the pedestal, and therefore the edge transport barrier, is the peak in the pressure gradient seen between $0.96 < \psi < 1$.

Studying the ELM-cycle in (a), it can be seen that in the first half of the ELM cycle, between the 20-40% and 40-60% phases, the pressure gradient increases towards the $n = \infty$ ballooning limit, and is up against the limit in the 40-60% interval. However, in the latter part of the ELM cycle, between the 60-80% and 80-99% phases, the $n = \infty$ ballooning limit increases allowing further increase of the pressure gradient. In the 80-99% pre-ELM interval, the pressure gradient has reached a sufficient value to drive the PB mode, which causes the triggering of the ELM. This pulse shows good agreement with the two EPED model constraints: the $n = \infty$ ballooning mode, shown to be a good proxy for the KBM in JET, constrains the pressure gradient in the pedestal, and evolution is terminated by the PB mode, triggering an ELM. This rapid increase in the $n = \infty$ ballooning limit in the latter part of the ELM cycle is due to second stability access, as described in subsection 2.4.1. As the pressure gradient increases, the bootstrap current density, J_{BS}, which dominates the current in the pedestal region, also increases and this occurs on the current diffusion timescale. Therefore, the second stable access region is reached when the $n = \infty$ ballooning limit increases rapidly for a small increase in current density.

Next consider pulse 84795, shown in figure 6.18 (b). This pulse reaches the PB boundary, but has more complex width evolution, as seen in 6.17 (b), and as such the proxy is crucial to determine whether the KBM criteria is satisfied. As the results in (b) show, despite the complex width evolution, the evolution of the pedestal in this pulse compared to the $n = \infty$ ballooning limit is very similar to 84797. However, in this pulse the $n = \infty$ ballooning limit starts to increase earlier in the ELM cycle in the 40-60% interval, which allows the pressure gradient to grow earlier in the ELM cycle. Therefore, second stability access is gained earlier in the ELM cycle at the 40-60% interval. It also shows that the $n = \infty$ ballooning limit is rapidly increasing in the final pre-ELM 80-99% phase of the ELM cycle. The pedestal pressure gradient is close to the $n = \infty$ ballooning limit throughout the ELM cycle, except in the 80-99% phase where the width of the pedestal region is still determined by the width of the $n = \infty$ ballooning limit, and therefore the width of the region with second stability access. This suggests that the KBM is constraining the pedestal in this pulse, and determines the width of the pedestal region. Therefore, despite the no clear trend in width evolution in this pulse, the pedestal is also constrained by both the physics constraints underpinning the EPED model.

Thirdly, consider pulse 84796, shown in figure 6.18 (c), which reaches the PB boundary. As figure (c) shows that despite the complex width evolution of the pedestal, the evolution of the pressure gradient compared to the $n = \infty$ ballooning limit is very similar to 84797 and 84795. Initially in the 20-40% interval the $n = \infty$ ballooning limit is flat and the pressure gradient sits below it. Next, the $n = \infty$ ballooning limit starts to increase earlier in the ELM cycle, which allows the pressure gradient to grow and shows second stability access is gained at the 40-60% interval. As with the final pre-ELM 80-99% phase of the ELM cycle in 84795, rapid growth in the $n = \infty$ ballooning limit is also seen in this pulse, but here this is earlier in the ELM cycle. However, some of this $n = \infty$ ballooning limit is lost in the final 80-99% pre-ELM phase of the ELM cycle, but there is still second stability access. This pulse shows that the KBM limit dominates the evolution of the pedestal pressure gradient by determining the pedestal width when there is second stable access, as the pedestal pressure gradient always fills the second stable access region, as shown in figure 6.18 (c). Therefore, this pulse is characteristically similar to pulse 85795.

Finally, consider the highest β_N pulse 84794, shown in figure 6.18 (d). This pulse reaches the PB boundary and has clearer width evolution than the previous two pulses, as seen in 6.17 (d). It does not show the characteristic pedestal widening before the ELM as described by the EPED model. As the figure (d) shows, the evolution of the pedestal gradient compared to the $n = \infty$ ballooning limit is very similar to all the other low gas pulses, shown in (a-c). Initially the pedestal gradient is constrained by the $n = \infty$ ballooning limit. Next, as with 84795 and 84796, the $n = \infty$ ballooning limit increases in the 40-60% interval, showing clear second stability access in this interval. This pulse shows the most rapid growth of the $n = \infty$ ballooning limit in all four pulses, with a very high peak in the limit in the 80-99% pre-ELM interval. Therefore this pulse has very clear second stability access. A possible interpretation is that in these phases the pedestal gradient cannot keep up with the rapid growth in the $n = \infty$ ballooning limit. This could be due to the pedestal growing on a transport time-scale, whereas $n = \infty$ ballooning limit grows on a faster time-scale, although full transport modelling would be necessary to confirm this. This pulse shows that the KBM limit dominates the evolution of the pedestal pressure gradient by determining the pedestal width when there is second stable access: the pedestal pressure gradient always fills the second stable access region, as shown in figure 6.18 (d). However, it is clear here that the pedestal gradient does not increase as fast as the $n = \infty$ ballooning limit, and as such is likely not strictly constrained by the KBM. Therefore, despite the no clear trend in width evolution in this pulse, the KBM limit dominates the evolution controlling the pedestal width and therefore, the pedestal is also dominated by the PB and KBM limits, as required by EPED.

6.6.3 Overview of low deuterium gas injection rate pulses

The analysis of the low triangularity and low D_2 gas injection rate pulses shows that all these pulses reach the peeling-ballooning (PB) boundary. This is consistent with analysis from [96]. All these pulses, despite three of the four pulses not having standard EPED-like width broadening of the pedestal towards the end of the ELM cycle, have their evolution governed by the $n = \infty$ ballooning limit, used here as a suitable proxy for the KBM [71]. Initially all pulses are constrained by the KBM until there is sufficient current density, and therefore low enough shear and second stability access occurs. All pulses appear to have the width of the pedestal in pressure gradient determined by the width of the peak in the $n = \infty$ ballooning limit, which constrains the width of the pressure pedestal, and therefore the pressure pedestal height that can be obtained. Therefore the EPED physics is satisfied for all these pulses, despite complex width evolution.

Inter-ELM pedestal electron density and temperature profile investigations on ASDEX Upgrade [138, 139] have shown that there are a characteristic sequence of phases in between ELMs: firstly a fast recovery phase, which would be neglected in this analysis as discussed in section 6.3.2, then a quiet slow pressure build-up phase and finally a strongly fluctuating phase before the next ELM occurs [138]. It was also found that sometimes the ELM was triggered immediately after recovery of the pressure profile, while in others the edge profiles reached their final shape a significant amount of time before the ELM crash [139]. Therefore, the observation that the ELM is triggered as soon as the final pressure pedestal height is reached, such as in pulse 84797, while in another pulse, such as 84795, it appears the pedestal saturates a significant amount of time before the ELM occurs agrees with the results seen in ASDEX Upgrade.

It should be stressed that the physics controlling the evolution of the width of the pedestal is not yet fully understood. However, this analysis shows that the complex behaviour of the width evolution can start to be understood. As described in section 2.6, other mechanisms such as micro-tearing modes may play a role [71, 112, 116], and in other tokamaks including MAST [107, 112] and DIII-D [113, 114], the pressure gradient appears to be fixed as the pedestal height and width increase monotonically. However, in these JET pulses the pressure pedestal gradient region is defined size of the second stability access region, as shown in figure 6.18. Therefore, this implies that the pedestal width evolution is at least partially determined by the region of the pressure gradient that has second stable access, in addition to any other physics which may govern the width. As the bootstrap current, J_{BS}, is proportional to the pressure gradient, this mechanism will be highly determined by how much current in the pedestal region there is for a given pressure gradient. The exact amount of current for a given pressure gradient will depend on a number of factors, including the current diffusion time and the collisionality (ν^*) and the dynamics of the relative evolution of the pressure gradient and current density. Specifically, they have different relative diffusion times so the increase in pressure gradient does not lead to an instantaneous increase in current density, so the pressure gradient can grow on the fast energy diffusion time-scale due to the high temperature and therefore low resistivity. This leads to inter-dependencies on plasma parameters such as impurity species, determining Z_{eff}, ν^* and resistivity, as well as D_2 gas injection rate and heating power. This complex mechanism has several feedbacks, which lead to very small changes in parameters causing a bifurcation of states in the plasma and needs further transport analysis. Simply stated, a very small change in, for example, the current density in the pedestal, could lead to the plasma not being able to enter second stability access. However, note that on ASDEX Upgrade that the current density building up on a slower transport timescale could not be confirmed, and that current diffusion seems to only play a minor role in the edge of the plasma [139].

6.7 Analysis of dataset: medium deuterium gas injection rate and low triangularity

This section considers the medium D_2 gas injection pulses 87338, 87341 and 87339, which are at low triangularity $\delta = 0.2$ and medium D_2 gas injection rate, $\Gamma_D = 8.4 \times 10^{21} es^{-1}$. These three pulses have a range of normalised beta, β_N, from 1.45 to 2.35.

6.7.1 Pressure pedestal height and width evolution

This section discusses the evolution of the ELM cycle for the ELM-synchronised 20-40%, 40-60%, 60-80% and 80-99% OPs and the PB boundary is also considered. The results of this study for the three medium D_2 gas injection rate (medium gas) pulses are shown in figure 6.19.

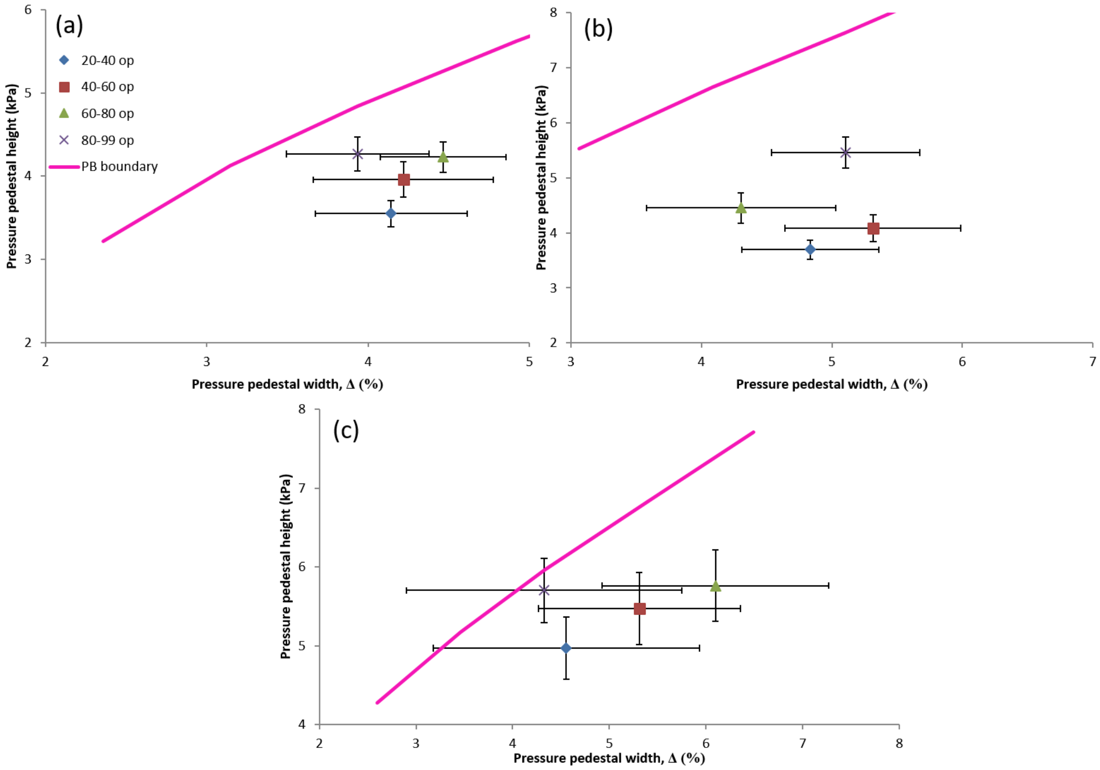

Figure 6.19: As for figure 6.17, but for medium gas injection, low triangularity pulses (a) 87338, $\beta_N = 1.45$, (b) 87341, $\beta_N = 2.0$, and (c) 87339, $\beta_N = 2.35$.

Figure 6.19 (a) shows the peeling-ballooning (PB) boundary and the OPs for pulse 87338. This is the lowest β_N pulse of the medium gas dataset and $\beta_N = 1.45$, $Z_{eff} = 1.35$ and the ELM frequency in the stationary phase is $f_{ELM} = 45$Hz. This f_{ELM} is significantly higher than the average frequency in the low gas injection pulses. Initially, between the first three phases of the ELM cycle, 20-40%, 40-60% and 60-80% the pedestal grows in height and widens. The evolution of the pulse is similar in the latter two phases of the ELM cycle to 84794, shown in figure 6.17 (d). Both this pulse and 84794 show a narrowing of the pedestal from the 60-80% to the pre-ELM phase 80-99%. This pulse therefore does not show a clear EPED-like widening in the latter stages of the ELM cycle. The pre-ELM 80-99% phase error bar is very close to the peeling-ballooning (PB) boundary, and therefore the pedestal is likely to be PB constrained; considering some of the errors that are difficult to quantify are not considered which would make the error bar on the width and height slightly larger than are presented, as discussed in section 6.3.4. This is consistent with the pre-ELM 70-99% results published in [96] which shows that the low $\beta_N = 1.45$ pulses at medium gas injection, are at the PB boundary. Therefore, this pulse does not exhibit EPED-like width evolution but the PB boundary is likely reached.

Figure 6.19 (b) shows the PB boundary and the OPs for pulse 87341. This is the second lowest β_N pulse and $\beta_N = 2.0$, $Z_{eff} = 1.48$ and a significantly higher ELM frequency in the stationary phase of $f_{ELM} = 69$Hz. As the figure (b) shows, this pulse has the characteristic widening between the latter two ELM cycle intervals, from 60-80% to 80-99%. The evolution between the first three phases of the ELM cycle, the 20-40%, 40-60% and 60-80% intervals, is likely un-physical due to the very large width error bars on this data. This therefore likely indicates little change in width over the first three phases of the ELM cycle. The height error bars are much smaller, and the evolution between these three OPs show an increase in height of the pedestal. The PB boundary is clearly not reached by the pre-ELM 80-99% phase. This is consistent with the results for this pulse for the larger 70-99% pre-ELM phase published in [96]. Therefore, the PB mode as the trigger for an ELM does not appear to explain the ELM here. However, the latter width evolution between the final two phases in the ELM cycle does appear to be consistent with EPED.

Figure 6.19 (c) shows the PB boundary and the OPs for pulse 87339. This is the highest β_N pulse and $\beta_N = 2.35$, $Z_{eff} = 1.45$ and a lower ELM frequency in the stationary phase of $f_{ELM} = 35$Hz. This is surprising, as in type I ELMy H-mode f_{ELM} is expected to increase with power [38]. However, note that the variation of ELM frequency with power for medium D_2 gas injection pulses, illustrated as the green points in figure 6.16 (b) in section 6.5, is significantly more erratic than for the other two gas injection rates. Studying the evolution of the total pressure pedestal height and width, illustrated in figure 6.19 (c), shows that the pedestal widens and grows in height throughout the first 3 phases of the ELM cycle, 20-40%, 40-60% and 60-80%. The pulse finally then narrows between the 60-80% and the pre-ELM 80-99% OP which is similar to pulse 87338. Therefore, this pulse also does not show a clear EPED widening in the latter stages of the ELM cycle. The final pre-ELM point for 80-99% is clearly at the PB boundary, satisfying the PB criterion. This finding does not agree with pre-ELM 70-99% analysis published in [96], which states that the intermediate (medium) and high D_2 gas injection rate pulses at the higher β_N values above $\beta_N = 1.5$ do not reach the PB boundary and are deeply stable, calculated for 70-99% up to $n = 50$ [96]. However, note that this pulse is not directly included in the stability analysis section in the paper, so the result in figure 6.19 (c) may not be a contradiction.

6.7.2 KBM proxy: n=∞ ballooning stability

Now the KBM constraint is considered in more detail using HELENA to calculate the ideal $n = \infty$ ballooning limit. The results for the three medium D_2 gas injection pulses, (a) 87338, (b) 87341 and (c) 87339, are shown in figure 6.20.

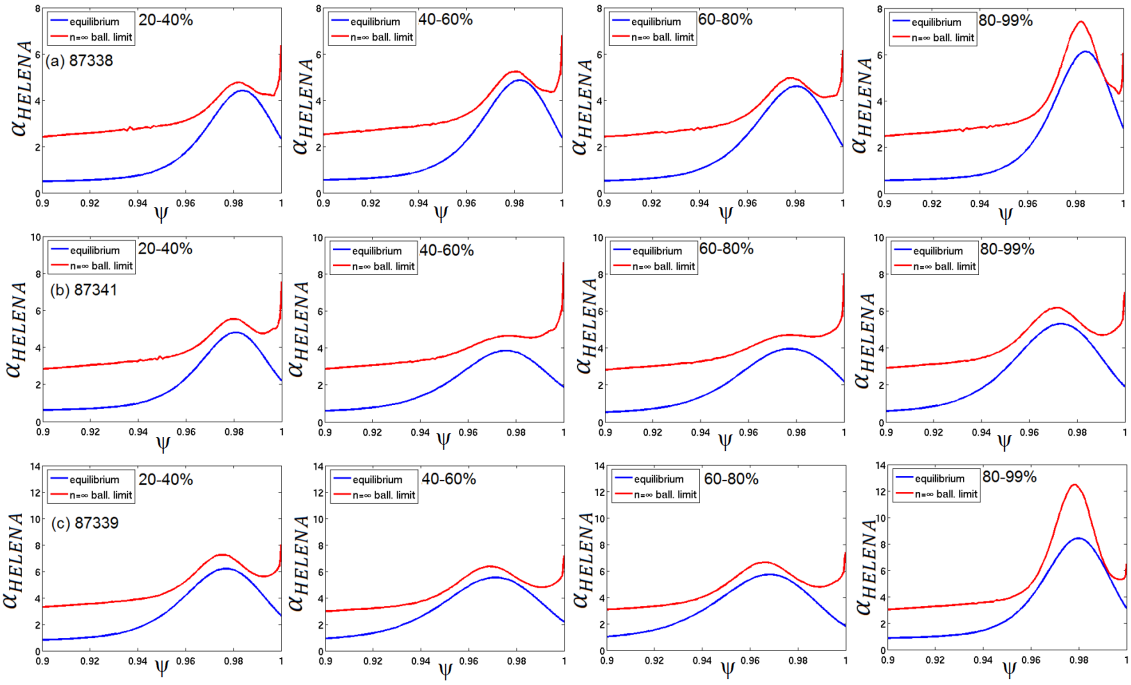

Figure 6.20: As for figure 6.18, but for low triangularity medium gas injection pulses (a) 87338, $\beta_N = 1.45$, (b) 87341, $\beta_N = 2.0$, and (c) 87339, $\beta_N = 2.35$.

Firstly, consider pulse 87338, shown in figure 6.20 (a). Recall this pulse just reaches the PB boundary. This figure shows that in the first three parts of the ELM cycle, 20-40%, 40-60% and 60-80%, the pressure gradient is up against the $n = \infty$ ballooning limit; there is little change in the pedestal height, and the pedestal very slightly widens by the 60-80% interval. However, in the last part of the ELM cycle, the 80-99% pre-ELM point, the $n = \infty$ ballooning limit increases. This allows further increase of the pressure gradient, and also results in a narrowing of the pressure gradient as the pedestal fills the $n = \infty$ ballooning limit. This rapid increase in the $n = \infty$ ballooning limit in the latter part of the ELM cycle is again due to the second stability access. In the last part of the ELM cycle, the 80-99% pre-ELM interval, the pressure gradient has reached a sufficient value to likely drive the PB mode, which causes the triggering of the ELM. Therefore this pulse shows good agreement with the two EPED model constraints: the KBM provides a constraint on the pedestal evolution and the PB mode triggers the ELM, despite fact that the pedestal does not widen before the ELM as described by EPED.

Next consider pulse 87341, shown in figure 6.20 (b). Recall that this pulses did not reach the PB boundary, but that the pedestal does widen between the last two phases of the ELM cycle. As this figure shows, the pressure gradient is constrained by the $n = \infty$ ballooning limit throughout the ELM cycle. As the ELM is approached in the 80-99% phase, the pedestal gradient has increased and the pedestal widens as the $n = \infty$ ballooning limit increases. Even though there is an increase in the limit, the initial and final stages of the ELM cycle are very similar, and the narrowing of the $n = \infty$ ballooning limit is not as pronounced as seen in the cases where second stability access occurs. Additionally, the pedestal is fully able to keep up with the increase in limit and maintains the same distance from the the $n = \infty$ ballooning limit throughout the ELM cycle. Thirdly, every case where there is second stability access, the outside edge of the pedestal gradient is always touching the the $n = \infty$ ballooning limit and also fully constrains the width, but this is not the case here. Therefore there is very likely no second stability access in this case. To obtain a more accurate conclusion, measurements of pedestal current density would be necessary. Pulse 87341 is therefore constrained by the KBM, indicating a role for the KBM physics limiting the pressure gradient in this pulse. Note this pulse still ELMs and the PB boundary is not reached. This could either be due to physics not in the PB model, or it could indicate that there is an alternate ELM trigger here. Therefore EPED would likely predict the KBM boundary, and there additionally is a widening of the pedestal just before the ELM, but not the final pedestal height as the PB mode does not appear to be the ELM trigger.

Finally consider pulse 87339, shown in figure 6.20 (c). Recall this pulse did reach the PB boundary, but narrows before the ELM. As this figure shows, the first three phases of the ELM cycle, 20-40%, 40-60% and 60-80%, have a similar form as the first and last phases of the previous pulse. These three phases all are closely constrained by the the $n = \infty$ ballooning limit and the top of the pedestal closely fills the limit. In the final 80-99% interval, the $n = \infty$ ballooning limit increases rapidly, and shows clear second stability access. Additionally, the pedestal has significantly increased in height and narrowed to fill the the $n = \infty$ ballooning limit. This increase in pedestal height is not as rapid as the increase in the $n = \infty$ ballooning limit. Therefore this pulse shows good agreement with the two EPED model constraints: the KBM provides a constraint on the pedestal evolution and then constrains the pedestal width, and the PB mode triggers the ELM despite the narrowing of the pedestal before the ELM contrary to the EPED model.

6.7.3 Overview of medium deuterium gas injection rate pulses

The picture of the behaviour of the pedestal in medium D_2 gas injection rate pulses, is more complex than at low D_2 gas injection rate. However, from the analysis of pulses 87338, 87341 and 87339 a pattern is emerging. Firstly lowest β_N pulse 87338 just reaches the PB boundary, this agrees with previous results [96]. The pedestal widens throughout the ELM cycle until the 80-99% pre-ELM interval, where the pulse suddenly narrows. This coincides with the pedestal gaining second stability access, forcing the pedestal into a narrower region governed by the $n = \infty$ ballooning limit, which grows in height and provides the second stability access. Secondly the middle β_N pulse 87341, clearly does not reach the PB limit, and does not have second stability access. This pulse is constrained by the $n = \infty$ ballooning limit. Interestingly this pulse also has the highest ELM frequency of all the pulses. Finally, the highest β_N pulse 87339 is characteristically similar to 87338, and also reaches the PB stability boundary. This is contrary to the pre-ELM 70-99% previous results [96]. This pulse displays the same pedestal evolution as 87338, with the pedestal widening until it narrows just before the ELM. This corresponds to the gaining of second stability access in the 80-99% pre-ELM interval. Both 87338 and 87339 show that in this phase of the ELM cycle that the width of the pressure pedestal is governed by the region of the pedestal which has second stability access. Therefore, this suggests that increasing the region with second stability access will increase the pedestal width, and therefore the achievable height. This is an important result, with implications for optimising the pedestal.

6.8 Analysis of dataset: high deuterium gas injection rate and low triangularity

This section considers the high D_2 gas injection pulses 87346, 87350 and 87342, which are all at low triangularity $\delta = 0.2$ and high D_2 gas injection rate, $\Gamma_D = 18 \times 10^{21} es^{-1}$.

6.8.1 Pressure pedestal height and width evolution

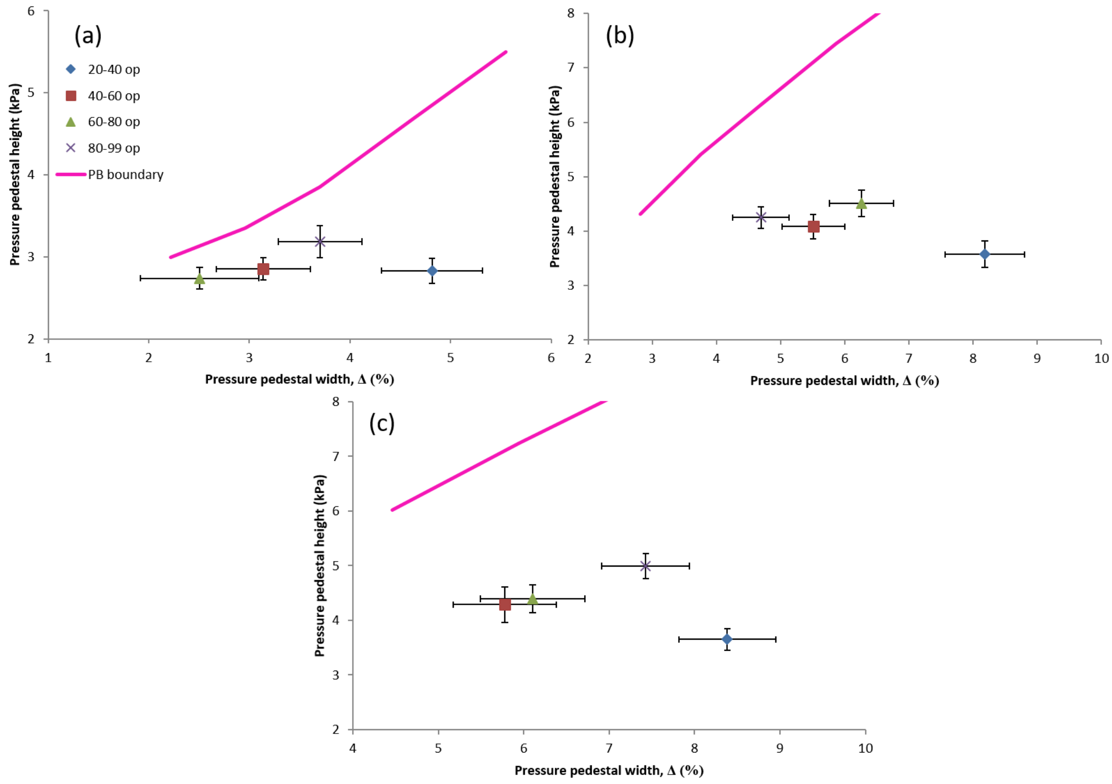

Figure 6.21: As for figure 6.17, but for high gas injection, low triangularity pulses (a) 87346, $\beta_N = 1.16$, (b) 87350, $\beta_N = 1.7$, and (c) 87342, $\beta_N = 1.95$.

This section details the evolution of the 20-40%, 40-60%, 60-80% and 80-99% OPs for the high gas injection pulses 87346, 87350 and 87342, compared to the PB boundary. The results of this study for the three high D_2 gas injection rate (high gas) pulses is shown in figure 6.21. Figure 6.21 (a) shows the PB boundary and the OPs for pulse 87346. This is the lowest β_N pulse of the high gas dataset and β_N = 1.16, Z_{eff} = 1.24 and the ELM frequency in the stationary phase is f_{ELM} = 48Hz. The evolution of this pulse does show EPED-like widening of the pedestal between the final two phases, 60-80% and 80-99%, of the ELM cycle. However, before this the pedestal narrows during the first three phases of the ELM cycle, with no significant change in height. The 80-99% OP is not at the PB boundary, and therefore not at the PB boundary when the ELM occurs. The OP is significantly further from the PB boundary than the low β_N medium gas pulse, 87338: and therefore does not appear to agree with the pre-ELM 70-99% analysis [96]. The pedestal width evolution between the final two phases is EPED-like. However, this result shows that additional physics is required to understand the ELM trigger here.

Figure 6.21 (b) shows the peeling-ballooning (PB) boundary and the OPs for pulse 87350. This is pulse has β_N = 1.7, which is identical to the low gas injection pulse 84795, Z_{eff} = 1.44 and an ELM frequency in the stationary phase of f_{ELM} = 98Hz. This f_{ELM} is significantly higher than any pulse seen in this analysis so far. There is an initial narrowing of the pedestal between the 20-40% and 40-60% phases. However, for the remainder of the evolution there no clear trend and the 80-99% OP is very far from the PB boundary, and therefore not at the PB boundary when the ELM occurs. This agrees with the pre-ELM 70-99% results [96]: pulses at high gas rate with a β_N greater than 1.5, achieve a pedestal height far below the height of the PB boundary. This shows that the pedestal does not show broadening before the ELM onset, and additional physics is also required to understand the ELM trigger here.

Finally, figure 6.21 (c) shows the peeling-ballooning (PB) boundary and the OPs for pulse 87342. This is the highest β_N pulse of the high gas dataset, with β_N = 1.95 which is much lower than the highest β_N achieved at low gas injection. It also has Z_{eff} = 1.52 and an ELM frequency in the stationary phase of f_{ELM} = 122Hz, which is the highest frequency of any of the low triangularity pulses analysed in this dataset. The range of $48 < f_{ELM} < 122$Hz at high gas injection rate illustrates the stronger scaling of f_{ELM} with P_{sep} compared to at low gas injection rate, illustrated in figure 6.16 (b). Initially between the first two phases of the ELM cycle, 20-40% and 40-60% there is significant narrowing of the pedestal. Throughout the rest of the ELM cycle, between the 40-60%, 60-80% and 80-99% phases the pedestal grows in height and widens. This evolution where the pedestal grows in height and width monotonically is characteristic of the widening described in the EPED model. However, as figure 6.21 (c) shows, the 80-99% is significantly far from the PB boundary. This result agrees with the pre-ELM 70-99% results [96]. Therefore, the evolution of the pedestal is EPED-like, but additional physics is again required to understand the ELM trigger.

6.8.2 KBM proxy: n=∞ ballooning stability

Now the KBM constraint is considered in more detail using the ideal $n = \infty$ ballooning limit. The results for the three high D_2 gas injection pulses, (a) 87346, (b) 87350 and

(c) 87342, are shown in figure 6.22.

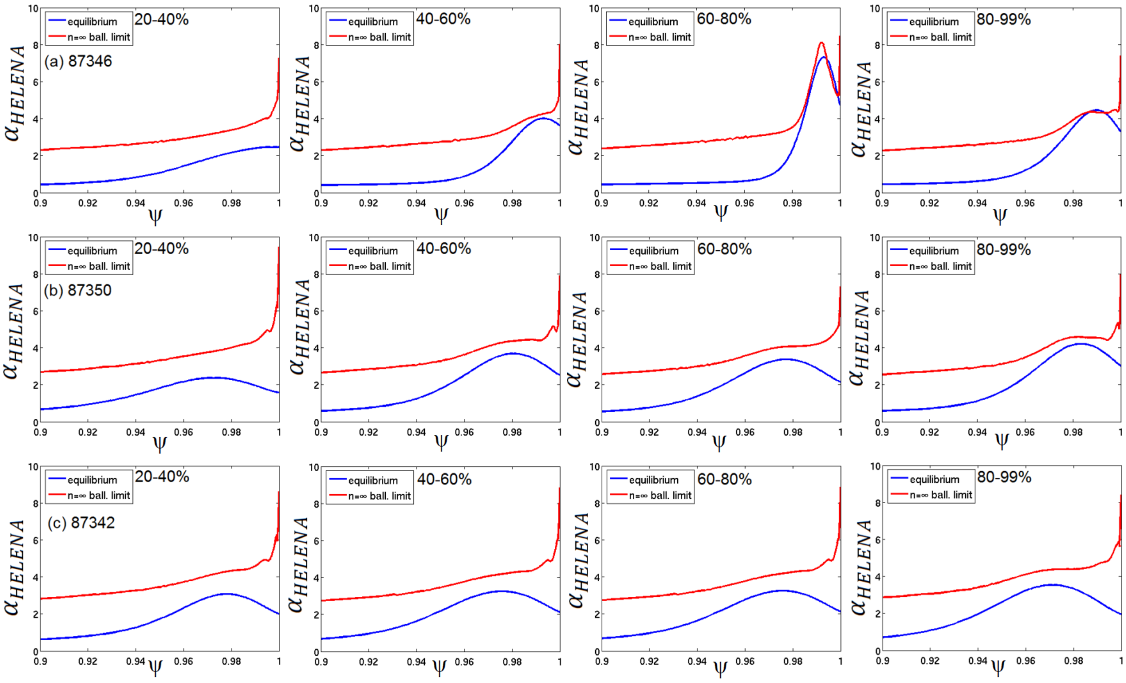

Figure 6.22: As for figure 6.18, but for low triangularity high gas injection pulses (a) 87346, $\beta_N = 1.16$, (b) 87350, $\beta_N = 1.7$, and (c) 87342, $\beta_N = 1.95$.

Firstly figure 6.22 (a) shows the results for pulse 87346. Recall that this pulse does not reach the PB boundary. The figure shows it can be seen that at the beginning of the ELM cycle, in the 20-40% phase, the pedestal is very small and $n = \infty$ ballooning limit is well above the pressure gradient: therefore, the pressure gradient is not constrained by the KBM. The pressure gradient then grows in the 40-60% phase and is against the $n = \infty$ ballooning limit, which constrains the pedestal gradient. In the 60-80% phase of the ELM cycle the $n = \infty$ ballooning limit has grown rapidly, providing the beginning of second stability access for the pressure gradient and controlling the width of the pedestal. Finally in the 80-99% pre-ELM phase an unknown change in the plasma occurs, causing the $n = \infty$ ballooning limit to drop and second stability access is lost. The pedestal in the pre-ELM phase is clearly constrained by the the $n = \infty$ ballooning limit, does not have second stability access and is unable to reach the PB boundary. Therefore, the pedestal widens before the ELM occurs as described by the EPED model and the pedestal is KBM constrained, but the pedestal does not reach the PB boundary.

Next figure 6.22 (b) shows the results for pulse 87346. Recall that this pulse does not reach the PB boundary. This shows that the pressure gradient is limited by the $n = \infty$ ballooning limit. Studying the ELM-cycle in (b), it can be seen that at the beginning of the ELM cycle, in the 20-40% phase the pedestal is very small and the $n = \infty$ ballooning limit is above the pressure gradient, and as such the pressure gradient is not constrained. The pressure gradient then increases to become much closer to the $n = \infty$ ballooning limit in the 40-60%, 60-80% and 80-99% phases. In the final pre-ELM phase, there is a slight increase of the $n = \infty$ ballooning limit above the pedestal, but there is not an indication of second stability access in this pulse, and a lower pedestal height is achieved. Therefore, despite the width evolution in this pulse, the pedestal is likely KBM constrained and fulfils the KBM criteria for EPED, but does not reaching the PB boundary.

Finally, consider pulse 87342, shown in figure 6.22 (c). Recall that this pulse does not reach the PB boundary. This figure shows that the pressure gradient is also broadly constrained by the $n = \infty$ ballooning limit. Initially, in the first 20-40% phase the pedestal is small and the pressure gradient is below the $n = \infty$ ballooning limit, suggesting it is not yet constrained. The pressure gradient then increases in the 40-60% phase so that the pedestal becomes close to the $n = \infty$ ballooning limit. This limits the achievable pedestal height in this pulse. There is no sign of second stability access in this pulse, and the pulse does not reach the PB boundary. This indicates a role of the KBM in this pulse, and the pedestal width shows EPED-like widening. This suggests that the KBM criteria are satisfied for this pulse, but PB theory does not explain the ELM trigger here.

6.8.3 Overview of high deuterium gas injection rate pulses

At high gas injection rate the pedestal does not reach the PB boundary in any of the cases. This is consistent at higher β_N with results for the pre-EM 70-99% interval [96], but not strictly consistent at low β_N, where the analysis shows that the pre-ELM 80-99% OP is not close to the PB boundary. Additionally, at greater β_N , the f_{ELM} is higher, and the pre-ELM 80-99% OP is further from the PB boundary. This also agrees with results for the pre-EM 70-99% interval [96]. None of these pulses have second stability access, but the pressure gradient in all three pulses is broadly constrained by the $n = \infty$ ballooning limit, and therefore is constrained by the KBM. This confirms that for this dataset of ten low triangularity pulses, reaching the PB boundary requires that the pedestal has second stability access. This is a key result. All this information suggests additional physics is required to explain the ELM trigger in these cases, and to try and address this the ELM characteristics of these three pulses will be analysed in section 6.10.

6.9 Analysis of dataset: s-α diagrams for 84797, 84795, 87350 and 87342

This section details further analysis for pulses 84797, 84795, 87350 and 87342, using $s - \alpha$ diagrams as another way of assessing the $n = \infty$ ideal ballooning stability. As there are four different types of behaviours seen in the pulses at low triangularity, there is an example pulse from each. These are all taken at $\psi = 0.98$, as this is the closest to the peak in the pressure gradient, shown in the $n = \infty$ ballooning diagrams, across the range of pulses analysed.

The first type of pulse observed is illustrated by pulse 84797. The pedestal shows

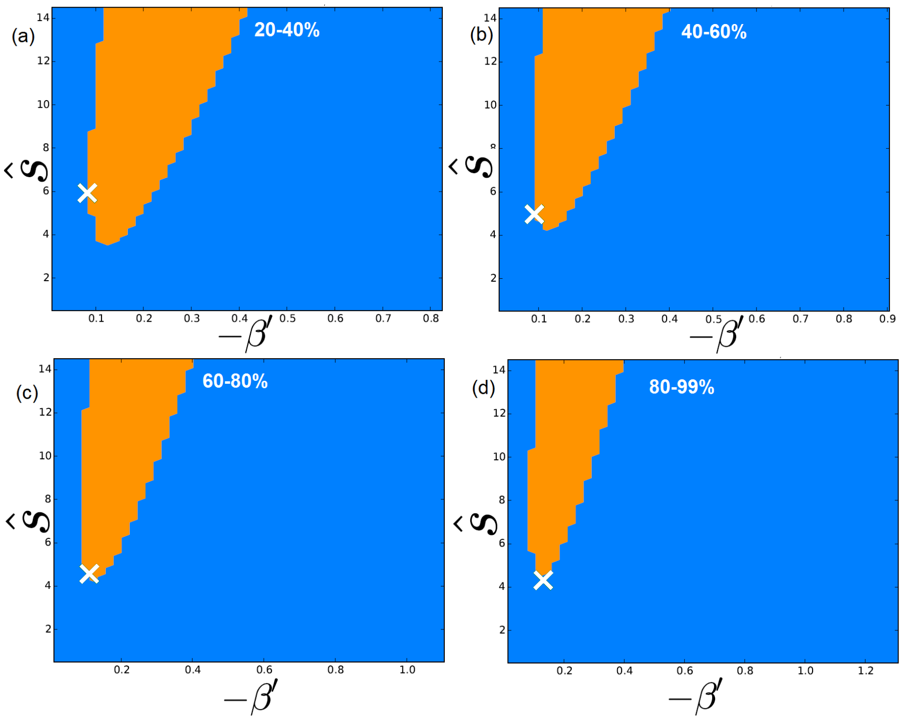

Figure 6.23: $s-\alpha$ diagram for 4 ELM cycle windows, (a) 20-40%, (b) 40-60%, (c) 60-80% and (d) 80-99% for pulse 84797 taken at $\psi = 0.98$, where the white cross is the OP, blue is the stable region and orange is the unstable region to ballooning modes. The x-axis is β', which is a normalised pressure gradient, proportional to α, and the y-axis is shear, s.

signs of broadening as the ELM is approached and the PB boundary is reached at the ELM onset. The $s-\alpha$ diagrams for all the four phases in the ELM cycle are shown in figure 6.23. As this figure shows, initially in the 20-40% and 40-60% phases of the ELM cycle there is not enough current in the pedestal region for second stability access to occur. However, as the current density in the pedestal begins to build, the OP moves downwards in shear as the pressure gradient is gradually building up in a self-consistent path, which is initially along the side of the unstable region. By the 60-80% phase the OP has moved to the bottom of the nose of the unstable region, but has not yet managed to travel under the unstable region. Finally in the 80-99% phase the OP has moved under the unstable region and achieves second stability access. This also agrees with the $n = \infty$ ballooning diagrams for the pulse, shown in figure 6.18 (a). Therefore this pulse shows how shear and pressure gradient travel in a self-consistent path, and that both the KBM and PB criteria are satisfied in this pulse.

The second type of pulse is illustrated by pulse 84795. This is a type of pulse which has no clear trend in the width evolution of the pedestal and the PB boundary is reached at the ELM onset. The $s-\alpha$ diagrams for all the four phases in the ELM cycle are shown in figure 6.24. Figure 6.24 (a) shows that initially in the 20-40% phase of the ELM cycle there is not enough current in the pedestal region for second stability access to occur. By the next 40-60% phase shear is reduced as the pressure has increased and second stability access is gained. The next 60-80% phase shows that second stability access remains. In the final 80-99% phase shear has further reduced and there is very clear second stability access far from the unstable region. All these findings agree with

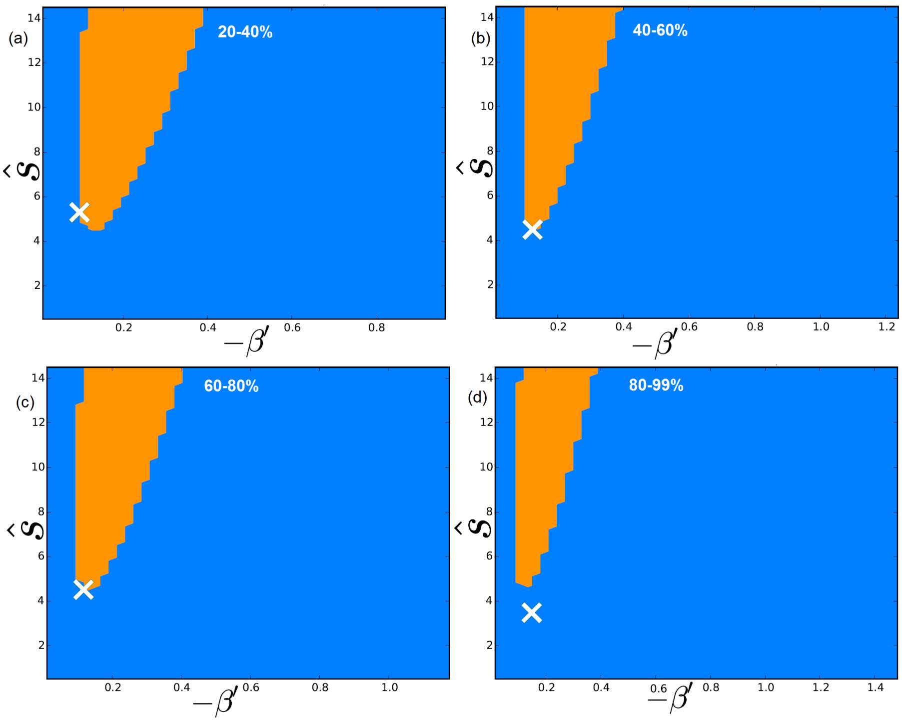

Figure 6.24: As in figure 6.23, but for pulse 84795.

the $n = \infty$ ballooning diagram for all the phases of the ELM cycle, shown in figure 6.18 (b). This rapid growth in the $n = \infty$ ballooning limit seen in the pre-ELM 80-99% phase is also seen here in the $s-\alpha$ diagram. Therefore this shows how shear and pressure gradient evolve despite no clear trend observed in the pedestal height and width. The $s-\alpha$ diagrams also illustrate how the dynamics of the variation of shear and pressure gradient between ELMs is a complex process.

The third type of pulse is observed is given by pulse 87350. This is a type of pulse which has no clear trend in the width evolution of the pedestal and the PB boundary is not reached at the ELM onset. The $s-\alpha$ diagrams for all the four phases in the ELM cycle is shown in figure 6.25. This figure shows that this pulse looks different to the previous two pulses, which reached the PB boundary. In the first 20-40% phase the OP is not up against the unstable region, and is not constrained in first stability space. This agrees with the $n = \infty$ ballooning diagram for this pulse, shown in figure 6.22 (b). However, in the other 40-60%, 60-80% and 80-99% phases, the OP is up against the unstable region, and therefore is constrained by the ideal ballooning limit. This also agrees with $n = \infty$ ballooning diagram for this pulse. Therefore this pulse is KBM limited once the ballooning unstable region is reached. As expected, there is no second stability access. This suggests there is not sufficient current density in the pedestal for the shear to be reduced significantly to allow the OP to travel under the unstable region and achieve second stability access. As discussed in subsection 2.4.1, the amount of current density at a certain pressure gradient is subtle and depends on a number of plasma parameters and complex feedback mechanisms. Therefore the pedestal, clamped by the KBM, was unable to obtain a high enough height to reach the PB boundary.

The fourth and final type of pulse is illustrated by pulse 87342. This is a type

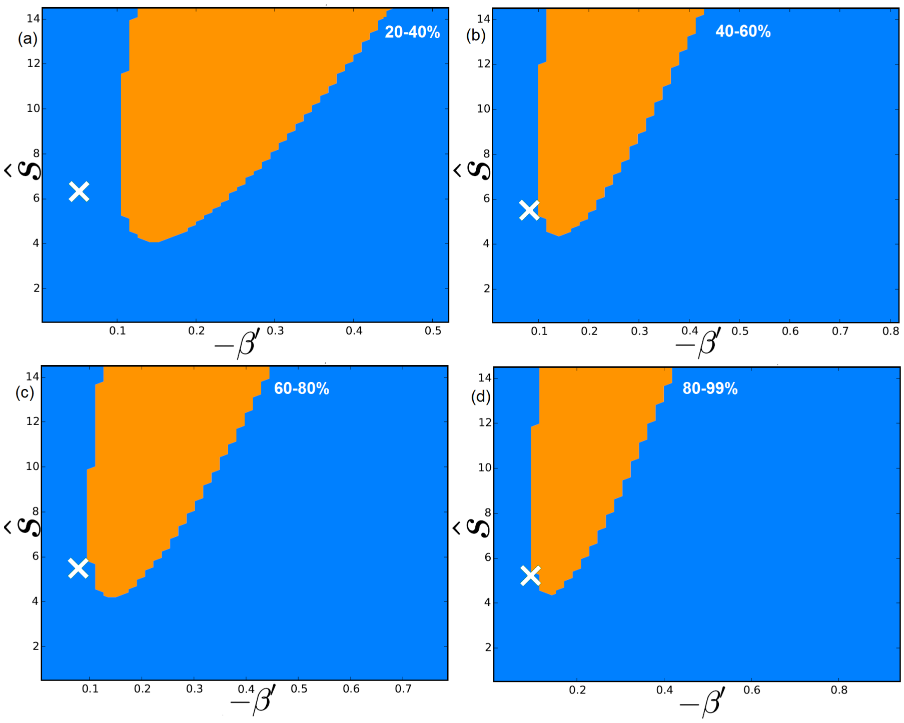

Figure 6.25: As in figure 6.23, but for pulse 87350.

of pulse which has broadening width evolution of the pedestal as the end of the ELM cycle is approached, but the PB boundary is not reached at the ELM onset. The $s-\alpha$ diagrams for all the four phases in the ELM cycle is shown in figure 6.26, this shows that this pulse looks similar to 87350. In the first 20-40% phase of the ELM cycle the OP is also not up against the unstable region and therefore this is not constrained in first stability space and is also not ballooning limited. This agrees with the $n = \infty$ ballooning diagram for this pulse, shown in 6.22 (c). In the 40-60%, 60-80% and 80-99% phases in the ELM cycle the OP is closer to the unstable region, but not up against the unstable region, as in 87350. This also agrees with $n = \infty$ ballooning diagrams for this pulse, which show that the equilibrium pressure gradient is near to the $n = \infty$ ballooning limit, but not right at the limit. The pedestal can therefore be considered broadly constrained by the ideal ballooning limit, and it is likely to be KBM limited.

All four of these pulses confirm that second stability access occurs in the pedestals that reach the PB boundary and that the evolution in $s-\alpha$ space shows whether a pedestal is constrained by the ballooning limit, and therefore the KBM limit. This is true regardless of whether there is no clear trend in the pedestal width evolution, or if there is EPED-like widening of the pedestal as the end of the ELM cycle is approached.

6.10 ELM trace comparison

This section uses the ELM traces from Beryllium-II (Be-II) emission from the inner divertor to begin to address the question of what causes the ELM to be triggered in pulses which do not reach the PB boundary. Firstly, consider the Be-II emission showing ELMs from two of the low D_2 gas injection rate pulses, 84797 and 84795, shown in figure 6.27 (a) and (b) respectively. Recall that these both reach the PB

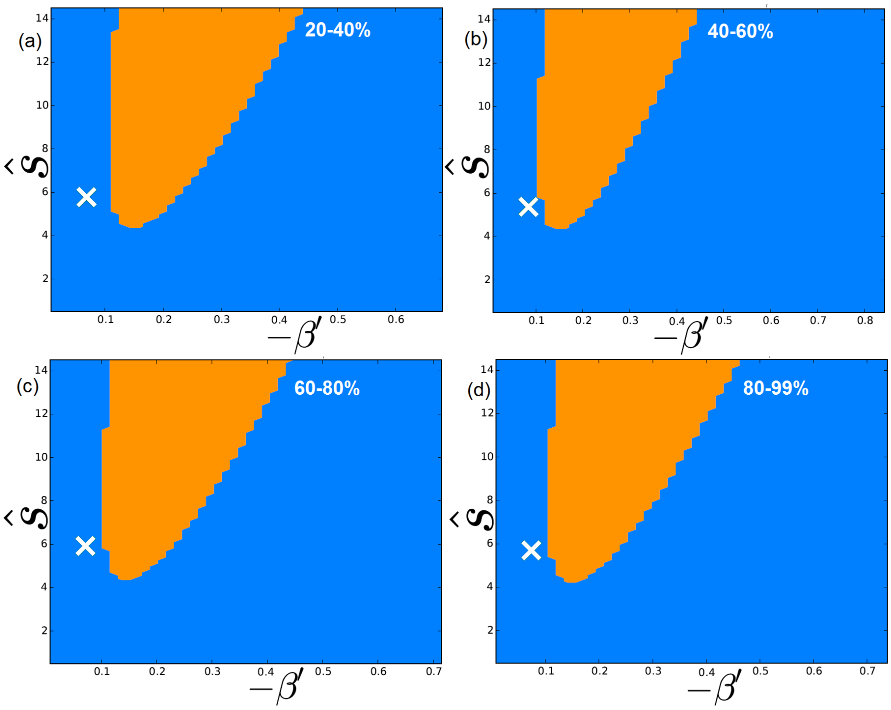

Figure 6.26: As in figure 6.23, but for pulse 87342.

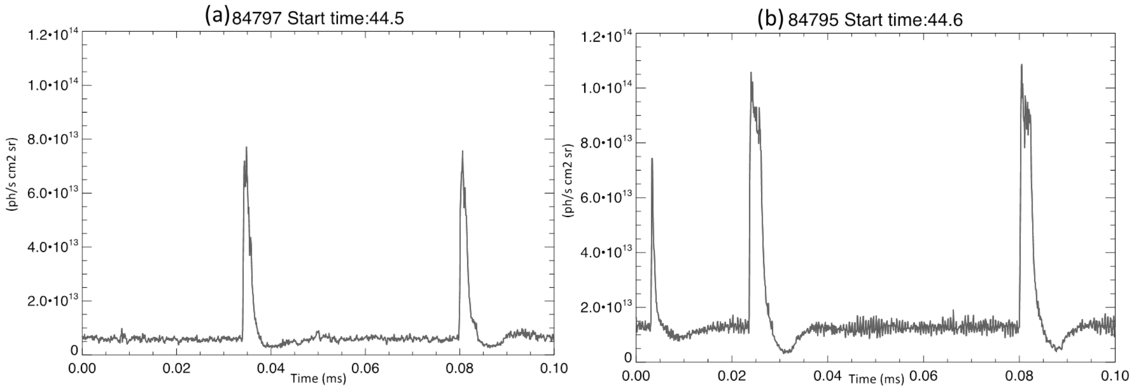

Figure 6.27: Be-II emission traces showing ELMs from low gas injection rate pulses (a) 84797 and (b) 84795 which do reach the peeling-ballooning (PB) boundary at the ELM onset.

boundary. As the figure shows, these traces have the classic ELM characteristics of type I ELMs: a sudden sharp rise to a peak in the emission, followed by a slower decay from the peak in the emission.

Now, the emission for the three high D_2 gas injection rate pulses can be considered in order of increasing β_N, and therefore increasing f_{ELM}: 87346, 87350 and 87342. Recall that none of these pulses reach the PB boundary when the ELM occurs. It was postulated in [96] that as these pulses that do not reach the PB boundary, despite the fact that the ELMs increase in frequency with power they could be of resistive nature, more like type III ELMs. Figure 6.28, shows the same Be-II emission traces for these pulses, (a) 87346, (b) 87350 and (c) 87342.

This figure 6.28 shows that these ELMs have a very different and much more symmetrical peak in the emission traces than the ELMs shown in figure 6.27. Now consider the Be-II emission traces separately; starting with the middle $\beta_N = 1.7$ pulse

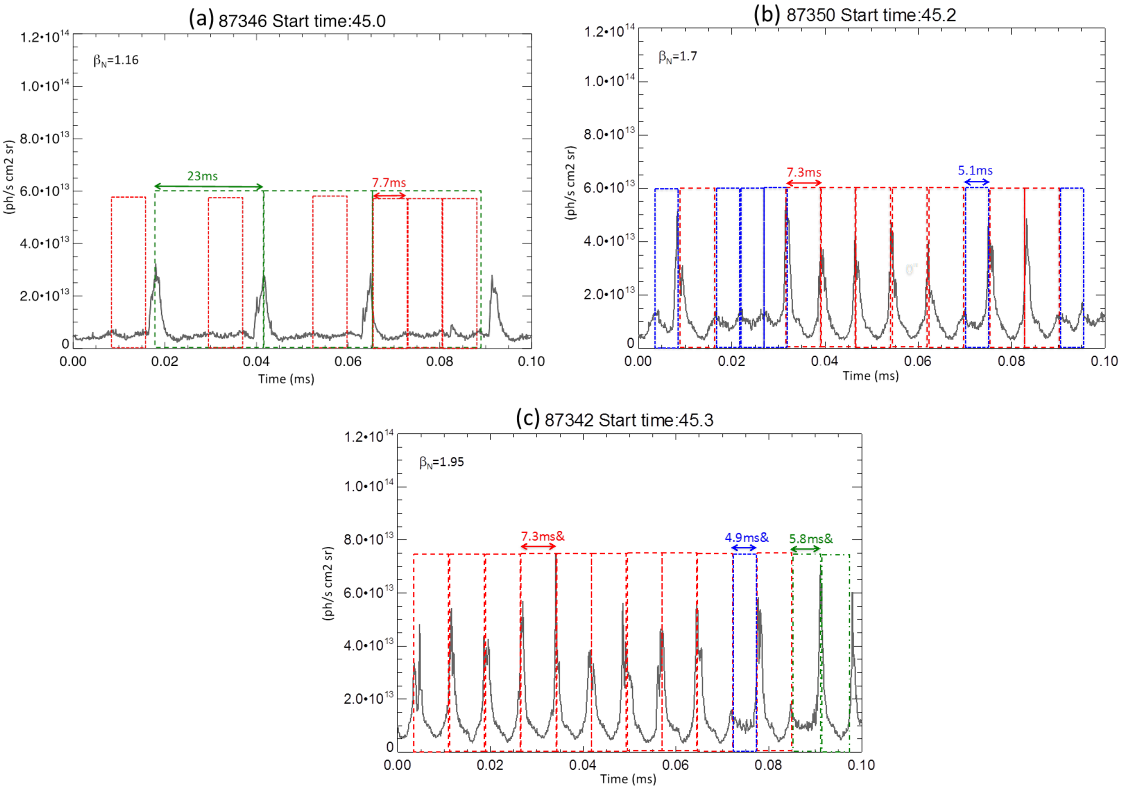

Figure 6.28: Be-II emission traces showing ELMs from high gas injection rate pulses (a) 87346 (b) 87350 and (c) 87342 which do not reach the peeling-ballooning (PB) boundary at the ELM onset.

87350 shown in (b), as this has more frequent ELMs than pulse 87346 shown in (a). As pulse 87350 shows, there are two different periodic behaviours in this pulse. The most prominent is the large spikes, which is the characteristic signature of an ELM event. The second is an underlying oscillation with low amplitude. In the figure there are also two different coloured dashed boxes: red, which correspond to intervals with a period of 7.3ms, and blue, which correspond to intervals with a period of 5.1ms. ELMs are usually quasi-periodic so the regularity of the events is remarkable. Following each ELM spike in the emission trace, the time to the next event, whether that be a low amplitude oscillation or another ELM, is exactly 7.3ms and this is denoted by the red boxes. At the end of a low amplitude oscillation the time until the next event, which can be either another oscillation or an ELM, is exactly 5.1ms and is denoted by the blue boxes. This remarkable periodicity suggests that these events are therefore caused by the same underlying instability, which can cause either the low amplitude oscillation or an ELM [130].

There are three different interpretations of this result. The first is that there is a plasma instability that is triggered as the plasma parameters pass through a threshold, and this instability can evolve: either into an oscillation, or erupting explosively such as in a purely explosive ballooning mode [84] that results in an ELM. The plasma then takes longer to recover after an ELM as it is a more significant event [130]. The second interpretation is that there is an instability that corresponds to the low amplitude oscillation, and this instability can sometimes then drive an ELM non-linearly [130].

The final explanation is that there is a feedback or power supply system that is driving the oscillation in the plasma, and this can sometimes trigger an ELM [130]. In previous work, a large database of 120 consecutively produced JET-ILW pulses with ELMs was analysed and showed similar results [165]. This research found that certain periods were statistically more common, and when comparing all the pulses together a clear link was observed between the plasma confinement, vertical plasma oscillations, ELM occurrence and an oscillation in a control coil current [165]. This is usually not observed when looking at individual pulses. Therefore, using this database approach reveals previously unobserved physics; through the unexpected link between small changes in plasma position and changes to edge transport and stability [165].

Next consider pulse 87342, which is shown in figure 6.28 (c), and has the highest ELM frequency and highest $\beta_N = 1.95$ of the three high gas injection rate pulses. This pulse has similar behaviour to the previous pulse 87350, seen in (b). However, the difference in this pulse to the previous pulse is the fact that almost every event results in an ELM. There are only two other events, shown as the blue box and the green box, which last 4.9ms and 5.8ms respectively. Note that the period to the next event following the ELM, denoted by the red box as in the previous pulse, also has a repeatable period of 7.3ms. The 7.3ms period is the same as the previous pulse, despite a change in the plasma parameters. Additionally, the period to the next event following an ELM is longer than the period to the next event after an oscillation, which is also the same as in the previous pulse, 87350. Periodic ELM events, as seen in both 87350 and 87342, are not commonly observed: quasi-periodic behaviour is typically the characteristic signature for ELM events [130].

Finally consider the trace for pulse 87346 which is shown in figure 6.28 (a). This pulse has the lowest $\beta_N = 1.16$ of the three pulses, and also has the lowest ELM frequency. This trace shows that there are two different periodic behaviours in this pulse: the spikes in the emission which is characteristic of the ELM event, and the underlying low amplitude oscillation. Firstly, the underlying low amplitude oscillation in this case denoted by the red boxes and has as a characteristic period of 7.7ms, which is longer than in the previous two pulses, but shorter than the period between the ELM events. Secondly, there are the green boxes which characterise the time between the larger ELM spikes. These green boxes show that the time between the first and second ELM, and the second and third ELM is exactly 23 ms, and the time between the third and fourth ELM is slightly longer at 27 ms. The longer period between the third and fourth ELM may be related to very small spike in the emission, just after 0.08ms and in the final red box. This could be a failed ELM, which caused partial relaxation of the profiles [130].

6.11 Analysis of dataset: high triangularity, low deuterium gas injection rate

In this section the high triangularity, δ = 0.4, low D_2 gas injection rate, $\Gamma_D = 2.9 \times 10^{21} es^{-1}$, pulses 84787, 84541 and 84788 are considered. These three pulses, have a range of normalised beta, β_N, from 1.36 to 3.0. Note that two of the three pulses 84787 and 84788, have been analysed using the 30% ELM synchronised windows: 10-40%, 40-70% and 70-99%, due to poor statistics.

6.11.1 Pressure pedestal height and width evolution

Here the evolution of the pedestal during the ELM cycle for the ELM-synchronised OPs are considered. The peeling-ballooning (PB) boundary is also considered to obtain the proximity of the OPs to the PB boundary. The results of this study for the three high δ, low D_2 gas injection rate pulses is shown in figure 6.29.

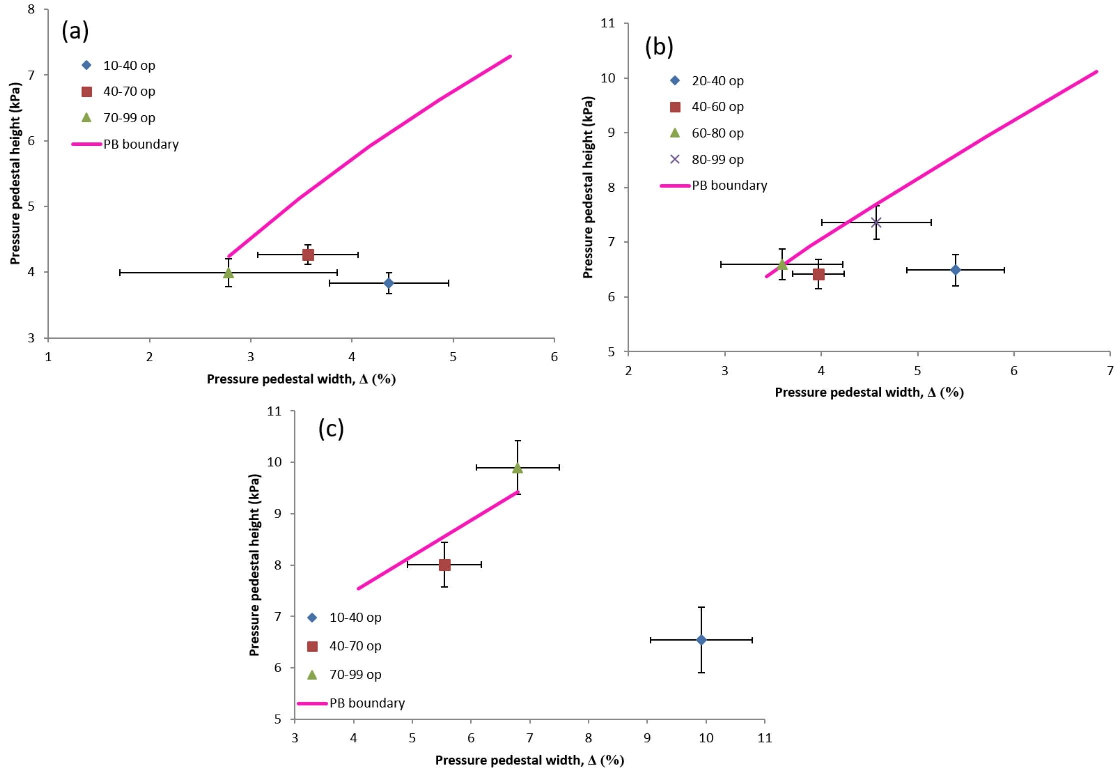

Figure 6.29: As figure 6.17, but for the low gas injection, high triangularity pulses (a) 84787, β_N = 1.36, (b) 84541 β_N = 2.36, and (c) 84788, β_N = 3.0. In (a+c) 10-40% OP is the blue diamond, 40-70% is the red square and 70-99% is the green triangle.

Firstly consider pulse 84787 which is shown in figure 6.29 (a). This is the lowest β_N pulse and β_N = 1.36, Z_{eff} = 1.15 and the ELM frequency in the stationary phase is f_{ELM} = 15Hz, which is similar to the low δ, low gas injection pulses. As the figure shows, this pulse does not exhibit the characteristic widening before the ELM, as described by EPED model. The pedestal narrows throughout the ELM cycle with no significant change in height. This pulse is clearly at the PB boundary within the error bars, if the PB boundary is extended as it should be. Therefore despite the narrowing width evolution, which is inconsistent with EPED, the PB criteria is satisfied.

Next consider pulse 84541 shown in figure 6.29 (b). This is the middle β_N pulse and β_N = 2.36, Z_{eff} = 1.05 and the ELM frequency in the stationary phase is f_{ELM} = 15Hz. As the figure (b) shows, this pulse does exhibit the characteristic widening before the ELM, as postulated by EPED model. The evolution is as follows: the pulse narrows through the first three phases of the ELM cycle: 20-40%, 40-60% and 60-80% with no significant change in the pedestal height. Then between the 60-80% and the pre-ELM 80-99% phase of the ELM cycle the pedestal exhibits the characteristic widening of the pedestal, with an increase in the pedestal height, which agrees with the EPED model. This pulse is also clearly at the PB boundary. Therefore this pulse is consistent with the EPED model evolution and it reaches the PB boundary.

Finally consider pulse 84788 shown figure 6.29 (c). This is the highest β_N pulse and β_N = 3.0, Z_{eff} = 1.26 and the ELM frequency in the stationary phase is f_{ELM} = 25Hz. This figure shows that firstly the pedestal narrows and increases in height between the 10-40% and 40-70% phases of the ELM cycle. Then, between the 40-70% and the pre-ELM 70-99% phases, the pedestal widens and increases in height which is characteristic of EPED. The pre-ELM 70-99% is just over the PB boundary, and therefore is PB limited. Therefore, this pulse is both consistent with the EPED model and it is PB limited when the ELM occurs.

6.11.2 KBM proxy: n=∞ ballooning stability

This section details the ideal $n = \infty$ ballooning limit for the same ELM-synchronised intervals as the pedestal evolution diagrams. The results are shown in figure 6.30, where (a) 84787, (b) 84541 and (c) 84788.

Firstly, consider pulse 84787 shown in figure 6.30 (a). Recall that this pulse reaches the PB boundary. This figure shows that firstly in the 10-40% phase the pedestal is small and constrained by the $n = \infty$ ballooning limit. Next, in the 40-70% phase, the $n = \infty$ ballooning limit has started to increase which allows the pressure gradient to increase and shows the beginning of second stability access. In the pre-ELM 70-99% phase there is rapid increase of the $n = \infty$ ballooning limit, and the pressure gradient has increased significantly. This shows clear second stability access for the pedestal. Therefore, the evolution of the pedestal, including the width, is controlled by the $n = \infty$ ballooning limit. This pedestal shows good agreement with the two constraints that underpin the EPED model: the gradient is constrained by KBMs, and then the evolution of the pedestal terminates when the PB boundary is reached.

Next consider pulse 84541, shown in figure 6.30 (b). Recall this pulse reaches the PB boundary. This figure shows that there is second stability access throughout every ELM interval. In the first 20-40% phase there is second stability access, and the pressure gradient fills the second stability region provided by the $n = \infty$ ballooning limit. Between the 20-40% and 40-60% intervals the narrowing of the pressure gradient

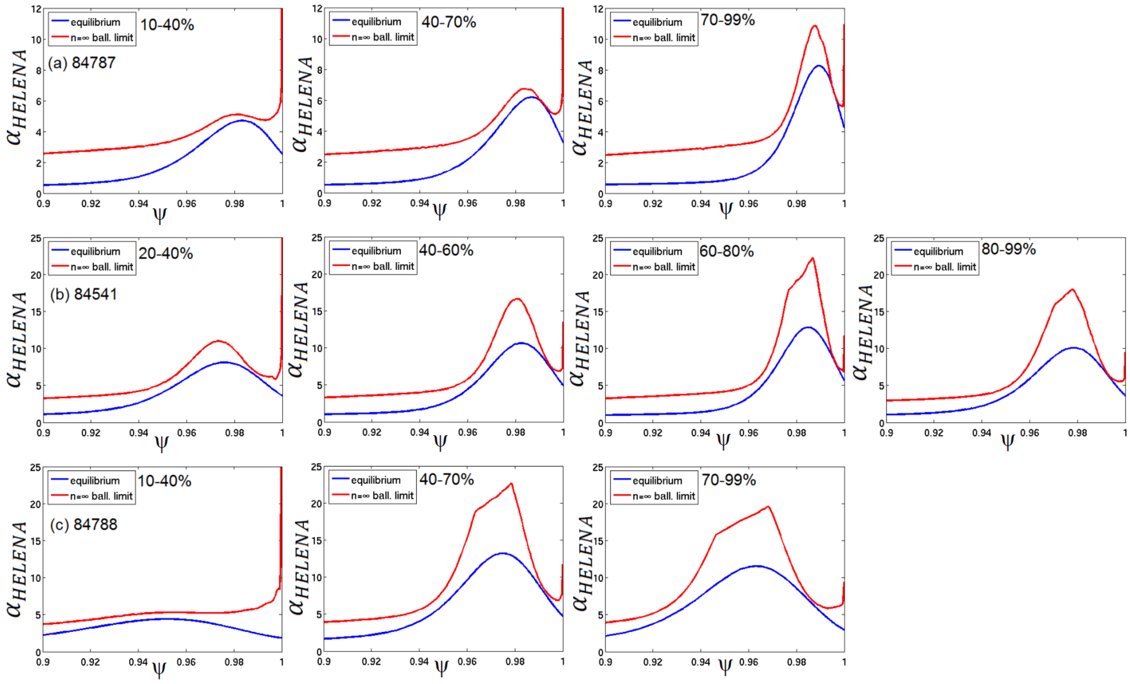

Figure 6.30: As in figure 6.18, but for the low gas injection high triangularity pulses (a) 84787, $\beta_N = 1.36$, (b) 84541 $\beta_N = 2.36$, and (c) 84788, $\beta_N = 3.0$.

can be seen as the $n = \infty$ ballooning limit region of second stability access narrows and increases rapidly. The pedestal gradient keeps increasing with a little narrowing between the 40-60% and 60-80% phases. Finally, the second stability region of the $n = \infty$ ballooning limit widens from the 60-80% to the 80-99% interval, allowing the pedestal to widen significantly. This agrees with the EPED model observations, and this pulse is also at the PB boundary and has second stability access. This pulse shows how the pedestal always fills the second stability region of the $n = \infty$ ballooning limit: if there is a narrowing or widening of this region, the pressure gradient will narrow or widen accordingly. This provides further evidence that the pedestal width can be maximised by maximising this second stability region, therefore allowing the pedestal to further increase in height and improving the plasma performance.

Finally, consider pulse 84788 which is shown in figure 6.30 (c), recalling that pulse is just over the PB boundary. The figure shows that initially in the 10-40% phase the pulse is constrained by the $n = \infty$ ballooning limit, the pedestal is very wide and there is no significant peak in the pressure gradient. However, by the 40-70% phase, there has been a rapid increase in the $n = \infty$ ballooning limit, creating a wide area of second stability access which the pedestal fills as the pressure gradient increases. In the final 70-99% phase the region of second stability access widens significantly, to become the widest second stable region in any of the pulses from the dataset, and with this the pedestal widens significantly. This agrees with the EPED model observations, and is also PB limited.

6.11.3 Overview of low deuterium gas injection rate, high triangularity pulses

All three pulses at high triangularity and low gas reach the PB boundary, which is expected as they are all at low gas injection rate and at high δ thus allowing higher pedestal heights to be obtained. Comparisons between the density and temperature pedestal gradients in ASDEX Upgrade and DIII-D indicate that the normalised pressure gradient, α, shows strong correlations with plasma shape in a way expected by peeling-ballooning theory [141]. It has also been shown that the pulses all have second stability access, which is also expected, given the findings at low δ, and that these pulses also have the highest pressure gradient pedestals in the dataset. Plasma parameters including shaping and β are known to change the width of the region of second stable access [90]. The increased triangularity, and also the improved β_N that is achieved in these pulses allows the widest region of second stable access seen in the dataset. These three pulses also show that as β_N increases, the width of the second stability access in the 80-99% pre-ELM interval also increases.

Two pulses, 84541 and 84788, which are the two highest β_N pulses with the widest second stability access show EPED behaviour, where the pedestal widens for an increase in height as the ELM is approached; the pedestal has been shown to be able to widen due to the widening of the second stability access region. All three pulses provide additional evidence that the width of the pedestal is controlled by the width of the second stability access region in the $n = \infty$ ballooning limit. Also shown is improvement of the width of the second stability access region by increasing β_N at high triangularity. This further suggests a route to optimise the pedestal performance by maximising this region.

6.12 Conclusions and further work

The analysis in this chapter was undertaken to study the inter-ELM evolution of the pedestal in JET-ILW plasmas, and considered the peeling-ballooning mode (PB) and kinetic ballooning mode (KBM) instabilities. The dataset comprises of ten low triangularity JET-ILW pulses at 1.4MA/1.7T, across three different D_2 gas injection rates: low, medium and high. Also in the dataset are three high triangularity, low D_2 gas injection rate pulses, at the same 1.4MA/1.7T. This analysis shows that there is no consistent relationship between the inter-ELM pedestal width evolution and $\beta_{p,ped}$. Additionally, the pedestal only sometimes has the characteristic monotonic increase in pedestal height and width towards the PB boundary as described by the $\sqrt{\beta_{p,ped}}$ scaling in the EPED model. Furthermore, in some pulses the PB was not reached before ELM onset occurred; typically in the high gas injection rate pulses. From this analysis there are four distinct types of pulses:

(a) The pedestal width shows signs of broadening as the ELM onset is approached, and the PB boundary is reached at ELM onset: pulses 84797, 84541 and 84788, which are all low gas injection pulses.

(b) The pedestal width evolution shows no clear trend, but the PB boundary is reached at ELM onset: pulses 84795, 84796, 84794, 87338, 87339, 84787. These are all low and medium gas injection pulses.

(c) The pedestal width evolution shows no clear trend, and the PB boundary is not reached at ELM onset: pulse 87350. This is a high gas injection pulse.

(d) The pedestal width shows signs of broadening as the ELM onset is approached, but the PB boundary is not reached at ELM onset: pulses 87341, 87346, 87342. These are medium and high gas injection pulses.

In all of the thirteen pulses the pressure gradient is close to the $n = \infty$ ideal MHD ballooning limit, which has previously shown to be a good proxy for the KBM. In the cases where there is second stability access, even if the pedestal gradient is not strictly limited by the KBM, the pedestal width is controlled by the size of the second stability access region. Therefore, the pressure gradient in the pedestal region evolves in the inter-ELM period constrained by the KBM. If the pulse reaches the PB boundary, the physics controlling the pedestal evolution and triggering the ELMs is consistent with the criteria for the EPED model, even in cases where there is complex width evolution. Likewise, if the pedestal does not reach the PB boundary, it still appears that the pedestal gradient is limited by KBMs, and there is no access to second stability. The pedestal either never has this access or, as in the case of pulse 87346, this access is lost before the final ELM cycle interval is reached. This implies that only the pulses that have second stability access have a sufficient pedestal pressure gradient, and therefore sufficient pedestal height, to reach the PB boundary. All the high gas injection pulses do not reach the PB boundary and their pedestal pressure gradient is constrained by the $n = \infty$ ballooning limit.

As previously mentioned, when the pedestal enters the second stability access region the pedestal width is governed very clearly by the width of the second stability access region. This is especially well illustrated by the high triangularity pulses. Note that the size of this region is very sensitive to many plasma parameters, such as collisionality, gas fuelling rate, and heating power, which influence the dynamics. This region is also crucially dependent on the current density, which depends on the pressure gradient, and the current and the pressure gradient have different diffusion times. This creates a complex, non-trivial feedback mechanism, making access to second stability a subtle process. Therefore, very small changes in plasma parameters could lead to a significant change in the width of this region, and thus the width of the high pressure gradient. This could explain the many various different inter-ELM pedestal width evolutions seen across this dataset. An interesting feature of second stability is also seen most prominently at high triangularity. This is the observation that the $n = \infty$ ballooning limit can increase so rapidly that the pedestal gradient in comparison is significantly lower than the limit. This could perhaps be to the fact that the pressure gradient in the pedestal can only increase on the transport time-scale, which is likely to be slower than the rapid increase in the $n = \infty$ ballooning limit, but transport analysis would be needed to confirm this. This can be visualised as travelling under the unstable region of the $s - \alpha$ diagram, the so-called nose, where the pressure gradient is able to increase rapidly for a small decrease in shear, due to a small increase in current density.

Analysis of the ELM characteristics of some of the low triangularity pulses shows remarkable differences between the pulses which reach the PB boundary at low gas injection rate, and the pulses which do not reach the PB boundary at high gas injection rate. The first notable difference is the characteristics of the ELM peak itself. In the low gas injection rate discharges, the characteristics are typical for a type I ELMy H-mode discharge: there is an initial sharp rise in the emission trace, which then has a longer tail of decay. However, in the high gas injection rate the rising and falling of the ELM peaks in the emission are much more symmetrical. Furthermore, in the high gas injection rate traces there is an additional low amplitude oscillation present in all of the pulses. Both the ELMs and oscillations provide surprisingly uniform periodicity, which is highly unusual since ELM events are typically quasi-periodic. The periodicity of the oscillations and ELM events provide evidence that they are likely caused by the same instability, and there are multiple interpretations for this. It could be a pure explosive ballooning mode, the oscillation itself could trigger the ELM non-linearly, or it could be operational, for example due to the control systems.

There is more work remaining to be done on this topic. These results show a new avenue to explore for optimising the pedestal in JET-ILW plasmas. This is key for obtaining the desired performance in the planned JET-ILW D-T experiments, as well as further ahead in the ITER tokamak. These results show that the area of second stable access influences the width of the pedestal region, and thus allows for a greater pedestal height and improved confinement. Stronger shaping in the high triangularity pulses has shown that this further widens the second stability region, which highlights the importance of plasma shaping. This suggests that maximising triangularity is a route for improving performance. An extension of this study is to study high D_2 gas injection rate pulses at high triangularity, to assess whether the PB boundary is reached in the scenario with the improved shaping at higher fuelling.

Another important direction is to extend the Be-II emission ELM traces study to longer times and more ELMs for the pulses already analysed, to see whether this behaviour is also seen in other times in the pulse. Also important is to identify the cause of the oscillations which would identify why these plasmas fail to reach the PB boundary. It could be that they are unrelated to the failure to reach the PB boundary, and this is due to lack of second stability access for the KBM. It could also be that the oscillations are the reason the plasma fails to reach the PB boundary, not the lack of second stability access. It could also be that the oscillations are caused by the lack of second stability access, and therefore both are determined by the same physics [130]. It is important also to perform this analysis on JET-C pulses with similar plasma parameters. This is because JET-C did not appear to have the same performance issues as are seen in JET-ILW plasmas. This would help to identify the differences between pedestals in the two different JET wall environments; therefore enabling the discovery of regimes which optimise the pedestal and the plasma confinement, in the future JET D-T campaign.

This analysis also shows that the pedestal region in this dataset may be sensitive to the plasma dynamics, such as fuelling and transport processes. Therefore, in order to predict future JET pedestals, unlike other tokamaks such as MAST and DIII-D which follow $\sqrt{\beta_{p,ped}}$ scaling, a dynamic model containing parameters such as the current and energy diffusion time-scales may be necessary. This would also provide improved predictability and understanding of the subtle transport and stability processes in the pedestal for ITER which, while not directly useful as ITER is likely to have ELM suppression or mitigation, will help improve ITER pedestal prediction.

Chapter 7

Conclusions and future work

7.1 Conclusions

The development of fusion as a commercially viable energy source is an attractive option for meeting the growing global energy demand. The tokamak is currently the most developed device for achieving controlled fusion, and the crucial step in the roadmap is the success of the ITER tokamak. In order for the ITER tokamak to achieve the goal of $Q = 10$, and demonstrate the viability of fusion, it has been designed to operate in the H-mode baseline scenario. H-mode is characterised by an edge transport barrier, known as the pedestal, which provides improved confinement. However, H-mode is coupled with the observation of the quasi-periodic bursts known as edge localised modes (ELMs). On the ITER scale these have the potential to cause serious damage, significantly limiting the lifetime of the divertor. Therefore, it is vital to understand the physics of ELMs in order to mitigate or suppress them. ELMs cause a periodic collapse of the pedestal and a loss of particles and energy from the plasma. ELMs are believed to be triggered by an ideal MHD instability known as the peeling-ballooning mode. While ideal MHD cannot explain the mechanism of the whole ELM cycle, it provides important information on the triggering of the instability and an indication of the growth rate of the mode. It also provides vital insight into the stability boundary, and therefore can be exploited to determine regimes of operation where ELMs are not triggered. In general the peeling-ballooning stability boundary has been found to be reached in type I ELMy H-mode plasmas.

This thesis has presented research investigating the edge stability of tokamak plasmas and the ELM phenomena, using ideal MHD. Chapter 2 presented the theory of ideal MHD, its applicability to tokamak plasmas, and an introduction to the ELITE code. The ELITE code was developed as an efficient tool for calculating intermediate-high n peeling-ballooning stability. It has been very successful, and has also been incorporated into the EPED model of pedestal structure.

Chapters 3 and 4 detail the extension of the ELITE code to arbitrary n. This was initially motivated by the appealing ELM-free mode of operation known as quiescent H-mode (QH-mode). The original QH-mode has a low n edge harmonic oscillation (EHO), which provides density control and keeps the pedestal near the kink/peeling boundary.

Chapter 3 shows the successful extension of the ELITE formalism to arbitrary n. This was achieved using a new expansion for the second perturbation U from its Euler equation, thereby keeps all remaining orders of U in the W term. Both perturbations were then Fourier decomposed, and matrix manipulation was performed to obtain a single set of Euler equations, which eliminates the second Fourier amplitude. This allowed the new arbitrary n equations to be solved using many of the same routines as the original ELITE equations.

Chapter 4 detailed the process and results of extensive benchmarking of the new arbitrary n ELITE formalism, both against original ELITE as well as GATO and MARG2D. This was performed for different tokamak poloidal cross section geometries. This was a vital step for verifying the results produced by the new formalism. The chapter also details other modifications of ELITE performed in the implementation process. Additionally, chapter 4 presented results from the development of a δW diagnostic in the original version of ELITE. The diagnostic allows the exact relative amplitude of all the drive terms in the δW equation to be determined. Analysis using the diagnostic has shown that, although the kink term is $O(n^{-1})$, it survives to very large n because of steep current density gradients in the pedestal. This result shows that the assumption in gyrokinetic codes that at high n the kink term is insignificant is not an accurate assumption, and may be important for a reliable prediction of the KBM stability in realistic low collisionality tokamak pedestals.

Chapter 5 details the analysis of DIII-D shot 163520, which allows comparison between the standard EHO and wide-pedestal QH-mode regimes. The results show that EHO QH-mode has a low n peeling mode present which is localised in the pedestal region. This shows that the arbitrary n ELITE code finds similar results to previously published research on DIII-D QH-modes. During most of the wide-pedestal QH-mode phases the plasma is predicted to be stable to $1 < n < 10$ modes, and sits below the peeling boundary. This is consistent with previous observations. To obtain the proximity to the stability boundary, the calculated current density was increased which shows that if this is increased by 20% an $n = 4$ mode is seen. In the final wide-pedestal phase, increasing the current density by 20% destabilises low n modes between $2 < n < 4$. The modes seen in wide-pedestal QH-mode are much more global than seen in the standard EHO phase. However, ELITE is unable to explain the low n ELM precursor seen on the magnetics. This could be due to the lack of flow shear in the arbitrary n formalism. Previous work has shown that low n modes in QH-mode are destabilised by flow shear, and therefore ELITE could be underestimating the low n peeling-ballooning stability.

Chapter 6 explores the inter-ELM pedestal evolution in JET-ILW plasmas, and compares the edge stability and pedestal evolution to the EPED criterion. Since the installation of the JET-ILW pedestal performance has significantly decreased from that obtained in JET-C plasmas. This has consequences for the upcoming JET D-T campaign, as well as for the performance of ITER. Previous research on the pre-ELM pedestal stability in JET-ILW plasmas showed that many pedestals fail to reach the peeling-ballooning boundary. Furthermore, JET pedestals have previously been found not to evolve with the characteristic $\sqrt{\beta_{p,ped}}$ scaling described by the EPED model. A dataset of thirteen JET-ILW pulses was analysed, ten at low triangularity and three at high triangularity. At low triangularity the pulses had three different gas injection rates: low, medium and high. The high triangularity pulses were all at low gas injection rate.

The analysis of the JET-ILW dataset in chapter 6 shows that there is no consistent relationship between pedestal evolution and $\sqrt{\beta_{p,ped}}$ scaling. However, all the pedestals were found to have a pedestal gradient close to the $n = \infty$ ballooning limit. The $n = \infty$ ballooning limit has been previously shown to be a good proxy for the KBM. Therefore, despite often complex pedestal width evolution, all pedestals are broadly constrained by the KBM. At ELM onset, pedestals that had reached the peeling-ballooning boundary were found to have second stability access. These were most likely to be the low gas fuelling discharges. The high gas discharges only had first stability access and therefore the pedestal gradient was constrained: the pedestal could not reach the height required to reach the peeling-ballooning boundary. In pulses that had second stability access, the width of the pedestal was constrained by the width of the second stability access region. This explains the variable pedestal evolution, and suggests that the pedestal height can be maximised by maximising the region of second stability access. This a complex feedback mechanism and therefore is a non-trivial problem, but suggests that subtle changes in the pedestal structure could lead to a significant change in the width of the second stability access region. Analysis of the ELM characteristics of some of the low triangularity pulses showed remarkable differences between the pulses which reach the peeling-ballooning boundary at low gas injection rate, and the pulses which do not reach the peeling-ballooning boundary at high gas injection rate. The high gas injection rate pulses are all found to have underlying oscillations, and remarkably periodic ELM events. This suggests an alternate mechanism that is not present in the low gas injection pulses.

7.2 Future Work

The work in this thesis presents many opportunities for future work. The first further work relates to the new arbitrary n ELITE formalism. Firstly, the arbitrary n ELITE needs to be made ready for release to the wider ELITE users community. Another critical extension to ELITE is to implement a non-zero core boundary condition, so that all low n modes can be studied, in particular $n = 1$. This would also be coupled with the inclusion of a more complex and realistic vacuum model at the plasma edge to account for a real wall in the plasma. Also important is the implementation a different radial coordinate: using x as the radial coordinate requires that q is monotonic: in low collisionality pedestals at low n this is often not the case and this extension will allow the ELITE code to become a more general. Equally important for the accurate study of analysis of low n dominated phenomena is to derive a further arbitrary n

ELITE formalism that includes flow shear, which is non trivial. This is important since, for example in QH-mode, flow shear is destabilising at low n and stabilising at intermediate-high n. Another extension is to implement the δW diagnostic in the arbitrary n ELITE such that the relative magnitudes of the drive can be determined across a full range of n. Finally, it would beneficial to incorporate arbitrary n ELITE into the EPED model to help resolve the kink/peeling boundary.

There is also further work to be done on the wide-pedestal QH-mode. This includes extending the study using arbitrary n ELITE so that a more detailed picture of the peeling-ballooning stability as ELMs return can be determined. It is important to resolve the mechanism that leads to the return of ELMs in wide-pedestal QH-mode. This is also an experimental research question, and more experiments on DIII-D are planned.

Finally, there is much further work to be done on the JET-ILW pedestal analysis presented in chapter 6. These results show a new avenue to explore for optimising the pedestal in JET-ILW plasmas. An extension of this study therefore is to study high D_2 gas injection rate pulses at high triangularity, to assess if the peeling-ballooning boundary is reached when there is improved shaping at higher fuelling. This would provide a more complete picture of the second stability access mechanism. Another important direction is to extend the Be-II emission ELM traces study to longer times and more ELMs for the pulses already analysed, to see whether this behaviour is also seen in other times in the pulse. Also important is to identify the cause of the oscillations. Furthermore, is important to perform a similar analysis on JET-C pulses with similar plasma parameters. This is because JET-C did not appear to have the same performance issues as are seen in JET-ILW plasmas: therefore this would help to identify the differences between pedestals in the two different JET wall environments. This analysis also shows that the JET-ILW pedestal region in this dataset may be sensitive to the dynamics, such as fuelling, and transport processes. Therefore, in order to predict future JET pedestals, a dynamic model containing parameters such as the current and energy diffusion time-scales may be necessary. This would also provide improved predictability and understanding of the subtle transport and stability processes in the pedestal for ITER.

Appendix A

The ELITE shooting algorithm

A.1 The ELITE shooting algorithm

Once the equation 2.66 with all the boundary conditions has been derived, this needs to be solved to find the eigenfunction and corresponding eigenvalue for the system. This is performed using a shooting algorithm. Start with equation 2.66, where $A^{k,m}$ is an $M \times M$ matrix, where there are M Fourier harmonics and the matrix elements depend on γ^2, and u_m is a column vector with M rows [130]. The equation 2.66 can be discretised onto a y grid labelled i and in place of ψ, using the formula where each element is labelled y_i. This is given by:

$$\underline{\underline{P}}^{(i)} \cdot \underline{u}^{(i+1)} + \underline{\underline{Q}}^{(i)} \cdot \underline{u}^{(i)} + \underline{\underline{S}}^{(i)} \cdot \underline{u}^{(i-1)} = 0 \tag{A.1}$$

where $\underline{u}^{(i)}$ is a vector of length M, which represents $u_m(x)$, $\underline{\underline{P}}^{(i)}$, $\underline{\underline{Q}}^{(i)}$ and $\underline{\underline{S}}^{(i)}$ are the coefficients of the equation acting at the $i+1$, i and $i-1$ grid points of the y grid respectively [29]. This equation is subject to a boundary condition at the plasma surface where $y = \Delta$ [130] as seen in equation 2.70. Now, $u_m(x)$ can be written as an expansion in a set of M linearly independent solutions, v_k, where m is the mth element of the solution vector, $\underline{v}_k$, each of the M Fourier harmonics. Therefore, $u_m(x)$ can be written as:

$$u_m(x) = \sum_{k=1}^{M} a_k v_{mk}(x) \tag{A.2}$$

where the independent solutions all satisfy equation A.1, and all satisfy the condition that $v_k \to 0$ in the plasma core, but the independent solutions do not necessarily satisfy the boundary condition at the plasma edge at $y = \Delta$. Therefore the solution $\underline{u}$ will satisfy $\underline{u} \to 0$ at the plasma core, and the coefficients, a_k can also be chosen such that $\underline{u}$ also satisfies the boundary condition at the plasma edge, $y = \Delta$. Therefore the equation

A.1 becomes:

$$\underline{\underline{P}}^{(i)} \cdot \underline{v}^{(i+1)} + \underline{\underline{Q}}^{(i)} \cdot \underline{v}^{(i)} + \underline{\underline{S}}^{(i)} \cdot \underline{v}^{(i-1)} = 0 \tag{A.3}$$

with the m suffix dropped [130]. To solve this $\underline{v}$ is expressed as a recurrence relation, given by:

$$\underline{v}^{(i)} = \underline{\underline{\alpha}}^{(i)} \cdot \underline{v}^{(i+1)} + \underline{\beta}^{(i)} \tag{A.4}$$

where $\underline{\underline{\alpha}}^{(i)}$ and $\underline{\beta}^{(i)}$ are a matrix and vector respectively, found at position i on the y grid. Now, this is substituted into equation A.3 [130]:

$$\begin{aligned} &\underline{\underline{P}}^{(i)} \cdot \underline{v}^{(i+1)} + \underline{\underline{Q}}^{(i)} \cdot \underline{v}^{(i)} + \underline{\underline{S}}^{(i)} \cdot \left[\underline{\underline{\alpha}}^{(i-1)} \cdot \underline{v}^{(i)} + \underline{\beta}^{(i-1)}\right] = 0 \\ &\left[\underline{\underline{Q}}^{(i)} + \underline{\underline{S}}^{(i)} \cdot \underline{\underline{\alpha}}^{(i-1)}\right] \cdot \underline{v}^{(i)} = -\underline{\underline{P}}^{(i)} \cdot \underline{v}^{(i+1)} - \underline{\underline{S}}^{(i)} \cdot \underline{\beta}^{(i-1)} \end{aligned} \tag{A.5}$$

Rearranging this equation for $\underline{v}^{(i)}$, incrementing the indices in equation A.4 by 1 and then comparing it to the rearranged form of equation A.5, provides the forms for $\underline{\underline{\alpha}}^{(i)}$ and $\underline{\beta}^{(i)}$ [130, 29]:

$$\begin{aligned} \underline{\underline{\alpha}}^{(i)} &= -\left[\underline{\underline{P}}^{(i)} \cdot \underline{\underline{\alpha}}^{(i-1)} + \underline{\underline{Q}}^{(i)}\right]^{-1} \cdot \underline{\underline{S}}^{(i)} \\ \underline{\beta}^{(i)} &= -\left[\underline{\underline{P}}^{(i)} \cdot \underline{\underline{\alpha}}^{(i-1)} + \underline{\underline{Q}}^{(i)}\right]^{-1} \cdot \left(\underline{\underline{P}}^{(i)} \cdot \underline{\beta}^{(i-1)}\right) \end{aligned} \tag{A.6}$$

these relations allow $\underline{\underline{\alpha}}^{(i)}$ and $\underline{\beta}^{(i)}$ to be calculated at all grid points given their value at a single grid point, i [29]. Also defined are:

$$\begin{aligned} \underline{\underline{\alpha}}^{(0)} &= 0 \\ \left[\underline{\beta}_k^{(0)}\right]_m &= \beta_{mk}^{(0)} = \delta_{mk} \end{aligned} \tag{A.7}$$

The first equation decouples the solution from the solution at the edge. The second created M linearly independent eigenvectors, where $1 \le k \le M$ [130]. Then the equations for $\underline{\underline{\alpha}}^{(i)}$ and $\underline{\beta}^{(i)}$, given in A.6, can be used to generate $\underline{\underline{\alpha}}^{(i)}$ and $\underline{\beta}^{(i)}$ into the core for each solution k. This shooting generates all of the $\underline{\underline{\alpha}}^{(i)}$ and $\underline{\beta}^{(i)}$ by starting at $i = 1$ at the edge, and shoots into the core to $i = N$. Now, the boundary conditions at the core, where on the grid $i = N$, used when the shooting algorithm reaches the core, needs to be considered. This is given by:

$$\underline{v}^{(i=N)} = 0 \tag{A.8}$$

This is the zero boundary condition at the core grid point. Once the core is reached and all the $\underline{\underline{\alpha}}^{(i)}$s and $\underline{\beta}^{(i)}$s are known, the code shoots from the core back to the edge, calculating at the $\underline{v}$s for all the grid points, until the edge of the plasma is reached. A detailed description of the algorithm, for a slightly different system which shoots in two directions and matches to a reference grid point in the centre, can be found in [29]. After the shooting returns to the edge, the equation A.4 is used to generate the solution vector, $\underline{v}_k$, in the three points closest to the plasma edge for each solution k, where $i = 1$ is the plasma edge on the grid [130]. These are given by $\underline{v}^{(1)}$, $\underline{v}^{(2)}$ and $\underline{v}^{(3)}$, and these are stored. Now the edge boundary condition is written in the form:

$$\underline{\underline{S}}' \cdot \frac{d\underline{u}}{d\psi} + \underline{\underline{S}} \cdot \underline{u} = 0 \tag{A.9}$$

The vector, $\underline{u}$ is fitted to a a quadratic over the final three y grid points, where $1 \leq y \leq 3$, such that the boundary condition, equation A.9, can be written in the form [130]:

$$\begin{aligned} \underline{\underline{S}} \cdot \underline{u}^{(1)} + \underline{\underline{S}}' \cdot \left[c_1 \underline{u}^{(1)} + c_2 \underline{u}^{(2)} + c_3 \underline{u}^{(3)} \right] &= 0 \\ c_1 &= \frac{(y_3 - 2y_1 + y_2)}{(y_3 - y_1)(y_1 - y_2)} \\ c_2 &= \frac{(y_1 - y_3)}{(y_3 - y_2)(y_1 - y_2)} \\ c_3 &= \frac{(y_1 - y_2)}{(y_3 - y_1)(y_3 - y_2)} \end{aligned} \tag{A.10}$$

where y_1, y_2 and y_3 are the three final grid points, $y = 1$, $y = 2$ and $y = 3$, respectively. Now $\underline{u}$ is considered in terms of components so that $\underline{u} = u_m$. This allows equation A.10 to be written in terms of components [130]:

$$\sum_{m'}^{M} \left[S'_{mm'} \cdot u^{(1)}_{m'} + S_{mm'} \cdot \left[c_1 u^{(1)}_{m'} + c_2 u^{(2)}_{m'} + c_3 u^{(3)}_{m'} \right] \right] = 0 \tag{A.11}$$

Recalling equation A.2, and using implied summation over repeated indices yields:

$$\left[S_{mm'} v^{(1)}_{m'k} + S'_{mm'} \left(c_1 v^{(1)}_{m'k} + c_2 v^{(2)}_{m'k} + c_3 v^{(3)}_{m'k} \right) \right] a_k = 0 \tag{A.12}$$

The part in the square brackets is defined as the T-matrix, which is summing over m':

$$T_{mk} = S_{mm'} v^{(1)}_{m'k} + S'_{mm'} \left(c_1 v^{(1)}_{m'k} + c_2 v^{(2)}_{m'k} + c_3 v^{(3)}_{m'k} \right) \tag{A.13}$$

The eigenvalue condition, which contains the T matrix and the final determination of the growth rate, γ, of the system is discussed in section 2.5.8.

Appendix B

Details of the derivation of the arbitrary n ELITE matrix elements

B.1 Solution of terms in the arbitrary n δW equation

This section details the integration by parts, if necessary, and the Fourier decomposition of all of the terms in the arbitrary n δW equation, to obtain the arbitrary n ELITE matrix elements. The δW equation has been reproduced here, from equation 3.7, for reference:

$$\begin{aligned}
\delta W =& \pi \int_{-\infty}^{\psi_a} d\psi \oint d\chi \Bigg[\frac{JB^2}{R^2 B_p^2} \left| k_\parallel X \right|^2 + \frac{R^2}{n^2 J} \left| \frac{\partial Y}{\partial \psi} \right|^2 \\
& - \frac{2Jp\prime}{B^2} \left[\frac{\partial}{\partial \psi} \left(p + \frac{B^2}{2} \right) |X|^2 - \frac{if}{2JB^2} \frac{\partial B^2}{\partial \chi} \frac{X^*}{n} \frac{\partial X}{\partial \psi} \right] \\
& - \frac{X^*}{n} JBk_\parallel \left(\sigma' X \right) + \frac{p'}{n} \left[PJBk_\parallel^* \left(\frac{X^*}{B^2} \right) + P^* JBk_\parallel \left(\frac{X}{B^2} \right) \right] \\
& + \frac{\partial}{\partial \psi} \left[\frac{1}{n} \sigma X Y^* \right] + \frac{R^2 p'^2}{n^2 J} \left| JBk_\parallel \left(\frac{X}{B^2} \right) \right|^2 \\
& + JB^2 |W|^2 + \frac{R^2}{n^2 J} \left| JBk_\parallel W \right|^2 - \frac{f}{n} \left[W^* JBk_\parallel W + WJBk_\parallel^* W^* \right] \\
& - \frac{f}{n} \left[W^* \left(\frac{\partial Y}{\partial \psi} + p' JBk_\parallel \left(\frac{X}{B^2} \right) \right) + W \left(\frac{\partial Y^*}{\partial \psi} + p' JBk_\parallel^* \left(\frac{X^*}{B^2} \right) \right) \right] \\
& + \frac{1}{n} \Bigg[JBk_\parallel^* W^* \left(P + \frac{R^2 p'}{nJ} JBk_\parallel \left(\frac{X}{B^2} \right) \right) \\
& + JBk_\parallel W \left(P^* + \frac{R^2 p'}{nJ} JBk_\parallel^* \left(\frac{X^*}{B^2} \right) \right) \Bigg] \Bigg]
\end{aligned} \tag{B.1}$$

where P is given by equation 3.8, and is reproduced here for reference:

$$P = \sigma X + \frac{R^2}{nJ} \frac{\partial Y}{\partial \psi} \tag{B.2}$$

There are two perturbation displacements to Fourier decompose, X and W and their forms are defined in section 3.4.1. The matrix elements are the flux surface averages of equilibrium quantities are given by S_i, as defined in equation 3.17, where L_i is the kernel and i denotes the kernel number. These are fully documented in appendix section B.4.

B.1.1 Term 1

This is the Fourier decomposition of term 1 of the arbitrary n δW equation, as explained in section 3.4.1. This term only contains the X perturbation displacement.

$$\begin{aligned}\delta W_1 =&\pi\int_{-\infty}^{\psi_a} d\psi \oint d\chi \frac{JB^2}{R^2B_p^2}\left|k_\parallel X\right|^2\\ =&\pi\int_{-\infty}^{\psi_a} d\psi \oint d\chi \frac{1}{JR^2B_p^2}\left(JBk_\parallel X\right)\left(JBk_\parallel^* X^*\right)\\ =&\pi\int_{-\infty}^{\psi_a} d\psi \oint d\omega \sum_{m,k}\frac{q}{\nu}u_k^*\left(\frac{-\nu}{q}\right)^2(k-nq)(m-nq)\frac{1}{JR^2B_p^2}u_m e^{i(k-m)\omega}\\ =&\pi\int_{-\infty}^{\psi_a} d\psi \sum_{m,k}u_k^*\frac{1}{q}S_1(k-nq)(m-nq)u_m\end{aligned} \tag{B.3}$$

where S_i are the matrix elements and the subscript, i, refers to the kernel number such that S_i is the flux surface average of kernels, L_i, given by equation 2.68. Thee kernels are completely listed in the appendix 3.17. This is similar for all the subsequent terms, including the inertia terms.

B.1.2 Term 2

Term 2 requires integration by parts. As explained in section 3.2.1, this produces plasma terms for term 2, and a surface term S_{u2}. This term only contains the X perturbation displacement.

$$\begin{aligned}\delta W_2 =&\pi\int_{-\infty}^{\psi_a} d\psi \oint d\chi \frac{R^2}{n^2J}\left|\frac{\partial Y}{\partial\psi}\right|^2\\ =&\pi\int_{-\infty}^{\psi_a} d\psi \oint d\chi\left[\frac{\partial}{\partial\psi}\left[\frac{R^2}{n^2J}Y^*\frac{\partial Y}{\partial\psi}\right]-\frac{1}{n^2}\frac{\partial}{\partial\psi}\left(\frac{R^2}{J}\right)Y^*\frac{\partial Y}{\partial\psi}-\frac{1}{n^2}\frac{R^2}{J}Y^*\frac{\partial^2 Y}{\partial\psi^2}\right]\\ =&S_{u2}+\pi\int_{-\infty}^{\psi_a} d\psi \oint d\chi\left[-\frac{1}{n^2}\frac{\partial}{\partial\psi}\left(\frac{R^2}{J}\right)Y^*\frac{\partial Y}{\partial\psi}-\frac{1}{n^2}\frac{R^2}{J}Y^*\frac{\partial^2 Y}{\partial\psi^2}\right]\\ S_{u2} =&\pi\int_{-\infty}^{\psi_a} d\psi \oint d\chi\frac{\partial}{\partial\psi}\left[\frac{R^2}{n^2J}Y^*\frac{\partial Y}{\partial\psi}\right]\end{aligned} \tag{B.4}$$

Now the plasma terms can be Fourier decomposed, to produce the matrix elements for term 2.

$$
\begin{aligned}
\delta W_2 =& \pi \int_{-\infty}^{\psi_a} d\psi \oint d\chi \frac{Y^*}{n^2}\left[-\frac{\partial}{\partial\psi}\left(\frac{R^2}{J}\right)\frac{\partial Y}{\partial\psi} - \frac{R^2}{J}\frac{\partial^2 Y}{\partial\psi^2}\right] \\
=& \pi \int_{-\infty}^{\psi_a} d\psi \oint d\omega \sum_{m,k} \frac{q}{\nu}\left(\frac{-\nu}{q}\right)(k-nq)u_k^* \frac{1}{n^2}\Bigg[-\frac{\partial}{\partial\psi}\left(\frac{R^2}{J}\right)n\nu\Bigg[\Bigg[\\
& \frac{(m-nq)}{nq}\left(im\omega' - \frac{\nu'}{\nu}\right) + \frac{mq'}{nq^2}\Bigg]u_m - \frac{(m-nq)}{nq}\frac{du_m}{d\psi}\Bigg] - \frac{R^2}{J}n^2\nu\Bigg[\Bigg[\\
& \frac{(m-nq)}{n^2q}\left(m^2\omega'^2 + 2im\omega'\frac{\nu'}{\nu} + im\omega'' - \frac{\nu''}{\nu}\right) + \frac{2mq'}{n^2q^2}\left(\frac{\nu'}{\nu} - im\omega' - \frac{q'}{q}\right) \\
& + \frac{mq''}{n^2q^2}\Bigg]u_m + 2\Bigg[\frac{(m-nq)}{n^2q}\left(im\omega' - \frac{\nu'}{\nu}\right) + \frac{mq'}{n^2q^2}\Bigg]\frac{du_m}{d\psi} \\
& - \frac{(m-nq)}{n^2q}\frac{d^2u_m}{d\psi^2}\Bigg]\Bigg] e^{i(k-m)\omega} \\
=& \pi \int_{-\infty}^{\psi_a} d\psi \sum_{m,k} u_k^*(k-nq)\Bigg[\Bigg[\frac{(m-nq)}{n^2q}\Bigg(\frac{-1}{q}S_2 + 2imS_5 + m^2S_7 + imS_8 \\
& - S_{14} + imS_{15}\Bigg) + \frac{2mq'}{n^2q^2}\left(S_3 - imS_6\right) + \frac{mf}{n^2q^2}\left(q'' - \frac{2q'^2}{q}\right)S_{12} + \frac{mq'}{n^2q^2}S_{16}\Bigg]u_m \\
& + \left[\frac{(m-nq)}{n^2q}\left(-2S_3 + 2imS_6 - S_{16}\right) + \frac{2mfq'}{n^2q^2}S_{12}\right]\frac{du_m}{d\psi} \\
& - \frac{(m-nq)}{n^2q}fS_{12}\frac{d^2u_m}{d\psi^2}\Bigg]
\end{aligned}
\tag{B.5}
$$

Finally, the surface term for term 2 can be Fourier decomposed to produce surface matrix elements.

$$
\begin{aligned}
S_{u2} =& \pi \int_{-\infty}^{\psi_a} d\psi \oint d\chi \frac{\partial}{\partial\psi}\left[\frac{R^2}{n^2J}Y^*\frac{\partial Y}{\partial\psi}\right] \\
=& \pi \oint d\omega \sum_{m,k} u_k^* \frac{q}{\nu}\left(\frac{-\nu}{q}\right)\frac{R^2}{n^2J}(k-nq)n\nu\Bigg[\Bigg[\frac{(m-nq)}{nq}\left(im\omega' - \frac{\nu'}{\nu}\right) + \frac{mq'}{nq^2}\Bigg]u_m \\
& - \frac{(m-nq)}{nq}\frac{du_m}{d\psi}\Bigg]e^{i(k-m)\omega} \\
=& \pi \sum_{m,k} u_k^*(k-nq)\Bigg[\Bigg[\frac{(m-nq)}{n^2q}\left(S_3 - imS_6\right) - \frac{mfq'}{n^2q^2}S_{12}\Bigg]u_m \\
& + \frac{(m-nq)}{n^2q}fS_{12}\frac{du_m}{d\psi}\Bigg]
\end{aligned}
\tag{B.6}
$$

B.1.3 Term 3

Now term 3 is Fourier decomposed. This term only contains the X perturbation displacement.

$$\begin{aligned}
\delta W_3 =& \pi \int_{-\infty}^{\psi_a} d\psi \oint d\chi - \frac{2Jp\prime}{B^2}\frac{\partial}{\partial\psi}\left(p+\frac{B^2}{2}\right)|X|^2 \\
=& \pi \int_{-\infty}^{\psi_a} d\psi \oint d\omega \sum_{m,k} -\frac{q}{\nu}u_k^* \frac{2Jp'}{B^2}\frac{\partial}{\partial\psi}\left(p+\frac{B^2}{2}\right)u_m e^{i(k-m)\omega} \\
=& \pi \int_{-\infty}^{\psi_a} d\psi \sum_{m,k} -u_k^* \frac{2qp'}{f} S_9 u_m
\end{aligned} \tag{B.7}$$

B.1.4 Term 4

Now term 4 is Fourier decomposed. This term only contains the X perturbation displacement.

$$\begin{aligned}
\delta W_4 =& \pi \int_{-\infty}^{\psi_a} d\psi \oint d\chi \left(-\frac{2Jp\prime}{B^2}\right)\left(-\frac{if}{2JB^2}\right)\frac{\partial B^2}{\partial\chi}\frac{X^*}{n}\frac{\partial X}{\partial\psi} \\
=& \pi \int_{-\infty}^{\psi_a} d\psi \oint d\omega \sum_{m,k} \frac{q}{\nu}u_k^* \left[\frac{ifp'}{nB^4}\left(-im\omega'\right)\frac{\partial B^2}{\partial\chi}u_m + \frac{ifp'}{nB^4}\frac{\partial B^2}{\partial\chi}\frac{du_m}{d\psi}\right] e^{i(k-m)\omega} \\
=& \pi \int_{-\infty}^{\psi_a} d\psi \sum_{m,k} u_k^* \left[\frac{mqp'}{n} S_{11} u_m + \frac{ip'q}{n} S_{10}\frac{du_m}{d\psi}\right]
\end{aligned} \tag{B.8}$$

B.1.5 Term 5

Now term 5 is Fourier decomposed. This term only contains the X perturbation displacement.

$$\begin{aligned}
\delta W_5 =& \pi \int_{-\infty}^{\psi_a} d\psi \oint d\chi - \frac{X^*}{n} JBk_{\parallel}\left(\sigma' X\right) \\
=& \pi \int_{-\infty}^{\psi_a} d\psi \oint d\omega \sum_{m,k} \frac{q}{\nu}u_k^* \left[\frac{-\sigma'}{n}\left(\frac{-\nu}{q}\right)(m-nq) - \frac{-i}{n}\frac{\partial\sigma'}{\partial\chi}\right] u_m e^{i(k-m)\omega} \\
=& \pi \int_{-\infty}^{\psi_a} d\psi \sum_{m,k} u_k^* \left[\frac{(m-nq)}{n} S_{19} + \frac{iq}{n} S_{18}\right] u_m
\end{aligned} \tag{B.9}$$

B.1.6 Term 6

Term 6 also requires integration by parts, producing plasma terms, and surface term S_{u6}. This term only contains the X perturbation displacement.

$$
\begin{aligned}
\delta W_6 =& \pi\int_{-\infty}^{\psi_a} d\psi \oint d\chi \frac{p'}{n}\left[PJBk_\parallel^*\left(\frac{X^*}{B^2}\right) + P^*JBk_\parallel\left(\frac{X}{B^2}\right)\right] \\
=& \pi\int_{-\infty}^{\psi_a} d\psi \oint d\chi \Bigg[\frac{p'}{n}\left[\sigma XJBk_\parallel^*\left(\frac{X^*}{B^2}\right) + \sigma X^*JBk_\parallel\left(\frac{X}{B^2}\right)\right] \\
&+ \frac{R^2p'}{n^2J}\frac{\partial Y}{\partial\psi}JBk_\parallel^*\left(\frac{X^*}{B^2}\right) + \frac{\partial}{\partial\psi}\left[\frac{R^2p'}{n^2J}Y^*JBk_\parallel\left(\frac{X}{B^2}\right)\right] \\
&- \frac{R^2p'}{n^2J}Y^*\frac{\partial}{\partial\psi}\left(JBk_\parallel\left(\frac{X}{B^2}\right)\right) - \frac{\partial}{\partial\psi}\left(\frac{R^2p'}{n^2J}\right)Y^*JBk_\parallel\left(\frac{X}{B^2}\right)\Bigg] \\
=& S_{u6} + \pi\int_{-\infty}^{\psi_a} d\psi \oint d\chi \Bigg[\frac{\sigma p'}{nB^2}\left[XY^* + YX^*\right] + \frac{ip'\sigma}{nB^4}\frac{\partial B^2}{\partial\chi}\left[XX^* - X^*X\right] \\
&- \frac{iR^2p'}{n^2JB^4}\frac{\partial B^2}{\partial\chi}X^*\frac{\partial Y}{\partial\psi} + \frac{R^2p'}{n^2JB^2}Y^*\frac{\partial Y}{\partial\psi} \\
&- \frac{R^2p'}{n^2J}Y^*\frac{\partial}{\partial\psi}\left[\frac{Y}{B^2} + \frac{i}{B^4}\frac{\partial B^2}{\partial\chi}X\right] - \frac{\partial}{\partial\psi}\left(\frac{R^2p'}{n^2J}\right)\left[\frac{|Y|^2}{B^2} + \frac{i}{B^4}Y^*X\right]\Bigg] \\
=& S_{u6} + \pi\int_{-\infty}^{\psi_a} d\psi \oint d\chi \Bigg[\frac{\sigma p'}{nB^2}\left[Y^*X + X^*Y\right] - \frac{iR^2p'}{n^2JB^4}\frac{\partial B^2}{\partial\chi}X^*\frac{\partial Y}{\partial\psi} \\
&+ \frac{R^2p'}{n^2JB^2}\left[Y^*\frac{\partial Y}{\partial\psi} - Y^*\frac{\partial Y}{\partial\psi}\right] + \frac{R^2p'}{n^2JB^4}\frac{\partial B^2}{\partial\psi}|Y|^2 - \frac{iR^2p'}{n^2J}\frac{\partial}{\partial\psi}\left(\frac{1}{B^4}\frac{\partial B^2}{\partial\chi}\right)Y^*X \\
&- \frac{iR^2p'}{n^2JB^4}\frac{\partial B^2}{\partial\chi}Y^*\frac{\partial X}{\partial\psi} - \frac{1}{B^2}\frac{\partial}{\partial\psi}\left(\frac{R^2p'}{n^2J}\right)|Y|^2 - \frac{i}{B^4}\frac{\partial B^2}{\partial\chi}\frac{\partial}{\partial\psi}\left(\frac{R^2p'}{n^2J}\right)Y^*X\Bigg] \\
=& S_{u6} + \pi\int_{-\infty}^{\psi_a} d\psi \oint d\chi \Bigg[\frac{\sigma p'}{nB^2}\left[Y^*X + X^*Y\right] - \frac{iR^2p'}{n^2JB^4}\frac{\partial B^2}{\partial\chi}X^*\frac{\partial Y}{\partial\psi} \\
&- \frac{iR^2p'}{n^2J}\frac{\partial}{\partial\psi}\left(\frac{1}{B^4}\frac{\partial B^2}{\partial\chi}\right)Y^*X - \frac{iR^2p'}{n^2JB^4}\frac{\partial B^2}{\partial\chi}Y^*\frac{\partial X}{\partial\psi} - \frac{\partial}{\partial\psi}\left(\frac{R^2p'}{n^2JB^2}\right)|Y|^2 \\
&- \frac{i}{B^4}\frac{\partial B^2}{\partial\chi}\frac{\partial}{\partial\psi}\left(\frac{R^2p'}{n^2J}\right)Y^*X\Bigg] \\
S_{u6} =& \pi\int_{-\infty}^{\psi_a} d\psi \oint d\chi \frac{\partial}{\partial\psi}\left[\frac{R^2p'}{n^2J}Y^*JBk_\parallel\left(\frac{X}{B^2}\right)\right]
\end{aligned}
\tag{B.10}
$$

Now the plasma terms can be Fourier decomposed, to produce the matrix elements for term 6.

$$\begin{aligned}
\delta W_6 =&\pi \int_{-\infty}^{\psi_a} d\psi \oint d\chi \Bigg[\frac{\sigma p'}{nB^2} \left[Y^* X + X^* Y \right] - \frac{iR^2 p'}{n^2 JB^4} \frac{\partial B^2}{\partial \chi} X^* \frac{\partial Y}{\partial \psi} \\
&- \frac{iR^2 p'}{n^2 J} \frac{\partial}{\partial \psi} \left(\frac{1}{B^4} \frac{\partial B^2}{\partial \chi} \right) Y^* X - \frac{iR^2 p'}{n^2 JB^4} \frac{\partial B^2}{\partial \chi} Y^* \frac{\partial X}{\partial \psi} - \frac{\partial}{\partial \psi} \left(\frac{R^2 p'}{n^2 JB^2} \right) |Y|^2 \\
&- \frac{i}{B^4} \frac{\partial B^2}{\partial \chi} \frac{\partial}{\partial \psi} \left(\frac{R^2 p'}{n^2 J} \right) Y^* X \Bigg] \\
=&\pi \int_{-\infty}^{\psi_a} d\psi \oint d\omega \sum_{m,k} u_k^* \frac{q}{\nu} \Bigg[\frac{\sigma p'}{nB^2} \left(\frac{-\nu}{q} \right) (k + m - 2nq) u_m \\
&- \frac{iR^2 p'}{n^2 JB^4} \frac{\partial B^2}{\partial \chi} n\nu \Bigg[\Bigg[\frac{(m - nq)}{nq} \left(im\omega' - \frac{\nu'}{\nu} \right) + \frac{mq'}{nq^2} \Bigg] u_m - \frac{(m - nq)}{nq} \frac{du_m}{d\psi} \Bigg] \\
&- \frac{i}{n^2} \frac{\partial}{\partial \psi} \left(\frac{R^2 p'}{JB^4} \frac{\partial B^2}{\partial \chi} \right) \left(\frac{-\nu}{q} \right) (k - nq) u_m \\
&- \left(\frac{-\nu}{q} \right)^2 \frac{\partial}{\partial \psi} \left(\frac{R^2 p'}{n^2 JB^2} \right) (m - nq)(k - nq) u_m \\
&- \frac{iR^2 p'}{n^2 JB^4} \frac{\partial B^2}{\partial \chi} \left(\frac{-\nu}{q} \right) (k - nq) \left[-im\omega' u_m + \frac{du_m}{d\psi} \right] \Bigg] e^{i(k-m)\omega} \\
=&\pi \int_{-\infty}^{\psi_a} d\psi \sum_{m,k} u_k^* \Bigg[\Bigg[- \frac{1}{n} (m + k - 2nq) S_{17} + \frac{mp'}{n^2} (m + k - 2nq) S_{11} \\
&- \frac{imq'p'}{n^2 q} S_{10} - \frac{1}{n^2 q} (m - nq)(k - nq) S_{20} + \frac{i}{n^2} (k - nq) S_{22} \\
&+ \frac{i}{n^2} (m - nq) S_{21} \Bigg] u_m + \frac{ip'}{n^2} (m + k - 2nq) \frac{du_m}{d\psi} \Bigg]
\end{aligned} \tag{B.11}$$

Finally, the surface term for term 6 can be Fourier decomposed to produce surface matrix elements.

$$\begin{aligned}
S_{u6} =&\pi \int_{-\infty}^{\psi_a} d\psi \oint d\chi \frac{\partial}{\partial \psi} \left[\frac{R^2 p'}{n^2 J} Y^* JBk_\parallel \left(\frac{X}{B^2} \right) \right] \\
=&\pi \oint d\omega \sum_{m,k} u_k^* \frac{q}{\nu} \frac{R^2 p'}{n^2 J} \left(\frac{-\nu}{q} \right) (k - nq) \Bigg[\frac{1}{B^2} \left(\frac{-\nu}{q} \right) (m - nq) \\
&+ \frac{i}{B^4} \frac{\partial B^2}{\partial \chi} \Bigg] u_m e^{i(k-m)\omega} \\
=&\pi \sum_{m,k} u_k^* (k - nq) \left[\frac{fp'}{n^2 q} (m - nq) S_{13} - \frac{ip'}{n^2} S_{10} \right] u_m
\end{aligned} \tag{B.12}$$

B.1.7 Term 7

Term 7 is the peeling term, and is solely a surface term. This only contains the X perturbation displacement. It is Fourier decomposed to produce surface matrix elements.

$$\begin{aligned}
S_{u7} =&\pi \int_{-\infty}^{\psi_a} d\psi \oint d\chi \frac{\partial}{\partial\psi}\left[\frac{1}{n}\sigma X Y^*\right] \\
=&\pi \oint d\omega \sum_{m,k} u_k^* \frac{q}{\nu}\frac{1}{n}\sigma\left(\frac{-\nu}{q}\right)(k-nq)u_m e^{i(k-m)\omega} \\
=&\pi \oint d\omega \sum_{m,k} u_k^* \frac{q}{\nu}\frac{1}{n}\left(-\frac{fp'}{B^2}-f'\right)\left(\frac{-\nu}{q}\right)(k-nq)u_m e^{i(k-m)\omega} \\
=&\pi \sum_{m,k} u_k^*\left[\frac{fp'}{n}S_{13}+\frac{f'}{n}S_{12}\right](k-nq)u_m
\end{aligned} \tag{B.13}$$

B.1.8 Term 8

Now term 8 is Fourier decomposed. This term only contains the X perturbation displacement.

$$\begin{aligned}
\delta W_8 =&\pi \int_{-\infty}^{\psi_a} d\psi \oint d\chi \frac{R^2 p'^2}{n^2 J}\left|JBk_{\parallel}\left(\frac{X}{B^2}\right)\right|^2 \\
=&\frac{R^2 p'^2}{n^2 J}\left[\frac{Y}{B^2}+\frac{i}{B^4}\frac{\partial B^2}{\partial\chi}X\right]\left[\frac{Y^*}{B^2}-\frac{i}{B^4}\frac{\partial B^2}{\partial\chi}X^*\right] \\
=&\pi \int_{-\infty}^{\psi_a} d\psi \oint d\chi \frac{R^2 p'^2}{n^2 J}\left[\frac{|Y|^2}{B^4}+\frac{1}{B^8}\left(\frac{\partial B^2}{\partial\chi}\right)^2|X|^2+\frac{i}{B^6}\frac{\partial B^2}{\partial\chi}\left(XY^*-YX^*\right)\right] \\
=&\pi \int_{-\infty}^{\psi_a} d\psi \oint d\omega \sum_{m,k} u_k^* \frac{q}{\nu}\frac{R^2 p'^2}{n^2 J}\Bigg[\left(\frac{-\nu}{q}\right)^2\frac{1}{B^4}(m-nq)(k-nq)+\frac{1}{B^8}\left(\frac{\partial B^2}{\partial\chi}\right)^2 \\
&+\frac{i}{B^6}\frac{\partial B^2}{\partial\chi}\left(\frac{-\nu}{q}\right)(k-m)\Bigg]u_m e^{i(k-m)\omega} \\
=&\pi \int_{-\infty}^{\psi_a} d\psi \sum_{m,k} u_k^*\left[\frac{p'^2}{n^2 q}S_4(m-nq)(k-nq)+\frac{qp'^2}{n^2}S_{23}-\frac{ip'^2}{n^2}(k-m)S_{24}\right]u_m
\end{aligned} \tag{B.14}$$

B.1.9 Term 9

Now term 9 is Fourier decomposed. This term only contains the W perturbation displacement.

$$\begin{aligned}
\delta W_9 =&\pi \int_{-\infty}^{\psi_a} d\psi \oint d\chi JB^2 |W|^2 \\
=&\pi \int_{-\infty}^{\psi_a} d\psi \oint d\omega \sum_{m,k} \frac{q}{\nu} w_k^* JB^2 w_m e^{i(k-m)\omega} \\
=&\pi \int_{-\infty}^{\psi_a} d\psi \sum_{m,k} w_k^* \frac{q}{f} S_{25} w_m
\end{aligned} \tag{B.15}$$

B.1.10 Term 10

Now term 10 is Fourier decomposed. This term only contains the W perturbation displacement.

$$\begin{aligned}\delta W_{10} =&\pi\int_{-\infty}^{\psi_a} d\psi \oint d\chi \frac{R^2}{n^2 J}\left|JBk_{\parallel}W\right|^2\\ =&\pi\int_{-\infty}^{\psi_a} d\psi \oint d\omega \sum_{m,k}\frac{q}{\nu}w_k^*\frac{R^2}{n^2 J}\left(\frac{-\nu}{q}\right)^2(m-nq)(k-nq)w_m e^{i(k-m)\omega}\\ =&\pi\int_{-\infty}^{\psi_a} d\psi \sum_{m,k} w_k^*\frac{f}{n^2 q}(m-nq)(k-nq)S_{12}w_m\end{aligned} \tag{B.16}$$

B.1.11 Term 11

Now term 11 is Fourier decomposed. This term only contains the W perturbation displacement.

$$\begin{aligned}\delta W_{11} =&\pi\int_{-\infty}^{\psi_a} d\psi \oint d\chi \left[-\frac{f}{n}\left[W^* JBk_{\parallel}W + WJBk_{\parallel}^*W^*\right]\right]\\ =&\pi\int_{-\infty}^{\psi_a} d\psi \oint d\omega \sum_{m,k}-\frac{q}{\nu}w_k^*\left(\frac{-\nu}{q}\right)(m+k-2nq)w_m e^{i(k-m)\omega}\\ =&\pi\int_{-\infty}^{\psi_a} d\psi \sum_{m,k} w_k^*\frac{f}{n}(m+k-2nq)S_{12}w_m\end{aligned} \tag{B.17}$$

B.1.12 Term 12

Term 12 requires integration by parts, and this produces plasma terms and surface term S_{u12}. This term also has integration by parts by the χ coordinate to reduce the number of terms produced by the parallel gradient operator. This term contains both the X and the W perturbation.

$$\begin{aligned}\delta W_{12} =&\pi\int_{-\infty}^{\psi_a} d\psi \oint d\chi\Bigg[-\frac{f}{n}\Bigg[W^*\left(\frac{\partial Y}{\partial\psi}+p'JBk_{\parallel}\left(\frac{X}{B^2}\right)\right)\\ &+W\left(\frac{\partial Y^*}{\partial\psi}+p'JBk_{\parallel}^*\left(\frac{X^*}{B^2}\right)\right)\Bigg]\Bigg]\\ =&\pi\int_{-\infty}^{\psi_a} d\psi \oint d\chi\Bigg[-\frac{f}{n}W^*\frac{\partial Y}{\partial\psi}-\frac{\partial}{\partial\psi}\left[\frac{f}{n}Y^*W\right]+\frac{f'}{n}Y^*W+\frac{f}{n}Y^*\frac{\partial W}{\partial\psi}\\ &-\frac{fp'}{nB^2}\left[XJBk_{\parallel}^*W^*+X^*JBk_{\parallel}W\right]\Bigg]\\ =&S_{u12}+\pi\int_{-\infty}^{\psi_a} d\psi \oint d\chi\Bigg[-\frac{f}{n}W^*\frac{\partial Y}{\partial\psi}+\frac{f'}{n}Y^*W+\frac{f}{n}Y^*\frac{\partial W}{\partial\psi}\\ &-\frac{fp'}{nB^2}\left[XJBk_{\parallel}^*W^*+X^*JBk_{\parallel}W\right]\Bigg]\\ S_{u12} =&\pi\int_{-\infty}^{\psi_a} d\psi \oint d\chi\frac{\partial}{\partial\psi}\left[-\frac{f}{n}Y^*W\right]\end{aligned} \tag{B.18}$$

Now the plasma terms can be Fourier decomposed, to produce the matrix elements for term 12.

$$
\begin{aligned}
\delta W_{12} =& \pi \int_{-\infty}^{\psi_a} d\psi \oint d\chi \bigg[- \frac{f}{n} W^* \frac{\partial Y}{\partial \psi} + \frac{f'}{n} Y^* W + \frac{f}{n} Y^* \frac{\partial W}{\partial \psi} \\
& - \frac{fp'}{nB^2} \left[XJBk_\parallel^* W^* + X^* JBk_\parallel W \right] \bigg] \\
=& \pi \int_{-\infty}^{\psi_a} d\psi \oint d\omega \sum_{m,k} \frac{q}{\nu} \bigg[- \frac{f}{n} w_k^* n\nu \bigg[\bigg[\frac{(m-nq)}{nq} \left(im\omega' - \frac{\nu'}{\nu} \right) + \frac{mq'}{nq^2} \bigg] u_m \\
& - \frac{(m-nq)}{nq} \frac{du_m}{d\psi} \bigg] + \frac{f'}{n} u_k^* \left(\frac{-\nu}{q} \right) (k-nq) w_m - \frac{fp'}{nB^2} \left(\frac{-\nu}{q} \right) \bigg[w_k^* (k-nq) u_m \\
& + u_k^* (m-nq) w_m \bigg] + \frac{f}{n} \left(\frac{-\nu}{q} \right) (k-nq) u_k^* \bigg[- im\omega' w_m + \frac{dw_m}{d\psi} \bigg]\bigg] e^{i(k-m)\omega} \\
=& \pi \int_{-\infty}^{\psi_a} d\psi \sum_{m,k} \bigg[u_k^* \bigg[\bigg[- \frac{f'}{n} (k-nq) S_{12} + \frac{im}{n} (k-nq) S_6 \\
& + \frac{fp'}{n} (m-nq) S_{13} \bigg] w_m - \frac{f}{n} (k-nq) S_{12} \frac{dw_m}{d\psi} \bigg] + w_k^* \bigg[\bigg[- \frac{im}{n} (m-nq) S_6 \\
& + \frac{1}{n} (m-nq) S_3 - \frac{mfq'}{nq} S_{12} + \frac{fp'}{n} (k-nq) S_{13} \bigg] u_m + \frac{f}{n} (m-nq) S_{12} \frac{du_m}{d\psi} \bigg]\bigg]
\end{aligned}
\tag{B.19}
$$

Finally, the surface term for term 12 can be Fourier decomposed to produce surface matrix elements.

$$
\begin{aligned}
S_{u12} =& \pi \int_{-\infty}^{\psi_a} d\psi \oint d\chi \frac{\partial}{\partial \psi} \left[- \frac{f}{n} Y^* W \right] \\
=& \pi \oint d\omega \sum_{m,k} u_k^* \frac{q}{\nu} \left(- \frac{f}{n} \right) \left(\frac{-\nu}{q} \right) (k-nq) w_m e^{i(k-m)\omega} \\
=& \pi \sum_{m,k} u_k^* \frac{f}{n} (k-nq) S_{12} w_m
\end{aligned}
\tag{B.20}
$$

B.1.13 Term 13

Term 13 also requires integration by parts, and this produces plasma terms and surface term S_{u13}. This term contains both the X and the W perturbation.

$$
\begin{aligned}
\delta W_{13} =& \pi \int_{-\infty}^{\psi_a} d\psi \oint d\chi \frac{1}{n}\bigg[JBk_{\parallel}^{*} W^{*} \left(P + \frac{R^2 p'}{nJ} JBk_{\parallel} \left(\frac{X}{B^2} \right) \right) \\
& + JBk_{\parallel} W \left(P^{*} + \frac{R^2 p'}{nJ} JBk_{\parallel}^{*} \left(\frac{X^{*}}{B^2} \right) \right) \bigg] \\
=& \pi \int_{-\infty}^{\psi_a} d\psi \oint d\chi \frac{1}{n}\bigg[JBk_{\parallel}^{*} W^{*} \left(\sigma X + \frac{R^2}{nJ} \frac{\partial Y}{\partial \psi} + \frac{R^2 p'}{nJ} JBk_{\parallel} \left(\frac{X}{B^2} \right) \right) \\
& + JBk_{\parallel} W \left(\sigma X^{*} + \frac{R^2}{nJ} \frac{\partial Y^{*}}{\partial \psi} + \frac{R^2 p'}{nJ} JBk_{\parallel}^{*} \left(\frac{X^{*}}{B^2} \right) \right) \bigg] \\
=& \pi \int_{-\infty}^{\psi_a} d\psi \oint d\chi \Bigg[\frac{\partial}{\partial \psi} \left[\frac{1}{n^2} \frac{R^2}{J} JBk_{\parallel} W Y^{*} \right] + \frac{1}{n} JBk_{\parallel}^{*} W^{*} \Bigg(\sigma X + \frac{R^2}{nJ} \frac{\partial Y}{\partial \psi} + \\
& \frac{iR^2 p'}{nJB^4} \frac{\partial B^2}{\partial \chi} X + \frac{R^2 p'}{nJB^2} Y \Bigg) + \frac{1}{n} JBk_{\parallel} W \Bigg(\sigma X^{*} - \frac{iR^2 p'}{nJB^4} \frac{\partial B^2}{\partial \chi} X^{*} + \frac{R^2 p'}{nJB^2} Y^{*} \Bigg) \\
& - \frac{1}{n^2} Y^{*} \left[\frac{\partial}{\partial \psi} \left(\frac{R^2}{J} \right) JBk_{\parallel} W + \frac{R^2}{J} \frac{\partial}{\partial \psi} \left(JBk_{\parallel} W \right) \right] \Bigg] \\
=& S_{u13} + \pi \int_{-\infty}^{\psi_a} d\psi \oint d\chi \Bigg[\frac{1}{n} JBk_{\parallel}^{*} W^{*} \Bigg(\sigma X + \frac{R^2}{nJ} \frac{\partial Y}{\partial \psi} + \frac{iR^2 p'}{nJB^4} \frac{\partial B^2}{\partial \chi} X \\
& + \frac{R^2 p'}{nJB^2} Y \Bigg) + \frac{1}{n} JBk_{\parallel} W \Bigg(\sigma X^{*} - \frac{iR^2 p'}{nJB^4} \frac{\partial B^2}{\partial \chi} X^{*} + \frac{R^2 p'}{nJB^2} Y^{*} \Bigg) \\
& - \frac{1}{n^2} Y^{*} \left[\frac{\partial}{\partial \psi} \left(\frac{R^2}{J} \right) JBk_{\parallel} W + \frac{R^2}{J} \frac{\partial}{\partial \psi} \left(JBk_{\parallel} W \right) \right] \Bigg] \\
S_{u13} =& \pi \int_{-\infty}^{\psi_a} d\psi \oint d\chi \frac{\partial}{\partial \psi} \left[\frac{1}{n^2} \frac{R^2}{J} JBk_{\parallel} W Y^{*} \right]
\end{aligned}
\tag{B.21}
$$

Now the plasma terms can be Fourier decomposed, to produce the matrix elements for term 13.

$$
\begin{aligned}
\delta W_{13} =& \pi\int_{-\infty}^{\psi_a} d\psi \oint d\chi \Bigg[\frac{1}{n}JBk_{\parallel}^{*}W^{*}\Bigg(\sigma X + \frac{R^2}{nJ}\frac{\partial Y}{\partial \psi} \\
&+ \frac{iR^2p'}{nJB^4}\frac{\partial B^2}{\partial \chi}X + \frac{R^2p'}{nJB^2}Y\Bigg) + \frac{1}{n}JBk_{\parallel}W\Bigg(\sigma X^{*} - \frac{iR^2p'}{nJB^4}\frac{\partial B^2}{\partial \chi}X^{*} \\
&+ \frac{R^2p'}{nJB^2}Y^{*}\Bigg) - \frac{1}{n^2}Y^{*}\Bigg[\frac{\partial}{\partial \psi}\left(\frac{R^2}{J}\right)JBk_{\parallel}W + \frac{R^2}{J}\frac{\partial}{\partial \psi}\left(JBk_{\parallel}W\right)\Bigg]\Bigg] \\
=& \pi\int_{-\infty}^{\psi_a} d\psi \oint d\omega \sum_{m,k}\frac{q}{\nu}\Bigg[w_k^{*}\Bigg[\left(\frac{-\nu}{q}\right)\frac{(k-nq)}{n}\sigma u_m + \left(\frac{-\nu}{q}\right)\frac{R^2}{n^2J}(k-nq)n\nu\Bigg[\\
&\Bigg(\frac{(m-nq)}{nq}\left(im\omega' - \frac{\nu'}{\nu}\right) - \frac{mq'}{nq^2}\Bigg)u_m - \frac{(m-nq)}{nq}\frac{du_m}{d\psi}\Bigg] \\
&+ \left(\frac{-\nu}{q}\right)\frac{(k-nq)}{n^2}\Bigg[\frac{iR^2p'}{JB^4}\frac{\partial B^2}{\partial \chi} + \left(\frac{-\nu}{q}\right)\frac{R^2p'}{JB^2}(m-nq)\Bigg]u_m\Bigg] \\
&+ u_k^{*}\Bigg[\left(\frac{-\nu}{q}\right)\frac{(m-nq)}{n}\Bigg[\sigma - \frac{iR^2p'}{nJB^4}\frac{\partial B^2}{\partial \chi} + \frac{R^2p'}{nJB^2}\left(\frac{-\nu}{q}\right)(k-nq)\Bigg]w_m \\
&- \frac{1}{n^2}\left(\frac{-\nu}{q}\right)(k-nq)\Bigg[\frac{\partial}{\partial \psi}\left(\frac{R^2}{J}\right)\left(\frac{-\nu}{q}\right)(m-nq)w_m \\
&+ \frac{R^2}{J}n\nu\Bigg[\Bigg(\frac{(m-nq)}{nq}\left(im\omega' - \frac{\nu'}{\nu}\right) + \frac{mq'}{nq^2}\Bigg)w_m - \frac{(m-nq)}{nq}\frac{dw_m}{d\psi}\Bigg]\Bigg]\Bigg]\Bigg]e^{i(k-m)\omega} \qquad \text{(B.22)} \\
=& \pi\int_{-\infty}^{\psi_a} d\psi \sum_{m,k}\Bigg[u_k^{*}\Bigg[\Bigg[\frac{fp'}{n}S_{13}(m-nq) + \frac{f'}{n}S_{12}(m-nq) \\
&+ \frac{ip'}{n^2}S_{10}(m-nq) + \frac{fp'}{n^2q}S_{13}(m-nq)(k-nq) - \frac{1}{n^2q}S_{16}(m-nq)(k-nq) \\
&+ \frac{im}{n^2q}S_{6}(m-nq)(k-nq) - \frac{1}{n^2q}S_{3}(m-nq)(k-nq) \\
&+ \frac{mfq'}{n^2q^2}S_{12}(k-nq)\Bigg]w_m - \frac{f}{n^2q}(m-nq)(k-nq)S_{12}\frac{dw_m}{d\psi}\Bigg] \\
&+ w_k^{*}\Bigg[\Bigg[\frac{fp'}{n}S_{13}(k-nq) + \frac{f'}{n}S_{12}(k-nq) - \frac{ip'}{n^2}S_{10}(k-nq) \\
&+ \frac{fp'}{n^2q}S_{13}(k-nq)(m-nq) - \frac{im}{n^2q}S_{6}(m-nq)(k-nq) \\
&+ \frac{1}{n^2q}S_{3}(m-nq)(k-nq) - \frac{mfq'}{n^2q^2}S_{12}(k-nq)\Bigg]u_m \\
&+ \frac{f}{n^2q}(m-nq)(k-nq)S_{12}\frac{du_m}{d\psi}\Bigg]\Bigg]
\end{aligned}
$$

Finally, the surface term for term 13 can be Fourier decomposed to produce surface matrix elements.

$$\begin{aligned}
S_{u13} =&\pi \int_{-\infty}^{\psi_a} d\psi \oint d\chi \frac{\partial}{\partial\psi}\left[\frac{1}{n^2}\frac{R^2}{J}JBk_{\parallel}WY^*\right] \\
=&\pi \oint d\omega \sum_{k,m} \frac{R^2}{n^2 J}\left(\frac{-\nu}{q}\right)^2 \frac{q}{\nu}(m-nq)(k-nq)u_k^* w_m e^{i(k-m)\omega} \\
=&\pi \sum_{m,k} u_k^* \frac{f}{n^2 q} S_{12}(m-nq)(k-nq)w_m
\end{aligned} \tag{B.23}$$

Therefore all the matrix elements have been determined for the δW equation that determines marginal stability.

B.2 Solution of the δW inertia terms

This section details the Fourier decomposition of the δW equation terms associated with inertia. The equation, equation 3.10, has been reproduced here for reference, where $\rho(\psi)$ is the mass density and γ^2 the eigenvalue of the system, equal to the growth rate squared. It is Fourier decomposed in the same way, for two perturbations X and W.

$$\begin{aligned}
\delta W_{inertia} =&\pi\gamma^2 \int_{-\infty}^{\psi_a} d\psi \oint d\chi J\rho \Bigg[\left(\frac{1}{R^2B_p^2} + \frac{R^2B_p^2p'^2}{n^2B^6}\right)|X|^2 + \frac{R^2B_p^2}{n^2B^2}\left|\frac{\partial X}{\partial\psi}\right|^2 \\
&+ \frac{R^2B_p^2}{n^2B^2}|W|^2 + \frac{R^2B_p^2}{n^2B^2}\left[W^*\frac{\partial X}{\partial\psi} + \frac{\partial X^*}{\partial\psi}W\right] \\
&+ \frac{R^2B_p^2p'}{n^2B^4}\left[X^*\frac{\partial X}{\partial\psi} + \frac{\partial X^*}{\partial\psi}X\right] + \frac{R^2B_p^2p'}{n^2B^4}\left[X^*W + W^*X\right]\Bigg]
\end{aligned} \tag{B.24}$$

B.2.1 Inertia term 1

Firstly inertia term 1 is Fourier decomposed. This term only contains the X perturbation.

$$\begin{aligned}
\delta W_{I1} =&\pi\gamma^2 \int_{-\infty}^{\psi_a} d\psi \oint d\chi J\rho\left(\frac{1}{R^2B_p^2} + \frac{R^2B_p^2p'^2}{n^2B^6}\right)|X|^2 \\
=&\pi\gamma^2 \int_{-\infty}^{\psi_a} d\psi \oint d\omega \sum_{m,k} \frac{q}{\nu} J\rho u_k^* \left(\frac{1}{R^2B_p^2} + \frac{R^2B_p^2p'^2}{n^2B^6}\right) u_m e^{i(k-m)\omega} \\
=&\pi\gamma^2 \int_{-\infty}^{\psi_a} d\psi \sum_{m,k} u_k^* \left[\frac{q}{f}S_{31} + \frac{qp'^2}{n^2 f}S_{32}\right]u_m
\end{aligned} \tag{B.25}$$

B.2.2 Inertia term 2

Inertia term 2 requires integration by parts to produce inertia plasma terms and inertia surface term S_{Iu2}. This term only contains the X perturbation.

$$
\begin{aligned}
\delta W_{I2} =& \pi\gamma^2 \int_{-\infty}^{\psi_a} d\psi \oint d\chi J\rho \frac{R^2 B_p^2}{n^2 B^2} \left| \frac{\partial X}{\partial \psi} \right|^2 \\
=& \pi\gamma^2 \int_{-\infty}^{\psi_a} d\psi \oint d\chi \Bigg[\frac{\partial}{\partial \psi} \left(\frac{J\rho R^2 B_p^2}{n^2 B^2} X^* \frac{\partial X}{\partial \psi} \right) - \frac{\partial}{\partial \psi} \left(\frac{J\rho R^2 B_p^2}{n^2 B^2} \right) X^* \frac{\partial X}{\partial \psi} \\
& - \frac{J\rho R^2 B_p^2}{n^2 B^2} X^* \frac{\partial^2 X}{\partial \psi^2} \Bigg] \\
=& S_{Iu2} + \pi\gamma^2 \int_{-\infty}^{\psi_a} d\psi \oint d\chi \Bigg[-\frac{\partial}{\partial \psi} \left(\frac{J\rho R^2 B_p^2}{n^2 B^2} \right) X^* \frac{\partial X}{\partial \psi} - \frac{J\rho R^2 B_p^2}{n^2 B^2} X^* \frac{\partial^2 X}{\partial \psi^2} \Bigg] \\
S_{Iu2} =& \pi\gamma^2 \int_{-\infty}^{\psi_a} d\psi \oint d\chi \frac{\partial}{\partial \psi} \left(\frac{J\rho R^2 B_p^2}{n^2 B^2} X^* \frac{\partial X}{\partial \psi} \right)
\end{aligned}
\tag{B.26}
$$

Now inertia term 2 can be Fourier decomposed to determine its matrix elements.

$$
\begin{aligned}
\delta W_{I2} =& \pi\gamma^2 \int_{-\infty}^{\psi_a} d\psi \oint d\chi \Bigg[-\frac{\partial}{\partial \psi} \left(\frac{J\rho R^2 B_p^2}{n^2 B^2} \right) X^* \frac{\partial X}{\partial \psi} - \frac{J\rho R^2 B_p^2}{n^2 B^2} X^* \frac{\partial^2 X}{\partial \psi^2} \Bigg] \\
=& \pi\gamma^2 \int_{-\infty}^{\psi_a} d\psi \oint d\omega \sum_{m,k} u_k^* \frac{q}{\nu} \Bigg[-\frac{\partial}{\partial \psi} \left(\frac{J\rho R^2 B_p^2}{n^2 B^2} \right) \left[-im\omega' u_m + \frac{du_m}{d\psi} \right] \\
& - \frac{J\rho R^2 B_p^2}{n^2 B^2} \left[\left(-m^2 \omega'^2 - im\omega'' \right) u_m - 2im\omega' \frac{du_m}{d\psi} + \frac{d^2 u_m}{d\psi^2} \right] \Bigg] e^{i(k-m)\omega} \\
=& \pi\gamma^2 \int_{-\infty}^{\psi_a} d\psi \sum_{m,k} u_k^* \Bigg[\left[\frac{imq}{n^2} S_{34} + \frac{m^2 q}{n^2 f} S_{38} + \frac{imq}{n^2 f} S_{37} \right] u_m \\
& - \frac{q}{n^2} \left[S_{33} - \frac{2im}{f} S_{36} \right] \frac{du_m}{d\psi} - \frac{q}{n^2 f} S_{35} \frac{d^2 u_m}{d\psi^2} \Bigg]
\end{aligned}
\tag{B.27}
$$

Finally the surface inertia term for term 2 can be Fourier decomposed.

$$
\begin{aligned}
S_{Iu2} =& \pi\gamma^2 \int_{-\infty}^{\psi_a} d\psi \oint d\chi \frac{\partial}{\partial \psi} \left(\frac{J\rho R^2 B_p^2}{n^2 B^2} X^* \frac{\partial X}{\partial \psi} \right) \\
=& \pi\gamma^2 \oint d\omega \sum_{m,k} u_k^* \frac{q}{\nu} \frac{J\rho R^2 B_p^2}{n^2 B^2} \left(-im\omega' u_m + \frac{du_m}{d\psi} \right) e^{i(k-m)\omega} \\
=& \pi\gamma^2 \sum_{m,k} u_k^* \left[-\frac{imq}{n^2 f} S_{36} u_m + \frac{q}{n^2 f} S_{35} \frac{du_m}{d\psi} \right]
\end{aligned}
\tag{B.28}
$$

B.2.3 Inertia term 3

Now inertia term 3 is Fourier decomposed. This term only contains the W perturbation.

$$\begin{aligned}
\delta W_{I3} =& \pi\gamma^2 \int_{-\infty}^{\psi_a} d\psi \oint d\chi J\rho \frac{R^2 B_p^2}{n^2 B^2} |W|^2 \\
=& \pi\gamma^2 \int_{-\infty}^{\psi_a} d\psi \oint d\omega \sum_{m,k} \frac{q}{\nu} w_k^* \frac{J\rho R^2 B_p^2}{n^2 B^2} w_m e^{i(k-m)\omega} \\
=& \pi\gamma^2 \int_{-\infty}^{\psi_a} d\psi \sum_{m,k} w_k^* \frac{q}{n^2 f} S_{35} w_m
\end{aligned} \tag{B.29}$$

B.2.4 Inertia term 4

Inertia term 4 requires integration by parts to produce inertia plasma terms and inertia surface term S_{Iu4}. This term contains both the X and W perturbations.

$$\begin{aligned}
\delta W_{I4} =& \pi\gamma^2 \int_{-\infty}^{\psi_a} d\psi \oint d\chi J\rho \frac{R^2 B_p^2}{n^2 B^2} \left[W^* \frac{\partial X}{\partial \psi} + \frac{\partial X^*}{\partial \psi} W \right] \\
=& \pi\gamma^2 \int_{-\infty}^{\psi_a} d\psi \oint d\chi \Bigg[\frac{J\rho R^2 B_p^2}{n^2 B^2} W^* \frac{\partial X}{\partial \psi} + \frac{\partial}{\partial \psi} \left(\frac{J\rho R^2 B_p^2}{n^2 B^2} X^* W \right) \\
& - \frac{\partial}{\partial \psi} \left(\frac{J\rho R^2 B_p^2}{n^2 B^2} \right) X^* W - \frac{J\rho R^2 B_p^2}{n^2 B^2} X^* \frac{\partial W}{\partial \psi} \Bigg] \\
=& S_{Iu4} + \pi\gamma^2 \int_{-\infty}^{\psi_a} d\psi \oint d\chi \Bigg[\frac{J\rho R^2 B_p^2}{n^2 B^2} W^* \frac{\partial X}{\partial \psi} - \frac{\partial}{\partial \psi} \left(\frac{J\rho R^2 B_p^2}{n^2 B^2} \right) X^* W \\
& - \frac{J\rho R^2 B_p^2}{n^2 B^2} X^* \frac{\partial W}{\partial \psi} \Bigg] \\
S_{Iu4} =& \pi\gamma^2 \int_{-\infty}^{\psi_a} d\psi \oint d\chi \frac{\partial}{\partial \psi} \left(\frac{J\rho R^2 B_p^2}{n^2 B^2} X^* W \right)
\end{aligned} \tag{B.30}$$

Now inertia term 4 can be Fourier decomposed to determine its matrix elements.

$$\begin{aligned}
\delta W_{I4} =& \pi\gamma^2 \int_{-\infty}^{\psi_a} d\psi \oint d\chi \Bigg[\frac{J\rho R^2 B_p^2}{n^2 B^2} W^* \frac{\partial X}{\partial \psi} - \frac{\partial}{\partial \psi} \left(\frac{J\rho R^2 B_p^2}{n^2 B^2} \right) X^* W \\
& - \frac{J\rho R^2 B_p^2}{n^2 B^2} X^* \frac{\partial W}{\partial \psi} \Bigg] \\
=& S\pi\gamma^2 \int_{-\infty}^{\psi_a} d\psi \oint d\omega \sum_{m,k} \frac{q}{\nu} \Bigg[w_k^* \frac{J\rho R^2 B_p^2}{n^2 B^2} \left[-im\omega' u_m + \frac{du_m}{d\psi} \right] \\
& + u_k^* \Bigg[- \frac{\partial}{\partial \psi} \left(\frac{J\rho R^2 B_p^2}{n^2 B^2} \right) w_m - \frac{J\rho R^2 B_p^2}{n^2 B^2} \left[-im\omega' w_m + \frac{dw_m}{d\psi} \right] \Bigg] \Bigg] e^{i(k-m)\omega} \\
=& \pi\gamma^2 \int_{-\infty}^{\psi_a} d\psi \sum_{m,k} \Bigg[w_k^* \left[-\frac{imq}{n^2 f} S_{36} u_m + \frac{q}{n^2 f} S_{35} \frac{du_m}{d\psi} \right] \\
& + u_k^* \Bigg[\left[-\frac{q}{n^2} S_{33} + \frac{imq}{n^2 f} S_{36} \right] w_m - \frac{q}{n^2 f} S_{35} \frac{dw_m}{d\psi} \Bigg] \Bigg]
\end{aligned} \tag{B.31}$$

Finally the surface inertia term for term 4 can be Fourier decomposed.

$$\begin{aligned} S_{Iu4} =& \pi\gamma^2 \int_{-\infty}^{\psi_a} d\psi \oint d\chi \frac{\partial}{\partial\psi}\left(\frac{J\rho R^2 B_p^2}{n^2 B^2} X^* W\right) \\ =& \pi\gamma^2 \oint d\omega \sum_{m,k} u_k^* \frac{q}{\nu} \frac{J\rho R^2 B_p^2}{n^2 B^2} w_m e^{i(k-m)\omega} \\ =& \pi\gamma^2 \sum_{m,k} u_k^* \frac{q}{n^2 f} S_{35} w_m \end{aligned} \tag{B.32}$$

B.2.5 Inertia term 5

Inertia term 5 requires integration by parts to produce inertia plasma terms and inertia surface term S_{Iu5}. This term contains only the X perturbation.

$$\begin{aligned} \delta W_{I5} =& \pi\gamma^2 \int_{-\infty}^{\psi_a} d\psi \oint d\chi J\rho \frac{R^2 B_p^2 p'}{n^2 B^4}\left[X^* \frac{\partial X}{\partial\psi} + \frac{\partial X^*}{\partial\psi} X\right] \\ =& \pi\gamma^2 \int_{-\infty}^{\psi_a} d\psi \oint d\chi \Bigg[\frac{J\rho R^2 B_p^2 p'}{n^2 B^4} X^* \frac{\partial X}{\partial\psi} + \frac{\partial}{\partial\psi}\left(\frac{J\rho R^2 B_p^2 p'}{n^2 B^4}|X|^2\right) \\ & - \frac{\partial}{\partial\psi}\left(\frac{J\rho R^2 B_p^2 p'}{n^2 B^4}\right)|X|^2 - \frac{J\rho R^2 B_p^2 p'}{n^2 B^4} X^* \frac{\partial X}{\partial\psi}\Bigg] \\ =& S_{Iu5} + \pi\gamma^2 \int_{-\infty}^{\psi_a} d\psi \oint d\chi \frac{\partial}{\partial\psi}\left(\frac{-J\rho R^2 B_p^2 p'}{n^2 B^4}\right)|X|^2 \\ S_{Iu5} =& \frac{\partial}{\partial\psi}\left(\frac{J\rho R^2 B_p^2 p'}{n^2 B^4}|X|^2\right) \end{aligned} \tag{B.33}$$

Now inertia term 5 can be Fourier decomposed to determine its matrix elements.

$$\begin{aligned} \delta W_{I5} =& \pi\gamma^2 \int_{-\infty}^{\psi_a} d\psi \oint d\chi \frac{\partial}{\partial\psi}\left(\frac{-J\rho R^2 B_p^2 p'}{n^2 B^4}\right)|X|^2 \\ =& \pi\gamma^2 \int_{-\infty}^{\psi_a} d\psi \oint d\omega \sum_{m,k} u_k^* \frac{q}{\nu}\frac{\partial}{\partial\psi}\left(\frac{-J\rho R^2 B_p^2 p'}{n^2 B^4}\right) u_m e^{i(k-m)\omega} \\ =& \pi\gamma^2 \int_{-\infty}^{\psi_a} d\psi \sum_{m,k} u_k^* \left[-\frac{q}{n^2} S_{39}\right] u_m \end{aligned} \tag{B.34}$$

Finally the surface inertia term for term 5 can be Fourier decomposed.

$$\begin{aligned} S_{Iu5} =& \pi\gamma^2 \int_{-\infty}^{\psi_a} d\psi \oint d\chi \frac{\partial}{\partial\psi}\left(\frac{J\rho R^2 B_p^2 p'}{n^2 B^4}|X|^2\right) e^{i(k-m)\omega} \\ =& \pi\gamma^2 \oint d\omega \sum_{m,k} u_k^* \frac{q}{\nu} \frac{J\rho R^2 B_p^2 p'}{n^2 B^4} u_m e^{i(k-m)\omega} \\ =& \pi\gamma^2 \sum_{m,k} u_k^* \frac{q p'}{n^2 f} S_{40} u_m \end{aligned} \tag{B.35}$$

B.2.6 Inertia term 6

The final inertia term is now Fourier decomposed. This term contains both the X and W perturbations.

$$\begin{aligned}\delta W_{I6} =&\pi\gamma^2\int_{-\infty}^{\psi_a}d\psi\oint d\chi J\rho\frac{R^2B_p^2p'}{n^2B^4}\left[X^*W+W^*X\right]\\ =&\pi\gamma^2\int_{-\infty}^{\psi_a}d\psi\oint d\omega\sum_{m,k}\frac{q}{\nu}\frac{J\rho R^2B_p^2p'}{n^2B^4}\left[u_k^*w_m+w_k^*u_m\right]e^{i(k-m)\omega}\\ =&\pi\gamma^2\int_{-\infty}^{\psi_a}d\psi\sum_{m,k}\left[w_k^*\frac{qp'}{n^2f}S_{40}u_m+u_k^*\frac{qp'}{n^2f}S_{40}w_m\right]\end{aligned} \tag{B.36}$$

Now the complete set of matrix elements have been derived, and form a pair of sets of coupled equations.

B.3 ELITE matrix elements

As detailed in section 3.4.2, once the complete set of matrix elements have been obtained these form two sets of coupled equations from the plasma terms. The subscript number on the matrix elements refers to the kernel number of that matrix element. These are fully listed in section B.4. The first set of coupled equations is the X equation, which consists of plasma terms that contain the X complex conjugate u_k^*. The X equation is given by 3.20. This contains matrix elements that act on both the Fourier amplitudes, u_m and w_m as explained in section 3.4.2. Firstly consider the u_m Fourier amplitudes. These are given the letter A, and when grouped, including inertia A_I, and are given by:

$$
\begin{aligned}
A''_{mk} &= -\frac{f}{n^2 q} S_{12} \\
A'_{mk} &= -\frac{2}{n^2 q} S_3 + \frac{2im}{n^2 q} S_6 - \frac{1}{n^2 q} S_{16} \\
A'_{m} &= \frac{ip'}{n^2} S_{10} \\
A'_{k} &= \frac{2mfq'}{n^2 q^2} S_{12} + \frac{ip'}{n^2} S_{10} \\
A' &= \frac{iqp'}{n} S_{10} \\
A_{mk} &= \frac{1}{q} S_1 - \frac{1}{q^2 n^2} S_2 + \frac{p'^2}{n^2 q} S_4 + \frac{2im}{n^2 q} S_5 + \frac{m^2}{n^2 q} S_7 + \frac{im}{n^2 q} S_8 - \frac{1}{n^2 q} S_{14} \\
&\quad + \frac{im}{n^2 q} S_{15} - \frac{1}{n^2 q} S_{20} \\
A_{m} &= \frac{mp'}{n^2} S_{11} - \frac{1}{n} S_{17} + \frac{1}{n} S_{19} + \frac{i}{n^2} S_{21} + \frac{ip'^2}{n^2} S_{24} \\
A_{k} &= \frac{2mq'}{n^2 q^2} S_3 - \frac{2im^2 q'}{n^2 q^2} S_6 + \frac{mp'}{n^2} S_{11} + \frac{mf}{n^2 q^2}\left(q'' - \frac{2q'^2}{q}\right) S_{12} + \frac{mq'}{n^2 q^2} S_{16} \\
&\quad - \frac{1}{n} S_{17} + \frac{i}{n^2} S_{22} - \frac{ip'^2}{n^2} S_{24} \\
A &= -\frac{2qp'}{f} S_9 - \frac{imq'p'}{n^2 q} S_{10} + \frac{mqp'}{n} S_{11} + \frac{iq}{n} S_{18} + \frac{qp'^2}{n^2} S_{23} \\
A''_{I} &= \frac{q}{n^2 f} S_{35} \\
A'_{I} &= \frac{q}{n^2}\left(S_{33} - \frac{2im}{f} S_{36}\right) \\
A_{I} &= -\frac{q}{f} S_{31} - \frac{qp'^2}{n^2 f} S_{32} - \frac{imq}{n^2} S_{34} - \frac{m^2 q}{n^2 f} S_{38} - \frac{imq}{n^2 f} S_{37} + \frac{q}{n^2} S_{39}
\end{aligned}
\tag{B.37}
$$

where a prime denotes a radial derivative on the u_m Fourier amplitudes, and the subscript m denotes an $(m - nq)$ and k denotes a $(k - nq)$ respectively. The X equation also contains matrix elements that act on the w_m Fourier amplitudes. These are given the letter B, and when grouped, including inertia B_I, are given by:

$$\begin{aligned}
B'_{mk} &= -\frac{f}{n^2q}S_{12}\\
B'_k &= -\frac{f}{n}S_{12}\\
B_{mk} &= -\frac{1}{n^2q}S_3+\frac{im}{n^2q}S_6+\frac{fp'}{n^2q}S_{13}-\frac{1}{n^2q}S_{16}\\
B_m &= \frac{ip'}{n^2}S_{10}+\frac{f'}{n}S_{12}+\frac{2fp'}{n}S_{13}\\
B_k &= \frac{im}{n}S_6+\left(\frac{mfq'}{n^2q^2}-\frac{f'}{n}\right)S_{12}\\
B'_I &= \frac{q}{n^2f}S_{35}\\
B_I &= \frac{q}{n^2}S_{33}-\frac{imq}{n^2f}S_{36}-\frac{p'q}{n^2f}S_{40}
\end{aligned}\tag{B.38}$$

where primes and subscripts have the same definitions. The second set of coupled equations, the W equation, is the collective group of terms containing the W complex conjugate, w_k^*. The W equation is given by 3.21. This contains matrix elements that act on both the u_m and w_m Fourier amplitudes, as explained in section 3.4.2. Firstly the w_m Fourier amplitudes are considered. These are given the letter C, and when grouped, including inertia C_I, are given by:

$$\begin{aligned}
C_{mk} &= \frac{f}{n^2q}S_{12}\\
C_m &= \frac{f}{n}S_{12}\\
C_k &= \frac{f}{n}S_{12}\\
C &= \frac{q}{f}S_{25}\\
C_I &= -\frac{q}{n^2f}S_{35}
\end{aligned}\tag{B.39}$$

where primes and subscripts have the same definitions. The W equation also contains matrix elements that act on the u_m Fourier amplitudes. These are given the letter D, and when grouped, including inertia D_I, are given by:

$$\begin{aligned}
D'_{mk} &= \frac{f}{n^2 q} S_{12} \\
D'_{m} &= \frac{f}{n} S_{12} \\
D_{mk} &= \frac{1}{n^2 q} S_3 - \frac{im}{n^2 q} S_6 + \frac{fp'}{n^2 q} S_{13} \\
D_{m} &= \frac{1}{n} S_3 - \frac{im}{n} S_6 \\
D_{k} &= -\frac{ip'}{n^2} S_{10} + \left(\frac{f'}{n} - \frac{mfq'}{n^2 q^2} \right) S_{12} + \frac{2fp'}{n} S_{13} \\
D &= -\frac{mfq'}{nq} S_{12} \\
D'_{I} &= -\frac{q}{n^2 f} S_{35} \\
D_{I} &= \frac{imq}{n^2 f} S_{36} - \frac{p'q}{n^2 f} S_{40}
\end{aligned} \tag{B.40}$$

where primes and subscripts have the same definitions. These form the complete set of plasma matrix elements. Now here are the matrix elements for the surface terms which form the boundary conditions. These are all with respect to u_k^*, and are given by equation 3.22. Note that a factor of $1/n$ has been factored from all the matrix elements here, as it is a common factor. There are matrix elements that act on the u_m Fourier amplitudes, A_S, including inertia A_{SI}, and matrix elements that act on the w_m Fourier amplitudes, B_S, including inertia B_{SI}. These are collectively are given by:

$$\begin{aligned}
A'_{Smk} &= \frac{f}{nq} S_{12} \\
A_{Smk} &= \frac{1}{nq} S_3 - \frac{im}{nq} S_6 \\
A_{Sk} &= -\frac{ip'}{n} S_{10} + \left(f' - \frac{mfq'}{nq^2} \right) S_{12} + \frac{mfp'}{nq} S_{13} \\
B_{Smk} &= \frac{f}{nq} S_{12} \\
B_{Sk} &= f S_{12} \\
A'_{SI} &= -\frac{q}{nf} S_{35} \\
A_{SI} &= \frac{imq}{nf} S_{36} - \frac{qp'}{nf} S_{40} \\
B_{SI} &= -\frac{q}{nf} S_{35}
\end{aligned} \tag{B.41}$$

where primes and subscripts have the same definitions. These complete all the matrix elements from the Fourier decomposition of equation 3.7 and equation 3.10.

B.4 Arbitrary n ELITE kernels

The new arbitrary n ELITE kernels, $L_i(\psi, \omega)$, are defined by equation 3.17, and are listed fully here.

$$L_1 = \frac{f}{R^4 B^2} \qquad L_2 = \frac{R^2 q}{J}\nu'' \qquad L_3 = \frac{R^2 \nu'}{J}$$

$$L_4 = \frac{f}{B^4} \qquad L_5 = \frac{R^2}{J}\nu'\omega' \qquad L_6 = f\omega'$$

$$L_7 = f(\omega')^2 \qquad L_8 = f\omega'' \qquad L_9 = \frac{R^2}{B^2}\frac{\partial}{\partial\psi}\left(p + \frac{B^2}{2}\right)$$

$$L_{10} = \frac{R^2}{JB^4}\frac{\partial B^2}{\partial\chi} \qquad L_{11} = \frac{R^2\omega'}{JB^4}\frac{\partial B^2}{\partial\chi} \qquad L_{12} = 1$$

$$L_{13} = \frac{1}{B^2} \qquad L_{14} = \nu'\frac{\partial}{\partial\psi}\left(\frac{R^2}{J}\right) \qquad L_{15} = \nu\omega'\frac{\partial}{\partial\psi}\left(\frac{R^2}{J}\right)$$

$$L_{16} = \nu\frac{\partial}{\partial\psi}\left(\frac{R^2}{J}\right) \qquad L_{17} = \frac{\sigma p'}{B^2} \qquad L_{18} = \frac{1}{\nu}\frac{\partial\sigma'}{\partial\chi}$$

$$L_{19} = \sigma' \qquad L_{20} = \nu\frac{\partial}{\partial\psi}\left(\frac{p'R^2}{JB^2}\right) \qquad L_{21} = \frac{R^2 p'\nu'}{JB^4\nu}\frac{\partial B^2}{\partial\chi}$$

$$L_{22} = \frac{\partial}{\partial\psi}\left(\frac{p'R^2}{JB^4}\frac{\partial B^2}{\partial\chi}\right) \qquad L_{23} = \frac{R^2}{\nu JB^8}\left(\frac{\partial B^2}{\partial\chi}\right)^2 \qquad L_{24} = \frac{R^2}{JB^6}\frac{\partial B^2}{\partial\chi}$$

$$L_{25} = R^2 B^2 \qquad L_{26} = \frac{\partial}{\partial\psi}\left(R^2 B^2\right) \qquad L_{27} = \frac{\omega' R^2}{J}\frac{\partial}{\partial\chi}\left(R^2 B^2\right)$$

$$L_{28} = \frac{\omega' R^2}{J}\frac{\partial}{\partial\chi}\left(\frac{R^2\nu'}{J}\right) \qquad L_{29} = \frac{1}{B^4}\frac{\partial B^2}{\partial\psi} \qquad L_{30} = \frac{\omega' R^2}{J}\frac{\partial}{\partial\chi}\left(\frac{R^2}{JB^4}\frac{\partial B^2}{\partial\chi}\right)$$

$$L_{31} = \frac{\rho}{B_p^2} \qquad L_{32} = \frac{\rho R^4 B_p^2}{B^6} \qquad L_{33} = \frac{1}{\nu}\frac{\partial}{\partial\psi}\left(\frac{\rho J R^2 B_p^2}{B^2}\right)$$

$$L_{34} = \frac{\omega'}{\nu}\frac{\partial}{\partial\psi}\left(\frac{\rho J R^2 B_p^2}{B^2}\right) \qquad L_{35} = \frac{\rho R^4 B_p^2}{B^2} \qquad L_{36} = \frac{\omega'\rho R^4 B_p^2}{B^2}$$

$$L_{37} = \frac{\omega''\rho R^4 B_p^2}{B^2} \qquad L_{38} = \frac{(\omega')^2\rho R^4 B_p^2}{B^2} \qquad L_{39} = \frac{1}{\nu}\frac{\partial}{\partial\psi}\left(\frac{\rho J R^2 B_p^2 p'}{B^4}\right)$$

$$L_{40} = \frac{\rho R^4 B_p^2}{B^4} \qquad L_{41} = \frac{\partial}{\partial\psi}\left(\frac{\rho R^4 B_p^2}{B^2}\right) \qquad L_{42} = \frac{\rho\omega' R^2}{J}\frac{\partial}{\partial\chi}\left(\frac{R^4 B_p^2}{B^2}\right)$$

$$L_{43} = \frac{\partial}{\partial\psi}\left(\frac{\rho\omega' R^4 B_p^2}{B^2}\right) \qquad L_{44} = \frac{\rho\omega' R^2}{J}\frac{\partial}{\partial\chi}\left(\frac{\omega' R^4 B_p^2}{B^2}\right) \qquad L_{45} = \frac{\partial}{\partial\psi}\left(\frac{\rho R^4 B_p^2}{B^4}\right)$$

$$L_{46} = \frac{\rho\omega' R^2}{J}\frac{\partial}{\partial\chi}\left(\frac{R^4 B_p^2}{B^4}\right)$$

Inverting C on the coarse mesh modifies two kernels, L_{25} and L_{26}, to:

$$L_{25} = R^2 B_p^2 \qquad\qquad L_{26} = \frac{\partial}{\partial\psi}\left(R^2 B_p^2\right)$$

B.5 E,F and G matrix elements and derivation of the kernel derivatives

This section details the matrix elements for $\underline{\underline{E}}$, $\underline{\underline{F}}$ and $\underline{\underline{G}}$ and the differentiation of the necessary kernels to obtain the matrix elements. These are necessary to eliminate the Fourier amplitude w_m and to create a single set of coupled original ELITE-like Euler equations, with modified coefficient matrices as detailed in section 3.5.

B.5.1 E matrix elements

Starting with the $\underline{\underline{E}}$ matrix elements. These are given by:

$$\underline{\underline{E}} = \frac{d\underline{\underline{C}}}{d\psi} \tag{B.42}$$

where the $\underline{\underline{C}}$ matrix elements are detailed in section B.3. To differentiate them, as shown in section 3.5.2, requires differentiating the factors that have a ψ dependence, and also the kernels using the equation 3.48. The $\underline{\underline{C}}$ matrix elements contain the following kernels that need differentiating to form the $\underline{\underline{E}}$ matrix elements. Note S_{12} is simply given by 1. Firstly, S_{25}, as shown in section 3.5.2.

$$\begin{aligned}
\frac{\partial S_{25}}{\partial\psi} &= \oint\left[\frac{\partial L_{25}}{\partial\psi} - \frac{q\omega'}{\nu}\frac{\partial L_{25}}{\partial\chi}\right]e^{i(k-m)\omega}d\omega \\
&= \oint\left[\frac{\partial}{\partial\psi}\left(R^2B^2\right) - \frac{q\omega' R^2}{fJ}\frac{\partial}{\partial\chi}\left(R^2B^2\right)\right]e^{i(k-m)\omega}d\omega \\
&= S_{26} - \frac{q}{f}S_{27}
\end{aligned} \tag{B.43}$$

The other differentiation required is S_{35}, from the inertia term. This is given by:

$$\begin{aligned}
\frac{\partial S_{35}}{\partial\psi} &= \oint\left[\frac{\partial L_{35}}{\partial\psi} - \frac{q\omega'}{\nu}\frac{\partial L_{35}}{\partial\chi}\right]e^{i(k-m)\omega}d\omega \\
&= \oint\left[\frac{\partial}{\partial\psi}\left(\frac{\rho R^4 B_p^2}{B^2}\right) - \frac{\rho q R^2\omega'}{fJ}\frac{\partial}{\partial\chi}\left(\frac{R^4B_p^2}{B^2}\right)\right]e^{i(k-m)\omega}d\omega \\
&= S_{41} - \frac{q}{f}S_{42}
\end{aligned} \tag{B.44}$$

Therefore the full set of $\underline{\underline{E}}$ matrix elements are given in the list below.

$$\begin{aligned}
E_{mk} &= \frac{1}{n^2 q}\left(f' - \frac{fq'}{q}\right) S_{12} \\
E_{m} &= \frac{2}{n}\left(f' - \frac{fq'}{q}\right) S_{12} \\
E &= \frac{q}{f}\left(\frac{q'}{q} - \frac{f'}{f}\right) S_{25} + \frac{q}{f} S_{26} - \left(\frac{q}{f}\right)^2 S_{27} - 2fq' S_{12} \\
E_{I} &= -\frac{1}{n^2 f}\left(q' - \frac{qf'}{f}\right) S_{35} - \frac{q}{n^2 f}\left(S_{41} - \frac{q}{f} S_{42}\right)
\end{aligned} \tag{B.45}$$

B.5.2 F matrix elements

Now the $\underline{\underline{F}}$ matrix elements. These are given by:

$$\underline{\underline{F}} = \frac{d\underline{\underline{D}}'}{d\psi} \tag{B.46}$$

where the $\underline{\underline{D}}'$ matrix elements are detailed in section B.3. As the $\underline{\underline{D}}'$ inertia matrix element is identical to the $\underline{\underline{C}}$ inertia matrix element, no more calculation is necessary. Therefore the $\underline{\underline{F}}$ matrix elements are listed here.

$$\begin{aligned}
F_{mk} &= \frac{1}{n^2 q}\left(f' - \frac{fq'}{q}\right) S_{12} \\
F_{m} &= \frac{1}{n}\left(f' - \frac{2fq'}{q}\right) S_{12} \\
F &= -fq' S_{12} \\
F_{I} &= -\frac{1}{n^2 f}\left(q' - \frac{qf'}{f}\right) S_{35} - \frac{q}{n^2 f}\left(S_{41} - \frac{q}{f} S_{42}\right)
\end{aligned} \tag{B.47}$$

B.5.3 G matrix elements

Finally the $\underline{\underline{G}}$ matrix elements. These are given by:

$$\underline{\underline{G}} = \frac{d\underline{\underline{D}}}{d\psi} \tag{B.48}$$

where the $\underline{\underline{D}}$ matrix elements are detailed in section B.3. The $\underline{\underline{C}}$ matrix elements contain the following kernels that need differentiating to form the $\underline{\underline{E}}$ matrix elements.

Firstly, S_3:

$$\begin{aligned}
\frac{\partial S_3}{\partial \psi} =& \oint \left[\frac{\partial L_3}{\partial \psi} - \frac{q\omega'}{\nu}\frac{\partial L_3}{\partial \chi} \right] e^{i(k-m)\omega} d\omega \\
=& \oint \left[\frac{\nu'' R^2}{J} + \nu' \frac{\partial}{\partial \psi}\left(\frac{R^2}{J}\right) - \frac{q\omega'}{\nu}\frac{\partial}{\partial \chi}\left(\frac{R^2 \nu'}{J}\right) \right] e^{i(k-m)\omega} d\omega \\
=& \frac{1}{q} S_2 + S_{14} - \frac{q}{f} S_{28}
\end{aligned} \tag{B.49}$$

Next S_6:

$$\begin{aligned}
\frac{\partial S_6}{\partial \psi} =& \oint \left[\frac{\partial L_6}{\partial \psi} - \frac{q\omega'}{\nu}\frac{\partial L_6}{\partial \chi} \right] e^{i(k-m)\omega} d\omega \\
=& \oint \left[f'\omega' + f\omega'' - \frac{q\omega' f}{\nu}\frac{\partial \omega'}{\partial \chi} \right] e^{i(k-m)\omega} d\omega \\
=& \oint \left[f'\omega' + f\omega'' - \frac{f\omega'\nu'}{\nu} + \frac{f\omega' q'}{q} \right] e^{i(k-m)\omega} d\omega \\
=& \oint \left[f'\omega' + f\omega'' - f'\omega' - \frac{f\omega' R^2}{J}\frac{\partial}{\partial \psi}\left(\frac{J}{R^2}\right) + \frac{f\omega' q'}{q} \right] e^{i(k-m)\omega} d\omega \\
=& \frac{q'}{q} S_6 + S_8 + S_{15}
\end{aligned} \tag{B.50}$$

using a relation in equation 3.46. Next is S_{10}:

$$\begin{aligned}
\frac{\partial S_{10}}{\partial \psi} =& \oint \left[\frac{\partial L_{10}}{\partial \psi} - \frac{q\omega'}{\nu}\frac{\partial L_{10}}{\partial \chi} \right] e^{i(k-m)\omega} d\omega \\
=& \oint \left[\frac{1}{p'}\frac{\partial}{\partial \psi}\left(\frac{R^2 p'}{JB^4}\frac{\partial B^2}{\partial \chi}\right) - \frac{p'' R^2}{JB^4}\frac{\partial B^2}{\partial \chi} - \frac{qR^2\omega'}{fJ}\frac{\partial}{\partial \chi}\left(\frac{R^2}{JB^4}\frac{\partial B^2}{\partial \chi}\right) \right] e^{i(k-m)\omega} d\omega \\
=& \frac{1}{p'}\left[S_{22} - p'' S_{10} \right] - \frac{q}{f} S_{30}
\end{aligned} \tag{B.51}$$

Now S_{13}:

$$\begin{aligned}
\frac{\partial S_{13}}{\partial \psi} =& \oint \left[\frac{\partial L_{13}}{\partial \psi} - \frac{q\omega'}{\nu}\frac{\partial L_{13}}{\partial \chi} \right] e^{i(k-m)\omega} d\omega \\
=& \oint \left[-\frac{1}{B^4}\frac{\partial B^2}{\partial \psi} + \frac{q\omega'}{\nu B^4}\frac{\partial B^2}{\partial \chi} \right] e^{i(k-m)\omega} d\omega \\
=& \frac{q}{f} S_{11} - S_{29}
\end{aligned} \tag{B.52}$$

Now, for the kernels from the inertia matrix elements, S_{36}:

$$\begin{aligned}\frac{\partial S_{36}}{\partial\psi} &= \oint\left[\frac{\partial L_{36}}{\partial\psi} - \frac{q\omega'}{\nu}\frac{\partial L_{36}}{\partial\chi}\right]e^{i(k-m)\omega}d\omega\\ &= \oint\left[\frac{\partial}{\partial\psi}\left(\frac{\rho\omega' R^4 B_p^2}{B^2}\right) - \frac{\rho q R^2\omega'}{fJ}\frac{\partial}{\partial\chi}\left(\frac{\omega' R^4 B_p^2}{B^2}\right)\right]e^{i(k-m)\omega}d\omega\\ &= S_{43} - \frac{q}{f}S_{44}\end{aligned} \tag{B.53}$$

Finally S_{40}:

$$\begin{aligned}\frac{\partial S_{40}}{\partial\psi} &= \oint\left[\frac{\partial L_{40}}{\partial\psi} - \frac{q\omega'}{\nu}\frac{\partial L_{40}}{\partial\chi}\right]e^{i(k-m)\omega}d\omega\\ &= \oint\left[\frac{\partial}{\partial\psi}\left(\frac{\rho R^4 B_p^2}{B^4}\right) - \frac{\rho R^2\omega' q}{fJ}\frac{\partial}{\partial\chi}\left(\frac{R^4 B_p^2}{B^4}\right)\right]e^{i(k-m)\omega}d\omega\\ &= S_{45} - \frac{q}{f}S_{46}\end{aligned} \tag{B.54}$$

Therefore the $\underline{\underline{G}}$ matrix elements are listed here.

$$\begin{aligned}
G_{mk} &= -\frac{im}{n^2 q}\left(S_8 + S_{15}\right) - \frac{q'}{n^2q^2}S_3 + \frac{1}{n^2 q}\left(\frac{1}{q}S_2 + S_{14} - \frac{q}{f}S_{28}\right)\\
&\quad + \frac{fp'}{n^2 q}\left(\frac{q}{f}S_{11} - S_{29}\right) + \frac{1}{n^2}\left(\frac{f'p'}{q} + \frac{fp''}{q} - \frac{fp'q'}{q^2}\right)S_{13}\\
G_m &= -\frac{im}{n}\left(S_8 + S_{15} + \frac{q'}{q}S_6\right) + \frac{1}{n}\left(\frac{1}{q}S_2 + S_{14} - \frac{q}{f}S_{28}\right)\\
&\quad - nq'\left(\frac{1}{n^2 q}S_3 - \frac{im}{n^2 q}S_6 + \frac{fp'}{n^2 q}S_{13}\right)\\
G_k &= \left[\frac{f''}{n} - \frac{m}{n^2q^2}\left(f'q' + fq'' - \frac{2fq'^2}{q}\right)\right]S_{12} + \frac{2}{n}\left(f'p' + fp''\right)S_{13}\\
&\quad + \frac{2p'}{n}\left(qS_{11} - fS_{29}\right) - \frac{i}{n^2}S_{22} + \frac{iqp'}{n^2 f}S_{30}\\
&\quad - nq'\left(\frac{1}{n^2 q}S_3 - \frac{im}{n^2 q}S_6 + \frac{fp'}{n^2 q}S_{13}\right)\\
G &= -\frac{m}{nq}\left(f'q' + fq'' - \frac{fq'^2}{q}\right)S_{12}\\
&\quad - nq'\left(\frac{1}{n}S_3 - \frac{im}{n}S_6 - \frac{ip'}{n^2}S_{10} + \left(\frac{f'}{n} - \frac{mfq'}{n^2q^2}\right)S_{12} + \frac{2fp'}{n}S_{13}\right)\\
G_I &= \frac{im}{n^2 f}\left(q' - \frac{qf'}{f}\right)S_{36} - \frac{1}{n^2 f}\left(p'q' - \frac{qp'f'}{f} + qp''\right)S_{40}\\
&\quad + \frac{imq}{n^2 f}\left(S_{43} - \frac{q}{f}S_{44}\right) - \frac{p'q}{n^2 f}\left(S_{45} - \frac{q}{f}S_{46}\right)
\end{aligned} \tag{B.55}$$

Appendix C

Details for running the arbitrary n ELITE code including input files

C.1 ELITE input files and versions

This section is divided into the following subsections. The first contains descriptions of the different ELITE versions. The second subsection is based on the ELITE user manual [99], but with the new additional parameters included. The third then contains each input file from each of the test case benchmarks, including running with the ideal wall and the test case for the original ELITE run with the delta W diagnostic. Also included is the input file used for the DIII-D QH-mode study from chapter 5, to show an experimental example. It should be noted however, that convergence testing real equilibria is challenging, and is likely case dependent, so this should be used as a guide only and individual convergence tests for each experimental equilibria should be performed.

C.1.1 ELITE versions

These are the names of the different versions of the ELITE plasma code, both up-down symmetric and non-up-down symmetric, with corresponding information to link the version to the results in chapter 4. All the different versions of arbitrary n ELITE can be run with full arbitrary n inertia (n1term=11) or the high n inertia approximation (n1term=10).

- “symlown_workplas16” - This is the up-down symmetric version of arbitrary n ELITE that has the C matrix calculated and inverted on the fine mesh. The original ELITE δW diagnostic, termscal.f90, here is normalised to the coefficient of growth rate in the inertial term and this was the version of termscal used in chapter 4 for dbm9 and the width study. This was used for the up-down symmetric arbitrary n ELITE benchmarks of the circa and dbm9 test cases. Requires selection of the correct eigenvalue label. In general, this is the first one, which is nearly zero and likely negative.

- “symplas16” - This is the other version of up-down symmetric version of arbitrary n ELITE that has the C matrix calculated and inverted on the coarse mesh. The original ELITE δW diagnostic, termscal.f90, here is normalised to the first field-line bending term, such that its output has the same normalisation as the non-up-down symmetric δW diagnostic. As with the other up-down symmetric version, requires selection of the correct eigenvalue label.

- “lown-workplas16” - This is the non-up-down symmetric version of arbitrary n ELITE that has the C matrix calculated and inverted on the fine mesh. This was used for the non-up-down symmetric arbitrary n ELITE benchmarks of the dbm8 and meudas1025 test cases with the GATO and MARG2D codes respectively. This version was also used for the DIII-D QH-mode study in chapter 5.

- “coarse-clown” - This is the intermediate version of non-up-down symmetric arbitrary n ELITE that has the C matrix calculated on the coarse mesh, but inverted on the fine mesh.

- “plas16” - This is the version of up-down symmetric version of arbitrary n ELITE that has the C matrix calculated and inverted on the coarse mesh. The original ELITE δW diagnostic, termscal.f90, for non-up-down symmetric equilibria is in this version, and is normalised to the first field-line bending term. This was used for the δW diagnostic analysis of QH-mode in chapter 5.

All three versions of the non-up-down symmetric arbitrary n ELITE were benchmarked in section 4.7. The benchmarks of the four test cases, in earlier sections used the versions of ELITE that where C are calculated and inverted on the fine mesh (workplas versions).

C.1.2 Input file parameters

This section details all the input file parameters necessary to run the new arbitrary n ELITE, the δW diagnostic in original ELITE, and running either of the ELITE formalisms with the ideal wall boundary condition. The parameters are discussed in groups. There are three parts to the ELITE code, the equilibrium part of the code which uses the &equil namelist, the vacuum part of the code that uses the &vac namelist, and the plasma part of the code, where the ELITE formalisms are, that uses the &plas namelist. There is also a namelist, &qref_modes, which contains parameters, such as the toroidal mode number n, which is used by all three parts of the code. The only namelist with new parameters is the &plas namelist and this includes new input parameters for arbitrary n ELITE, the ideal wall and the δW diagnostic.The &plas namelist is split into three tables: two with existing parameters, and one with new parameters. All the other namelists are discussed in single tables. All the tables that contain the existing parameters from the original ELITE have been written based on the ELITE manual [99], where there is more detail on these parameters in general than described here. It is also important to consider the parameter convergence discussion in section 4.8.

The first table, table C.1, contains information on the input variables used by the equilibrium code, “equil”. The second table, table C.2, contains information on the input variables used by the vacuum code, “vac”. The third table, table C.3, contains the variables for the “qref_modes” namelist used by all three parts of the ELITE code. The fourth and fifth tables, tables C.4 and C.5, contain the existing variables in the “plas” namelist. Some parameters used with other meshes (i.e. not “mesh type 2”) are in some of the input files, but are not used and therefore are not described here, and are defined in [99]. The final table, table C.6, contains the new “plas” namelist parameters for the recent extensions of ELITE.

Variable	Options	Comments
shape	toq, eqbm, dqds, gato, eqdsk	Existing parameter, see [99]. Defines the type of equilibrium file. EQDSK (g-file) is for EFIT.
setdel	.t. or .f.	Existing parameter, see [99] Default is .f. but used .t. for QH-mode case. If true, modifies the q-profile so that the parameter Δ is fixed.
del_fix	0 <del_fix< 1	Existing parameter, see [99]. Used if setdel=.t.Fixes Δ value
percenflux	typically 0.994-0.998	Existing parameter, see [99]. Only used in EFIT file cases to choose cut off for interpolation of flux surfaces. Increase to convergence, but will not work with 1.0.
npts	integer	Existing parameter, see [99]. Number of poloidal mesh points to read in and store equilibrium data on. If toq or eqbm must equal number in input file. If EFIT should be increased to convergence along with &plas parameter ns, so that they have same converged value.

Table C.1: Input parameters in the &equil namelist, run by the equilibrium part of the ELITE code.

Variable	Options	Comments
npts	integer	Existing parameter, see [99]. Number of poloidal mesh points on the plasma boundary. Should be increased to convergence.
ng	integer power of 2	Existing parameter, see [99]. Vacuum contribution evaluated with tent functions. Should be increased to convergence.

Table C.2: Input parameters in the &vac namelist, run by the vacuum part of the ELITE code.

Variable	Options	Comments
nn	integer	Existing parameter, see [99]. Toroidal mode number, n
nmlow	integer	Existing parameter, see [99]. The number of additional poloidal harmonics retained in the plasma, with lower but sequential mode numbers than those that are resonant in the plasma. Should be increased to convergence.
nmvac	integer	Existing parameter, see [99].The number of poloidal harmonics resonant in the vacuum. Should be increased to convergence.
psimin	0<psimin<1	Existing parameter, see [99]. ELITE does not work at psimin=0, needs to be non zero, as there is not presently an on-axis boundary condition. However, it should be decreased such that the whole eigenfunction is captured in the range from psimin to the plasma edge.
nmwinhalf	integer	Existing parameter, see [99]. Relates to windowing, which is not implemented in arbitrary n ELITE, or in the δW diagnostic.
nxinterp	integer	Existing parameter, see [99]. Only used in EFIT cases, the number of radial equilibrium surfaces to be interpolated to from EFIT file. Should be increased to convergence.
dens	.t. or .f.	Existing parameter, see [99]. .f. except for EFIT cases, where it can be optionally used to allow a density profile to be read in from an equilibrium p-file.

Table C.3: Input parameters in the &qref_modes namelist, used by all three parts of the ELITE code.

C.1.3 Input files for arbitrary n ELITE benchmarks and QH-mode DIII-D discharge 163520, the δW diagnostic and the ideal wall benchmark

This section contains the arbitrary n ELITE input files for the four test cases presented in chapter 4, additionally including the "circa" test case run in the presence of an ideal wall. It also contains an input file for the original ELITE δW diagnostic analysis performed on test case "dbm9", also presented in chapter 4. Finally it contains an example input file which was used for DIII-D discharge 163520, to show an experimental example.

Figure C.1 shows the input file used to create the arbitrary n ELITE results for the circular cross section benchmark with an ideal wall, using the "circa" test case, shown in section 4.3. The input file is shown for an example toroidal mode number of $n = 20$. The n1term switch for the high n approximation of the inertia, n1term=10,

Variable	Options	Comments
meshtype	integer	Existing parameter, see [99]. Use mesh type 2 for arbitrary n ELITE, which is an even spaced mesh. This makes ndist the total number of x mesh points
ndist	integer	Existing parameter, see [99]. Number of x mesh points in a given range. In mesh type 2 this is the total range between psimin and 1, which is the plasma edge. Should be increased to convergence.
gamsq	real	Existing parameter, see [99]. The initial guess for the growth rate squared. If set to 0, inertia terms are switched off and if also run with only 1 iteration, will provide a quick stability test. If equilibrium unstable, an initial guess should be given. ELITE will then iterate over the growth rate to find the true growth rate.
igam	integer of 1 or greater	Existing parameter, see [99]. The number of iterations to find the growth rate from the initial guess. May need increasing to give code enough iterations to converge on the growth rate.
newtstep	default 0.2, can be decreased e.g. 0.05/0.01	Existing parameter, not in reference. Parameter to set the size of the initial step of Newton iteration. If having trouble converging to a growth rate, this parameter can decrease from default (0.2) to for example, 0.05 or 0.01. This is in case the large Newton iteration steps step over the converged value of the growth rate. Decreasing will require a corresponding increase of igam to reach convergence.

Table C.4: The first of two tables of existing input parameters in the &plas namelist, used by the plasma part of the ELITE code.

was also used. n was varied from $n = 12$ to $n = 30$.

Figure C.2 shows the input file used to create the arbitrary n ELITE results for the circular cross section benchmark, using the "circa" test case, shown in section 4.3. The input file is shown for an example toroidal mode number of $n = 5$. The n1term switch for the high n approximation of the inertia, n1term=10, was also used. n was varied from $n = 1$ to $n = 20$, but $n = 1$ and $n = 2$ were unable to be used as the eigenfunction was significantly interacting with the axis.

Figure C.3 shows the input file used to create the arbitrary n ELITE results for the up-down symmetric D-shaped benchmark, using the "dbm9" test case, shown in section 4.4. The input file is shown for an example toroidal mode number of $n = 5$. The n1term switch for the high n approximation of the inertia, n1term=10, was also used. n was varied from $n = 1$ to $n = 20$, but $n = 1$ and $n = 2$ were unable to be used as the eigenfunction was significantly interacting with the axis. The number of vacuum modes, nmvac, was changed as n was varied to maintain convergence: from $n = 1 - 5$ nmvac=11, from $n = 6 - 14$ nmvac=15, and from $n = 15 - 20$ nmvac=17.

Variable	Options	Comments
ns	integer	Existing parameter, see [99]. Mesh that the equilibrium poloidal mesh is splined to. Used when solving for the eigenfunction to manipulate the equilibrium quantities. Should be increased to convergence. When running with EFIT it should be increased to convergence with npts from &equil, such that they both have the same converged value.
updownsym	.t. or .f.	Existing parameter, see [99]. States whether the equilibrium is up-down symmetric or not. For general EFIT cases use .f. and if up-down symmetric code is faster with this set to .t. as it uses the up-down symmetric version of ELITE.
vacuum	.t. or .f.	Existing parameter, see [99]. In general leave set to .t. unless want to run with an ideal wall, then set to .f.
nowindow	.t. or .f.	Existing parameter, see [99]. Original ELITE is optimised to run with this set to .f. However, with arbitrary n ELITE and with the δW diagnostic this should be set to .t. The windowing has not been implemented in these extensions. It does not make sense for low n modes which extend much further across the plasma, and the diagnostic is only run rarely, so it is best to not possibly place a mistake in the code trying to implement windowing.
funcal	.t. or .f.	Existing parameter, not in reference. Determines whether the eigenfunction is calculated for plotting. Required δW diagnostic since needs reconstructing. In general, this should be set to .t. since eigenfunction yields important convergence information, in particular whether the chosen value of psimin captures the whole eigenfunction. Only set to .f. if running ELITE in a script type manner, for example in a varyped run.

Table C.5: The second of two tables of existing input parameters in the &plas namelist, used by the plasma part of the ELITE code.

Figure C.4 shows the input file used to create the original n ELITE results for the up-down symmetric D-shaped δW diagnostic analysis, using the "dbm9" test case, shown in section 4.9. The input file is shown for an example toroidal mode number of $n = 16$.The n1term switch for original ELITE, n1term=2, was used. n was varied from $n = 6$ to $n = 100$. The minimum ψ was changed as n was varied to improve the speed of the calculation at high n, where the mode is more edge localised, and therefore the eigenfunction became zero closer to the plasma edge: from $n = 6 - 16$ psimin=0.05, from $n = 20$ psimin=0.5, and from $n = 25 - 100$ psimin=0.6.

Figure C.5 shows the input file used to create the arbitrary n ELITE results for the non-up-down symmetric D-shaped benchmark, using the "dbm8" test case,

Variable	Options	Comments
n1term	2,10,11	Determines which ELITE is run: 2 uses the original ELITE code, 11 uses the full arbitrary n ELITE code and 10 uses arbitrary n ELITE with the high n inertia approximation.
termscalc	.t. or .f.	This is the flag for the δW diagnostic. where .t. turns on the diagnostic. In general, leave as .f. as diagnostic slows code.
idealwall	.t. or .f.	This is the flag for the ideal wall boundary condition. To run set to .t. and this needs to be run with double shooting and vacuum=.f. In general, leave idealwall as .f.
psimax	1.0	Maximum ψ i.e. value of ψ on the plasma boundary. In general always 1.0
shootpsi	real (e.g. 0.95)	Position in ψ about which the double shooting is performed. 1.1 turns off double shooting algorithm, and is the default. In general, do not want to run with double shooting unless want to use ideal wall boundary condition. If required, should be placed within the eigenfunction of the instability, for example 0.95. Moving the position of shootpsi should not change result, unless the position chosen is too far from the instability.

Table C.6: New input parameters in the &plas namelist, used by the plasma part of the ELITE code.

shown in section 4.5. The input file is shown for an example toroidal mode number of $n = 10$. The n1term switch for the high n approximation of the inertia, n1term=10, was also used. n was varied from $n = 1$ to $n = 20$, but $n = 1$ was unable to be used as the eigenfunction was significantly interacting with the axis. The number of vacuum modes, nmvac, was changed as n was varied to maintain convergence: from $n = 1 - 9$ nmvac=15, and from $n = 10 - 20$ nmvac=17.

Figure C.6 shows the input file used to create the arbitrary n ELITE results for the non-up-down symmetric EFIT-style benchmark, using the “meudas1025” test case, shown in section 4.6. The input file is shown for an example toroidal mode number of $n = 5$. The n1term switch for the high n approximation of the inertia, n1term=10, was also used. n was varied from $n = 1$ to $n = 9$, but $n = 1$ was stable. The minimum ψ was changed as n was varied to improve the speed of the calculation as n increases, necessary due to the high resolution and number of modes used: the mode becomes more edge localised, and therefore the eigenfunction tends to zero nearer the edge of the plasma: for $n = 2 - 3$ psimin=0.25, for $n = 4 - 8$ psimin=0.3 and for $n = 9$ psimin=0.45.

Figure C.7 shows an example input file used to create the arbitrary n ELITE results for the EFITs of the different times in DIII-D QH-mode shot 163520, shown in chapter 5. The input file is shown for an example toroidal mode number of $n = 5$, and

n was varied across the different time windows: the range of n depended on the time in the shot. The minimum ψ was changed as n was varied to improve the speed of the calculation as n increases, necessary due to the high resolution and number of modes used: the mode becomes more edge localised, and therefore the eigenfunction tends to zero nearer the edge of the plasma: for $n = 1-3$ psimin=0.05, for $n = 4$ psimin=0.1, for $n = 5-9$ psimin=0.3 and for $n = 10$ psimin=0.35. Additionally, the number of vacuum modes, nmvac, was changed as n was varied to maintain convergence: for $n = 1$ nmvac=21, $n = 2$ nmvac=23, $n = 3-4$ nmvac=25, $n = 5$ nmvac=27, $n = 6$ nmvac=29 and $n = 7-10$ nmvac=31.

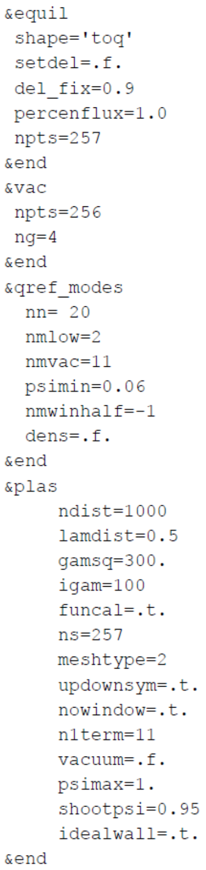

```
&equil
 shape='toq'
 setdel=.f.
 del_fix=0.9
 percenflux=1.0
 npts=257
&end
&vac
 npts=256
 ng=4
&end
&qref_modes
  nn= 20
  nmlow=2
  nmvac=11
  psimin=0.06
  nmwinhalf=-1
  dens=.f.
&end
&plas
     ndist=1000
     lamdist=0.5
     gamsq=300.
     igam=100
     funcal=.t.
     ns=257
     meshtype=2
     updownsym=.t.
     nowindow=.t.
     n1term=11
     vacuum=.f.
     psimax=1.
     shootpsi=0.95
     idealwall=.t.
&end
```

Figure C.1: Input file for an arbitrary n ELITE run using the circular cross section test case, “circa”, in the presence of an ideal wall, where $n = 20$.

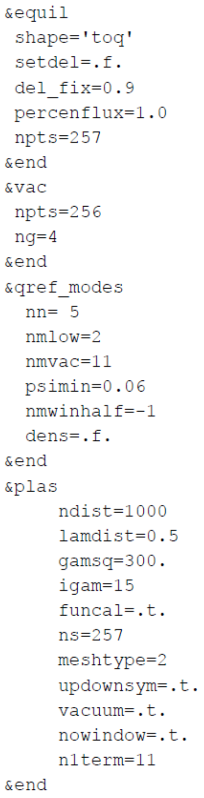

```
&equil
 shape='toq'
 setdel=.f.
 del_fix=0.9
 percenflux=1.0
 npts=257
&end
&vac
 npts=256
 ng=4
&end
&qref_modes
  nn= 5
  nmlow=2
  nmvac=11
  psimin=0.06
  nmwinhalf=-1
  dens=.f.
&end
&plas
     ndist=1000
     lamdist=0.5
     gamsq=300.
     igam=15
     funcal=.t.
     ns=257
     meshtype=2
     updownsym=.t.
     vacuum=.t.
     nowindow=.t.
     n1term=11
&end
```

Figure C.2: Input file for an arbitrary n ELITE run using the circular cross section test case, “circa”, where $n = 5$.

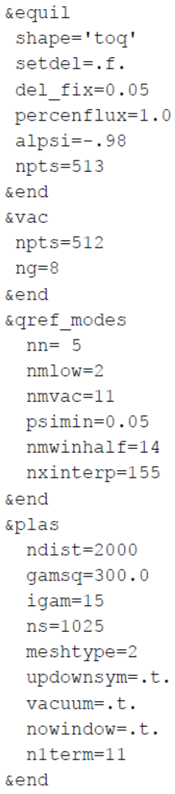

```
&equil
 shape='toq'
 setdel=.f.
 del_fix=0.05
 percenflux=1.0
 alpsi=-.98
 npts=513
&end
&vac
 npts=512
 ng=8
&end
&qref_modes
  nn= 5
  nmlow=2
  nmvac=11
  psimin=0.05
  nmwinhalf=14
  nxinterp=155
&end
&plas
  ndist=2000
  gamsq=300.0
  igam=15
  ns=1025
  meshtype=2
  updownsym=.t.
  vacuum=.t.
  nowindow=.t.
  n1term=11
&end
```

Figure C.3: Input file for an arbitrary n ELITE run using the up-down symmetric D-shaped test case, “dbm9”, test case where $n = 5$.

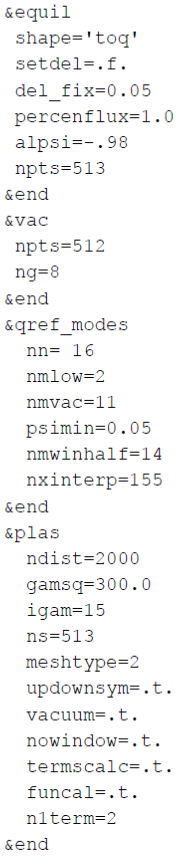

```
&equil
 shape='toq'
 setdel=.f.
 del_fix=0.05
 percenflux=1.0
 alpsi=-.98
 npts=513
&end
&vac
 npts=512
 ng=8
&end
&qref_modes
  nn= 16
  nmlow=2
  nmvac=11
  psimin=0.05
  nmwinhalf=14
  nxinterp=155
&end
&plas
  ndist=2000
  gamsq=300.0
  igam=15
  ns=513
  meshtype=2
  updownsym=.t.
  vacuum=.t.
  nowindow=.t.
  termscalc=.t.
  funcal=.t.
  n1term=2
&end
```

Figure C.4: Input file for an original ELITE run using the δW diagnostic for up-down symmetric D-shaped test case, “dbm9”, test case where $n = 16$.

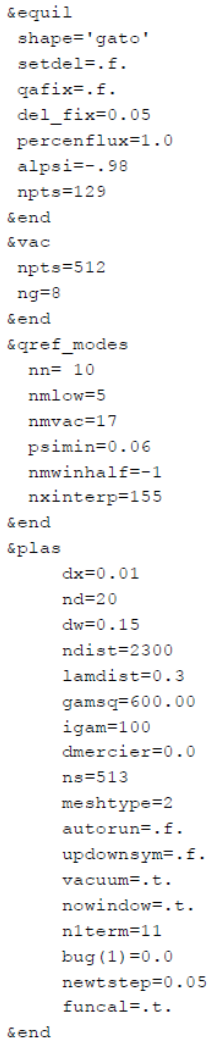

```
&equil
 shape='gato'
 setdel=.f.
 qafix=.f.
 del_fix=0.05
 percenflux=1.0
 alpsi=-.98
 npts=129
&end
&vac
 npts=512
 ng=8
&end
&qref_modes
  nn= 10
  nmlow=5
  nmvac=17
  psimin=0.06
  nmwinhalf=-1
  nxinterp=155
&end
&plas
     dx=0.01
     nd=20
     dw=0.15
     ndist=2300
     lamdist=0.3
     gamsq=600.00
     igam=100
     dmercier=0.0
     ns=513
     meshtype=2
     autorun=.f.
     updownsym=.f.
     vacuum=.t.
     nowindow=.t.
     n1term=11
     bug(1)=0.0
     newtstep=0.05
     funcal=.t.
&end
```

Figure C.5: Input file for an arbitrary n ELITE run using the non-up-down symmetric D-shaped test case, “dbm8”, where $n = 10$.

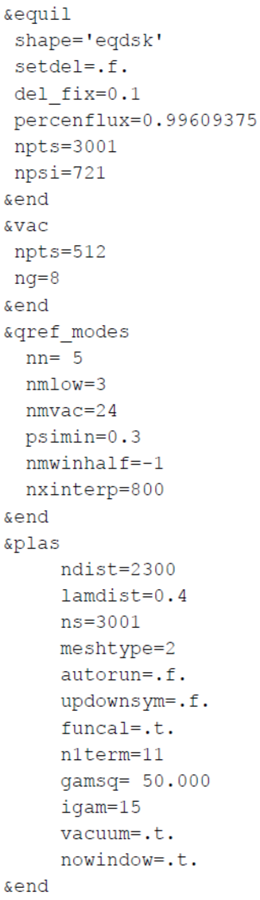

```
&equil
 shape='eqdsk'
 setdel=.f.
 del_fix=0.1
 percenflux=0.99609375
 npts=3001
 npsi=721
&end
&vac
 npts=512
 ng=8
&end
&qref_modes
  nn= 5
  nmlow=3
  nmvac=24
  psimin=0.3
  nmwinhalf=-1
  nxinterp=800
&end
&plas
     ndist=2300
     lamdist=0.4
     ns=3001
     meshtype=2
     autorun=.f.
     updownsym=.f.
     funcal=.t.
     n1term=11
     gamsq= 50.000
     igam=15
     vacuum=.t.
     nowindow=.t.
&end
```

Figure C.6: Input file for arbitrary n ELITE runs using the EIFT-style non-up-down symmetric test case, “meudas1025”, where $n = 5$.

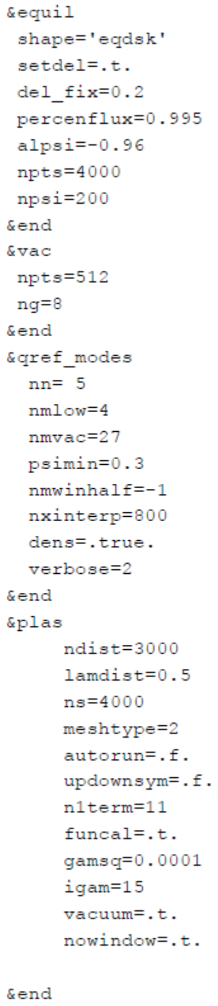

```
&equil
 shape='eqdsk'
 setdel=.t.
 del_fix=0.2
 percenflux=0.995
 alpsi=-0.96
 npts=4000
 npsi=200
&end
&vac
 npts=512
 ng=8
&end
&qref_modes
  nn= 5
  nmlow=4
  nmvac=27
  psimin=0.3
  nmwinhalf=-1
  nxinterp=800
  dens=.true.
  verbose=2
&end
&plas
     ndist=3000
     lamdist=0.5
     ns=4000
     meshtype=2
     autorun=.f.
     updownsym=.f.
     n1term=11
     funcal=.t.
     gamsq=0.0001
     igam=15
     vacuum=.t.
     nowindow=.t.

&end
```

Figure C.7: Input file for arbitrary n ELITE runs for the EFIT of experimental DIII-D shot 163520 where $n = 5$.

Bibliography

[1] United Nations Department of Economic and Social Affairs Population Division. World Population Prospects, the 2015 Revision. `http://esa.un.org/unpd/wpp/DataQuery/`, 2015.

[2] US Energy Information Administration and USA Energy Information Administration. EIA projects world energy consumption will increase 56% by 2040. `http://www.eia.gov/todayinenergy/detail.cfm?id=12251{#}`, 2013.

[3] M. Kikuchi, K. Lackner, and M. Quang. Fusion Physics. IAEA, 1st edition, 2012.

[4] UK Government. Climate change explained. `https://www.gov.uk/guidance/climate-change-explained`.

[5] BBC. Australia's Great Barrier Reef hit by 'worst' bleaching. `http://www.bbc.co.uk/news/world-australia-35914009`, 2016.

[6] World Energy Council. World Energy Resources: Uranium and Nuclear. `http://www.worldenergy.org/wp-content/uploads/2013/09/WER_2013_4_Uranium_and_Nuclear.pdf`, 2013.

[7] Culham Centre for Fusion Energy. Why fusion is needed. `www.ccfe.ac.uk/Why{_}fusion.aspx`, 2012.

[8] J. A. Wesson. Tokamaks. Oxford University Press, 4th edition, 2011.

[9] F. F. Chen. Introduction to Plasma Physics and Controlled Fusion. 2nd edition, 1984.

[10] J. P. Freidberg. Plasma Physics and Fusion Energy. Cambridge University Press, 1st edition, 2007.

[11] R. J. Goldston and P. H. Rutherford. Introduction to Plasma Physics. Taylor & Francis, 1st edition, 1995.

[12] O. A. Hurricane, D. A. Callahan, D. T. Casey, P. M. Celliers, C. Cerjan, E. L. Dewald, T. R. Dittrich, T. Döppner, D. E. Hinkel, L. F. Berzak Hopkins, J. L. Kline, S. Le Pape, T. Ma, A. G. MacPhee, J. L. Milovich, A. Pak, H.-S. Park, P. K. Patel, B. A. Remington, J. D. Salmonson, P. T. Springer, and R. Tommasini. Fuel gain exceeding unity in an inertially confined fusion implosion. Nature, 506(7488):343–8, 2014.

[13] Culham Centre for Fusion Energy. How fusion works. `www.ccfe.ac.uk/How{_}fusion{_}works.aspx`, 2012.

[14] EUROfusion and UKAEA. Snowflake and the multiple divertor concepts. `https://www.euro-fusion.org/newsletter/divertor-concepts/`, 2016.

[15] C. S. Pitcher and P. C. Stangeby. Experimental divertor physics. Plasma Physics and Controlled Fusion, 39(6):779–930, 1997.

[16] J. Jacquinot, V. P. Bhatnagar, J. G. Cordey, L. D. Horton, D. F. H. Start, R. Barnsley, P. Breger, J. P. Christiansen, S. Clement, S. J. Davies, J. K. Ehrenberg, L.-G. Eriksson, G. M. Fishpool, M. Gadeberg, P. J. Harbour, H. J. Jäckel, K. D. Lawson, J. Lingertat, C. G. Lowry, C. F. Maggi, G. F. Matthews, R. D. Monk, D. P. O'Brien, E. Righi, G. Saibene, R. Sartori, B. Schunke, A. C. C. Sips, M. F. Stamp, D. Stork, J. D. Strachan, A. Tanga, K. Thomsen, and the JET Team. Overview of ITER physics deuterium-tritium experiments in JET. Nuclear Fusion, 39(2):235–253, 2002.

[17] B. J. Green and the ITER International Team. ITER: burning plasma physics experiment. Plasma Physics and Controlled Fusion, 45(5):687–706, 2003.

[18] P. C. Stangeby. The Plasma Boundary of Magnetic Fusion Devices. Taylor & Francis, 1st edition, 2000.

[19] E. J. Doyle, R. J. Groebner, K. H. Burrell, P. Gohil, T. Lehecka, N. C. Luhmann Jr., H. Matsumoto, T. H. Osborne, W. A. Peebles, and R. Philipona. Modifications in Turbulence and Edge Electric-Fields at the L-H Transition in the Diii-D Tokamak. Physics of Fluids B, 3(8):2300–2307, 1991.

[20] J. W. Connor and H. R. Wilson. A review of theories of the L-H transition. Plasma Physics and Controlled Fusion, 42(1):R1–R74, 2000.

[21] F. Wagner, G. Becker, K. Behringer, D. Campbell, A. Eberhagen, W. Engelhardt, G. Fussmann, O. Gehre, J. Gernhardt, G. V. Gierke, G. Haas, M. Huang, F. Karger, M. Keilhacker, O. Kluber, M. Kornherr, K. Lackner, G. Lisitano, G. G. Lister, H. M. Mayer, D. Meisel, E. R. Muller, H. Murmann, H. Niedermeyer, W. Poschenrieder, H. Rapp, H. Rohr, F. Schneider, G. Siller, E. Speth, A. Stabler, K. H. Steuer, G. Venus, O. Vollmer, and Z. Yu. Regime of improved confinement and high beta in neutral-beam-heated divertor discharges of the ASDEX tokamak. Physical Review Letters, 49(19):1408–1412, 1982.

[22] A. Kirk, G. F. Counsell, G. Cunningham, J. Dowling, M. Dunstan, H. Meyer, M. Price, S. Saarelma, R. Scannell, M. Walsh, H. R. Wilson, and the MAST Team. Evolution of the pedestal on MAST and the implications for ELM power loadings. Plasma Physics and Controlled Fusion, 49(8):1259–1275, 2007.

[23] H. R. Wilson, S. C. Cowley, A. Kirk, and P. B. Snyder. Magneto-hydrodynamic stability of the H-mode transport barrier as a model for edge localized modes: an overview. Plasma Physics and Controlled Fusion, 48(5A):A71–A84, 2006.

[24] M. E. Fenstermacher, T. H. Osborne, A. W. Leonard, P. B. Snyder, D. M. Thomas, J. A. Boedo, T. A. Casper, R. J. Groebner, M. Groth, M. A. H. Kempenaars, A. Loarte, G. R. McKee, W. M. Meyer, G. Saibene, M. A. VanZeeland, X. Q. Xu, L. Zeng, and the DIII-D Team. Structure, stability and ELM dynamics of the H-mode pedestal in DIII-D. Nuclear Fusion, 45(12):1493–1502, 2005.

[25] P. B. Snyder, H. R. Wilson, T. H. Osborne, and A. W. Leonard. Characterization of peeling-ballooning stability limits on the pedestal. Plasma Physics and Controlled Fusion, 46(5A):A131–A141, 2004.

[26] T. H. Osborne, J. R. Ferron, R. J. Groebner, L. L. Lao, A. W. Leonard, M. A. Mahdavi, R. Maingi, R. L. Miller, A. D. Turnbull, M. R. Wade, and J. G. Watkins. The effect of plasma shape on H-mode pedestal characteristics on DIII-D. Plasma Physics and Controlled Fusion, 42(5A):A175–A184, 2000.

[27] P. B. Snyder, N. Aiba, M. Beurskens, R. J. Groebner, L. D. Horton, A. E. Hubbard, J. W. Hughes, G. T. A. Huysmans, Y. Kamada, A. Kirk, C. Konz, A. W. Leonard, J. Lönnroth, C. F. Maggi, R. Maingi, T. H. Osborne, N. Oyama, A. Pankin, S. Saarelma, G. Saibene, J. L. Terry, H. Urano, and H. R. Wilson. Pedestal stability comparison and ITER pedestal prediction. Nuclear Fusion, 49(8):085035, aug 2009.

[28] R. J. Bickerton, J. W. Connor, and J. B. Taylor. Diffusion Driven Plasma Currents and Bootstrap Tokamak. Nature Physical Science, 229(4):110–112, 1971.

[29] D. Dickinson. Effects of profiles on microinstabilities in tokamaks. PhD thesis, Univeristy of York, 2012.

[30] C. E. Kessel. Bootstrap current in a tokamak. Nuclear Fusion, 34(9):1221–1238, 1994.

[31] Dudson, B. D. MSc in Fusion Energy: Magnetic Confinement Fusion Course Notes. `www-users.york.ac.uk/~bd512//teaching/mcf.html`, 2011.

[32] O. Sauter, C. Angioni, and Y. R. Lin-Liu. Neoclassical conductivity and bootstrap current formulas for general axisymmetric equilibria and arbitrary collisionality regime. Physics of Plasmas, 6(7):2834, 1999.

[33] O. Sauter, C. Angioni, and Y. R. Lin-Liu. Erratum: Neoclassical conductivity and bootstrap current formulas for general axisymmetric equilibria and arbitrary collisionality regime [Phys. Plasmas 6, 2834 (1999)]. Physics of Plasmas, 9(12):5140, 2002.

[34] S. Koh, C. S. Chang, S. Ku, J. E. Menard, H. Weitzner, and W. Choe. Bootstrap current for the edge pedestal plasma in a diverted tokamak geometry. Physics of Plasmas, 19(7):072505, 2012.

[35] A. W. Leonard. Edge-localized-modes in tokamaks. Physics of Plasmas, 21(9):090501, sep 2014.

[36] P. B. Snyder, H. R. Wilson, J. R. Ferron, L. L. Lao, A. W. Leonard, T. H. Osborne, A. D. Turnbull, D. Mossessian, M. Murakami, and X. Q. Xu. Edge localized modes and the pedestal: A model based on coupled peeling-ballooning modes. Physics of Plasmas, 9(5):2037–2043, 2002.

[37] J. W. Connor. Edge-localized modes - physics and theory. Plasma Physics and Controlled Fusion, 40(5):531–542, 1998.

[38] H. Zohm. Edge localized modes (ELMs). Plasma Physics and Controlled Fusion, 38(2):105–128, 1996.

[39] G. Federici, A. Loarte, and G. Strohmayer. Assessment of erosion of the ITER divertor targets during type I ELMs. Plasma Physics and Controlled Fusion, 45(9):1523–1547, 2003.

[40] ITER Physics Basis Editors. Chapter 1: Overview and summary. Nuclear Fusion, 39(12):2137–2172, 1999.

[41] A. Loarte, G. Saibene, R. Sartori, V. Riccardo, P. Andrew, J. Paley, W. Fundamenski, T. Eich, A. Herrmann, G. Pautasso, A. Kirk, G. Counsell, G. Federici, G. Strohmayer, D. Whyte, A. Leonard, R. A. Pitts, I. Landman, B. Bazylev, and S. Pestchanyi. Transient heat loads in current fusion experiments, extrapolation to ITER and consequences for its operation. Physica Scripta, 2007(T128):222–228, 2007.

[42] ITER Organisation. International Tokamak Physics Activity. `https://www.iter.org/org/team/fst/itpa`, 2016.

[43] K. H. Burrell, K. Barada, X. Chen, A. M. Garofalo, R. J. Groebner, C. M. Muscatello, T. H. Osborne, C. C. Petty, T. L. Rhodes, P. B. Snyder, W. M. Solomon, Z. Yan, and L. Zeng. Discovery of stationary operation of quiescent H-mode plasmas with net-zero neutral beam injection torque and high energy confinement on DIII-D. Physics of Plasmas, 23(5):056103, 2016.

[44] A. Loarte, G. Saibene, R. Sartori, D. J. Campbell, M. Becoulet, L. Horton, T. Eich, A. Herrmann, G. Matthews, N. Asakura, A. Chankin, A. Leonard, G. Porter, G. Federici, G. Janeschitz, M. Shimada, and M. Sugihara. Characteristics of type I ELM energy and particle losses in existing devices and their extrapolation to ITER. Plasma Physics and Controlled Fusion, 45(9):1549–1569, 2003.

[45] M. Becoulet, G. T. A. Huysmans, Y. Sarazin, X. Garbet, Ph. Ghendrih, P. Monier-Garbet, J. M. Ane, P. Thomas, A. Grosman, V. Parail, H. Wilson, P. Lomas, P. DeVries, K. D. Zastrow, G. F. Matthews, J. Lonnroth, S. Gerasimov, S. Sharapov, M. Gryaznevich, G. Counsell, A. Kirk, M. Valovic, R. Buttery, A. Loarte, G. Saibene, R. Sartori, A. Leonard, P. Snyder, L. L. Lao, P. Gohil, T. E. Evans, R. A. Moyer, Y. Kamada, A. Chankin, N. Oyama, T. Hatae, N. Asakura, O. Tudisco, E. Giovannozzi, F. Crisanti, C. P. Perez, H. R. Koslowski, T. Eich, A. Sips, L. Horton, A. Herrmann, P. Lang, J. Stober, W. Suttrop, P. Beyer, S. Saarelma, and EFDA-JET Workprogramme Collaborators. Edge localized mode physics and operational aspects in tokamaks. Plasma Physics and Controlled Fusion, 45(12A):A93–A113, 2003.

[46] P. T. Lang, A. Loarte, G. Saibene, L. R. Baylor, M. Becoulet, M. Cavinato, S. Clement-Lorenzo, E. Daly, T. E. Evans, M. E. Fenstermacher, Y. Gribov, L. D. Horton, C. Lowry, Y. Martin, O. Neubauer, N. Oyama, M. J. Schaffer, D. Stork, W. Suttrop, P. Thomas, M. Tran, H. R. Wilson, A. Kavin, and O. Schmitz. ELM control strategies and tools: status and potential for ITER. Nuclear Fusion, 53(4):043004, 2013.

[47] A. Loarte, G. Huijsmans, S. Futatani, L. R. Baylor, T. E. Evans, D. M. Orlov, O. Schmitz, M. Becoulet, P. Cahyna, Y. Gribov, A. Kavin, A. Sashala Naik, D. J. Campbell, T. Casper, E. Daly, H. Frerichs, A. Kischner, R. Laengner, S. Lisgo, R. A. Pitts, G. Saibene, and A. Wingen. Progress on the application of ELM control schemes to ITER scenarios from the non-active phase to DT operation. Nuclear Fusion, 54(3):033007, 2014.

[48] R. A. Moyer, T. E. Evans, T. H. Osborne, P. R. Thomas, M. Becoulet, J. Harris, K. H. Finken, J. A. Boedo, E. J. Doyle, M. E. Fenstermacher, P. Gohil, R. J. Groebner, M. Groth, G. L. Jackson, R. J. La Haye, C. J. Lasnier, A. W. Leonard, G. R. McKee, H. Reimerdes, T. L. Rhodes, D. L. Rudakov, M. J. Schaffer, P. B. Snyder, M. R. Wade, G. Wang, J. G. Watkins, W. P. West, and L. Zeng. Edge localized mode control with an edge resonant magnetic perturbation. Physics of Plasmas, 12(5):056119, 2005.

[49] T. E. Evans, R. A. Moyer, K. H. Burrell, M. E. Fenstermacher, I. Joseph, A. W. Leonard, T. H. Osborne, G. D. Porter, M. J. Schaffer, P. B. Snyder, P. R. Thomas, J. G. Watkins, and W. P. West. Edge stability and transport control with resonant magnetic perturbations in collisionless tokamak plasmas. Nature Physics, 2(6):419–423, 2006.

[50] T. E. Evans, M. E. Fenstermacher, R. A. Moyer, T. H. Osborne, J. G. Watkins, P. Gohil, I. Joseph, M. J. Schaffer, L. R. Baylor, M. Becoulet, J. A. Boedo, K. H. Burrell, J. S. Degrassie, K. H. Finken, T. Jernigan, M. W. Jakubowski, C. J. Lasnier, M. Lelmen, A. W. Leonard, J. Lonnroth, E. Nardon, V. Parail, O. Schmitz,

B. Unterberg, and W. P. West. RMP ELM suppression in DIII-D plasmas with ITER similar shapes and collisionalities. Nuclear Fusion, 48(2):024002, 2008.

[51] M. Becoulet, G. Huysmans, P. Thomas, E. Joffrin, F. Rimini, P. Monier-Garbet, A. Grosman, P. Ghendrih, V. Parail, P. Lomas, G. Matthews, H. Wilson, M. Gryaznevich, G. Counsell, A. Loarte, G. Saibene, R. Sartori, A. Leonard, P. Snyder, T. Evans, P. Gohil, R. Moyer, Y. Kamada, N. Oyama, T. Hatae, K. Kamiya, A. Degeling, Y. Martin, J. Lister, J. Rapp, C. Perez, P. Lang, A. Chankin, T. Eich, A. Sips, J. Stober, L. Horton, A. Kallenbach, W. Suttrop, S. Saarelma, S. Cowley, J. Lonnroth, M. Shimada, A. Polevoi, and G. Federici. Edge localized modes control: Experiment and theory. Journal of Nuclear Materials, 337-339(1-3):677–683, 2005.

[52] R. Maingi, K. Tritz, E. D. Fredrickson, J. E. Menard, S. A. Sabbagh, D. Stutman, M. G. Bell, R. E. Bell, C. E. Bush, D. A. Gates, D. W. Johnson, R. Kaita, S. M. Kaye, H. W. Kugel, B. P. LeBlanc, D. Mueller, R. Raman, A. L. Roquemore, and V. A. Soukhanovskii. Observation of a high performance operating regime with small edge-localized modes in the National Spherical Torus Experiment. Nuclear Fusion, 45(4):264–270, 2005.

[53] D. G. Whyte, A. E. Hubbard, J. W. Hughes, B. Lipschultz, J. E. Rice, E. S. Marmar, M. Greenwald, I. Cziegler, A. Dominguez, T. Golfinopoulos, N. Howard, L. Lin, R. M. McDermott, M. Porkolab, M. L. Reinke, J. Terry, N. Tsujii, S. Wolfe, S. Wukitch, and Y. Lin. I-mode: an H-mode energy confinement regime with L-mode particle transport in Alcator C-Mod. Nuclear Fusion, 50(10):105005, 2010.

[54] J. R. Walk, J. W. Hughes, A. E. Hubbard, J. L. Terry, D. G. Whyte, A. E. White, S. G. Baek, M. L. Reinke, C. Theiler, R. M. Churchill, J. E. Rice, P. B. Snyder, T. Osborne, A Dominguez, and I. Cziegler. Edge-localized mode avoidance and pedestal structure in I-mode plasmasa). Physics of Plasmas, 21(5):056103, may 2014.

[55] N. Oyama, Y. Sakamoto, A. Isayama, M. Takechi, P. Gohil, L. L. Lao, P. B. Snyder, T. Fujita, S. Ide, Y. Kamada, Y. Miura, T. Oikawa, T. Suzuki, H. Takenaga, K. Toi, and the JT-60 Team. Energy loss for grassy ELMs and effects of plasma rotation on the ELM characteristics in JT-60U. Nuclear Fusion, 45(November):871–881, 2005.

[56] G. Saibene, R. Sartori, A. Loarte, D. J. Campbell, P. J. Lomas, V. V. Parail, K. D. Zastrow, Y. Andrew, S. Sharapov, A. Korotkov, M. Becoulet, G.T. A. Huysmans, H. R. Koslowski, R. Budny, G.D Conway, J. Stober, W. Suttrop, A. Kallenbach, M. Von Hellermann, and M. Beurskens. Improved performance of ELMy H-modes at high density by plasma shaping in JET. Plasma Physics and Controlled Fusion, 44(9):1769–1799, 2002.

[57] M. J. Leyland, M. N. A. Beurskens, L. Frassinetti, T. Osborne, P. B. Snyder, C. Giroud, S. Jachmich, G. Maddison, P. Lomas, C. Perez von Thun, S. Saarelma, G. Saibene, K. J. Gibson, and EFDA-JET Collaborators. Pedestal study across a deuterium fuelling scan for high δ ELMy H-mode plasmas on JET with the carbon wall. Nuclear Fusion, 53(8):083028, 2013.

[58] K. H. Burrell, M. E. Austin, D. P. Brennan, J. C. DeBoo, E. J. Doyle, P. Gohil, C. M. Greenfield, R. J. Groebner, L. L. Lao, T. C. Luce, M. A. Makowski, G. R. McKee, R. A. Moyer, T. H. Osborne, M. Porkolab, T. L. Rhodes, J. G. Rost, M. J. Schaffer, B. W. Stallard, E. J. Strait, M. R. Wade, G. Wang, J. G. Watkins, W. P. West, and L. Zeng. Quiescent H-mode plasmas in the DIII-D tokamak. Plasma Physics and Controlled Fusion, 44(5A):A253–A263, 2002.

[59] W. Suttrop, M. Maraschek, G. D. Conway, H. U. Fahrbach, G. Haas, L. D. Horton, T. Kurki-Suonio, C. J. Lasnier, A. W. Leonard, C. F. Maggi, H. Meister, A. Muck, R. Neu, I. Nunes, Th. Putterich, M. Reich, A. C. C. Sips, and the Asdex Upgrade Team. ELM-free stationary H-mode plasmas in the ASDEX Upgrade tokamak. Plasma Physics and Controlled Fusion, 45(8):1399–1416, 2003.

[60] P. B. Snyder, K. H. Burrell, H. R. Wilson, M. S. Chu, M. E. Fenstermacher, A. W. Leonard, R. A. Moyer, T. H. Osborne, M. Umansky, W. P. West, and X. Q. Xu. Stability and dynamics of the edge pedestal in the low collisionality regime: physics mechanisms for steady-state ELM-free operation. Nuclear Fusion, 47(8):961–968, aug 2007.

[61] K. H. Burrell, M. E. Austin, D. P. Brennan, J. C. DeBoo, E. J. Doyle, C. Fenzi, C. Fuchs, P. Gohil, C. M. Greenfield, R. J. Groebner, L. L. Lao, T. C. Luce, M. A. Makowski, G. R. McKee, R. A. Moyer, C. C. Petty, M. Porkolab, C. L. Rettig, T. L. Rhodes, J. G. Rost, B. W. Stallard, E. J. Strait, E. J. Synakowski, M. R. Wade, J. G. Watkins, and W. P. West. Quiescent double barrier high-confinement mode plasmas in the DIII-D tokamak. Physics of Plasmas, 8(5):2153, 2001.

[62] K. H. Burrell, T. H. Osborne, P. B. Snyder, W. P. West, M. E. Fenstermacher, R. J. Groebner, P. Gohil, A. W. Leonard, and W. M. Solomon. Quiescent H-mode plasmas with strong edge rotation in the cocurrent direction. Physical Review Letters, 102(15):155003, 2009.

[63] A. M. Garofalo, W. M. Solomon, J. K. Park, K. H. Burrell, J. C. DeBoo, M. J. Lanctot, G. R. McKee, H. Reimerdes, L. Schmitz, M. J. Schaffer, and P. B. Snyder. Advances towards QH-mode viability for ELM-stable operation in ITER. Nuclear Fusion, 51(8):083018, 2011.

[64] W. Suttrop, V. Hynönen, T. Kurki-Suonio, P. T. Lang, M. Maraschek, R. Neu, A. Stäbler, G. D. Conway, S. Hacquin, M. Kempenaars, P. J. Lomas, M. F. F. Nave, R. A. Pitts, K. D. Zastrow, the ASDEX Upgrade Team, and Contributors

To the JET-EFDA Workprogramme. Studies of the Quiescent H-mode regime in ASDEX Upgrade and JET. Nuclear Fusion, 45(7):721–730, 2005.

[65] Y. Sakamoto, H. Shirai, T. Fujita, S. Ide, T. Takizuka, N. Oyama, and Y. Kamada. Impact of toroidal rotation on ELM behaviour in the H-mode on JT-60U. Plasma Physics and Controlled Fusion, 46(5A):A299–A304, 2004.

[66] P. B. Snyder, T. H. Osborne, K. H. Burrell, R. J. Groebner, A. W. Leonard, R. Nazikian, D. M. Orlov, O. Schmitz, M. R. Wade, and H. R. Wilson. The EPED pedestal model and edge localized mode-suppressed regimes: Studies of quiescent H-mode and development of a model for edge localized mode suppression via resonant magnetic perturbations. Physics of Plasmas, 19(5):056115, 2012.

[67] G. F. Matthews, M. Beurskens, S. Brezinsek, M. Groth, E. Joffrin, A. Loving, M. Kear, M.-L. Mayoral, R. Neu, P. Prior, V. Riccardo, F. Rimini, M. Rubel, G. Sips, E. Villedieu, P. de Vries, and M. L. Watkins. JET ITER-like wall-overview and experimental programme. Physica Scripta, T145:014001, 2011.

[68] J. P. Freidberg. Ideal MHD. Cambridge University Press, 1st edition, 2014.

[69] H. Grad and H. Rubin. Hydromagnetic equilibria and force-free fields. Journal of Nuclear Energy (1954), 386:190–197, 1958.

[70] V. D. Shafranov. Equilibrium of a plasma toroid in a magnetic field. Soviet Physics JETP, 37 (10)(4):775–779, 1960.

[71] S. Saarelma, M. N. A. Beurskens, D. Dickinson, L. Frassinetti, M. J. Leyland, and C. M. Roach. MHD and gyro-kinetic stability of JET pedestals. Nuclear Fusion, 53(12):123012, 2013.

[72] R. L. Miller, M. S. Chu, J. M. Greene, Y. R. Lin-Liu, and R. E. Waltz. Noncircular, finite aspect ratio, local equilibrium model. Physics of Plasmas, 5(4):973, 1998.

[73] C. Konz and R. Zille. HELENA Manual: Fixed Boundary Equilibrium Solver. Max-Planck-Institut fur Plasmaphysik, (October), 2007.

[74] L.L. Lao. EFIT Equilibrium and Reconstruction Fitting Code. `https://fusion.gat.com/theory/Efit`, 2015.

[75] G.T. A. Huysmans, J. P. Goedbloed, and W. Kerner. Isoparametric Bicubic Hermite Elements for Solution of the Grad-Shafranov Equation. Proc. Int. Conf. on Computational Physics (Amsterdam, The Netherlands, 1991), pages 371–376, 1991.

[76] R. L. Miller. Overview of TOQ. `https://fusion.gat.com/THEORY/toq/overview.html`.

[77] L. L. Lao, H. St. John, R. D. Stambaugh, A. G. Kellman, and W. Pfeiffer. Reconstruction of current profile parameters and plasma shapes in tokamaks. Nuclear Fusion, 25(11):1611–1622, 1985.

[78] Q Peng, J Schachter, D P Schissel, and L L Lao. EFIT - an Interactive Approach To High Temperature Fusion Plasma Magnetic Equilibrium Fitting. General Atomics, (June), 1999.

[79] I. B. Bernstein, E. A. Frieman, M. D. Kruskal, and R. M. Kulsrud. An Energy Principle for Hydromagnetic Stability Problems. Proceedings of the Royal Society A: Mathematical, Physical and Engineering Sciences, 244:17–40, 1958.

[80] J. W. Connor, R. J. Hastie, and J. B. Taylor. Shear, periodicity, and plasma ballooning modes. Physical Review Letters, 40(6):396–399, 1978.

[81] G. T. A. Huysmans, S. E. Sharapov, A. B. Mikhailovskii, and W. Kerner. Modeling of diamagnetic stabilization of ideal magnetohydrodynamic instabilities associated with the transport barrier. Physics of Plasmas, 8(10):4292–4305, 2001.

[82] C. Mercier. Un critere necessaire de stabilite hydromagnetique pour un plasma en symetrie de revolution. Nuclear Fusion, 1(1):47–53, 1960.

[83] J. W. Connor, R. J. Hastie, H. R. Wilson, and R. L. Miller. Magnetohydrodynamic stability of tokamak edge plasmas. Physics of Plasmas, 5(7):2687, 1998.

[84] H. R. Wilson and S. C. Cowley. Theory for explosive ideal magnetohydrodynamic instabilities in plasmas. Physical Review Letters, 92(17):175006, 2004.

[85] J. M. Greene and M. S. Chance. The second region of stability against ballooning modes. Nuclear Fusion, 21(4):453–464, 1981.

[86] H. R. Wilson and R. L. Miller. Access to second stability region for coupled peeling-ballooning modes in tokamaks. Physics of Plasmas, 6(3):873, 1999.

[87] C. M. Bishop. Bifurcated temperature profiles and the H-mode. Nuclear Fusion, 27(11):1765–1771, 1987.

[88] C. C. Hegna, J. W. Connor, R. J. Hastie, and H. R. Wilson. Toroidal coupling of ideal magnetohydrodynamic instabilities in tokamak plasmas. Physics of Plasmas, 3(2):584, 1996.

[89] H. Takahashi, M. S. Chance, C. E. Kessel, B. LeBlanc, J. Manickam, and M. Okabayashi. Use of the S- alpha diagram for representing tokamak equilibria in profile modification research. Nuclear Fusion, 32(5):815–824, 1992.

[90] C. M. Bishop. Stability of localized MHD modes in divertor tokamaks - a picture of the H-mode. Nuclear Fusion, 26(8):1063–1071, 1986.

[91] P. B. Snyder, R. J. Groebner, A. W. Leonard, T. H. Osborne, and H. R. Wilson. Development and validation of a predictive model for the pedestal height. Physics of Plasmas, 16(5):056118, 2009.

[92] P. B. Snyder, H. R. Wilson, and X. Q. Xu. Progress in the peeling-ballooning model of edge localized modes: Numerical studies of nonlinear dynamics. Physics of Plasmas, 12(5):056115, 2005.

[93] S. Saarelma, A. Alfier, M. N. A. Beurskens, R. Coelho, H. R. Koslowski, Y. Liang, I. Nunes, and JET-EFDA Contributors. MHD stability analysis of small ELM regimes in JET. Plasma Physics and Controlled Fusion, 51(3):035001, 2009.

[94] P. B. Snyder, H. R. Wilson, J. R. Ferron, L. L. Lao, A. W. Leonard, D. Mossessian, M. Murakami, T. H. Osborne, A. D. Turnbull, and X. Q. Xu. ELMs and constraints on the H-mode pedestal: peeling-ballooning stability calculation and comparison with experiment. Nuclear Fusion, 44(2):320–328, 2004.

[95] G. Saibene, N. Oyama, J. Lönnroth, Y. Andrew, E. de la Luna, C. Giroud, G.T. A. Huysmans, Y. Kamada, M. A. H. Kempenaars, A. Loarte, D. McDonald, M. F. F. Nave, A. Meiggs, V. Parail, R. Sartori, S. Sharapov, J. Stober, T. Suzuki, M. Takechi, K. Toi, and H. Urano. The H-mode pedestal, ELMs and TF ripple effects in JT-60U/JET dimensionless identity experiments. Nuclear Fusion, 47(8):969–983, 2007.

[96] C. F. Maggi, S. Saarelma, F. J. Casson, C. Challis, E. de la Luna, L. Frassinetti, C. Giroud, E. Joffrin, J. Simpson, M. Beurskens, I. Chapman, J. Hobirk, M. Leyland, P. Lomas, C. Lowry, I. Nunes, F. Rimini, A. C. C. Sips, and H. Urano. Pedestal confinement and stability in JET-ILW ELMy H-modes. Nuclear Fusion, 55(11):113031, 2015.

[97] A. W. Leonard, R. J. Groebner, T. H. Osborne, and P. B. Snyder. Influence of global beta, shape, and rotation on the H-mode pedestal structure in DIII-D. Physics of Plasmas, 15(5):056114, 2008.

[98] H. R. Wilson, P. B. Snyder, G. T. A. Huysmans, and R. L. Miller. Numerical studies of edge localized instabilities in tokamaks. Physics of Plasmas, 9(4):1277, 2002.

[99] P. B. Snyder, H. R. Wilson, and S. Saarelma. A Practical User's Guide for ELITE. 2006.

[100] P. B. Snyder. Private Communication, 2016.

[101] L. C. Bernard, F. J. Helton, and R. W. Moore. GATO: An MHD stability code for axisymmetric plasmas with internal separatrices. Computer Physics Communications, 24(3-4):377–380, 1981.

[102] A. D. Turnbull. GATO. `https://fusion.gat.com/THEORY/gato/`, 2007.

[103] S. Tokuda and T. Watanabe. A new eigenvalue problem associated with the two-dimensional Newcomb equation without continuous spectra. Physics of Plasmas, 6(8):3012–3026, 1999.

[104] S. Tokuda and T. Watanabe. MARG2D code: Eigenvalue Problem for Two Dimensional Newcomb Equation. Plasma Physics and Fusion Technology, 29(8):113, 1997.

[105] M. L. Boas. Mathematical Methods in the Physical Sciences. Wiley, 3rd edition, 2006.

[106] J. W. Connor, R. J. Hastie, and J. B. Taylor. High Mode Number Stability of an Axisymmetric Toroidal Plasma. Proceedings of the Royal Society A: Mathematical, Physical and Engineering Sciences, 365(1720):1–17, 1979.

[107] D. Dickinson, S. Saarelma, R. Scannell, A. Kirk, C. M. Roach, and H. R. Wilson. Towards the construction of a model to describe the inter-ELM evolution of the pedestal on MAST. Plasma Physics and Controlled Fusion, 53(11):115010, 2011.

[108] F. Jenko and W. Dorland. Nonlinear electromagnetic gyrokinetic simulations of tokamak plasmas. Plasma Physics and Controlled Fusion, 43(12A):A141–A150, 2001.

[109] E. A. Belli and J. Candy. Fully electromagnetic gyrokinetic eigenmode analysis of high-beta shaped plasmas. Physics of Plasmas, 17(11):112314, 2010.

[110] M. J. Pueschel, M. Kammerer, and F. Jenko. Gyrokinetic turbulence simulations at high plasma beta. Physics of Plasmas, 15(10):102310, 2008.

[111] P. B. Snyder, R. J. Groebner, J. W. Hughes, T. H. Osborne, M. Beurskens, A. W. Leonard, H. R. Wilson, and X. Q. Xu. A first-principles predictive model of the pedestal height and width: development, testing and ITER optimization with the EPED model. Nuclear Fusion, 51(10):103016, 2011.

[112] D. Dickinson, C. M. Roach, S. Saarelma, R. Scannell, A. Kirk, and H. R. Wilson. Kinetic instabilities that limit β in the edge of a tokamak plasma: A picture of an H-mode pedestal. Physical Review Letters, 108(13):135002, 2012.

[113] R. J. Groebner, P. B. Snyder, T. H. Osborne, A. W. Leonard, T. L. Rhodes, L. Zeng, E. A. Unterberg, Z. Yan, G. R. McKee, C. J. Lasnier, J. A. Boedo, and J. G. Watkins. Limits to the H-mode pedestal pressure gradient in DIII-D. Nuclear Fusion, 50(6):064002, 2010.

[114] R. J. Groebner, C. S. Chang, J. W. Hughes, R. Maingi, P. B. Snyder, X. Q. Xu, J. A. Boedo, D. P. Boyle, J. D. Callen, J. M. Canik, I. Cziegler, E. M. Davis, A. Diallo, P. H. Diamond, J. D. Elder, D. P. Eldon, D. R. Ernst, D. P.

Fulton, M. Landreman, A. W. Leonard, J. D. Lore, T. H. Osborne, A. Y. Pankin, S. E. Parker, T. L. Rhodes, S. P. Smith, A. C. Sontag, W. M. Stacey, J. Walk, W. Wan, E. H. J. Wang, J. G. Watkins, A. E. White, D. G. Whyte, Z. Yan, E. A. Belli, B. D. Bray, J. Candy, R. M. Churchill, T. M. Deterly, E. J. Doyle, M. E. Fenstermacher, N. M. Ferraro, A. E. Hubbard, I. Joseph, J. E. Kinsey, B. LaBombard, C. J. Lasnier, Z. Lin, B. L. Lipschultz, C. Liu, Y. Ma, G. R. McKee, D. M. Ponce, J. C. Rost, L. Schmitz, G. M. Staebler, L. E. Sugiyama, J. L. Terry, M. V. Umansky, R. E. Waltz, S. M. Wolfe, L. Zeng, and S. J. Zweben. Improved understanding of physics processes in pedestal structure, leading to improved predictive capability for ITER. Nuclear Fusion, 53(9):093024, 2013.

[115] B. LaBombard, J. W. Hughes, N. Smick, A. Graf, K. Marr, R. McDermott, M. Reinke, M. Greenwald, B. Lipschultz, J. L. Terry, D. G. Whyte, S. J. Zweben, and Alcator C-Mod Team. Critical gradients and plasma flows in the edge plasma of Alcator C-Mod. Physics of Plasmas, 15(5):056106, 2008.

[116] D. Dickinson, C. M. Roach, S. Saarelma, R. Scannell, A. Kirk, and H. R. Wilson. Microtearing modes at the top of the pedestal. Plasma Physics and Controlled Fusion, 55(7):074006, 2013.

[117] T. H. Osborne, K. H. Burrell, R. J. Groebner, L. L. Lao, A. W. Leonard, R. Maingi, R. L. Miller, G. D. Porter, G. M. Staebler, and A. D. Turnbull. H-mode pedestal characteristics in ITER shape discharges on DIII-D. Journal of Nuclear Materials, 266-269:131–137, 1999.

[118] R. J. Groebner and T. H. Osborne. Scaling studies of the high mode pedestal. Physics of Plasmas, 5(5):1800, 1998.

[119] A. Kirk, T. O'Gorman, S. Saarelma, R. Scannell, H. R. Wilson, and the MAST Team. A comparison of H-mode pedestal characteristics in MAST as a function of magnetic configuration and ELM type. Plasma Physics and Controlled Fusion, 51(6):065016, 2009.

[120] A. Sykes, R. J. Akers, L. C. Appel, E. R. Arends, P. G. Carolan, N. J. Conway, G. F. Counsell, G. Cunningham, A. Dnestrovskij, Yu. N. Dnestrovskij, A. R. Field, S. J. Fielding, M. P. Gryaznevich, S. Korsholm, E. Laird, R. Martin, M. P. S. Nightingale, C. M. Roach, M. R. Tournianski, M. J. Walsh, C. D. Warrick, H. R. Wilson, S. You, MAST Team, and NBI Team. First results from MAST. Nuclear Fusion, 41(10):1423–1433, 2001.

[121] I. H. Hutchinson, R. L. Boivin, F. Bombarda, P. T. Bonoli, S. Fairfax, C. Fiore, J. A. Goetz, S. N. Golovato, R. S. Granetz, M. J. Greenwald, S. F. Horne, A. E. Hubbard, J. H. Irby, B. LaBombard, B. Lipschultz, E. S. Marmar, G. M. McCracken, M. Porkolab, J. E. Rice, J. A. Snipes, Y. Takase, J. L. Terry, S. M. Wolfe, C. Christensen, D. T. Garnier, M. A. Graf, T. Hsu, T. Luke, M. J. May,

A. Niemczewski, G. Tinios, J. Schachter, and J. Urbahn. First results from Alcator-C-MOD. Physics of Plasmas, 1(5):1511, 1994.

[122] H. Urano, T. Takizuka, Y. Kamada, N. Oyama, H. Takenaga, and the JT-60 Team. Dimensionless parameter dependence of H-mode pedestal width using hydrogen and deuterium plasmas in JT-60U. Nuclear Fusion, 48(4):045008, 2008.

[123] O. Gruber, H. S. Bosch, S. Günter, A. Herrmann, A. Kallenbach, M. Kaufmann, K. Krieger, K. Lackner, V. Mertens, R. Neu, F. Ryter, J. Schweinzer, A. Stäbler, W. Suttrop, R. Wolf, and et Al. Overview of ASDEX Upgrade results. Nuclear Fusion, 39(9Y):1321, 1999.

[124] M. N. A. Beurskens, T. H. Osborne, P. A. Schneider, E. Wolfrum, L. Frassinetti, R. Groebner, P. Lomas, I. Nunes, S. Saarelma, R. Scannell, P. B. Snyder, D. Zarzoso, I. Balboa, B. Bray, M. Brix, J. Flanagan, C. Giroud, E. Giovannozzi, M. Kempenaars, A. Loarte, E. De La Luna, G. Maddison, C. F. Maggi, D. McDonald, R. Pasqualotto, G. Saibene, R. Sartori, E. Solano, M. Walsh, L. Zabeo, the DIII-D Team, the ASDEX Upgrade Team, and JET-EFDA Contributors. H-mode pedestal scaling in DIII-D, ASDEX upgrade, and JET. Physics of Plasmas, 18(5):056120, 2011.

[125] B. D. Scott. Computation of electromagnetic turbulence and anomalous transport mechanisms in tokamak plasmas. Plasma Physics and Controlled Fusion, 45(12A):A385–A398, 2003.

[126] P. B. Snyder and G. W. Hammett. Electromagnetic effects on plasma microturbulence and transport. Physics of Plasmas, 8(3):744–749, 2001.

[127] W. M. Tang, J. W. Connor, and R. J. Hastie. Kinetic-ballooning-mode theory in general geometry. Nuclear Fusion, 20(11):1439–1453, 1980.

[128] T. M. Bird and C. C. Hegna. A model for microinstability destabilization and enhanced transport in the presence of shielded 3D magnetic perturbations. Nuclear Fusion, 53(1):013004, 2013.

[129] R.M.O. Galvao and J Rem. Application of the Suydam Method To the Ballooning Stability Problem. Computer Physics Communications, 22(4):399–402, 1981.

[130] H. R. Wilson. Private Communication, 2016.

[131] F. Liu, G. T. A. Huijsmans, A. Loarte, A. M. Garofalo, W. M. Solomon, P. B. Snyder, M. Hoelzl, and L. Zeng. Nonlinear MHD simulations of Quiescent H-mode plasmas in DIII-D. Nuclear Fusion, 55(11):113002, 2015.

[132] X. Chen. Private Communication, 2016.

[133] Xi Chen, K. H. Burrell, N. M. Ferraro, T. H. Osborne, M. E. Austin, A. M. Garofalo, R. J. Groebner, G. J. Kramer, N. C. Luhmann Jr., G. R. McKee, C. M. Muscatello, R. Nazikian, X. Ren, P. B. Snyder, W. M. Solomon, B. J. Tobias, and Z. Yan. Rotational shear effects on edge harmonic oscillations in DIII-D quiescent H-mode discharges. Nuclear Fusion, 56(7):076011, 2016.

[134] K. H. Burrell. Private Communication, 2016.

[135] T. H. Osborne. Private Communication, 2016.

[136] M. G. Dunne, S. Rathgeber, A. Burckhart, R. Fischer, L. Giannone, P. J. Mccarthy, P. A. Schneider, E. Wolfrum, and the ASDEX Upgrade Team. Impact of Te and ne on edge current density profiles in ELM mitigated regimes on ASDEX Upgrade. Nuclear Fusion, 55(1):013013, 2015.

[137] C. F. Maggi, R. J. Groebner, N. Oyama, R. Sartori, L. D. Horton, A. C. C. Sips, W. Suttrop, the ASDEX Upgrade Team, A. Leonard, T. C. Luce, M. R. Wade, the DIII-D Team, Y. Kamada, H. Urano, the JT-60U Team, Y. Andrew, C. Giroud, E. Joffrin, E. de la Luna, and JET-EFDA Contributors. Characteristics of the H-mode pedestal in ASDEX Upgrade , DIII-D , JET and JT-60U. Nuclear Fusion, 47(7):535–551, 2007.

[138] E. Wolfrum, A. Burckhart, R. Fischer, N. Hicks, C. Konz, B. Kurzan, B. Lagner, T. Putterich, H. Zohm, and the ASDEX Upgrade Team. Investigation of inter-ELM pedestal profiles in ASDEX Upgrade. Plasma Physics and Controlled Fusion, 51(12):124057, 2009.

[139] A. Burckhart, E. Wolfrum, R. Fischer, K. Lackner, H. Zohm, and the ASDEX Upgrade Team. Inter-ELM behaviour of the electron density and temperature pedestal in ASDEX Upgrade. Plasma Physics and Controlled Fusion, 52(10):105010, 2010.

[140] P. A. Schneider, E. Wolfrum, R. J. Groebner, T. H. Osborne, M. N. A. Beurskens, M. G. Dunne, J. R. Ferron, S. Gunter, B. Kurzan, K. Lackner, P. B. Snyder, H. Zohm, the ASDEX Upgrade Team, the DIII-D Team, and JET-EFDA Contributors. Differences in the H-mode pedestal width of temperature and density. Plasma Physics and Controlled Fusion, 54(10):105009, 2012.

[141] P. A. Schneider, E. Wolfrum, R. J. Groebner, T. H. Osborne, M. N. A. Beurskens, M. G. Dunne, B. Kurzan, T. Putterich, E. Viezzer, the ASDEX Upgrade Team, the DIII-D Team, and JET-EFDA Contributors. Analysis of temperature and density pedestal gradients in AUG , DIII-D and JET. Nuclear Fusion, 53(7):073039, 2013.

[142] P. A. Schneider, L. Barrera Orte, A. Burckhart, M. G. Dunne, C. Fuchs, A. Gude, B. Kurzan, W. Suttrop, E. Wolfrum, and the ASDEX Upgrade Team. Pedestal

and edge localized mode characteristics with different first wall materials and nitrogen seeding in ASDEX Upgrade. Plasma Physics and Controlled Fusion, 57(1):014029, 2015.

[143] E. Wolfrum, E. Viezzer, A. Burckhart, M. G. Dunne, P. A. Schneider, M. Willensdorfer, E. Fable, R. Fischer, D. Hatch, F. Jenko, B. Kurzan, P. Manz, S. K. Rathgeber, and the ASDEX Upgrade Team. Overview of recent pedestal studies at ASDEX Upgrade. Nuclear Fusion, 55(5):053017, 2015.

[144] D. R. Hatch, D. Told, F. Jenko, H. Doerk, M. G. Dunne, E. Wolfrum, E. Viezzer, the ASDEX Upgrade Team, and M. J. Pueschel. Gyrokinetic study of ASDEX Upgrade inter-ELM pedestal profile evolution. Nuclear Fusion, 55(6):063028, 2015.

[145] M. N. A. Beurskens, J. Schweinzer, C. Angioni, A. Burckhart, C. D. Challis, I. Chapman, R. Fischer, J. Flanagan, L. Frassinetti, C. Giroud, J. Hobirk, E. Joffrin, A. Kallenbach, M. Kempenaars, M. Leyland, P. Lomas, G. Maddison, M. Maslov, R. McDermott, R. Neu, I. Nunes, T. Osborne, F. Ryter, S. Saarelma, P. A. Schneider, P. Snyder, G. Tardini, E. Viezzer, E. Wolfrum, the ASDEX Upgrade Team, and JET-EFDA Contributors. The effect of a metal wall on confinement in JET and ASDEX Upgrade. Plasma Physics and Controlled Fusion, 55(12):124043, 2013.

[146] C. D. Challis, J. Garcia, M. Beurskens, P. Buratti, E. Delabie, P. Drewelow, L. Frassinetti, C.. Giroud, N. Hawkes, J. Hobirk, E. Joffrin, D. Keeling, D. B. King, C. F. Maggi, J. Mailloux, C. Marchetto, D. McDonald, I. Nunes, G. Pucella, S. Saarelma, J. Simpson, and JET Contributors. Improved Confinement in JET High beta Plasmas with an ITER-Like Wall. Nuclear Fusion, 55(5):053031, 2015.

[147] M. J. Leyland, M. N. A. Beurskens, L. Frassinetti, C. Giroud, S. Saarelma, P. B. Snyder, J. Flanagan, S. Jachmich, M. Kempenaars, P. Lomas, G. Maddison, R. Neu, I. Nunes, K. J. Gibson, and JET-EFDA Contributors. The H-mode pedestal structure and its role on confinement in JET with a carbon and metal wall. Nuclear Fusion, 55(1):013019, 2015.

[148] M. J. Leyland. The pedestal structure in high performance JET plasmas. PhD thesis, University of York, 2014.

[149] L. Frassinetti, M. N. A. Beurskens, R. Scannell, T. H. Osborne, J. Flanagan, M. Kempenaars, M. Maslov, R. Pasqualotto, M. Walsh, and JET-EFDA Contributors. Spatial resolution of the JET Thomson scattering system. Review of Scientific Instruments, 83(1):013506, 2012.

[150] M. J. Leyland, M. N. A. Beurskens, J. C. Flanagan, L. Frassinetti, K. J. Gibson, M. Kempenaars, M. Maslov, and R. Scannell. Edge profile analysis of Joint European Torus (JET) Thomson scattering data: Quantifying the systematic error

due to edge localised mode synchronisation. Review of Scientific Instruments, 87(1):013507, 2016.

[151] C. F. Maggi. Private Communication, 2016.

[152] E. R. Arends. Density gradients in spherical tokamak plasmas. PhD thesis, Technische Universiteit Eindhoven, 2003.

[153] R. Scannell, M. Beurskens, P. G. Carolan, A. Kirk, M. Walsh, T. O'Gorman, and T. H. Osborne. Deconvolution of Thomson scattering temperature profiles. Review of Scientific Instruments, 82(5):053501, 2011.

[154] R. J. Groebner, D. R. Baker, K. H. Burrell, T. N. Carlstrom, J. R. Ferron, P. Gohil, L. L. Lao, T. H. Osborne, D. M. Thomas, W. P. West, J. A. Boedo, R. A. Moyer, G. R. McKee, R. D. Deranian, E. J. Doyle, C. L. Rettig, T. L. Rhodes, and J. C. Rost. Progress in quantifying the edge physics of the H mode regime in DIII-D. Nuclear Fusion, 41(12):1789–1802, 2001.

[155] S. Saarelma and J. Simpson. Stability analysis guide and training on JET. `http://users.euro-fusion.org/tfwiki/index.php/T13-18:{_}Coordination{_}of{_}modelling{_}of{_}ELMs{_}and{_}pedestal` password required, 2014.

[156] S. Saarelma. Private Communication, 2016.

[157] A. Kallenbach, N. Asakura, A. Kirk, A. Korotkov, M. A. Mahdavi, D. Mossessian, and G. D. Porter. Multi-machine comparisons of H-mode separatrix densities and edge profile behaviour in the ITPA SOL and Divertor Physics Topical Group. Journal of Nuclear Materials, 337-339(1-3 SPEC. ISS.):381–385, 2005.

[158] E. A. Belli and J. Candy. Kinetic calculation of neoclassical transport including self-consistent electron and impurity dynamics. Plasma Physics and Controlled Fusion, 50(9):095010, 2008.

[159] A. B. Mikhailovskii, G. T. A. Huysmans, W. O. K. Kerner, and S. E. Sharapov. Optimization of computational MHD normal-mode analysis for tokamaks. Plasma Physics Reports, 23(10):844–857, 1997.

[160] M. J. Leyland. Private Communication, 2016.

[161] L. Frassinetti. Private Communication, 2016.

[162] W. Dorland, C. M. Roach, and D. Dickinson. The Gyrokinetics Project. `https://sourceforge.net/p/gyrokinetics/code/HEAD/tree/`, 2016.

[163] D. Dickinson. Private Communication, 2016.

[164] C. M. Bishop, P. Kirby, J. W. Connor, R. J. Hastie, and J B Taylor. Ideal MHD ballooning stability in the vicinity of a separatrix. Nuclear Fusion, 24(12):1579–1584, 1984.

[165] A. J. Webster, J. Morris, T. N. Todd, S. Brezinsek, P. Coad, J. Likonen, M. Rubel, and JET-EFDA Contributors. Resonant-like behaviour during edge-localised mode cycles in the Joint European Torus. Physics of Plasmas, 22(8):082501, 2015.